Improving the sensitivity and stability of a cold-atom gyroscope with real-time control methods

Mohamed Guessoum

SORBONNE UNIVERSITÉS

SYRTE l'Observatoire de Paris | PSL

SYstèmes de Référence Temps-Espace

THÈSE DE DOCTORAT
DE SORBONNE UNIVERSITÉS

Spécialité : Physique

École doctorale nº564: Physique en Île-de-France

réalisée

au SYRTE, Observatoire de Paris

présentée par

Mohamed GUESSOUM

pour obtenir le grade de :

DOCTEUR DE SORBONNE UNIVERSITÉS

Sujet de la thèse :

Improving the sensitivity and stability of a cold-atom gyroscope with real-time control methods

soutenue le October 2023

devant le jury composé de :

M.	Simon BERNON	Rapporteur
M.	Jean-François CLEMENT	Rapporteur
Mme	Saïda GUELLATI-KHELIFA	Examinatrice
Mme	Agnès MAITRE	Examinatrice
M.	Yann KERSALE	Examinateur
M.	Thomas LEVEQUE	Membre Invité
M.	Arnaud LANDRAGIN	Membre Invité
M.	Remi GEIGER	Directeur de thèse

Acknowledgements

Firstly, I would like to extend my sincere appreciation to Thomas Lévèque, Yann Kersalé, Agnès Maitre, Saïda Guellati-Khelifa, Jean-François Clément, and Simon Bernon for their participation in the examination of my thesis. Special thanks to Jean-François Clément and Simon Bernon for taking on the roles of referees.

My thesis work was supervised by Remi Geiger and guided by Arnaud Landragin. I am immensely grateful for their support, advice, and the enriching discussions we shared.

I am particularly grateful to my fellow PhD students who collaborated with me on the gyroscope project: Romain Gautier, who guided me through the initial handling of the gyroscope during my first year, and Nathan Marlière, who not only is continuing my research but also provided invaluable assistance in my final months. My thanks also extend to the postdoctoral researchers: Quentin Bouton, who worked alongside me in my first year, and Charbel Cherfane, who contributed to the gyroscope project during my last year.

My research was conducted within the Atomic Interferometry and Inertial Sensors team at SYRTE. I want to thank all its members for their insightful exchanges, both during and outside our team meetings: the permanent staff members, Frank Pereira Dos Santos, Sébastien Merlet, Carlos Garrido Alzar, Quentin Beaufils, and Leonid Sidorenkov, as well as the doctoral students, postdocs, and engineers who were part of the team during my PhD research: Luc, Raphael, Yahn, Jöel, Etienne, Maxime, Diego, Rayan, Jean-Marc, Valentin, Franck, and Robin.

I am indebted to Michel Lours, José Pinto, and Laurent Volodimer from the electronics department for their expert advice and for the circuits they have crafted and repaired. My gratitude goes to the MUTA service, especially to David Holleville and Bertrand Venon for the urgency with which they handled mechanical parts. I am also thankful to the members of the mechanical workshop for their skilled manufacturing. Appreciation is due to Pascal Blondé, Maxime, and Teddy from the IT service. I am grateful for the administrative and management team, particularly Marine Pailler, for her assistance with administrative procedures. My heartfelt thanks to all members of SYRTE for their warm welcome and the scientifically stimulating conversations we've had.

In addition to my professional circle, the unwavering support of my family has been a cornerstone of my journey. I owe a profound debt of gratitude to my father, whose belief in my abilities never wavered, and to my brothers Tahar and Sofiane, whose financial support was crucial in making my transition to France possible. My sisters: Akila, Nassima and Hala have been a constant source of encouragement, and their support has been invaluable. My late mother, who instilled in me the value of education from childhood, has been a guiding light throughout my life; this thesis is dedicated to her memory, with all my love and respect. I must also express my deepest appreciation to my fiancée, Fatima, whose unconditional support has been a source of comfort and strength. Her presence and encouragement have been a pillar of strength during the challenging times of my PhD journey. Each of you has contributed to this achievement in your unique way, and I am eternally grateful.

Finally, I am grateful to SIRTEQ for making my research possible by funding my thesis.

Contents

I Introduction **7**
- I.1 Atomic interferometry and inertial sensing . . . 7
- I.2 Gyroscope technologies . . . 7
- I.3 Performance . . . 9
- I.4 Purpose of the thesis work . . . 11
- I.5 Plan of the thesis . . . 12

II Principles of atomic interferometry **13**
- II.1 Stimulated Raman Transitions . . . 13
  - II.1.a Three-level system . . . 14
  - II.1.b Effective Two-level system . . . 16
  - II.1.c Transfer Matrix . . . 18
  - II.1.d Atomic optics . . . 18
  - II.1.e Velocity selectivity . . . 19
- II.2 Effective Rabi frequency and light shifts . . . 20
  - II.2.a Effective Rabi frequency . . . 20
  - II.2.b Differential lightshift . . . 20
  - II.2.c Mean lightshift . . . 22
- II.3 Atomic interferometry and inertial sensing . . . 23
  - II.3.a The 4-pulse geometry: the atomic gyroscope . . . 24
  - II.3.b Transition probability . . . 25
  - II.3.c Phase of the interferometer . . . 25
  - II.3.d Measuring phase shift for an atom interferometer . . . 26
  - II.3.e Fundamental limit: Quantum Shot Noise . . . 26
- II.4 Sensitivity function . . . 27
- II.5 Conclusion . . . 30

III Experimental setup **31**
- III.1 Structure of the experiment . . . 31
- III.2 Sequence of measurement . . . 34
  - III.2.a Trapping and cooling . . . 34
  - III.2.b Magnetic State Selection: Stern Gerlach . . . 35
  - III.2.c Interrogation region . . . 36
  - III.2.d Detection . . . 40
- III.3 Lasers setup . . . 43
  - III.3.a Trapping and cooling / Detection . . . 43

III.3.b Raman pulses generation. 47
III.4 Complementary sensors 51
III.4.a Seismometers 51
III.4.b Tilt monitoring and control 53
III.4.c Orientation and position sensors 53
III.5 Real-time vibrations compensation and mid-fringe lock 55
III.5.a Real-time compensation (RTC) 57
III.5.b Mid-fringe lock (MFL) 59
III.6 Interferometer configurations 61
III.6.a Simple-Joint Mode 61
III.6.b Double-Joint Mode 63
III.6.c Parasitic interferometers and time assymetry 64
III.6.d Gyroscope measurements and data analysis 66
III.7 Stern-Gerlach coil replacement 67
III.8 Software 72
III.8.a Sequencer software 72
III.8.b Software acquisition 73
III.8.c Lasers auto-relock 74
III.9 Conclusion 75

IV Sagnac Effect Measurements over a year **79**
IV.1 The Sagnac Effect 80
IV.2 Scale factor estimation 82
IV.2.a Measurement of the interrogation time, $2T$ 82
IV.2.b The effective wave-number, k_{eff} 82
IV.2.c Local gravity, g 82
IV.2.d Raman collimators angle, θ_0 83
IV.2.e Earth Rotation rate and latitude, Ω_E and ψ 84
IV.2.f Wave-vectors difference, ϵ 85
IV.3 Scale factor measurement 87
IV.3.a Preparation phase: Trajectories alignement 87
IV.3.b Rotating the experiment 89
IV.4 Results 91
IV.5 Conclusion 96

V Real-time control of the atom interferometer phase for the double diffraction regime **97**
V.1 Frequency jumps 98
V.1.a Lightshift variation 99
V.1.b Effective Rabi frequency Ω_{eff} compensation 100
V.1.c Upgrading the lasers system 102
V.1.d Measuring the scale factor, L 103
V.2 Mirror position jumps 107
V.2.a System design and implementation 107
V.2.b Measurement of the scale factor for the piezo mirror. 109
V.3 Implementing RTC for vibrations 111

VI Conclusion and perspectives **115**

A Sagnac Effect **117**
A.1 Calculation of the area . . . 117
A.2 Analytic analysis of the Sagnac Effect . . . 118
A.2.a Trajectories . . . 118
A.2.b Raman beams . . . 119
A.2.c Rotating the experiment . . . 120
A.2.d Phase shift due to the interferometer (pur gyroscope) . . . 120
A.2.e Higher order terms . . . 120
a) Experimental measurement simulation: . . . 120
b) Introducing non-equal k (NEK) . . . 121
c) Correcting NEK with a symmetric dT_s . . . 121

B Sensitivity function for rotations **123**
B.1 Time domain . . . 123
B.2 Frequency Domain . . . 124
B.3 Sagnac phase derivation . . . 124

C Publications **127**
C.1 Papers . . . 127
C.2 Conferences . . . 127

Conclusion **142**

Chapter I

Introduction

I.1 Atomic interferometry and inertial sensing

Since the emergence of atom interferometers (AI) in the 1990s [1, 2], AIs are being fruitfully used for metrology as well as for technological purposes. They lay out the working principle of atomic clocks [3, 4] and demonstrated huge potential in the inertial sensing field.

AI-based inertial sensors such as gravimeters [5], gradiometers [6] and gyroscopes [7], have seen an impressive improvement in performance as well as compactness showing an unprecedented high measurement sensitivity and stability and promise to surpass other state-of-art technologies. These sensors are being used already in geophysics field applications [8, 9, 10, 11] and used to scope new fundamental physics aspects such as Einstein's equivalence principle test [12], fine-structure constant measurements [13], gravitational constant [14], and detection of gravitational waves [15]. In this thesis, we will be interested in a particular type of inertial sensor which is the cold-atom gyroscope.

I.2 Gyroscope technologies

A gyro is a device that depending on its composition can fulfill two functions: measure or maintain the orientation, θ of a system with respect to a reference axis (gyroscope) or provide information about the rate at which the orientation of a system varies when it is rotating that is its angular velocity Ω ("gyrometer" or rate-gyro)[2]. In essence, while a gyroscope is primarily about maintaining a stable orientation, a "gyrometer" inherently measures the rate of change in orientation. Gyroscopes can be categorized into two types: those based on Newtonian mechanical principles, such as rotating disks or Coriolis vibratory systems, and those that leverage the Sagnac effect, specifically involving interferometers with a physical area (either light or matter-waves).

A conventional mechanical gyroscope comprises a flywheel that spins around its axis of symmetry, supported by a gimbal that allows the axis to rotate freely. The conservation of angular momentum ensures that the orientation of the flywheel is maintained, regardless of how the base moves. Measuring the deflection of the spinning axis pro-

[2] In English literature, the use of the words gyroscope and "gyrometer" can sometimes be blurry and both words may be used interchangeably to describe the two instruments.

vides information about the angular displacement of the platform. However, because this system relies on moving parts, it is susceptible to issues such as friction, wear and tear, or imperfections in the flywheel. These factors can introduce residual torques in the presence of gravity, which in turn limits the accuracy of the gyroscope [16].

The most recognized technology is Electrostatically Suspended Gyroscopes (ESG) which emerged in the 1960s. It consists of a spherical rotor that is levitated and spun using electrostatic forces. The rotor is kept in a vacuum chamber to minimize friction. Nowadays, ESG technology continues to be employed in naval navigation systems, often in conjunction with laser-based technologies. The most sensitive ESGs are those developed for the Gravity-Probe-B (GP-B) space mission, where the rotor is a very-high quality quartz sphere (0.1 ppm precision level), coated with a Niobium superconducting layer and levitated in a nano-g environment. With that, GP-B ESG achieved very good long-term stability (Table I.1) that allowed to perform tests on general relativity [17].

For optical gyroscopes two main types are used: Ring Laser Gyroscopes (RLG), which were introduced in the 1960s, and Fiber Optic Gyroscopes (FOG), which came into prominence in the 1980s. In an RLG device, laser light circulates in counter-propagating loops using three mirrors arranged in a triangular cavity. Furthermore, to prevent interaction between the light path and the air, the cavity is vacuumed. They are extensively used in aeronautical navigation for both civil airplanes (Airbus, Boeing) and jet-fighters (Rafale) navigation systems [18, 19].

In FOGs, light circulates in optical fiber loops. FOG has a high sensitivity achieved by a very long fiber length (kilometers) and the area of the fiber coil and since it does not have any moving parts, this technology is suited for harsh environments such as underground navigation (civil engineering), where shocks and vibrations are commonplace and also for rotational seismology applications [20].

Another technology, extremely compact, yet proven its ability to meet performance benchmarks typically achieved by optical technologies (RLG and FOG), is HRG (Hemispherical Resonator Gyroscope). HRG consists of a thin shell in the shape of a hemisphere typically made from quartz. The shell is driven into resonance using electrodes, where it vibrates in a specific pattern and tends to continue to resonate in the same plane even if its support rotates. When the gyro is subjected to rotation, the vibration pattern changes due to the Coriolis effect which can be detected and measured. The entire system is housed within a high-vacuum, bell-shaped enclosure. Advancements in high-precision manufacturing, particularly lithography, have minimized imperfections and defects of these resonators, thereby enhancing their reliability. These gyros are widely used for tactical military-grade applications [21].

Cold-atom gyroscopes have the potential to achieve unparalleled performance levels. At present, they are mainly lab-scale experiments predominantly situated within R&D centers, serving as reference units and they are too bulky to be integrated into commercial navigation systems. However, with proper engineering, as has been done for the cold-atom gravimeter [22], compact or even on-chip versions may be available in the market in the coming years. Their working principle and performance will be explained in this thesis. In our case, we mainly focus on exploiting applications where other gyroscopes lack of performance to test fundamental physics and also to develop new techniques to improve this type of technology.

I.3 Performance

A gyroscope can be modeled as a system that measures an observable:

$$S(t) = \alpha_0\,\Omega(t) + \beta_0 + \varepsilon(t), \tag{I.1}$$

where α_0 represents the scale factor which reflects sensitivity to rotations, and β_0 denotes the measurement bias when no input is provided. Both parameters can be determined through system calibration. The error term $\varepsilon(t)$ encompasses various contributions defining a gyroscope's quality and can be expressed as:

$$\varepsilon(t) = \tilde{\alpha}(t)\,\Omega(t) + \tilde{\beta}(t) + \tilde{\varepsilon}(t) \tag{I.2}$$

The initial two terms shed light on how the parameters influencing the scale factor and the bias might undergo gradual deterministic variations over time due to environmental conditions like temperature fluctuations, friction or stress. Conversely, the term $\tilde{\varepsilon}(t)$ outlines an intrinsic stationary noise limit tied to the instrument. Of course, in the industry, factors such as size, robustness, dynamic range, and the sampling rate of gyroscopes are also taken into consideration.

Distinctively, Sagnac gyroscopes, when compared to their mechanical counterparts, exhibit minimal variations in scale factor and bias. Consequently, the dominant noise is essentially the limiting noise $\tilde{\varepsilon}(t)$. Fundamentally, this noise equates to photon noise in optical gyroscopes and quantum projection noise in atomic gyroscopes, both of which are proportional to $1/\sqrt{N}$, where N is the number of detected particles and averages out as $1/\sqrt{\tau}$, where τ is integration time.

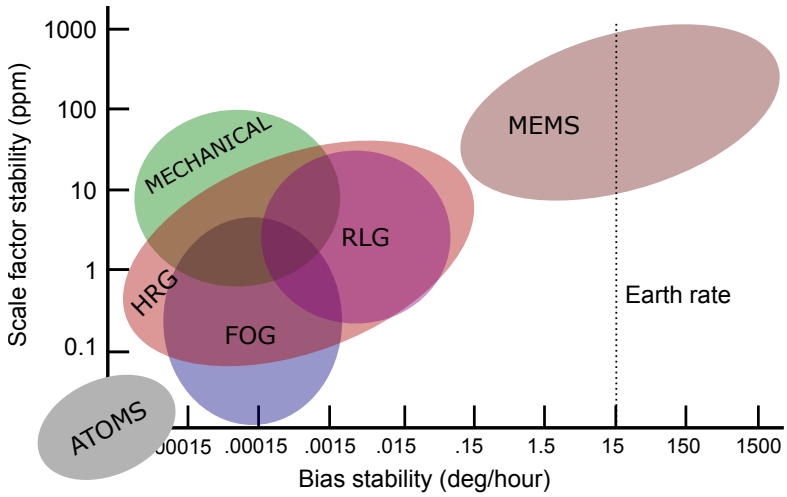

FIGURE I.1: The expected performance of each technology.

In table I.1, we present the performances in terms of sensitivity and stability [1] of some gyroscope technologies to give an idea about the state-of-art of each instrument. Our gyroscope is the state-of-art of this kind of technology presenting the largest Sagnac

[1] Usually the sensitivity at one second or angular random walk (ARW) is expressed in ($\mathrm{deg}/\sqrt{\mathrm{hr}}$) for commercial products where:

$$1\,\mathrm{rad.s^{-1}}/\sqrt{\mathrm{Hz}} = \left(\frac{180}{\pi} \times 3600\right) \frac{1}{\sqrt{3600}} = 3.4 \times 10^3\,\mathrm{deg}/\sqrt{\mathrm{hr}}$$

area. Certainly, the choice hinges on the specific use-case and there are additional factors to consider when comparing gyroscopes, such as cost, robustness, dynamical range, bandwidth, and size. For instance, microelectromechanical system (MEMS) gyroscopes are low-cost, remarkably small devices making them well-suited for automotive and industrial settings where high performance is not a critical requirement and GPS recalibration is feasible. For RLG, we presented a commercial version from Honeywell [23] as well as geant infrastructures [24, 25].

Gyroscope technology		Area	Sensitivity ($\mathrm{rad.s^{-1}/\sqrt{Hz}}$)	Stability ($\mathrm{rad.s^{-1}}$)	Integration time (s)
Atoms: Lab scale experiments					
4-pulse					
SYRTE 2023		$11\,\mathrm{cm^2}$	3×10^{-8}	2.3×10^{-10}	6×10^3
Wuhan 2020	[26]	$5.92\,\mathrm{cm^2}$	1.2×10^{-7}	2.5×10^{-8}	100
3-pulse					
Wuhan 2022	[27]	$120\,\mathrm{mm^2}$	1.5×10^{-7}	9.5×10^{-10}	2.3×10^3
Hanover 2015	[28]	$41\,\mathrm{mm^2}$	1.2×10^{-7}	2.6×10^{-8}	100
SYRTE 2009	[29]	$4\,\mathrm{mm^2}$	2.4×10^{-7}	1×10^{-8}	1600
Thermal jets					
Stanford 2000	[7]	$24\,\mathrm{mm^2}$	6×10^{-10}	2×10^{-9}	120
Optical					
FOG blueSeis-3A*	[20]	$200\,\mathrm{m^2}$	1.5×10^{-8}	5×10^{-10}	3×10^3
RLG (GG1320)*	[23]	$60\,\mathrm{cm^2}$	4×10^{-6}	2×10^{-8}	3.6×10^4
G-Ring laser	[24]	$16\,\mathrm{m^2}$	1.2×10^{-11}	7×10^{-13}	10^3
LNGS (Italy)	[25]	$13\,\mathrm{m^2}$	1.8×10^{-11}	4×10^{-14}	3×10^5
Mechanical					
ESG GP-B (space)	[17]	-	5.9×10^{-7}	3.4×10^{-13}	1.4×10^4
Others					
HRG* (Safran)	[21]	-	5.8×10^{-8}	3.4×10^{-10}	3.6×10^4
NMR	[30]	-	5×10^{-7}	4×10^{-9}	-
He Superfluid	[31]	-	8×10^{-9}	-	-
NV center	[32]	-	10^{-5}	-	-

TABLE I.1: **State-of-art of gyroscopes for different technologies.** For each technology we give the angular random walk of the instrument which is simply given by the sensitivity of the instrument at 1s, the known stability of the system with the corresponding integration time. For Sagnac bases gyroscopes, we gave the area of the interferometer.
(*) commercial products

I.4 Purpose of the thesis work

The cold-atom gyroscope which is the subject of this thesis results from collaborative and iterative work over 15 years. Following the first generation of cold-atom gyroscope using two cold-atom clouds which ended in 2007 [33]. A new experiment was designed by A. Ladragin and built by Thomas Levèque [34] in 2008. The very first atomic interferometer measurements using Raman transitions by Matthieu Meunier [35] in 2013. Indranil Dutta [36] implemented continuous measurements with no deadtimes using a 4-pulse configuration with vibration correlations using a classical sensor. Denis Savoie [37] extended Dutta's work by implementing interleaved measurements and implementing real-time compensation for vibrations and mid-fringe locking. Then, Matteo Altorio [38] studied the systematic effects linked to trajectories alignment, and also worked on new time asymmetries to reject parasitic interferometers. He also installed the rotation platform under the experiment as an initiative to perform Sagnac Effect measurement. Romain Gautier [33] implemented a new measurement axis, tested the quasi-double joint mode, and performed Sagnac measurements.

I joined the team for a six-month master's internship and I began my PhD in October 2020 and spent a year working alongside Romain. I assisted the replacement of the 2D MOT, which had suffered severe damage during the COVID pandemic due to an air-conditioning system failure. After restoring the interferometer on the X-axis, we focused on testing the Y-axis of the gyroscope and successfully established a second axis for measurements and promptly started the Sagnac effect campaign. In parallel, I crafted a system to automate the tilt control of the experiment and developed new software to control the experimental sequence using Python. When Romain left the lab in November 2021, I was left with an experiment that was rather mature and had given results, but it was necessary to continue improving the control to improve the stability, be able to take long measurement campaigns, and introduce new techniques. For that purpose, it was required to significantly rework the various control methods, which is the main topic of this thesis. I also continued to perform the Sagnac effect measurements in intervals of three months along the year to test if there were any fluctuations in what we measured. In between, with the help of post-doc C. Cherfan, we worked on the implementation of new techniques to control the phase of the interferometer as an initiative to transition to Raman double-diffraction regime to improve both the sensitivity and stability of the gyroscope.

I.5 Plan of the thesis

Chapter II: Principles of atomic interferometry

This chapter provides an overview of the fundamental concepts underlying state-labeled atom interferometry. We show how Stimulated Raman Transition can be employed to control the internal and external states of the atoms to implement atomic optics. Also, we will delve into how the 4-pulse sequence is utilized for measuring rotation rates. Finally, we will establish the sensitivity function tool used to quantify the phase contribution of various noises within the system.

Chapter III: Experimental setup

In this chapter, we will describe the experimental setup behind the interferometric measurement. We will explore the sensor head structure and laser setups used for preparing, launching, interrogating, and detecting atoms. The chapter further sheds light on our methods for managing vibrations - the predominant noise source in the gyroscope as we will see. Additionally, we will elucidate the sequence of measurements leading to the extraction of rotation rate readings, and conclude with a description of the software facilitating control and data acquisition.

Chapter IV: Sagnac effect measurements over a year

Here, we will detail a fundamental physics test with the cold-atom gyroscope which consists of a validity test of the Sagnac Effect on matter-wave interferometers. The experimental characterization of the scale factor will be discussed and the results from a year-long measurement campaign will be highlighted, showcasing our achievement in attaining unprecedented accuracy in quantifying this effect.

Chapter V: Real-time control of the atom interferometer phase for the double diffraction regime

Here, we introduce innovative techniques for the real-time control of the interferometer phase. We will explore and characterize two novel methods. The details of implementing each approach, along with their respective validation tests, will be provided. Additionally, we will discuss the modifications made to our experimental setup to facilitate these techniques. To conclude, a comparative analysis will be made, highlighting the performance of each method in relation to the current one.

Chapter II

Principles of atomic interferometry

In this chapter, we will be going through a theoretical description of the building blocks of an atomic interferometer. In our case, we use Stimulated Raman Transitions, a two-photon process to coherently manipulate atoms. These transitions are used to implement atomic optics (mirrors and beamsplitters) by driving transitions between two ground states ($|g\rangle$ and $|e\rangle$) and realized using two counter-propagating laser beams that are far detuned from an intermediate state $|i\rangle$ with frequency difference that matches the energy difference between the ground states. These ground states are often chosen to two hyperfine states of the atom and $|i\rangle$ would be an electronically excited state. One feature of Raman transitions is that they provide control over both the internal state of the atom and also its external momentum state. Also, we will see how this can be used to construct an atomic interferometer and how this can be related to measuring an inertial quantity such as rotation rate. Finally, I will present, the sensitivity function formalism which enables quantifying the contribution of different noise sources on the interferometer phase.

II.1 Stimulated Raman Transitions

Stimulated Raman transitions are now a very common technique in the realm of atomic physics. It was introduced in 1991 at Stanford University [1] and demonstrated the advantage of labeling the internal states with the change of momentum energy in an atomic interferometer[39]. This section aims to describe the dynamics of an atom when it is subjected to lasers in a Raman scheme. We will start with an atom of three energy levels and show how the problem can be reduced to an effective two-level system. By making a few transformations, we can find a reference frame in which the Hamiltonian is time-independent. The final result will be a transfer matrix that describes the evolution of a given state over time. Throughout the calculations, we will define some important quantities that will be used in the context of this thesis.

II.1.a Three-level system

We consider a three-level atom under interaction with two counter-propagating laser beams with frequencies ω_1 and ω_2. A scheme of this process is depicted in Figure II.1. The laser frequencies are far detuned from the intermediate state $|\mathrm{i}\rangle$ so that no single-photon electric dipole transition is allowed. Nevertheless, we will show that, through a two-photon transition, when the frequency difference matches the hyperfine splitting (clock frequency) ω_{HFS} between the ground states, the system can be described as an effective two-level system and the lasers can couple transitions from state $|\mathrm{g}\rangle$ to state $|\mathrm{e}\rangle$.

In general, we can describe our atom by its quantum state $|\psi(t)\rangle$ as a superposition of its basis states,

$$|\psi(t)\rangle = a_{\mathrm{g}}(t)\,|\mathrm{g},\mathbf{p}_{\mathrm{g}}\rangle + a_{\mathrm{e}}(t)\,|\mathrm{e},\mathbf{p}_{\mathrm{e}}\rangle + a_{\mathrm{i}}(t)\,|\mathrm{i},\mathbf{p}_{\mathrm{i}}\rangle\,, \tag{II.1}$$

where, $a_j(t)$ are time dependent quantum amplitudes and $\mathbf{p}_j$ are the momentum of each state. The Schrodinger equation gives the dynamics of that system and its evolution in time,

$$i\hbar\frac{\mathrm{d}}{\mathrm{d}t}\,|\psi(t)\rangle = \hat{H}\,|\psi(t)\rangle\,, \tag{II.2}$$

where $\hat{H} = \hat{H}_A + \hat{H}_{\mathrm{ext}} = \hat{H}_{\mathrm{int}} + \hat{H}_{\mathrm{ext}} + \hat{H}_I$ is the Hamiltonian written as a sum of three terms:

- $\hat{H}_{\mathrm{int}} = \sum_n \hbar\omega_n\,|n\rangle\,\langle n|$ describes the internal electronic structure.
- $\hat{H}_{\mathrm{ext}} = \hat{\mathbf{p}}^2/2m$ ($\hat{\mathbf{p}}$ being the momentum operator and m is the atomic mass)
- $\hat{H}_{\mathrm{I}} = -\hat{\mathbf{d}}\cdot\mathbf{E}$ is the interaction Hamiltonian, where $\hat{\mathbf{d}}$ is the electric dipole operator and $\mathbf{E}$ is the electric field due to the two counter-propagating laser beams,

$$\mathbf{E} = \frac{1}{2}\left(\mathbf{E}_1 e^{i(-\omega_1 t+\mathbf{k}_1\cdot\mathbf{r}+\phi_1^0)} + \mathbf{E}_2 e^{i(-\omega_2 t+\mathbf{k}_2\cdot\mathbf{r}+\phi_2^0)}\right) + \text{c.c.}, \tag{II.3}$$

  where $\mathbf{k}_1 \approx -\mathbf{k}_2$ are the wave vectors for each beam, $\mathbf{E}_i$ are the amplitude vectors of the electric field and $\phi_i(t,\mathbf{r}) = \mathbf{k}_i\cdot\mathbf{r}(t) + \phi_i^0$ are the phases of laser i field at a time t and a position $\mathbf{r}$ in space.

In the limit where spontaneous emission is ignored, we choose a closed-momentum family, where an atom in the state $|\mathrm{g},\mathbf{p}\rangle$ absorbs a photon from the laser 1, gets transferred to state $|\mathrm{i},\mathbf{p}+\hbar\mathbf{k}_1\rangle$, then via stimulated emission, it emits a photon in laser 2 to end up in the state $|\mathrm{e},\mathbf{p}+\hbar\mathbf{k}_{\mathrm{eff}}\rangle$, where $\mathbf{k}_{\mathrm{eff}} = \mathbf{k}_1 - \mathbf{k}_2$ is the effective wavevector. Here, we can see the interest of using the two-photon Raman transitions since they allow a transfer of momentum which corresponds to $2v_{\mathrm{rec}}$ ($\sim 7\,\mathrm{mm.s^{-1}}$ for ^{133}Cs atom).

We present in figure (II.1) the energy levels of interest and the configuration of the lasers. We define some characteristic frequencies:

- The frequency difference between the two internal ground states $|\mathrm{g},\mathbf{p}\rangle$ and $|\mathrm{e},\mathbf{p}+\hbar\mathbf{k}_{\mathrm{eff}}\rangle$, $\omega_{\mathrm{HFS}} = \omega_{\mathrm{e}} - \omega_{\mathrm{g}}$.
- The frequency detuning Δ between laser 1 and the transition between the ground state $|\mathrm{g},\mathbf{p}\rangle$ and $|\mathrm{i},\mathbf{p}+\hbar\mathbf{k}_1\rangle$,

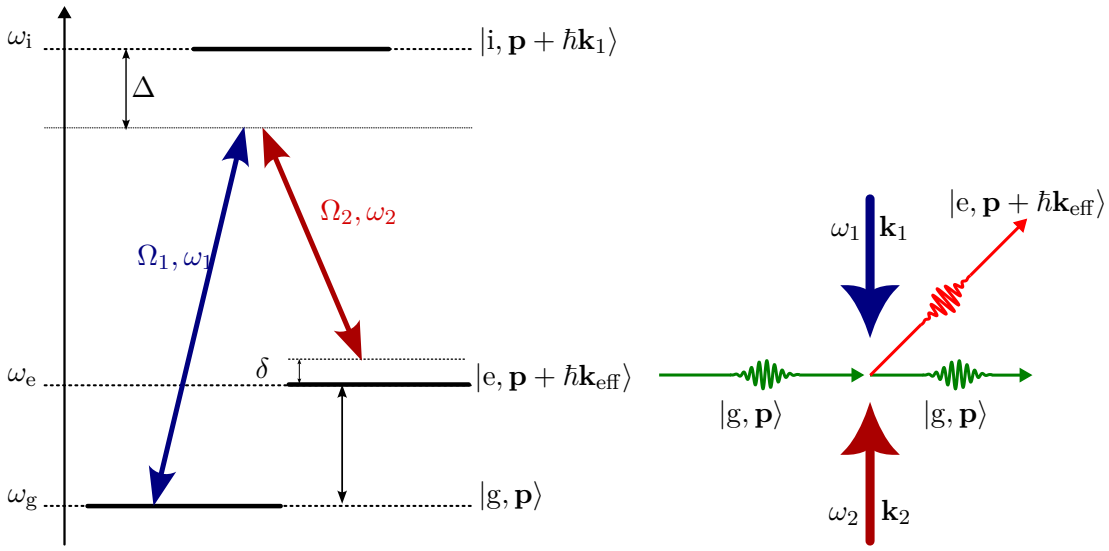

FIGURE II.1: (left) Energy levels for three state $|g\rangle$, $|e\rangle$ and $|i\rangle$. The two-counter propagating lasers configuration is depicted in blue (red), with frequencies ω_1 (ω_2) and a wavevector of $\mathbf{k}_1$ ($\mathbf{k}_2$), respectively. Also, the characteristic frequencies are represented in the energy diagram (not to scale). (left) Momentum transfer in Raman transition for counter-propagating laser in a case where the initial state is driven into a superposition of the ground states that get separated in space (one atom phenomenon).

- The Raman detuning δ, which is given by the difference between the relative lasers frequency $\omega_L = \omega_1 - \omega_2$ and the frequency between the two state $|g, \mathbf{p}\rangle$ and $|e, \mathbf{p} + \hbar\mathbf{k}_{eff}\rangle$ which includes also the kinetic energy part, this detuning is given by:

$$\begin{aligned}\delta &= (\omega_1 - \omega_2) - \frac{E_g - E_e}{\hbar} \\ &= (\omega_1 - \omega_2) + (\omega_g + \frac{1}{\hbar}\frac{\mathbf{p}^2}{2m}) - (\omega_e + \frac{1}{\hbar}\frac{(\mathbf{p} + \hbar\mathbf{k}_{eff})^2}{2m}) \\ &= (\omega_L - \omega_{HFS}) - \mathbf{k}_{eff} \cdot \mathbf{v} - \frac{\hbar k_{eff}^2}{2m}\end{aligned}$$

  where we identify, the lasers relative detuning $\delta_L = \omega_L - \omega_{HFS}$, the Doppler frequency shift $\omega_{Doppler} = \mathbf{k}_{eff} \cdot \mathbf{v}$, which is a velocity-selective term, and the two-photon recoil frequency, $\omega_{recoil} = \hbar k_{eff}^2/2m$.

  We will see in what follows that the presence of lasers will introduce a differential light shift δ^{AC} between the two ground states. By setting the detuning to the differential light shift frequency, i.e, $\delta = \delta^{AC}$, the resonance condition is verified when

$$\boxed{\delta_L = \omega_{recoil} + \omega_{Doppler} + \delta^{AC}.} \tag{II.4}$$

Solving equations

In what follows we denote Ω_k^{ij}, the one photon Rabi frequency which quantifies the coupling strength between a laser k and the transition from level $|i = i\rangle$ to $|j = g, e\rangle$, defined as:

$$\Omega_k^{ij} = -\frac{\langle j|\, \hat{\mathbf{d}} \cdot \mathbf{E}_k \,|i\rangle}{\hbar}. \tag{II.5}$$

here we assume that the laser 1 (2) couples only state $|\mathrm{g}\rangle$ ($|\mathrm{e}\rangle$) and $|\mathrm{i}\rangle$. Hence, we simplify notation by setting $\Omega_1 \equiv \Omega_1^{\mathrm{ig}}$ and $\Omega_2 \equiv \Omega_2^{\mathrm{ie}}$. With this assumption, the Hamiltonian can be written as,

$$\hat{H} = \begin{pmatrix} E_{\mathrm{g}} & 0 & \hat{H}_{\mathrm{gi}} \\ 0 & E_{\mathrm{e}} & \hat{H}_{\mathrm{ei}} \\ \hat{H}_{\mathrm{gi}}^* & \hat{H}_{\mathrm{ei}}^* & E_{\mathrm{i}} \end{pmatrix}, \tag{II.6}$$

where $E_k = \hbar\omega_k + \mathbf{p}_k^2/2m$ is the energy eigenvalue of the Hamiltonian without the interaction term and the diagonal terms are,

$$\hat{H}_{\mathrm{gi}} = \frac{\hbar\Omega_1}{2}\left(e^{-i(\omega_1 t+\phi_1)} + e^{i(\omega_1 t+\phi_1)}\right) \tag{II.7}$$

$$\hat{H}_{\mathrm{ei}} = \frac{\hbar\Omega_2}{2}\left(e^{-i(\omega_2 t+\phi_2)} + e^{i(\omega_2 t+\phi_2)}\right) \tag{II.8}$$

To solve the time-dependent Schrodinger equation II.2, the first simplification is to pass from the "Schrodinger picture" into the "interaction picture" by performing the transformation $\hat{T}(t) = e^{iE_n t/\hbar}\mathbf{I}$ on the state $|\psi(t)\rangle$. Under this transformation, the Hamiltonian can be written as[1]

$$\hat{\tilde{H}} = \begin{pmatrix} 0 & 0 & \hat{H}_{\mathrm{gi}} \\ 0 & 0 & \hat{\tilde{H}}_{\mathrm{ei}} \\ \hat{\tilde{H}}_{\mathrm{gi}}^* & \hat{\tilde{H}}_{\mathrm{ei}}^* & 0 \end{pmatrix}, \tag{II.9}$$

where the new elements are written in terms of the already defined Δ and δ. Also, under the rotating-wave approximation, terms that oscillate in optical frequencies quickly average out to zero and can be ignored. We get,

$$\hat{\tilde{H}}_{\mathrm{gi}} = \frac{\hbar}{2}\Omega_1 e^{-i\phi_1} e^{i\Delta t} \tag{II.10}$$

$$\hat{\tilde{H}}_{\mathrm{ei}} = \frac{\hbar}{2}\Omega_2 e^{-i\phi_2} e^{i(\Delta-\delta)t} \tag{II.11}$$

The Schrodinger equation under the Hamiltonian results in the following system of equations:

$$\begin{aligned} i\frac{\mathrm{d}}{\mathrm{d}t}b_{\mathrm{g}}(t) &= \frac{\Omega_1}{2}e^{i(\Delta t-\phi_1)}b_{\mathrm{i}}(t) \\ i\frac{\mathrm{d}}{\mathrm{d}t}b_{\mathrm{e}}(t) &= \frac{\Omega_2}{2}e^{i((\Delta-\delta)t-\phi_2)}b_{\mathrm{i}}(t) \\ i\frac{\mathrm{d}}{\mathrm{d}t}b_{\mathrm{i}}(t) &= \frac{\Omega_1^*}{2}e^{i(\Delta t-\phi_1)}b_{\mathrm{g}}(t) + \frac{\Omega_2^*}{2}e^{i((\Delta-\delta)t-\phi_2)}b_{\mathrm{e}}(t). \end{aligned} \tag{II.12}$$

II.1.b Effective Two-level system

We can demonstrate that the intermediate level $|\mathrm{i}\rangle$ can be adiabatically eliminated in the limit where $\Delta \gg (\Omega 1\mathrm{g}, \Omega_{2\mathrm{e}}, \delta)$, i.e. the atom has a negligible probability to be at the

[1] When a unitary transformation $\hat{T}$ is applied at the state $|\psi\rangle$, we have $|\tilde{\psi}\rangle = \hat{T}|\psi\rangle$ and the Hamiltonian $\hat{H}$ is transformed to $\hat{\tilde{H}}$ given by:

$$\hat{\tilde{H}} = \hat{T}\hat{H}\hat{T}^\dagger + i\hbar\frac{\partial\hat{T}}{\partial t}\hat{T}^\dagger$$

level $|i\rangle$. Therefore, the problem can be reduced to an effective two-level system where transitions are driven only between $|\mathrm{g}\rangle$ and $|\mathrm{e}\rangle$.

> In fact, the system of equations II.12 can be solved under this assumption since the amplitude $b_\mathrm{i}(t)$ is oscillating very rapidly compared to $b_\mathrm{g}(t)$ and $b_\mathrm{e}(t)$. The latter amplitudes are considered constants, which allow integrating $b_\mathrm{i}(t)$, which is found to be
>
> $$b_\mathrm{i}(t) = \frac{1}{2\Delta} e^{-i\Delta t} \left(\Omega_1^* e^{i\phi_1} b_\mathrm{g}(t) + \Omega_2^* e^{i(\delta t + \phi_2)} b_\mathrm{e}(t) \right). \tag{II.13}$$
>
> By plugging this equation II.12, the time evolution of states $|\mathrm{g}\rangle$ and $|\mathrm{e}\rangle$ is uncoupled from the state $|\mathrm{i}\rangle$.

The evolution of the effective system is described by this Hamiltonian given in its matrix form in the basis $\{|\mathrm{g}\rangle, |\mathrm{e}\rangle\}$:

$$\hat{\tilde{H}} = \frac{\hbar}{2} \begin{pmatrix} 2\Omega_\mathrm{e}^\mathrm{AC} & \Omega_\mathrm{eff} e^{i(\delta t + \varphi)} \\ \Omega_\mathrm{eff}^* e^{-i(\delta t + \varphi)} & 2\Omega_\mathrm{g}^\mathrm{AC} \end{pmatrix}, \tag{II.14}$$

here we identify, the effective two-photon Rabi frequency Ω_eff, the AC Stark effect or light shifts $\Omega_\mathrm{g,e}^\mathrm{AC}$ to levels $|\mathrm{g}\rangle$ and $|\mathrm{e}\rangle$, and the relative laser phase φ, defined as:

$$\boxed{\begin{aligned} \Omega_\mathrm{eff} &= \frac{\Omega_1 \Omega_2^*}{2\Delta} && \text{(II.15)} \\ \Omega_\mathrm{g}^\mathrm{AC} &= \frac{|\Omega_1|^2}{4\Delta} + \frac{|\Omega_2|^2}{4(\Delta - \omega_\mathrm{HFS})} && \text{(II.16)} \\ \Omega_\mathrm{e}^\mathrm{AC} &= \frac{|\Omega_1|^2}{4(\Delta + \omega_\mathrm{HFS})} + \frac{|\Omega_2|^2}{4\Delta} && \text{(II.17)} \\ \varphi &= \mathbf{k}_\mathrm{eff} \cdot \mathbf{r} + (\phi_1^0 - \phi_2^0) && \text{(II.18)} \end{aligned}}$$

With that, we can also define some important quantities, the differential lightshift δ_AC, the mean light shift δ_0^AC, and the generalized Rabi frequency Ω_R, where

$$\delta^\mathrm{AC} = \Omega_\mathrm{e}^\mathrm{AC} - \Omega_\mathrm{g}^\mathrm{AC} \tag{II.19}$$

$$\delta_0^\mathrm{AC} = \Omega_\mathrm{e}^\mathrm{AC} + \Omega_\mathrm{g}^\mathrm{AC} \tag{II.20}$$

$$\Omega_R = \sqrt{\Omega_\mathrm{eff}^2 + (\delta - \delta^\mathrm{AC})^2} \tag{II.21}$$

We note that the mean light-shift δ_0^AC acts as a uniform energy shift on the system and can be removed using the transformation $e^{i\delta_0^\mathrm{AC} t/2}\mathbf{I}$ on the state. This transformation will change the diagonal terms in the Hamiltonian (Eq II.14) to $\mp\delta^\mathrm{AC}$. The simplest form of the Hamiltonian is obtained by performing a rotation on the state with a rate δ using the transformation[1] $R = e^{-i\delta t \sigma_z/2}$, where σ_z is the z-axis Pauli matrix.

We finally obtain a time-independent Hamiltonian given by :

$$\boxed{\hat{H}_\mathrm{eff} = \frac{\hbar}{2} \begin{pmatrix} \delta - \delta^\mathrm{AC} & \Omega_\mathrm{eff} e^{i\varphi} \\ \Omega_\mathrm{eff}^* e^{-i\varphi} & \delta^\mathrm{AC} - \delta \end{pmatrix}.} \tag{II.22}$$

In section II.19, we will show how to control and cancel the differential light shift contribution. Therefore, this term will be set to zero for what follows.

[1] Consider using the identity, $e^{i\theta\sigma_z} = \cos\theta\mathbf{I} + i\sin\theta\sigma_z$.

II.1.c Transfer Matrix

The evolution of the quantum state in time under this time-independent Hamiltonian is given by the evolution operator $\hat{U} = \exp\left(-\frac{i}{\hbar}\hat{H}_{\text{eff}}(t-t_0)\right)$. Given that, the solution of equation II.2 is simply given by:

$$|\psi(t)\rangle = \hat{U}\,|\psi(t_0)\rangle\,, \tag{II.23}$$

where,

$$\boxed{\hat{U}(t,t_0) = \begin{pmatrix} C^* & -iS^* \\ -iS & C \end{pmatrix}.} \tag{II.24}$$

here, C and S are defined as:

$$C = \cos\left(\frac{\Omega_{\text{eff}}(t-t_0)}{2}\right) + i\frac{\delta}{\Omega_{\text{eff}}}\sin\left(\frac{\Omega_{\text{eff}}(t-t_0)}{2}\right) \tag{II.25}$$

$$S = e^{i\varphi}\frac{\Omega_{\text{eff}}}{\Omega_R}\sin\left(\frac{\Omega_{\text{eff}}(t-t_0)}{2}\right) \tag{II.26}$$

> This evolution operator can be easily evaluated when considering that $\hat{H}_{\text{eff}}$ can be written as:
>
> $$\hat{H}_{\text{eff}} = \frac{\hbar}{2}\mathbf{\Omega}\cdot\hat{\sigma}, \tag{II.27}$$
>
> where $\hat{\sigma}$ is the Pauli vector and $\mathbf{\Omega}$ is defined as:
>
> $$\mathbf{\Omega} = \Omega_{\text{eff}}\cos(\varphi)\mathbf{x} + \Omega_{\text{eff}}\sin(\varphi)\mathbf{y} + \delta\mathbf{z}. \tag{II.28}$$
>
> And using the identity:
>
> $$e^{i\theta\mathbf{n}\cdot\hat{\sigma}} = \mathbf{I}\cos\theta + i\sin\theta\,\mathbf{n}\cdot\hat{\sigma}. \tag{II.29}$$

II.1.d Atomic optics

The atom in the presence of laser light undergoes Rabi oscillations where it oscillates between the ground states. The transition probability of an atom initially at the state $|\psi(t_0=0)\rangle = |\mathrm{e}\rangle$, after a duration τ, assuming that the resonance condition is verified ($\delta = 0$), and lightshifts are compensated for, is given by:

$$P = |\langle \mathrm{e}\,|\psi\rangle\,|^2 = \sin^2\left(\frac{\Omega_R\tau}{2}\right) \tag{II.30}$$

By tweaking this duration, we consider the two following cases:

- The duration is set to have $\Omega_R\tau = \pi/2$, in this case, the pulse creates a coherent superposition of states: $|\mathrm{g},\mathbf{p}\rangle$ and $|\mathrm{e},\mathbf{p}+\hbar\mathbf{k}_{\text{eff}}\rangle$, and spatially separates the two states. This $\pi/2$-pulse is the atomic analogous of a *beamsplitter* in optics. The corresponding transfer matrix is:

$$\hat{U}_{\pi/2} = \frac{1}{\sqrt{2}}\begin{pmatrix} 1 & -ie^{i\varphi} \\ -ie^{-i\varphi} & 1 \end{pmatrix}. \tag{II.31}$$

- When $\Omega_R\tau = \pi$, this π-pulse transfers the state to from $|\mathrm{a}\rangle$ to $|\mathrm{b}\rangle$ and vice-versa. With momentum transfer, the states are spatially deflected. Therefore, the π-pulse is called a *mirror* pulse.

$$\hat{U}_\pi = \begin{pmatrix} 0 & -ie^{i\varphi} \\ -ie^{-i\varphi} & 0 \end{pmatrix}. \tag{II.32}$$

  The imprinted phase is φ when the state goes from $|\mathrm{g}\rangle \to |\mathrm{e}\rangle$, and $-\varphi$ when it goes from $|\mathrm{e}\rangle \to |\mathrm{g}\rangle$ with a common static phase offset that can be ignored.

- In a free-propagation where no laser light is present. The transfer matrix is given by:

$$\hat{U}_{\mathrm{free}}(t, t_0) = \mathbf{I} - i\frac{\delta}{2}(t - t_0)\hat{\sigma_z}. \tag{II.33}$$

II.1.e Velocity selectivity

So far, we described the Raman process for a single atom. However, in the lab, we use an atomic cloud which has a thermal distribution. Therefore, not all the atoms are in resonance with the lasers due to the Doppler term in equation (II.4). To model this, let consider a gaussian velocity-distribution $G(v)$ centered at zero,

$$G(v) = \frac{1}{\sigma\sqrt{2\pi}} \exp\left(-\frac{1}{2}\frac{v^2}{\sigma^2}\right) \tag{II.34}$$

where, $\sigma = \sqrt{k_B T/m}$ is defined for an atomic cloud of a temperature T. We define τ as the duration of a π-pulse applied on an atom[1] with zero-velocity class and we assume that the resonance condition is met. In that case, $\Omega_{\mathrm{eff}}\tau = \pi$, and we write using the transfer matrix, the transition probability P of an atom with a velocity $\mathbf{v}$,

$$P(\mathbf{v}) = \left(\frac{\Omega_{\mathrm{eff}}}{\Omega_R}\sin\frac{\Omega_{\mathrm{eff}}\tau}{2}\right)^2 = \left(\frac{\pi}{2}\right)^2 \mathrm{sinc}^2\left(\frac{\pi}{2}\sqrt{1 + \left(\frac{\mathbf{k}_{\mathrm{eff}}\cdot\mathbf{v}}{\Omega_{\mathrm{eff}}}\right)^2}\right). \tag{II.35}$$

Considering this equation we see that for a given effective Rabi frequency Ω_{eff} (for a certain detuning Δ and lasers power), the Raman pulse has a selection "bandwidth" in momentum space. The higher Ω_{eff}, the larger that bandwidth. Depending on the application, one can use Raman transition as a selection pulse for example [40]. In our case where we want to transfer all the atoms, this can be a limiting factor when the atomic source has a large-width momentum distribution.

The population of atoms that contribute to the transition can be obtained by weighting the contribution of all velocities along the $\mathbf{k}_{\mathrm{eff}}$ vector with the function $G(v)$

$$P = \int G(v)P(v)\mathrm{d}v. \tag{II.36}$$

In Figure (II.2), we show how this effect deteriorates the efficiency of the Raman pulses and cause a damping effect for the Rabi oscillations. Note that, other averaging effects may be also included inside the model such as the Rabi frequency inhomogeneities in space due to lasers beam profile, and also decoherence processes such as the spontaneous emission. This equation can be used also to interpret Raman spectroscopy results where the Raman detuning is experimentally scanned to seek resonance peaks or to probe the velocity distribution (using long-duration pulses) of an atomic cloud.

[1] We consider using rectangular pulses shape.

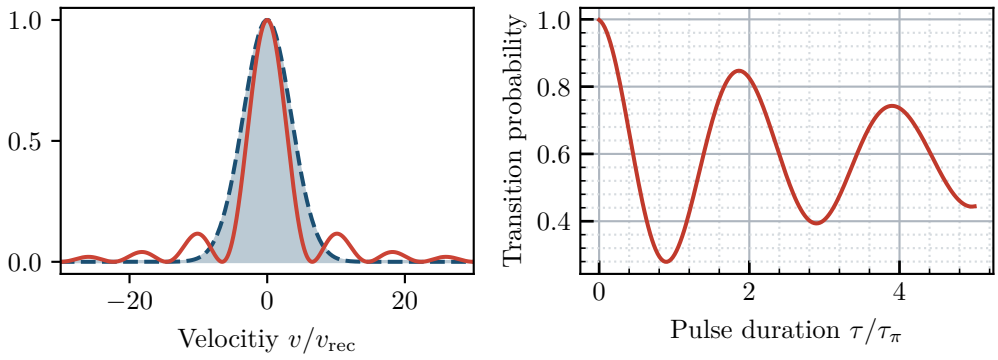

FIGURE II.2: Modeling Raman velocity (**left**) We plot in dashed-blue the velocity distribution of an atomic cloud (normalized), and the probability of transition of the Raman beams (solid orange) as a function of velocity classes expressed in units of v_{rec}. (**right**) Rabi oscillation over time in units τ_π. Due to averaging effects, the optimal pulse duration is shifted slightly to the left. We used ^{133}Cs atom and experimental parameters $\Omega_{\mathrm{eff}} = 2\pi \times 31$ kHz and a temperature of 1.2μK.

II.2 Effective Rabi frequency and light shifts

In this section, we will take into account the hyperfine structure of the D_2 line of ^{133}Cs atom (Figure II.3). We will show how the intermediate level $|\mathrm{i}\rangle$ is defined in a multilevel system and also derive the expression of both the effective Rabi frequency Ω_{eff} and the differential lightshift frequency δ^{AC}. In this picture, we map the ground state $|\mathrm{g}\rangle$ to $|F = 3\rangle$, the excited state $|\mathrm{e}\rangle$ to $|F = 4\rangle$ and for what concern the intermediate level $|\mathrm{i}\rangle$, we will sum over the different paths allowed by selection rules that leads from $|F = 3, 4\rangle$ to the hyperfine structure states $|F' = 2, 3, 4, 5\rangle$. In what follows, the indices i and j in Ω_k^{ij}, refers to levels $F = j$ and $F' = i$, respectively. Also we define Δ_j as the frequency difference relative to the state $|F' = 3\rangle$ as presented in figure (II.3)

II.2.a Effective Rabi frequency

By generalizing equation II.15, we write

$$\Omega_{\mathrm{eff}} = \sum_{j=3}^{4} \frac{\Omega_1^{3j}\Omega_2^{3j}}{2(\Delta + \Delta_j)}. \tag{II.37}$$

Using the dipole matrix elements given in [41], we find

$$\boxed{\Omega_{\mathrm{eff}} = \frac{\Omega_1\Omega_2}{2}\left(\frac{1}{16\Delta} + \frac{5}{48(\Delta + \Delta_4)}\right)} \tag{II.38}$$

here, $\Omega_k = 2DE_k/\hbar$ are the simplified Rabi frequencies which can be numerically evaluated given the laser field intensity $I_k = E_k^2/2\mu_0 c$ and the dipole moment D.

II.2.b Differential lightshift

The differential lightshift δ^{AC} defined in equation II.19 appears in both the imprinted phase (opposite signs) and also the generalized Rabi frequency Ω_R. As we will demon-

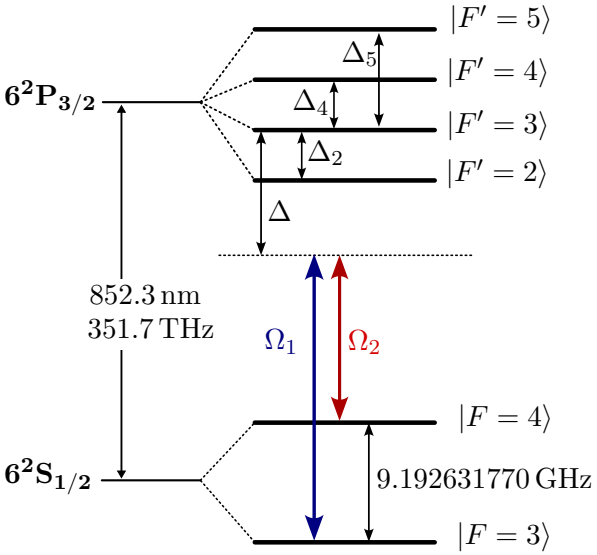

FIGURE II.3: The hyperfine structure of the D_2 transition of cesium ^{133}Cs atom. We denote the different detunings Δ_i from the energy level $|F'=3\rangle$. The splitting of the ground state is what we denote ω_{HFS} since it is the current definition of the second.

strate, this lightshift can be compensated for by choosing the optimal power ratio of the two lasers. From equations (II.16 and II.17), we have:

$$\Omega_{\mathrm{g}}^{\mathrm{AC}} = \sum_{j=2}^{4} \left(\frac{|\Omega_1^{3j}|^2}{4\Delta_j} + \frac{|\Omega_2^{3j}|^2}{4(\Delta_j - \omega_{\mathrm{HFS}})} \right) \tag{II.39}$$

$$\Omega_{\mathrm{e}}^{\mathrm{AC}} = \sum_{j=3}^{5} \left(\frac{|\Omega_1^{3j}|^2}{4(\Delta_j + \omega_{\mathrm{HFS}})} + \frac{|\Omega_2^{4j}|^2}{4\Delta_j} \right) \tag{II.40}$$

Similarly to what we did before, we get

$$\Omega_{\mathrm{g}}^{\mathrm{AC}} = g(\Delta) \times \Omega_1^2 + g(\Delta + \omega_{\mathrm{HFS}}) \times \Omega_2^2 \tag{II.41}$$

$$\Omega_{\mathrm{e}}^{\mathrm{AC}} = e(\Delta - \omega_{\mathrm{HFS}}) \times \Omega_1^2 + e(\Delta) \times \Omega_2^2 \tag{II.42}$$

here, the functions g and e are defined as:

$$g(\Delta) = \frac{1}{4}\left(\frac{5}{24\Delta} + \frac{1}{8(\Delta + \Delta_2)} \right)$$

$$e(\Delta) = \frac{1}{4}\left(\frac{1}{120\Delta} + \frac{1}{8(\Delta + \Delta_2)} + \frac{1}{5(\Delta + \Delta_3)} \right)$$

With that given, setting the differential lightshift δ^{AC} to zero comes down to choosing the adequate power ratio $R(\Delta)$ for a given value of detuning Δ. This ratio is given by:

$$R(\Delta) = \frac{I_2}{I_1} = \frac{\Omega_2^2}{\Omega_1^2} = \frac{g(\Delta) - e(\Delta - \omega_{\mathrm{HFS}})}{e(\Delta) - g(\Delta + \omega_{\mathrm{HFS}})}. \tag{II.43}$$

This function is plotted in Figure II.4. Note that the choice of Δ will be a compromise since lower detuning leads to stronger coupling frequency Ω_{eff} and at the same time will increase the spontaneous emission rate which scales also as Γ/Δ, Γ being the line width (or decay rate) of the transition.

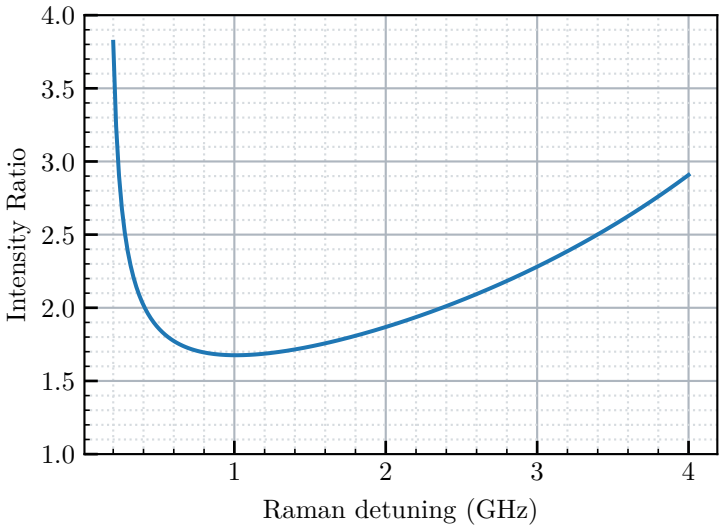

FIGURE II.4: Optimal intensity ratio $R(\Delta)$ to cancel the differential light shift δ^{AC} vs Raman detuning Δ. In our experiment, we usually use a detuning $\Delta \sim 500\,\mathrm{MHz}$. Therefore, we expect a ratio of R close to 1.86.

II.2.c Mean lightshift

The mean lightshift δ_0^{AC} appears as a global phase shift for the quantum states and intervenes whenever laser light is present. Therefore, the phase contribution is ideally identical for both arms of the interferometer and therefore canceled out. This statement is of course valid in the ideal case where two atom wavepackets see the same laser intensity. Due to the spatial separation during the π-pulses which is at the order of 1 cm, an imperfect spatial profile intensity may cause unwanted phase shifts.

II.3 Atomic interferometry and inertial sensing

In this section, we will present how can we use atomic interferometry to measure inertial quantities. The tools that we introduced in the previous section can be used to implement an interferometer in the same fashion as optical interferometers. As we will show, the interferometer consists of a series of short Raman pulses of a duration τ separated by a free evolution during a time T, the sequence of pulses will create a geometry, in space and time, formed by the interfering paths.

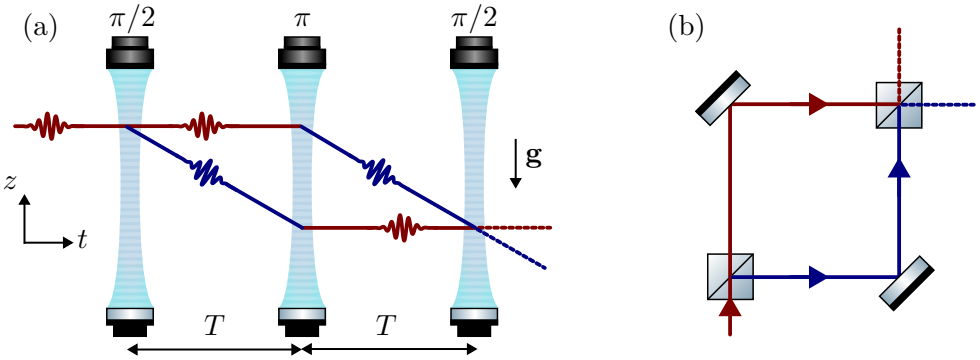

FIGURE II.5: (a) The space-time representation of a 3-pulse interferometer. (b) The optical Mach-Zehnder interferometer.

The simplest geometry consists of a 3-pulse sequence ($\pi/2$-π-$\pi/2$), which is the atomic analog of the optical Mach-Zehnder interferometer (Figure II.5). The pulses are separated by a time interval of T for a total duration of $2(T+\tau)$, where τ is the duration of a $\frac{\pi}{2}$-pulse.

The first $\frac{\pi}{2}$-pulse (a beamsplitter) will create an equal superposition of ground states. After that, the two states are kept separating freely in space for a duration of T. Then, a π-pulse (mirror) is applied to redirect the arms of the interferometer while flipping their internal states. After a second period of propagation T, the final $\pi/2$-pulse will recombine the states where they interfere and translate the superposition of states into a difference of probability of the atom to be in each state.

To calculate the output of such an interferometer, let's consider a uniformly accelerated atom with an acceleration $\mathbf{a}$. Given the initial conditions $(\mathbf{r}_0, \mathbf{v}_0)$, the classical trajectory of this atom is given by,

$$\mathbf{r}(t) = \mathbf{a}\frac{t^2}{2} + \mathbf{v}_0(t) + \mathbf{r}_0. \tag{II.44}$$

We use now the imprinted phase expression,

$$\varphi(\mathbf{r}, t) = \mathbf{k}_{\text{eff}} \cdot \mathbf{r}(t), \tag{II.45}$$

and we denote φ_i the imprinted phase for the pulse i. With that, the accumulated phase for each arm is:

$$\Phi_{\text{top}} = \varphi_1 - \varphi_2 + 0$$
$$\Phi_{\text{bot}} = 0 + \varphi_2 - \varphi_3.$$

Therefore, the phase difference at the output is given by

$$\Delta\Phi_{\text{acc}} = \mathbf{k}_{\text{eff}} \cdot [\mathbf{r}_1(0) - 2\mathbf{r}_2(T) + \mathbf{r}_3(2T)] \tag{II.46}$$
$$= \mathbf{k}_{\text{eff}} \cdot \mathbf{a}T^2 \tag{II.47}$$

We can see now that the phase difference at the output of the interferometer is directly proportional to an inertial quantity (in this case: acceleration). The ratio between the phase difference and the inertial quantity is called the scale factor and here it scales as T^2. In the case of a free-falling atom under gravity, the 3-pulse interferometer is an atomic gravimeter.

II.3.a The 4-pulse geometry: the atomic gyroscope

Following the same logic, we can show that a geometry of a 4-pulse interferometer ($\pi/2$-π-π-$\pi/2$) separated by intervals ($T/2$-T-$T/2$), is insensitive to constant (DC) accelerations.

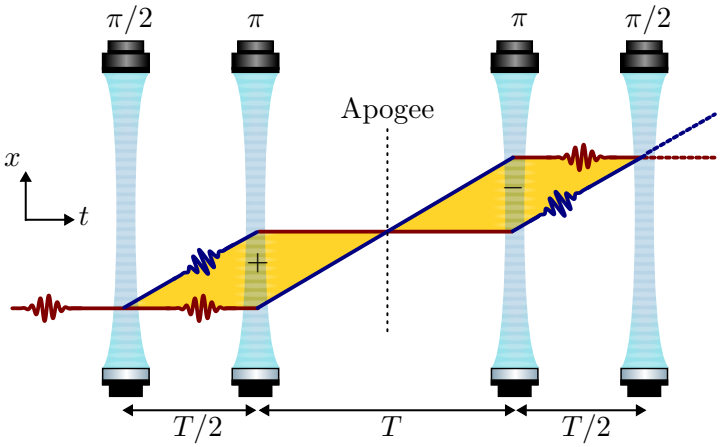

FIGURE II.6: The space-time representation of a 4-pulse interferometer. Shaded in yellow, is the physical area enclosed by the interferometer. The symmetry in this geometry with respect to the apogee results in the cancelation of the DC acceleration (gravity).

In our experiment, the physical implementation of this configuration corresponds to an atom launched upwards in a fountain configuration. Considering an interferometer centered on the apogee of the atom's trajectory, we have a folded geometry that can be seen as two effective 3-pulse interferometers with opposite signs which cancels the acceleration phase part. In this configuration, the phase difference is given by

$$\boxed{\Delta\Phi = \varphi_1 - 2\varphi_2 + 2\varphi_3 - \varphi_4} \tag{II.48}$$

by substituting phase contributions φ_i, the phase difference due to acceleration $\Delta\Phi_{\text{acc}}$ is zero. However, if we take into consideration the Coriolis force, the equation of motion of an object close to the surface of Earth under the Coriolis effect writes as:

$$\ddot{\mathbf{r}} = \mathbf{g} - 2\boldsymbol{\Omega} \times \dot{\mathbf{r}}, \tag{II.49}$$

where $\boldsymbol{\Omega}$ is the rotation rate. The analytic solution to this equation can be found in Appendix A. Using equation II.48 we get:

$$\boxed{\Delta\Phi_{\text{rot}} = \frac{T^3}{2}(\mathbf{k}_{\text{eff}} \times \mathbf{g}) \cdot \boldsymbol{\Omega}}. \tag{II.50}$$

This phase is a manifestation of a universal effect: the Sagnac effect on an atomic (matter-wave) interferometer and by using its general expression,

$$\Delta\Phi_{\text{rot}} = \Delta\Phi_{\text{Sagnac}} = \frac{4\pi E}{hc^2}\mathcal{A} \cdot \boldsymbol{\Omega}, \tag{II.51}$$

we identify the area $\mathcal{A}$ of the 4 pulse-interferometer given by

$$\boxed{\mathcal{A} = \frac{T^3}{4}\frac{\hbar}{m}\mathbf{k}_{\text{eff}} \times \mathbf{g},} \tag{II.52}$$

the area calculated using experimental parameters is approximately $\approx 11\,\text{cm}^2$. While the area of other implementations such as optical gyroscopes can very large. One of the many advantages of using an atomic interferometer is that the particle's energy that appears in the Sagnac effect expression can be bigger by orders of magnitude ($\sim 10^{11}$) for a massive particle ($E = mc^2$) than the energy of a photon ($E = h\nu$). Also, the scale factor which is a limiting factor for most gyroscopes in the case where it is not fully controlled or affected by external factors can be well controlled and determined in the case of the atomic gyroscope with metrological precision using frequency measurement (more details in Chapter IV). It is worth noting that the area of 11cm^2 in this work is currently the largest area known for an atomic gyroscope and can be interpreted as a macroscopic manifestation of a quantum system.

II.3.b Transition probability

At the output of the interferometer, the states get recombined and interfere. To establish a relation between the transition probability P and the phase shift $\Delta\Phi$, we calculate the full transfer matrix of the interferometer,

$$\hat{U}_{\text{interferometer}} = \hat{U}_{\pi/2}(\varphi_4) \times \hat{U}_{\pi}(\varphi_3) \times \hat{U}_{\pi}(\varphi_2) \times \hat{U}_{\pi/2}(\varphi_1). \tag{II.53}$$

Once evaluated, the transition probability is simply given by $|\langle \text{e}|\, \hat{U}_{\text{int}}\, |\text{e}\rangle|^2$. We find

$$\boxed{P = \frac{1}{2}\left(1 - \cos\Delta\Phi\right).} \tag{II.54}$$

This equation describes the interference pattern where fringes appear on the transition probability and are scanned via the interferometer phase.

II.3.c Phase of the interferometer

When taking into account the classical paths of two arms of the interferometer, the phase shift of the interferometer is given by three main contributions (for more details, see [42]):

$$\Delta\Phi = \Delta\Phi_{\text{laser}} + \Delta\Phi_{\text{prop}} + \Delta\Phi_{\text{sep}}, \tag{II.55}$$

where,

- $\Delta\Phi_{\text{laser}}$ is the lasers' phase contribution which we have already discussed above.
- $\Delta\Phi_{\text{sep}} = \mathbf{p}\cdot\Delta\mathbf{r}/\hbar$ is the phase due to the spatial separation $\Delta\mathbf{r}$ of the two atomic wavepackets (with a mean momentum $\mathbf{p}$) during the recombining pulse. In the case of a closed interferometer, this phase equals zero.
- $\Delta\Phi_{\text{prop}}$ is the propagation phase calculated using Feynman path integral formalism. This contribution is zeroed in the case where the Hamiltonian is quadratic in position and momentum [43].

II.3.d Measuring phase shift for an atom interferometer

As we have seen, the transition probability of a given state at the output of the interferometer is directly linked to the phase shift of the interference fringes. The interest of using Raman transition is that they allow measuring this phase shift simply by measuring the population of the atoms, N_g and N_e, in the two internal states $|\mathrm{g}\rangle$ and $|\mathrm{e}\rangle$ which have distinguishable energy levels and thus, can be addressed by tuning a laser frequency to the state of interest. The atoms in that state can be detected via fluorescence or absorption configuration and the number of atoms in different states can be detected using photodetectors or photodiodes in the limit of their quantum efficiency. Considering the state $|\mathrm{e}\rangle$ for example, we have

$$P_e = \frac{N_\mathrm{e}}{N_\mathrm{g} + N_\mathrm{e}} = P_0 - \frac{C}{2}\cos(\Delta\Phi_\mathrm{tot}), \tag{II.56}$$

where P_0 is an offset and C is the contrast which quantifies the visibility of interference fringes. The latter is limited by the efficiency of the Raman pulses that may drive atoms in an unwanted state which leads to a loss of coherence or parasitic interferometers.

II.3.e Fundamental limit: Quantum Shot Noise

Atom interferometers are ultimately limited by quantum projection noise (QSN). This noise originates from the counting statistics of uncorrelated particles. The randomness arises from the quantum nature of the atoms which behave unpredictably when measured.

Let consider an atom with a quantum state, $|\psi\rangle = a\,|\mathrm{g}\rangle + b\,|\mathrm{e}\rangle$. A measurement on an atom, let's say in the state $|\mathrm{e}\rangle$, corresponds to the projection operator $\Pi_e = |\mathrm{e}\rangle\langle\mathrm{e}|$, will result in 1 or 0 with a probability of $P = |b|^2$ and $1-P = |a|^2$, respectively. Statistically, the mean value of P is associated with a variance:

$$\sigma_P^2 = \langle\Pi_e^2\rangle - \langle\Pi_e\rangle^2 = \langle\Pi_e\rangle - \langle\Pi_e\rangle^2 = P - P^2 = P(1-P). \tag{II.57}$$

When considering uncorrelated measurement done on N_det atoms, we take the variance of the mean and we have $\sigma_P^2 = P(1-P)/N_\mathrm{det}$. This can be written as a standard error of the interferometer's phase as follows (Eq. II.54):

$$\sigma_\Phi = \sigma_P \frac{\partial\Phi}{\partial P} = \sqrt{\frac{P(P-1)}{N_\mathrm{det}}}\frac{2}{C\sin\Delta\Phi}, \tag{II.58}$$

when the interferometer is operated at its mid-fringe, i.e, $\Delta\Phi = \pi/2$, the standard error becomes:

$$\boxed{\sigma_\Phi = \frac{1}{C\sqrt{N_\mathrm{det}}}} \tag{II.59}$$

II.4 Sensitivity function

The sensitivity function is a tool to characterize the impact of the fluctuations in the Raman laser phase φ on the transition probability and, consequently, on the interferometric phase [44]. It is defined as

$$g_\varphi(t) = 2 \lim_{\delta\varphi \to 0} \frac{\delta P(\Delta\Phi, t)}{\delta\varphi}, \tag{II.60}$$

where, at the output of the interferometer, the transition probability is given by,

$$P = \frac{1 - \cos\Delta\Phi}{2}. \tag{II.61}$$

Considering an interferometer operating at its linear range i.e. at the mid-fringe ($\Delta\Phi = \pi/2$), we can write

$$g_\varphi(t) = \lim_{\delta\varphi \to 0} \frac{\delta\Delta\Phi(\delta\varphi, t)}{\delta\varphi}. \tag{II.62}$$

Using equation II.48, we can see that if we have a phase perturbation $\delta\varphi$ between two consecutive pulses, the phase difference can be easily evaluated as $\Delta\Phi = \pi/2 \pm \delta\varphi$ (for example, if we consider the first two pulses, $\Delta\Phi = \pi/2 - \delta\varphi$). Therefore, the sensitivity function for these intervals of time is evaluated as $g_\varphi(t) = \pm 1$. In the case where the same perturbation occurs at time t inside a Raman pulse, the sensitivity function is calculated by writing the transfer matrix for this pulse as a product of two matrices,

$$\hat{U}(t_0 + \tau, t_0, \varphi) = \hat{U}(t_0 + \tau, t, \varphi + \delta\varphi)\hat{U}(t, t_0, \varphi). \tag{II.63}$$

By taking $t = 0$ at the center of the interferometer, the sensitivity function (Figure II.7) is calculated[1] to be an odd function that is piecewise-defined as,

$$g_\varphi(t) = \begin{cases} -\sin\left(\Omega_R(t + t_1)\right) & \text{if } t \in [-t_1, -t_2] \\ -1 & \text{if } t \in [-t_2, -t_3] \\ +\sin(\Omega_R(t + \frac{T}{2})) & \text{if } t \in [-t_3, -t_4] \\ +1 & \text{if } t \in [-t_4, -t_4] \\ -\sin\left(\Omega_R(t - \frac{T}{2})\right) & \text{if } t \in [+t_4, +t_3] \\ -1 & \text{if } t \in [+t_3, +t_2] \\ +\sin\left(\Omega_R(t - t_1)\right) & \text{if } t \in [+t_2, +t_1] \\ 0 & \text{otherwise} \end{cases} \tag{II.64}$$

where, $t_1 = T + \tau/2$, $t_2 = T - \tau/2$, $t_3 = \frac{T}{2} + \tau$, $t_4 = \frac{T}{2} - \tau$ and τ is the duration of a $\frac{\pi}{2}$-pulse. This is an odd function and thus the integral equals zero. Since $\tau \ll T$, this function can be simplified by ignoring sine transitions and can be re-written as,

$$g_\varphi(t) = \begin{cases} -1 & \text{if } t \in [-T, -T/2] \\ +1 & \text{if } t \in [-T/2, T/2] \\ -1 & \text{if } t \in [T/2, T] \\ 0 & \text{otherwise} \end{cases} \tag{II.65}$$

[1] Full analytic calculations in my GitHub repository: link

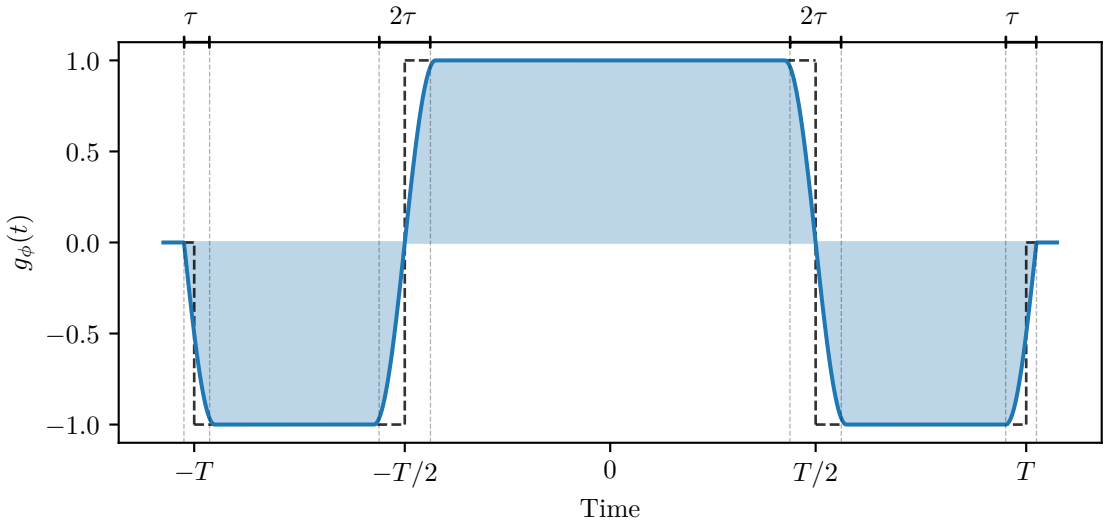

FIGURE II.7: Sensitivity function to phase $g_\varphi(t)$ for the 4-pulse interferometer (blue curve). The total duration is $2T + \tau$. Represented in black dashed lines, the simplified version of it where we ignore the duration of pulses. The duration of the pulses is exaggerated for visualization purposes. We note that $\tau \sim$ few μs where $2T \sim 1$s.

Therefore, the phase shift induced by Raman phase fluctuations can be calculated via the sensitivity function using,

$$\Delta\Phi = \int_{-\infty}^{+\infty} g_\varphi(t)\mathrm{d}\varphi(t) = \int_{-\infty}^{+\infty} g_\varphi(t)\frac{\mathrm{d}\varphi(t)}{\mathrm{d}t}\mathrm{d}t. \tag{II.66}$$

Frequency domain

Since the phase noise is usually a continuous time-varying signal with no defined function, a natural way to analyze its impact on the interferometer's phase is by going to the frequency domain. In practice, we measure the Power Spectral Density (PSD) related to phase noise (unit: $\mathrm{rad}^2/\mathrm{Hz}$), $S_\varphi(\omega)$. Therefore, we need to have a frequency representation for the sensitivity function (as a transfer function) $H_\varphi(\omega)$ to weigh the noise spectrum.

The transfer function is defined as $H_\varphi(\omega) = \omega G(\omega)$, where $G(\omega)$ is the the Fourier transform of $g_\varphi(t)$,

$$G(\omega) = \int_{-\infty}^{+\infty} e^{-i\omega t} g_\varphi(t)\mathrm{d}t = -i\int_{-\infty}^{+\infty} \sin(\omega t) g_\varphi(t)\mathrm{d}t. \tag{II.67}$$

Considering a sinusoidal modulation of phase noise $\varphi(t) = \sqrt{2}A\cos(\omega t + \psi)$, we apply equation (II.66)

$$\Delta\Phi = -\sqrt{2}A\cos(\psi)\omega\int_{-\infty}^{+\infty} g_\varphi(t)\sin(\omega t)\mathrm{d}t \tag{II.68}$$

$$= -\sqrt{2}A\cos(\psi)|\omega G(\omega)| \tag{II.69}$$

In this equation, ψ is randomly fluctuating when performing successive measurements. For that, an interesting quantity is the standard deviation (RMS value) over these fluctuations which results,

$$\sigma_\varphi = A|H_\varphi(\omega)|. \tag{II.70}$$

In general, for a given power spectral density $S_\varphi(\omega)$, the standard deviation of the phase noise is given by[1],

$$\boxed{\sigma_\varphi^2 = \frac{1}{2\pi}\int_0^{+\infty} |H_\varphi(\omega)|^2 S_\varphi(\omega)\mathrm{d}\omega} \tag{II.71}$$

Furthermore, the transfer function can be calculated using the definition in equation (II.64).

$$H_\varphi(\omega) = \frac{2\pi}{4\omega^2 - \pi^2}\left[2\omega\tau\cos\left(\omega(T+\frac{\tau}{2})\right) - 2\pi\sin\left(\frac{\omega\tau}{2}\right) + \pi\sin\left(\omega(T-\frac{\tau}{2})\right)\right] \tag{II.72}$$

For the sake of simplicity, we assumed that the condition $\Omega_R\tau = \pi/2$ is verified and since $\tau \ll T$, we neglect the small pulse duration τ compared to T. In consideration of that, we obtain:

$$\boxed{H_\varphi(\omega) = 8\sin\left(\frac{\omega T}{2}\right)\sin^2\left(\frac{\omega T}{4}\right)} \tag{II.73}$$

As displayed in Figure II.8, this function has an oscillating behavior where it goes to zero for frequencies that are multiples of $1/T$. In addition, this function describes the filtering properties of our interferometer and here we can see that it acts as a first order low pass filter for frequencies $\omega \gg \Omega_R$.

Sensitivity to acceleration

As we will show later, the experiment will be exposed to all sorts of vibrations that will eventually move the retro-reflecting mirrors which will change the phase of the laser. Since the atoms are inertial during their free fall, in their point-of-view, vibrations are seen as random accelerations. As we have explained previously, the 4-pulse interferometer is not sensitive to DC accelerations due to its symmetry. However, when dynamic accelerations are present in the system, this will no longer be valid. This section aims to evaluate the impact of such vibrations on the phase of our interferometer using the tools that we have developed. Using equation II.18, we can can establish a relation between an acceleration a and the phase,

$$\mathbf{k}_{\text{eff}} \cdot \mathbf{a} = \frac{\mathrm{d}^2\varphi}{\mathrm{d}t^2}. \tag{II.74}$$

With that given, the sensitivity function for acceleration $g_a(t)$ can be written as:

$$\frac{1}{k_{\text{eff}}}\frac{\mathrm{d}^2 g_a(t)}{\mathrm{d}t^2} = g_\varphi(t). \tag{II.75}$$

For practical reasons[2], we give also sensitivity to velocity $g_v(t)$,

$$\frac{1}{k_{\text{eff}}}\frac{\mathrm{d}g_v(t)}{\mathrm{d}t} = g_\varphi(t). \tag{II.76}$$

[1] Papoulis, Athanasios, and S. Unnikrishna Pillai. Probability, random variables and stochastic processes. 2002. p.324

[2] Vibrations in our experiment are measured using seismometers that outputs a signal of velocity.

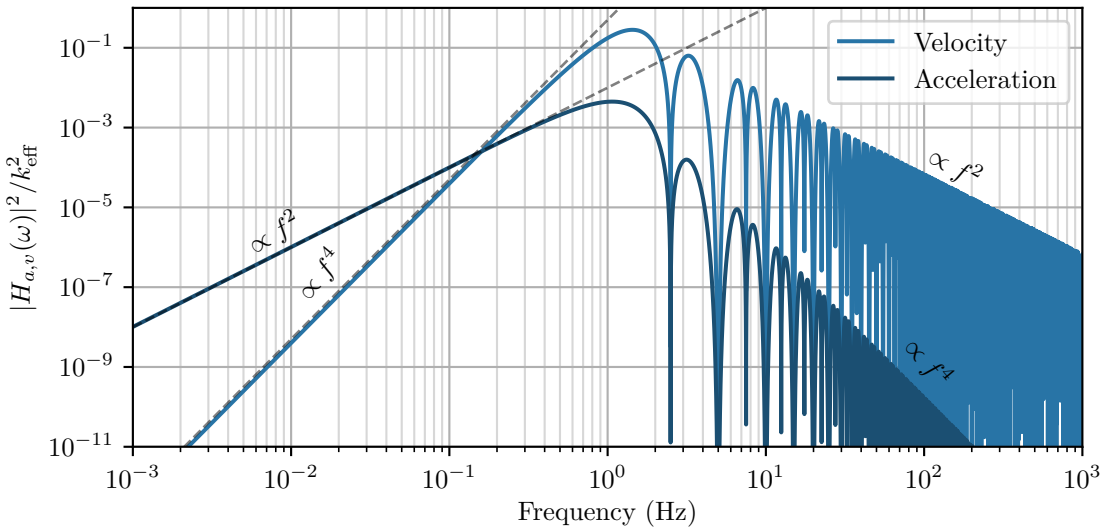

FIGURE II.8: Transfer functions for both acceleration and velocity in the frequency domain for an interferometer with $T = 400$ms.

.

Using Fourier transform, we pass to the frequency domain. We have the following transfer functions,

$$\boxed{H_a(\omega) = \frac{k_{\text{eff}}}{\omega^2} H_\phi(\omega) = 8\frac{k_{\text{eff}}}{\omega^2} \sin\left(\frac{\omega T}{2}\right) \sin^2\left(\frac{\omega T}{4}\right)} \tag{II.77}$$

$$\boxed{H_v(\omega) = 8\frac{k_{\text{eff}}}{\omega} \sin\left(\frac{\omega T}{2}\right) \sin^2\left(\frac{\omega T}{4}\right)} \tag{II.78}$$

Similarly, for acceleration (velocity) spectrum $S_a(\omega)$ ($S_v(\omega)$) in units of $\text{m}^2.\text{s}^{-4}/\text{Hz}$ ($\text{m}^2.\text{s}^{-2}/\text{Hz}$), respectively, the RMS value of the resultant phase noise is given by:

$$\boxed{\sigma_\varphi^2 = \frac{1}{2\pi} \int_0^{+\infty} |H_{a,v}(\omega)|^2 S_{a,v}(\omega) \mathrm{d}\omega} \tag{II.79}$$

II.5 Conclusion

In this chapter, we have seen that an atomic interferometer consists of performing a series of light pulses to create a particular geometry in space and time. The light pulses act as atomic optics to coherently control the states of the atom. These atom optics can be implemented via stimulated Raman transitions. The atomic interferometer can be tailored to measure specific inertial quantities via the phase difference in its output. We also showed that this phase difference is a consequence of the imprinted phase accumulated by the atom during its interaction with the lasers. The knowledge of this phase difference is accessible, thanks to Raman transitions again, on the difference of population in each state. This phase can be contaminated with other sources of noise which can be quantified using the sensitivity function formalism. In the following chapter, we will show how all of this can be implemented in an experimental environment and the technical subtleties that we should consider.

Chapter III

Experimental setup

To experimentally implement an atomic interferometer, we need two main ingredients: cold atoms and lasers. The science chamber is where these two meet and interact with each other. Our experimental setup for the atomic gyroscope consists mainly of a sensor head which is a large vacuum system (the science chamber). This sensor head is provided via optical fibers carrying diverse laser frequencies for preparing the atomic source, Raman interrogation and detection. The need for cold atoms arises from the requirement for a coherent source that does not expand too quickly as it propagates during the measurement cycle.

The experiment was largely built since 2008 [34] and then further improved by 5 generations of PhD students [35, 36, 37, 38, 45]. Also, several experimental setups date back to the first generation of the cold-atom gyroscope [33]. In this chapter, I will explain some aspects for completeness and describe the experimental setup, beginning with an overview of the sensor head structure and its various components. Then, I will outline the steps required to perform a complete measurement cycle. After that, I will describe the dedicated laser setups that enable us to generate all the required frequencies. Additionally, I will discuss the software used to control and monitor the experiment and acquire results for analysis. We will also explore the various interferometer configurations that we can use to mitigate unwanted effects. Finally, we will address the issue of vibrations in the experiment and explain how we can correlate and compensate for them.

III.1 Structure of the experiment

The gyroscope experiment primarily consists of a vacuum chamber made of titanium. Is surrounded by two layers of magnetic shields to isolate the interior from external magnetic shields. Due to the fountain configuration being used, the vacuum chamber has been designed to maximize its height, limited by the ceiling of the laboratory, to enable long interrogation times. As a result, it features a height of 1.7 meters.

To maintain a high vacuum level of 10^{-9}mbar, getters and ion pumps are employed. To define the quantization axis, four vertical copper bars are used to generate a constant magnetic field that can be switched between the X and Y direction. The entire structure is placed on a vibration-isolating platform, which sits on a rotation stage platform that

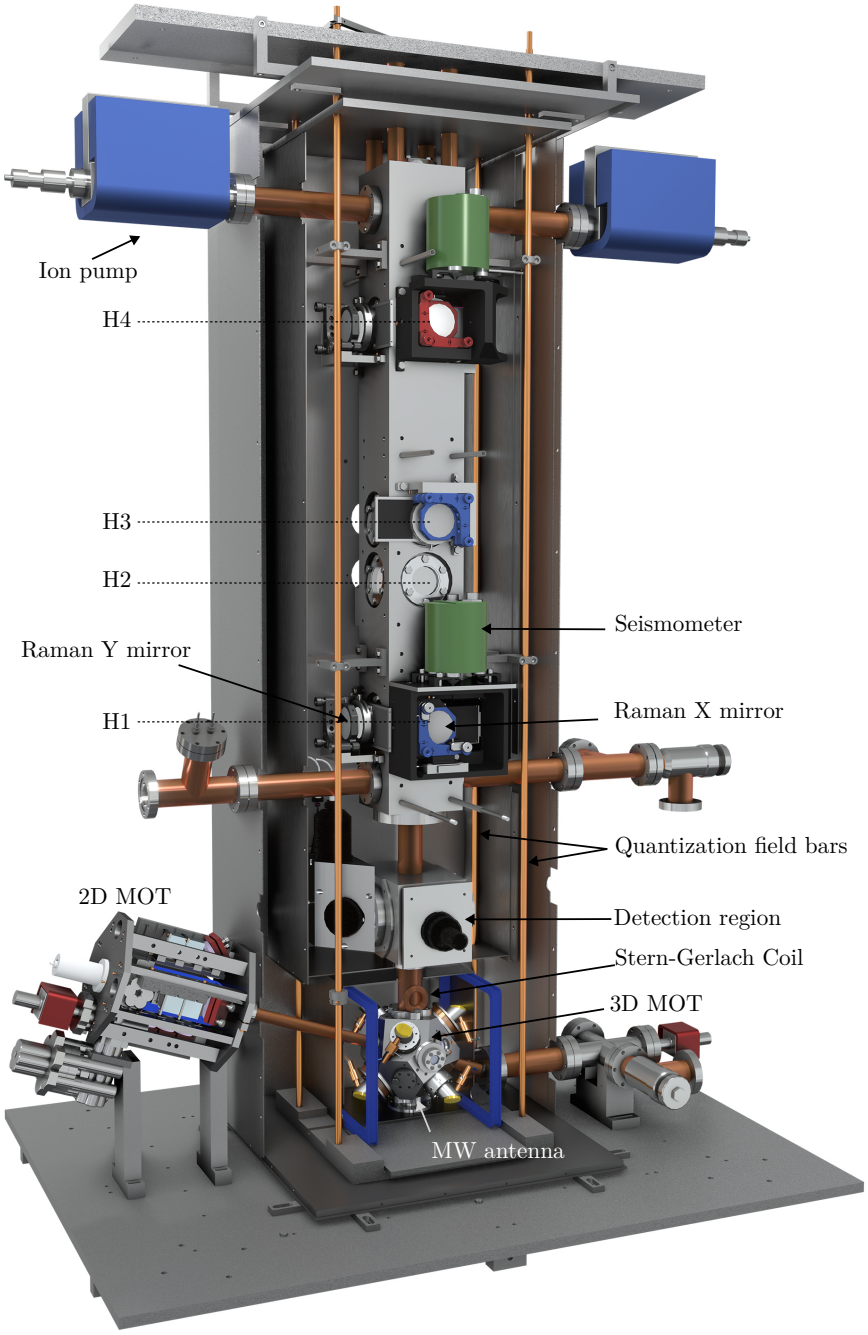

FIGURE III.1: Rendered 3D model of the atom gyroscope experiment.

allows for a full turn and the ability to change the orientation of the experiment. Both of these stages will be discussed thoroughly in what follows. The complete sensor head drawing is provided in (Figure III.1). The vacuum chamber can be seen as three main blocks:

1) Trapping Region: The trapping region is depicted in Figure III.2. In order to trap and cool atoms, we initially load them inside a longitudinal 2D Magneto-Optical Trap (MOT). The atoms are provided from a vapor cell and get confined in the 2D MOT using two orthogonal cooling beams (carrying cooling and repumping laser frequencies). A pushing beam is then applied to send the atoms into the 3D MOT region.

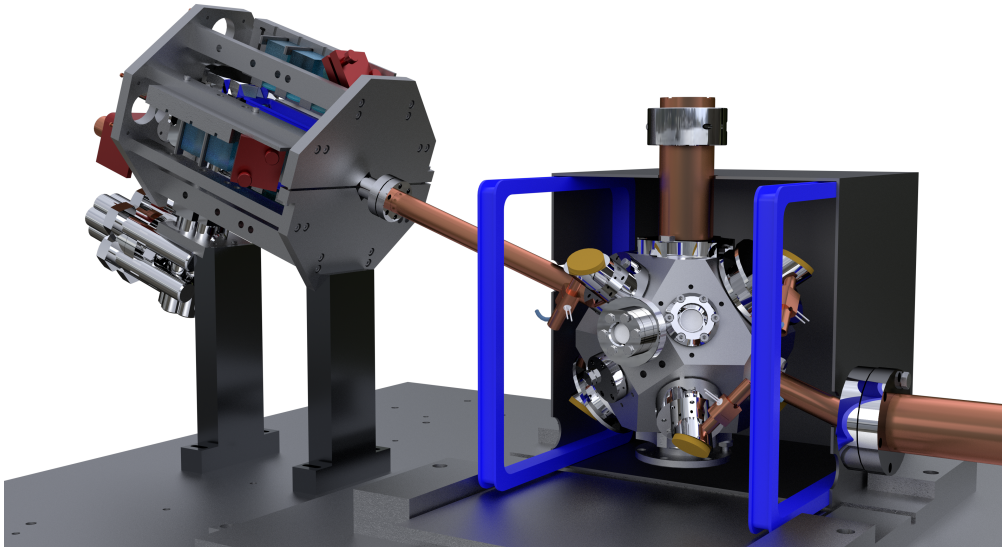

Figure III.2: Trapping region sectioned

In this region, we have six cooling beams forming three orthogonal pairs of counter-propagating beams in a σ^+/σ^- polarization. The magnetic-field gradients for both MOTs are generated using coils in anti-Helmholtz configuration where the zero of the magnetic field is located in the center of the trap. In addition, we use compensation coils (in a Helmholtz configuration) to compensate for the bias field due to the quantization bars in the X-Axis. During my thesis, I added a second pair (Blue squares in figure III.2) to compensate in the Y-direction when we switch the B-Field. Each coil features 20 turns.

2) Interrogation Region: Consists of a 1 m long chamber with four windows on each side at four different heights H1 to H4. The windows give access to the atomic cloud to perform Raman transitions.

3) Detection Region: In this area, an optical system generates three retro-reflected sheets of resonant light. Two of these sheets are formed by the detection laser beam, both having identical dimensions of $3 \times 1\,\text{cm}$. Between these two, there's a third sheet with dimensions $3 \times 0.2\,\text{cm}$, produced by a repumping beam. Photodiodes are installed on each side of the chamber to monitor the fluorescence of the atoms as they pass through these light sheets.

Additionally, the sensor head incorporates other complementary sensors and control systems onboard which we will detail in section III.4.

III.2 Sequence of measurement

III.2.a Trapping and cooling

The preparation stage is presented in Figure III.3. The goal of this is to trap and cool an atomic cloud that will be launched vertically toward the interrogation region and undergo the interferometer pulses. For that, a control sequence is implemented to drive the detuning of the lasers, the optical power of the top and bottom cooling beams, and the timings of mechanical shutters timings and other instrument triggers. The sequence goes this way:

- **2D MOT**: The cooling beams for the 2D MOT are on for a duration of $\sim$ 150 ms. An atomic beam is captured and simultaneously pushed toward the 3D MOT region providing it with a flux of relatively slow atoms.
- **3D MOT**: In the middle of the previous step we capture the atoms inside the 3D MOT. The lasers are at full power and the detuning is set to -1.6Γ (see lasers configuration).
- **Optical molasses**: We pass to an optical molasses regime by cutting the magnetic field and switching the detuning to -3Γ for a duration of 6 ms.
- **Drop-Recapture**: An additional step is used for optimization purposes. The lasers then are shut off and we let the cloud fall for 30 ms due to gravity. After that, the lasers are turned on to recapture the optical molasses which will be offset by 4mm to the bottom.
- **Launching**: At this stage, the launch mechanism is engaged. Here, we use the moving molasses technique which consists of symmetrical detuning between top and bottom beams (which are controlled independently via two AOMs) that will create an unbalance in the trapping forcing pushing the atoms upwards. The relation between the detuning $\delta\nu$ and the launch velocity v_0 is given by [46]: $v_0 = \sqrt{3}\,\lambda\,\delta\nu$.
- **Sub-Doppler cooling**: To cool the atoms even further, we apply the polarization gradient cooling technique while the atoms are traversing the beams, we linearly ramp both the detuning of the lasers (toward -17Γ) and the power optical power (toward adiabatic shut-down).
- **Reset**: After a few milliseconds, the laser's frequency is brought back to the cooling frequency since the same laser is used for detection. Also, the AOMs (optical power) are turned on while the shutters remain closed.

The parameters (timings, duration, and values) for sub-Doppler cooling ramps are adjusted experimentally to optimize the number of atoms and the temperature of the atomic cloud. We will give the estimated value of these two in the detection section.

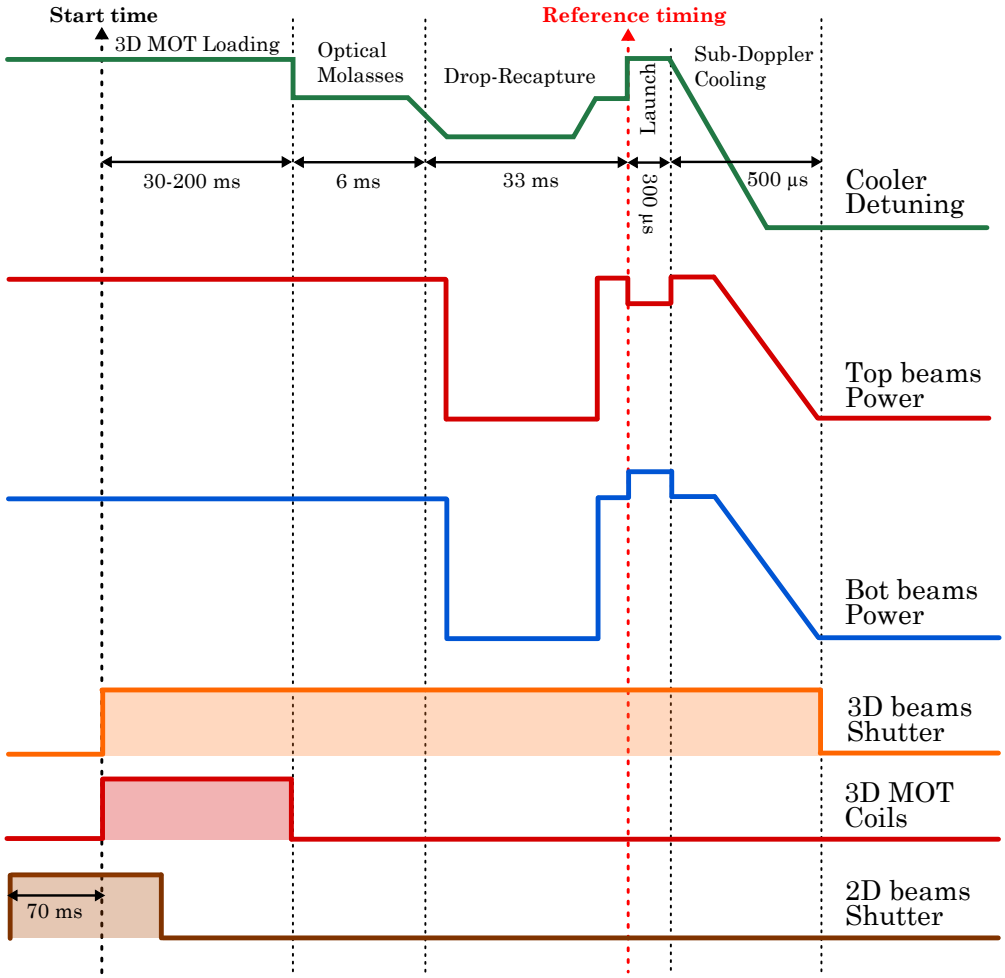

FIGURE III.3: Cooling sequence. Here we present the key steps to trap, cool and launch the atoms toward the interrogation region.

III.2.b Magnetic State Selection: Stern Gerlach

The launched atoms are in the hyperfine state $|F = 4\rangle$, populating all the 9 magnetic states $m_F = 0, \pm1, \pm2, \pm3, \pm4$. In this step, we want to select only the atoms in the sub-level $m_F = 0$ to participate in the interferometer, being insensitive to the first order to magnetic field fluctuations.

Until 2016, we used to perform a microwave π-pulse to drive the atom in the transition: $|F = 4, m_F = 0\rangle \rightarrow |F = 3, m_F = 0\rangle$ followed by a pusher beam to discard the atoms in $F = 4$. This pusher beam affected the interferometer performance when ran at high sampling rates since it scatters toward the interferometry region and caused decoherence effects. A better solution was inspired by the Stern-Gerlach experiment (1922), where a strong magnetic-field gradient is applied on the atoms that result in a force

$$\mathbf{F} = -\nabla(\boldsymbol{\mu} \cdot \mathbf{B}). \tag{III.1}$$

Here, $\mu = g_F \mu_B m_F$, where μ_B is the Bohr magneton and $g_F = 1/4$ is Landé g-factor for the $F = 4$ energy level. This force will deflect all atoms but those in $|F = 4, m_F = 0\rangle$ (1/9 of the initial population). For an efficient rejection, the force needs to be strong enough to prevent atoms from falling into the detection system. In our case, we use

a coil attached to the tube 25 cm above the 3D MOT which features 80 turns with a diameter of 4 cm.

> Considering an atom in $m_F = 1$ launched at $5\,\mathrm{mm.s^{-1}}$ at $(t = 0, z = 0)$. Here, we want to calculate the minimum magnetic-field gradient needed to deflect an atom in the $m_F = 1$ state. Considering an interaction of a time $\Delta t = D/v_0$, where D is the diameter of the coil, the atom acquires a velocity $v_x = F\Delta t/m$. The goal is to prevent to magnetic state to fall into the detection zone after the time-of-flight, $t_{\mathrm{tof}} \approx 1\mathrm{s}$. This corresponds to a displacement, $\Delta x = v_x t_{\mathrm{tof}} \sim 5\,\mathrm{cm}$.

In December 2020, the coil had a malfunction and had to be replaced with a new one. The characterization of the latter will be discussed later (section III.7) since it involves the use of other systems that we will discuss in what follows.

III.2.c Interrogation region

The interrogation region is cuboid-shaped and features four windows on each side, positioned at various heights. For the interferometer setup, we utilize two windows, requiring the presence of collimators at H1 and H4, along with their respective retro-reflecting mirrors. This geometric arrangement enables us to perform Raman laser interrogation on the atomic cloud along two perpendicular directions, X and Y. Consequently, it imposes limitations on the duration of the interferometer. As a result, the timing of pulses for a specific configuration is precisely determined by setting the appropriate launch velocity.

> To calculate the launch velocity for an interferometer done on heights h_B (bottom) and h_T (top) which are imposed by geometry, we need to determine the duration of the interferometer $2T$ and the timing of the first pulse. For that, we simply use the trajectory equation of a projectile launched at $z_0 = 0$ with a velocity v_0,
>
> $$z(t) = -\frac{1}{2}gt^2 + v_0 t\,, \qquad v(t) = -gt + v_0.$$
>
> For a symmetrical interferometer, at the apogee is restraint at $t = t_a = t_1 + T$, hence $v_0 = gt_a$. We use the timing of the first pulse where $z(t_1) = h_1$ and we get $t_a = \sqrt{T^2 + 2h_B/g}$. Finally, by using $z(t_a - \frac{T}{2}) = h_T$, the 4-pulse interferometer timings are:
>
> $$\boxed{T = \sqrt{\frac{8}{3g}(h_T - h_B)} \quad \text{and} \quad t_1 = \sqrt{\frac{2}{3g}(4h_T - h_B)} - T}$$
>
> Similarly, for a 3-pulse interferometer, we get:
>
> $$\boxed{T = \sqrt{\frac{h_T - h_B}{g}}, \quad t_1 = \sqrt{\frac{9h_T - h_B}{4g}} - \frac{3T}{2} \quad \text{and} \quad v_0 = g(t_1 + \frac{3T}{2})}.$$

Additionally, the detection timing (time-of-flight) can be calculated and found to be,

$$t_{\text{det}} = t_a + \sqrt{t_a^2 - 2h_{\text{det}}/g}$$

During my thesis, I worked mainly with the interferometer H1-H4. Note that we can use H1-H3 configuration in the X direction by moving the H4 Raman collimator to the correct position and for whatever concerns the retro-reflecting mirror for H3, it is already integrated into the vacuum chamber. Table III.1 gives a numerical evaluation for different possible configurations.

Windows	v_0(m.s^{-1})	$\delta\nu$ (MHz)	t_1 (ms)	$2T$ (ms)	t_{det} (ms)	Area (cm^2)
4P (H4-H1)	5.04	3.42	114	800	966	11.00
4P (H3-H1)	4.24	2.87	146	572	788	4.02
3P (H4-H1)	4.80	3.25	122	490	913	6.90
3P (H3-H1)	4.09	2.77	154	350	755	2.54

TABLE III.1: Timings and parameters for some allowed interferometer configurations with the resultant area.

To perform Raman pulses at the level of a window, a collimator is installed on one side and a retro-reflection mirror on the other side. The beams coming from the collimator pass through the two windows and then through a quarter-wave plate to the mirror.

Polarization: In this arrangement, multiple possible transition types can occur (Figure III.4):

- **counter-propagating transitions**: where two pairs are possible: ($\mathbf{k}_4$ with $-\mathbf{k}_3$ and $-\mathbf{k}_4$ with $\mathbf{k}_3$) leading to a diffraction of $\pm k_{\text{eff}}$ which are degenerated in frequency if the velocity of the atoms in the direction of the Raman beams is zero.
- **co-propagating transitions**: performed by the two incident beams or with the two retro-reflected beams.

Due to selection rules and the polarization of the beams, only one of the two configurations is allowed. And to have transitions between the two ground states with $m_F = 0$, the beams must be circularly polarized with the same handedness i.e. σ_3^+/σ_4^+ or σ_3^-/σ_4^-. The incident beams have the same linear polarization which can be decomposed as $(\sigma^+ \pm \sigma^-)/\sqrt{2}$ and the half-wave plate rotates the polarization of the retro-reflected beams to ensure a counter-propagating transition scheme.

Doppler Effect: For the counter-propagating configuration, two transitions are possible according to the two directions of the effective wave vector $\pm\mathbf{k}_{\text{eff}}$. In order to lift the degeneracy of these two transitions, we introduce a Doppler effect between the Raman beam and the atoms by tilting the beam with respect to the horizontal direction. It is then possible to favor one or the other of the diffraction directions by adjusting the frequency difference of the Raman lasers.

Considering a tilt angle $\theta_0 \sim 4°$ between the direction orthogonal to the atomic trajectory and the direction of the Raman beams, the result-in Doppler effect given by:

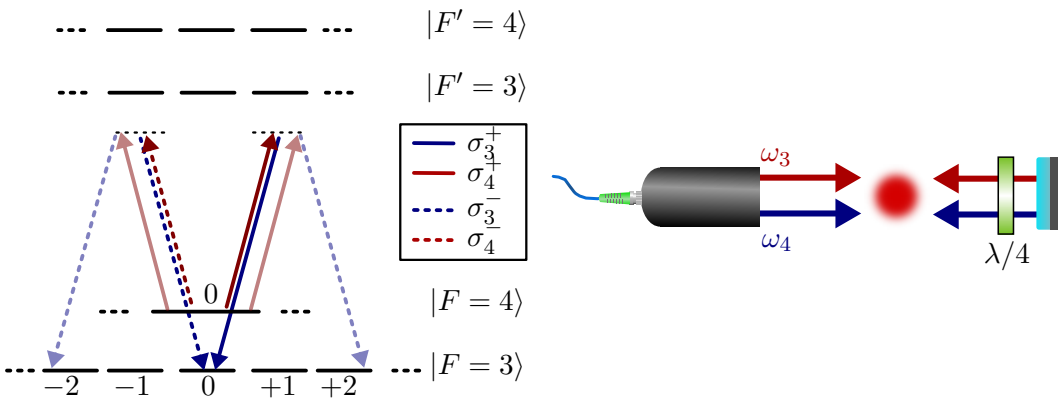

FIGURE III.4: Transitions allowed by a retro-reflected Raman beams configuration. The co-propagating transitions (transparent lines) drive the atoms to unwanted m_F states. The contra-propagation is the one used in our experiment and they correspond to a pair of beams with the same polarization as ($\sigma^{\pm}$, $\sigma^{\pm}$).

$$\omega_{\text{Doppler}} = \mathbf{k}_{\text{eff}} \cdot \mathbf{v} = k_{\text{eff}} v \sin\theta_0. \tag{III.2}$$

By varying the value of the Raman detuning, δ_L, we can highlight the two considered transitions referred to from now on as $\pm k_{\text{eff}}$. In Figure III.5, We show an experimental Raman spectroscopy where the parameter δ_L is swept and we reveal the two peaks at $\pm\omega_{\text{Doppler}}$, symmetric with respect to $(\omega_{\text{HFS}} + \omega_{\text{recoil}})$, corresponding respectively to the two transitions $\pm k_{\text{eff}}$.

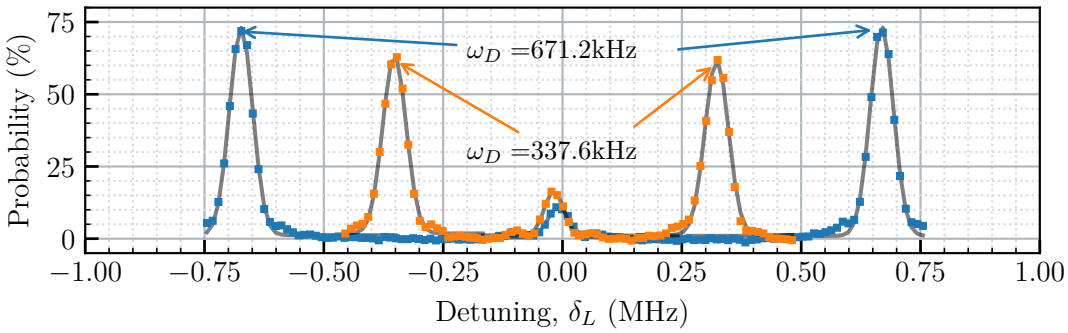

FIGURE III.5: Raman spectroscopy done at the level of two collimators H1 (blue) and H4 (orange). We plot the transition probability as a function of the detuning δ_L

.

In the case of our experiment, the atoms are launched in the vertical direction. The Doppler effect thus evolves over time in the following way:

$$\omega_{\text{Doppler}}(t) = (v_0 - gt) k_{\text{eff}} \sin\theta_0. \tag{III.3}$$

which means that the resonance conditions also depend on time. Experimentally, we solve this by implementing a linear frequency ramp[1] on the lasers' relative frequency, in order to ensure that the resonance condition is verified as the atoms travel inside

[1]Since we interrogate the atoms only at specific timings, this can also be implemented by frequency jumps (ladder instead of ramp).

the interferometer, and follow with to the Doppler shift evolution in time for a chosen transition peak ($\pm k_{\text{eff}}$).

Beam profile and Rabi oscillations: For the X direction, we use flat-top (or "top-hat") collimators [47] located. The system was upgraded before I arrived in 2018 and has been thoroughly characterized in [48]. In essence, these beams offer less intensity inhomogeneities, producing a flat intensity profile with a standard deviation of 11%. They produce beams of 28 mm in diameter, presenting phase variations of $\lambda/60$ RMS and $\lambda/3$ peak-to-valley. Figure III.6 displays the Rabi oscillations for both the H1 and H4 windows, both when atoms are ascending and descending. The benefit of using top-hat beams is especially apparent during the descent pulses when the atomic cloud is relatively larger and more sensitive to intensity inhomogeneities. This leads to better transfer, which in turn improves the contrast of the interferometer.

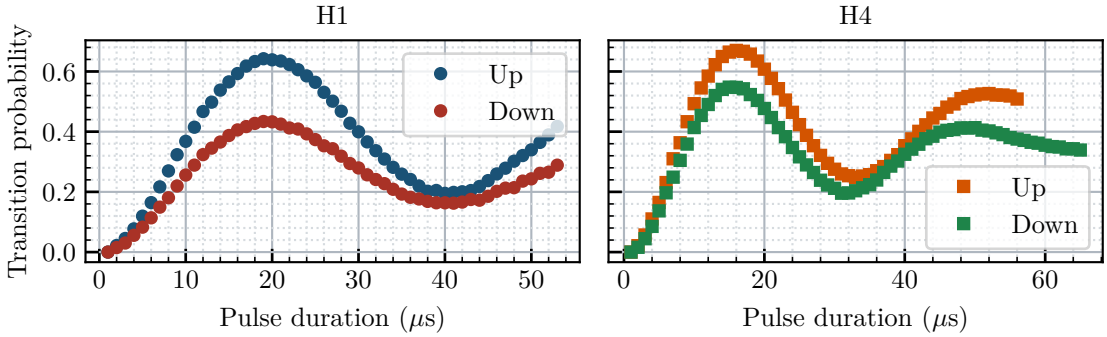

Figure III.6: Rabi oscillation for the four pulses of the interferometer, done on the X-axis which uses top-hat beams.

The collimators for the Y-axis are compact and are directly mounted onto the vacuum chamber. These systems emit a Gaussian beam with a $1/e^2$ diameter of 23 mm. Given their small size, the effects of the atomic cloud's expansion become more noticeable when performing Rabi oscillations, as shown in Figure III.7.

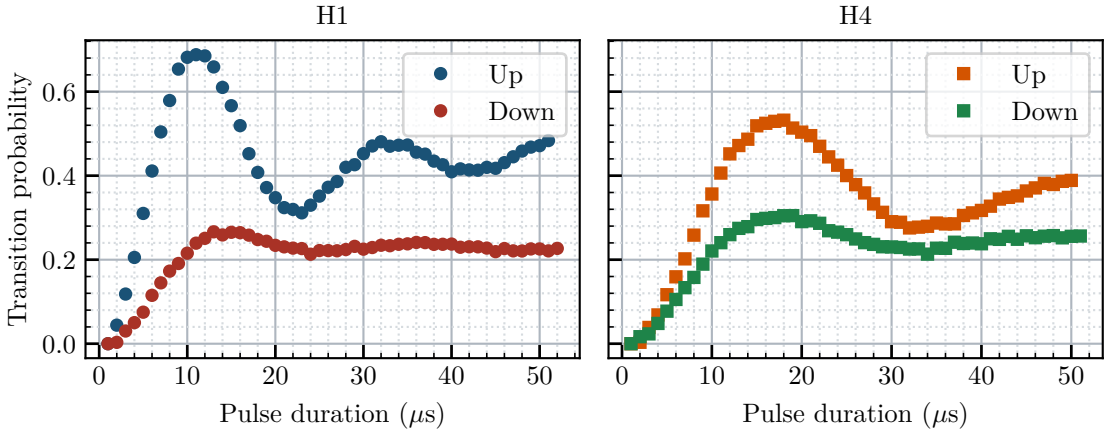

Figure III.7: Rabi oscillation for the four pulses of the interferometer, done on the Y-axis using Gaussian beams.

III.2.d Detection

After the Raman interrogation, the atomic cloud falls into the detection region. In this phase, our objective is to determine the number of atoms in each state in order to calculate the transition probability.

The detection system we use is based on the same design as the first version of the atomic gyroscope [33] and illustrated in Figure III.8. Detailed characterizations of the system can be found in previous works [36, 35], and the most recent modifications were made during the thesis of Denis Savoie [37]. In the following, we will provide a brief overview of how this system operates.

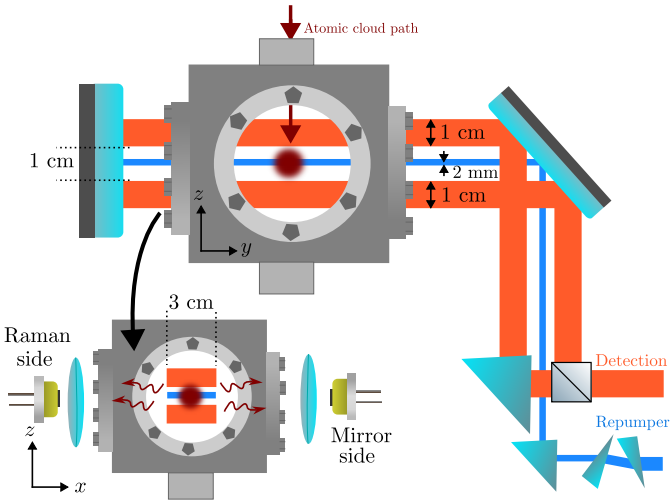

FIGURE III.8: Detection zone schematics (not to scale). The atomic cloud fall on two detection lightsheets each of 1 cm width. Between the two sheets, atoms are repumped using a lightsheet of 0.2 cm width. The fluorescence light is collected by two photodiodes on the x-axis placed on both sides of the chamber.

The detection process involves monitoring the fluorescence of the atoms using photodiodes as they pass through the lightsheets. The integral of the fluorescence signal is directly proportional to the number of atoms in state $|F = 4\rangle$. Therefore, the first lightsheet provides information about N_4, while the third lightsheet provides the total number of atoms, N_{tot}, as the atoms in state $|F = 3\rangle$ are repumped to state $|F = 4\rangle$ after passing through the first lightsheet.

We use two bi-quadrant photodiodes placed on the Raman X collimator side (Raman photodiode), and one on the opposite side (mirror photodiode). Each photodiode collects the light from both the top and bottom lightsheets, with a total collection efficiency of 2% for each quadrant. The signal is then amplified to remove the background offset and further amplified to be acquired on a PCIe-6341 card with a voltage noise of $0.3\,\text{mV}/\sqrt{\text{Hz}}$. The four generated signals (or what we call the time-of-flight) are acquired using a triggered task during 80 ms (Figure III.9).

These signals are treated in real-time inside the acquisition software to remove offset and then integrated. The integrals S_b and S_t, for each side, are proportional to the number of atoms N_4 and N_{tot}. The true number of atoms necessitates the knowledge of laser intensity which may have changed since the last time it was measured. In [49], an integral of 3 mV.s corresponds to 5.4×10^5 atoms. For the signals in figure III.9, we have ~ 4 mV.s which means that the number of detected atoms is approximately 7.5×10^5.

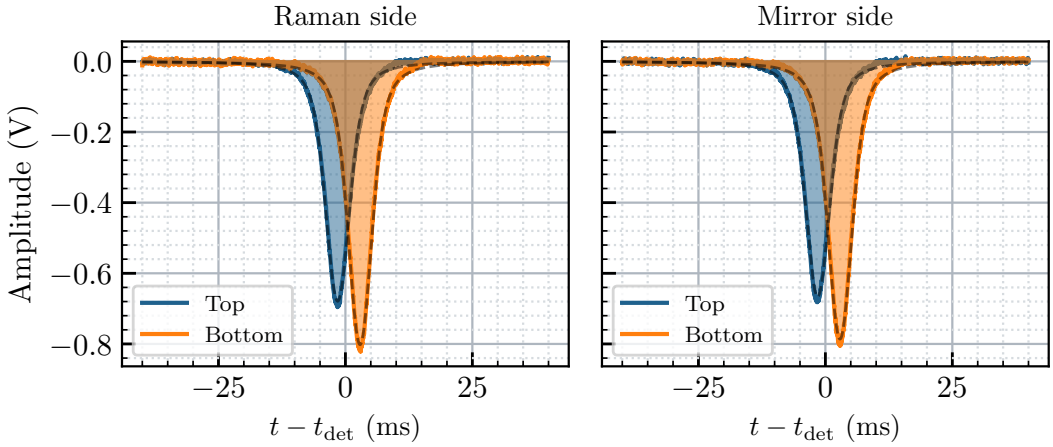

Figure III.9: Detection fluorescence signals for each quadrant for both sides. These signals are used to calculate the transition probability. The dashed lines are fitting curves using a Voigt function.

However, the detection process is prone to crosstalks, where a portion of the signal from one lightsheet leaks to the other quadrant and vice-versa. We account for these crosstalk effects by applying the following transformation to the integrated values (S_b and S_t):

$$\begin{pmatrix} N_3 \\ N_4 \end{pmatrix} = \begin{pmatrix} 1 & C_{bt} \\ C_{tb} & 1 \end{pmatrix} \begin{pmatrix} K_b S_b \\ K_t S_t \end{pmatrix}, \tag{III.4}$$

where, $K_{t,b}$ are normalization factors and C_{ij} are the crosstalks coefficients from lightsheet i to lightsheet j. Experimentally, the coefficients C_{tb} are straightforward to adjust, since we prepare the atoms at $|F = 4\rangle$, we need to verify a measured probability of zero when no Raman pulses are present. For what the coefficients C_{bt}, we perform a π-pulse with a microwave antenna just after the launch to transfer the atoms to $|F = 3\rangle$ followed by a pusher beam (the detection beam) to push what left in $|F = 4\rangle$. With that, we can time these coefficients to have no detected atoms in the top lightsheet.

Cloud Temperature: The time-of-flight (TOF) measurement also provides information about the temperature of the atomic cloud. This is because the TOF is a result of the convolution of the spatial extent of the atoms and the light sheet. We developed a simple model to estimate this temperature from the FWHM of the TOF. The model simulates the ballistic expansion of the cloud given by $\sigma_r(t) = \sqrt{\sigma_{r_0}^2 + t^2 \frac{k_B T}{m}}$, convoluted by a flat light sheet of $L = 1\,\mathrm{cm}$, resulting in:

$$V_{\mathrm{tof}}(t) \propto \sqrt{\frac{\pi}{2}}\sigma_r(t) \left[\mathrm{erf}\left(\frac{L/2 - z(t)}{\sqrt{2}\sigma_r(t)} \right) - \mathrm{erf}\left(\frac{-L/2 - z(t)}{\sqrt{2}\sigma_r(t)} \right) \right], \tag{III.5}$$

For different temperatures, we simulate the TOF signal and extract the FWHM of the resultant signal (as depicted in Figure III.10). We measure a FWHM of 5.4 ms, which corresponds to an estimated temperature T of 1.6 μK ($2.8 v_{\mathrm{rec}}$).

Another method to measure the temperature consists of probing the transverse velocity distribution of the atomic cloud. This is accomplished by using a Raman pulse with high-frequency resolution (i.e., low Rabi frequency) and scanning the detuning to interrogate the different velocity classes within the atomic cloud (as shown in Figure

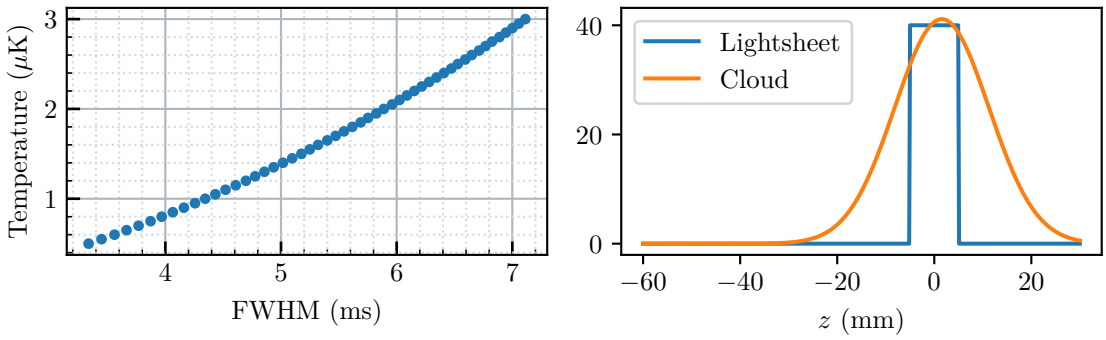

FIGURE III.10: (**left**) The correspondence between FWHM (in ms) and temperature of the atoms (in μK). (**right**) The convolution model at $t = t_{\text{det}}$ where we plot the cloud size and the lightsheet of a cloud with $T = 1.6\,\mu$K.

III.11). Notably, these two methods do not yield identical results which is likely due to detection issues when using the Raman method where the size of the atomic cloud becomes bigger than the size of the lightsheet, hence, the velocity distribution will be truncated by the detection. This suggests that Raman spectrum is representative of the temperature of the cloud. Therefore, we prefer to use the first method because it takes into account the size of the atomic cloud.

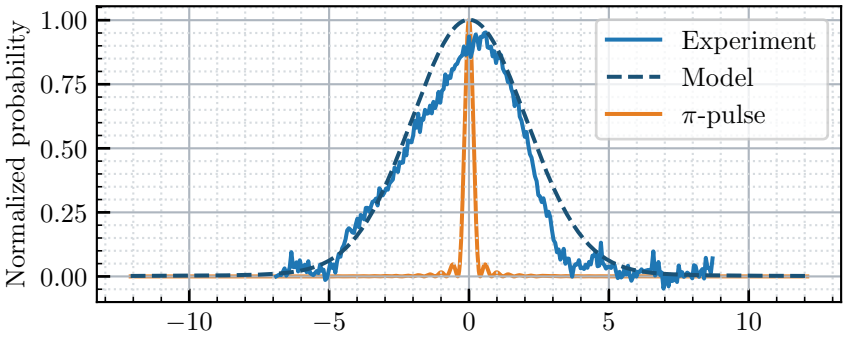

FIGURE III.11: Velocity distribution of the atomic cloud (blue) measured using a π-pulse with a duration of 300 μs (modeled in orange). This is fitted (dashed lines) with a model of a velocity distribution with a $\sigma = 2v_{\text{rec}}$.

Detection noise: The detection or probability noise may come from several sources, including electronics, photon shot noise, Raman laser beams, and others. Here, I will present the total noise contribution, which can be measured by performing the same sequence used for phase measurement but shifting all four pulses by 100 μs so that no interference occurs. With this adjustment, we can monitor the transition probability signal over time and perform an Allan variance analysis, which results in an Allan deviation of $\sigma_P = 1.8 \times 10^{-3}$. This can be expressed as phase noise $\sigma_\Phi = 18\,$mrad, which translates to a rotation noise of $\sigma_{\text{rot}} = 3.9\,\text{nrad.s}^{-1}$ for an interferometer with $2T = 800\,$ms and a contrast of 20%. This value is below the gyroscope's sensitivity to rotations at a single shot by a factor of 8. Although it's not currently a limiting factor, it could become one in the future.

III.3 Lasers setup

III.3.a Trapping and cooling / Detection

In this optical bench, we generate the frequencies needed for trapping and detecting the atoms. The main bench is depicted in Figure III.13 and its extension is Figure III.15. It hosts two master lasers (extended-cavity diode laser: ECDL) and two slaves that provide the necessary optical power for the cooling process.

Repumping laser (L1) (ECDL): This laser is the optical reference for all the lasers in the experiment. It is locked on the cross-over transition between $|6S_{1/2}, F = 3\rangle$ and $|6P_{3/2}, F' = 2/3\rangle$ based on saturated absorption spectroscopy (SAS) signal shown in Figure III.12. The 8mW power of this laser is distributed as follows:

- SAS spectroscopy (100 μW): The beam is retroreflected inside a Cesium vapor cell and frequency modulated using an EOM.
- Cooling repumper: Superimpposed with 3D slave beams (shifted to $|6P_{3/2}, F' = 3\rangle$).
- Beatnote with L2 (0.5 mW).
- Beatnote with L3 (3.5 mW) via optical fiber.
- Detection repumper: featured with a mechanical shutter. And shifted to level $|6P_{3/2}, F' = 3\rangle$ using an AOM at 75.65 MHz and sent via optical fiber to the sensor head.
- Repumper to the 2D MOT 2D bench (0.5 mW) via optical fiber.

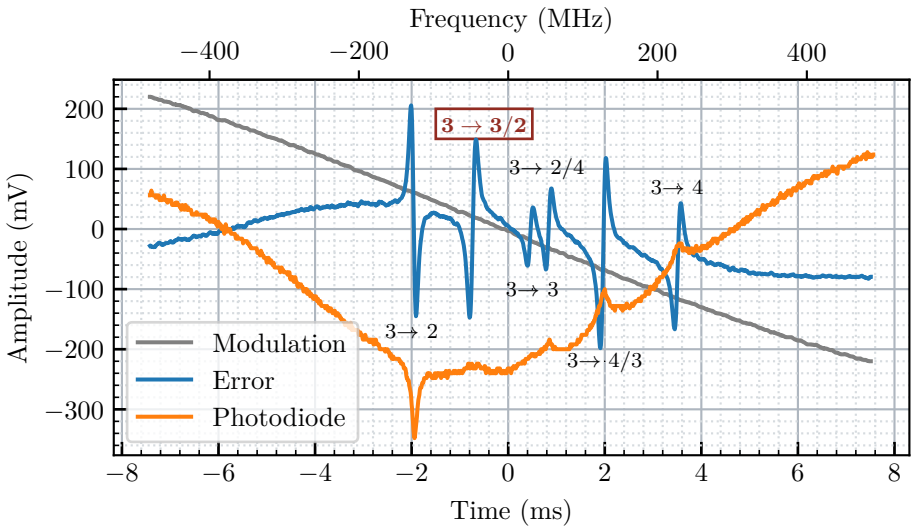

Figure III.12: Saturated absorption spectroscopy and error signal for L1. This corresponds the hyperfine resonance spectrum for $|F = 3\rangle \rightarrow |F' = 2, 3, 4\rangle$ transitions on the Cesium 133 D_2 line.

Cooling laser (L2) (ECDL): Locked on the L1 laser using a frequency offset lock method based on a comparison between the beatnote signal (at 8.8 GHz) and a 9 GHz local oscillator (LO). The frequency offset is set so that the laser is predominantly tuned to the cooling transition $|6S_{1/2}, F = 4\rangle \rightarrow |6P_{3/2}, F' = 5\rangle$.

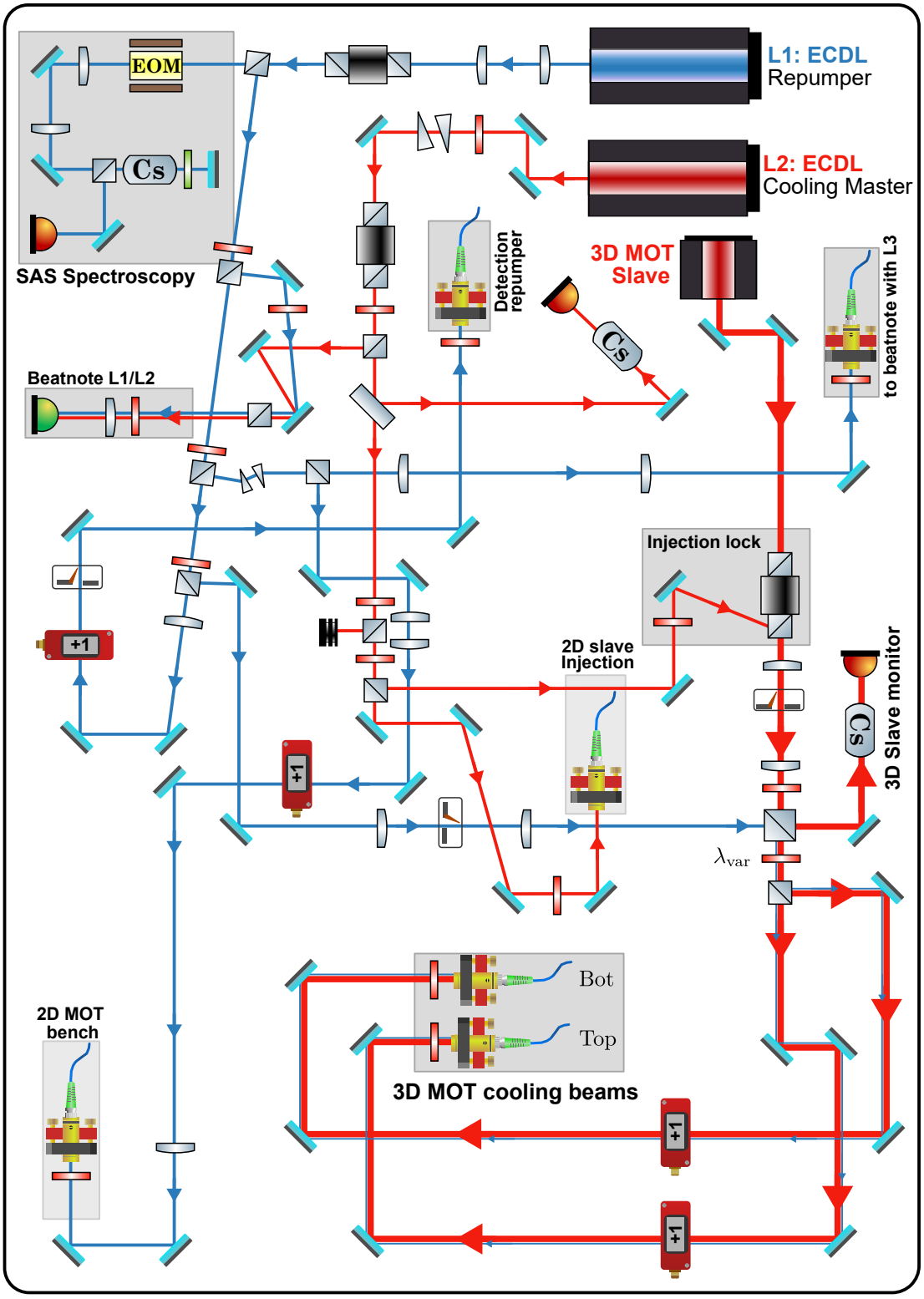

FIGURE III.13: Optical bench for cooling and trapping lasers.

This laser frequency is voltage-controlled (Figure III.14), allowing for detuning adjustments of the laser. The voltage is manipulated to induce frequency jumps, assisted by a feedforward mechanism on the piezo, during the cooling sequence. The main beam is distributed to do the following:

- Spectroscopy monitoring.
- Beatnote with L1 for frequency lock.
- Injection for the slave 3D ($\sim 200\,\mu$W).
- Injection for the slave 2D (optical fiber).

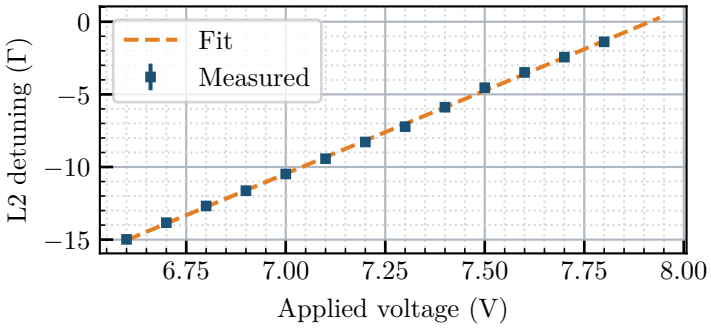

Figure III.14: Detuning of L2 (in units of Γ) with respect to the transition $|F = 4\rangle \rightarrow |F' = 5\rangle$ after the AOM with frequency 75 MHz as a function of the voltage offset. The measurements were extracted by monitoring the beatnote frequency of L1/L2.

3D and 2D MOT slaves: These lasers are frequency-locked using the injection locking technique on L2 and the injection is monitored by monitoring the absorption signal of these two lasers. The 3D slave is located on the main bench and outputs around 100 mW which gets superimposed with the cooling laser, split into two paths for top and bottom trap beams and sent via optical fibers to the sensor head ($\sim$ 30 mW for each after the AOM). On the other hand, the 2D MOT sits on a separate bench (Figure III.15) where a portion is used for detection (~ 15 mW) and what is left (~ 200 mW) is used for the cooling inside the 2D MOT.

Splitter Box: On the sensor head side, we have a homemade fibered box that has three inputs: Top, Bottom, and 2D fibers. The beams are split using beamsplitters and half-wave plates to output the six 3D MOT beams (3.1 to 3.6), the 2D MOT beams and the pusher beam. Photodiodes are integrated to monitor the power of each input fiber.

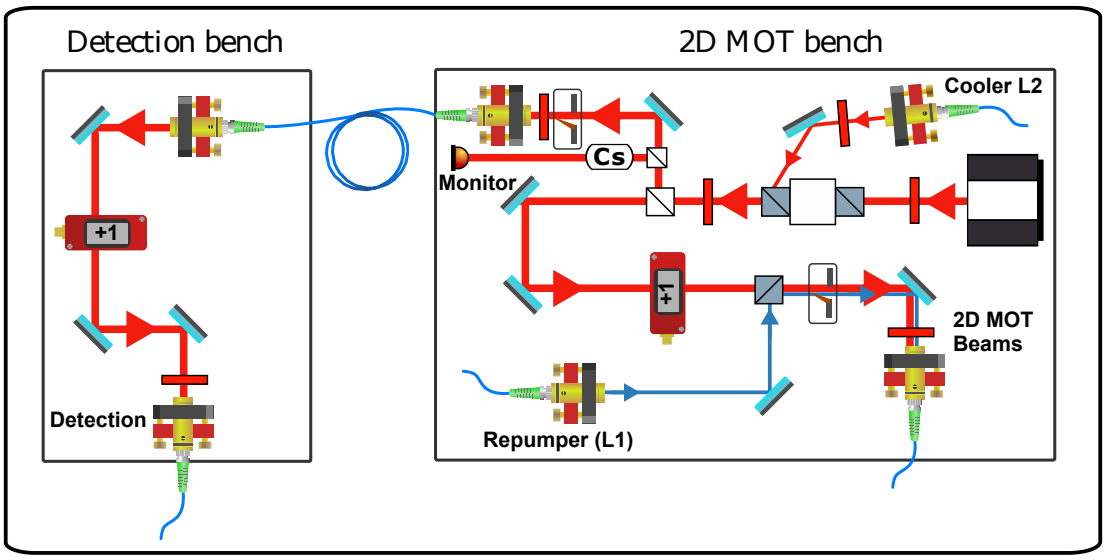

FIGURE III.15: Second stage of the cooling bench. Here we generate the beams for the 2D MOT and also for detection.

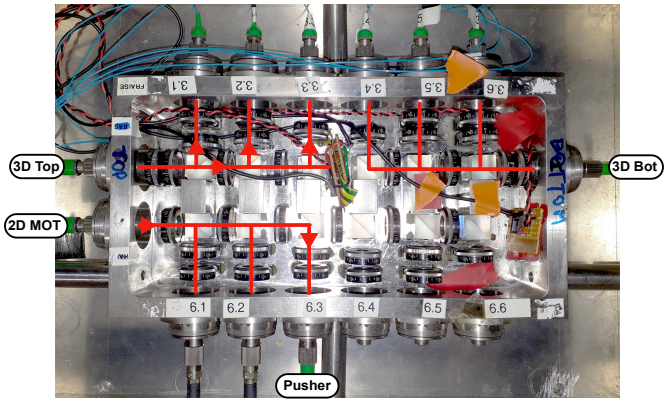

FIGURE III.16: Splitter box for MOT beams

III.3.b Raman pulses generation.

To generate Raman pulses, we use two lasers (ECDL): L3 and L4, as shown in the detailed setup in Figure III.19. These two lasers are locked together in phase to form the beams used for the interrogation of the atoms (ω_3 and ω_4). The L4 laser was replaced in 2020 by R. Gautier (more detailed characterizations are provided in [45]).

L3 Laser: L3 is locked to the repumper laser (L1). The locking method for L3 has been changed during my thesis, transitioning from a frequency offset lock to a phase-locked loop (PLL). More details about the new locking scheme of this laser will be discussed in section V.1. Here, we note this laser will define the Raman detuning frequency Δ which is fixed (for now) at 350 MHz (the frequency of the beatnote).

L4 Laser: L4 is locked on L3 which is done via a beatnote. As shown in the optical setup, the two lasers are superposed using a polarizing beamsplitter to form a bi-frequency beam with orthogonal linear polarizations. This beam is split into two using a combination of a motorized half-wave plate[1] and a polarizing beamsplitter.

The reflected part goes into a photoconductor that monitors the beatnote of the two frequencies. This beatnote frequency f_{beat} which we want to be at $\omega_L \approx 9.192\,\text{GHz}$ is sent to the locking chain (Figure III.17) where it get mixed with a microwave frequency at $f_{\text{DRO}} - f_{\text{DDS}}$. Here, $f_{\text{DRO}} = 9.4\,\text{GHz}$, is generated electronically inside a frequency chain, which we will not detail, and locked on the stable maser reference signal.

From this frequency, i.e f_{DRO}, we subtract (using a mixer) an RF frequency $f_{\text{DDS}} \sim 16\,\text{MHz}$ generated by DDS (AD9959), which will provide the degree-of-freedom to slightly change the relative frequency of the Raman beams, δ_L (few MHz), to perform Raman spectroscopy, for example. Furthermore, when the lasers are locked, the phase of this signal can be modified digitally via the DDS which will eventually change the relative phase of the two lasers ϕ_L mentioned above.

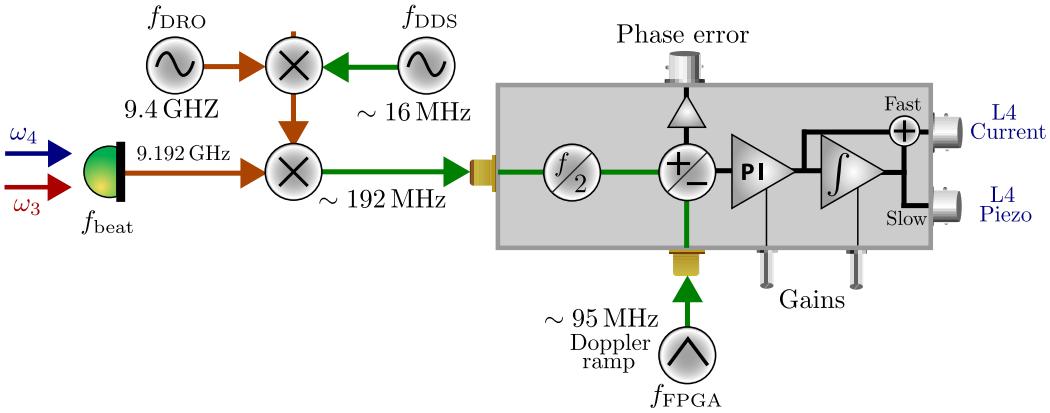

FIGURE III.17: Phase-lock scheme for the Raman laser L4.

The resultant frequency, $f_{\text{DRO}} - f_{\text{DDS}} - f_{\text{beat}}$ is approximately 190 MHz (RF range), goes to the PLL circuit where is get divided by two and compared with a reference frequency, f_{FPGA}, operating at around 95 MHz. The phase difference is then generated via a phase-frequency component, gets integrated in two stages and fed back to the L4 laser's piezo (slow) and current (fast) drivers closing the locking loop. In Figure III.18,

[1] This motorized waveplate was added recently, in order to automate the differential lightshift adjustments as it provides control over the power ratio of L3 and L4.

we show the beatnote of the two lasers when the PLL is engaged featuring 2 MHz of bandwidth.

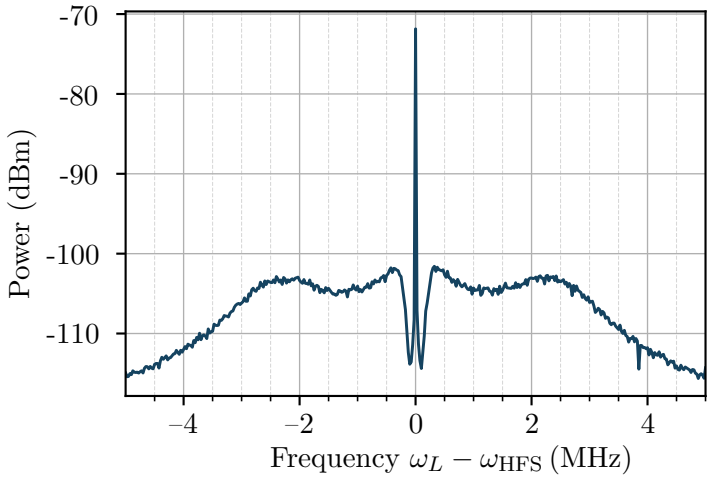

FIGURE III.18: Beatnote of lasers L3 and L4 when both are locked.

In fact, the reference frequency is not necessarily constant, as this is where the Doppler ramp is implemented. This frequency is generated using another DDS (AD9852), which provides a 48-bit frequency resolution and is clocked by a 500 MHz maser-derived signal. It is controlled via an FPGA, hence the designation f_{FPGA}, allowing a time resolution of 100 ns. We note that the effect of the ramp's discretization on the interferometer's phase has been studied in detail, particularly in the context of the atom gravimeter [50]. These studies were considered for the 4-pulse and the phase bias is null.

Amplification: We transfer the transmitted fraction of the bi-frequency beam via an optical fiber to the second bench on the left. The total power of the beam after the fiber is ~ 11 mW. This light is used to inject a Tapered Amplifier (TA) from EagleYard. This amplification technique was fruitfully studied and the results were published in [51]. We operate the TA at a current of 1.7 A which outputs typically ~ 600 mW of optical power. The main drawback is the generation of lateral sidebands which may lead to the formation of parasitic interferometers (more details in [45]).

Raman pulses: Post-amplification, the beam passes through an AOM which diffracts in the -1 order and operates at a frequency of $f_{\mathrm{AOM}} = 80$ MHz. This frequency is generated by a module designed by the SYRTE electronics department. The module facilitates control over the RF power sent to the AOM via a digital trigger. A TTL signal, which is generated by the experiment's sequencer and contains all the pulses of the interferometer, is used. When the TTL signal is high, light passes through the optical path X, and when it's low, the light is directed to the Raman Y-axis (this distributes the power between the two axes by deviating the beam). For both axes, we use a liquid crystal half-wave plate controlled by a second TTL signal to switch between the two outputs of a polarizing beam splitter. This splitter directs the Raman pulses either into H1 or H4 collimators on the sensor head. Furthermore, to ensure that no light passes when there are no pulses, a mechanical shutter is used in front of the beam's path.

Phase noise: The PLL circuit features a monitoring output for the phase error signal inside the loop. With that, we can perform an FFT measurement, and weigh the phase spectrum with the sensitivity function to phase variations, in order to calculate the phase contribution of this noise on the interferometer. This led to a total in-loop noise

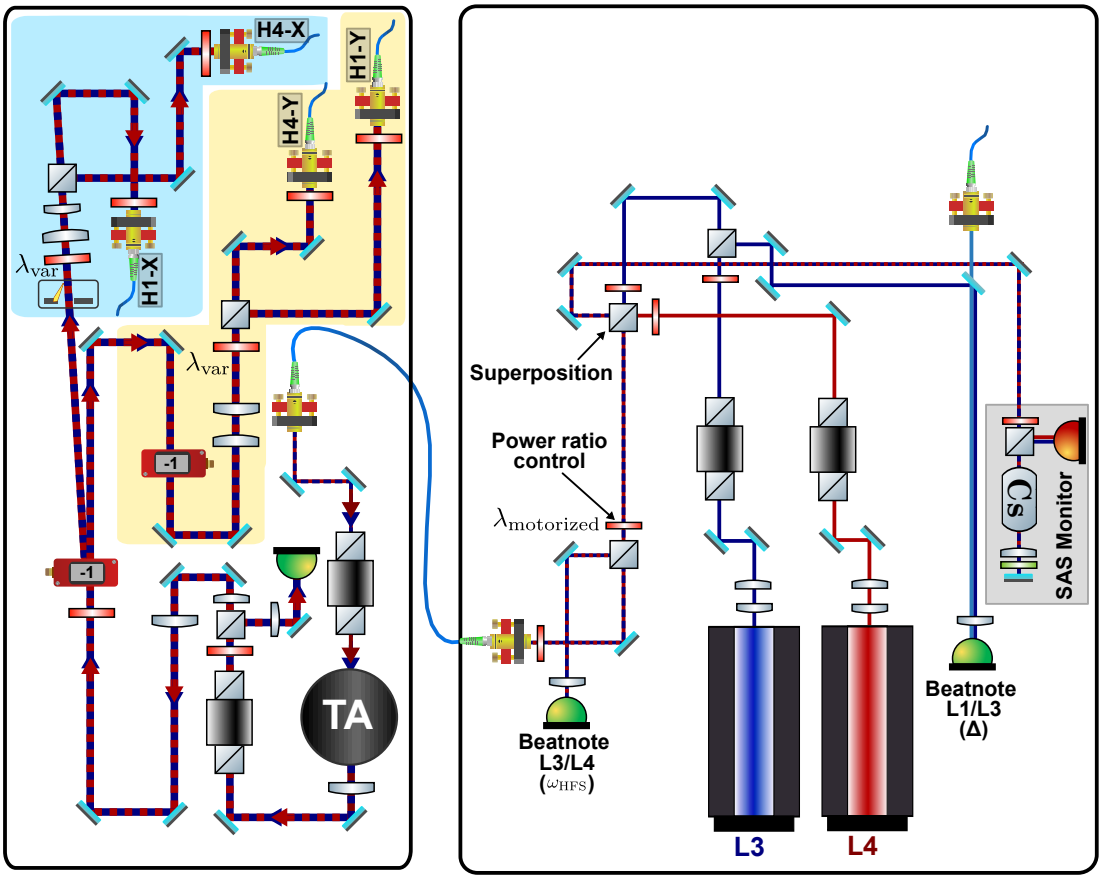

FIGURE III.19: Optical bench for the generation of Raman beams.

of 3.5 mrad and 4.6 mrad outside the locking loop. The latter was done by comparing a second beatnote after the amplification stage and comparing it with the same frequency reference. With that, the residual phase noise is far from being a limiting factor for our measurements.

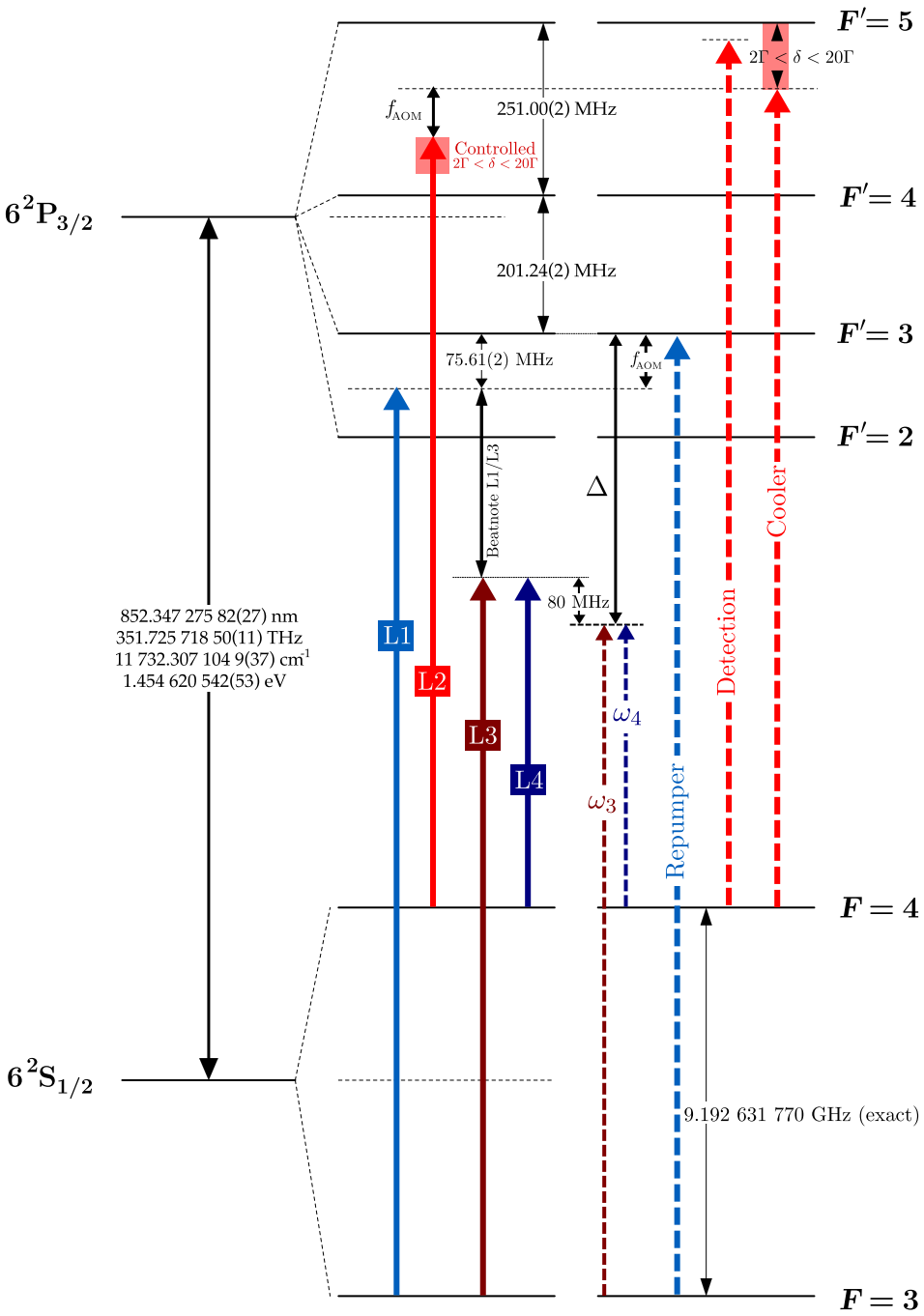

FIGURE III.20: Cesium D_2 transition hyperfine structure with lock frequencies of the ECDL lasers (solid lines) and the frequencies used across the experiment (dashed lines).

III.4 Complementary sensors

III.4.a Seismometers

The vibrations are monitored using two seismometers (Trillium Compact 120s) positioned as closely as possible to the top and bottom retro-reflecting mirrors of the Raman X-axis. These seismometers provide velocity measurements (with a sensitivity of 750V/m.s^{-1}) in the three axes: X, Y, and Z. Their transfer function remains flat within the range of 0.1 to 10 Hz.

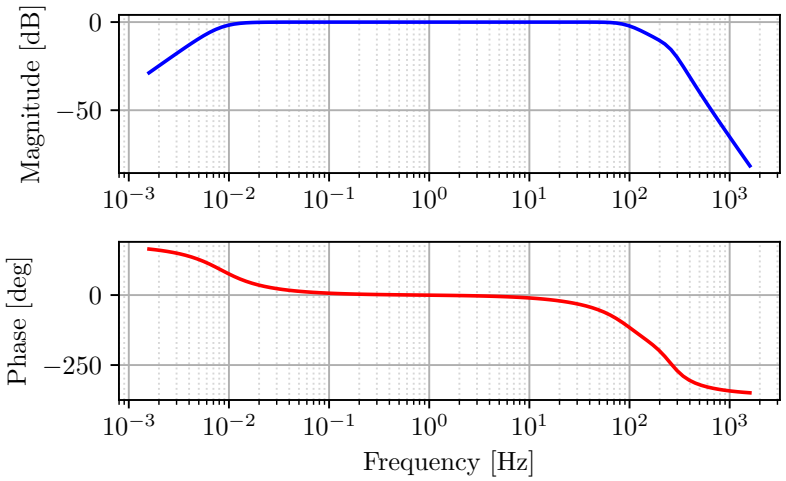

Figure III.21: Transfer function of the seismometers.

The signals of the seismometer are acquired on a differential configuration NI PCIe-6341 16-bit card (±1V range) with low-pass filtering at a cutoff frequency of 300 Hz on its input ports. We present in Figure III.22, the amplitude spectral density (ASD) of accelerations derived from the signals of the two seismometers.

The phase contribution of each frequency band to the vibration phase noise can be calculated using the tools that we developed in section II.4. The results are presented in the following table:

f-**Band**	10^{-4}-0.001	0.001-0.01	0.01-0.1	0.1-1	1-10	10-100	**Total**
Acc X	0.00	0.00	0.01	1.67	0.56	0.15	1.77
Acc Y	0.00	0.00	0.00	1.63	0.63	0.15	1.75
Acc Z	0.00	0.00	0.00	0.62	0.39	0.11	0.74
Rot X	0.37	1.82	0.85	0.64	0.09	0.07	2.14
Rot Y	0.38	1.27	0.50	0.54	0.08	0.07	1.52
Rot Z	2.16	0.83	0.29	0.11	0.05	0.02	2.34

For acceleration, the noise dominates in the band 0.1-1 Hz where the sensitivity function is at its maximum value. And for rotation, the noise raises at low frequencies.

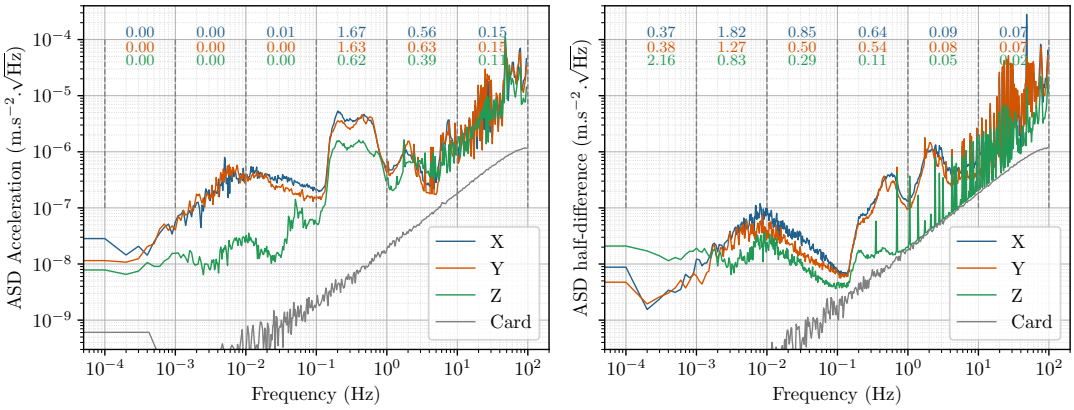

FIGURE III.22: ASD of accelerations calculated using the seismometers' signals. (**left**) The half-sum of the top and bottom signal. (**right**) The half-difference which represents rotation.

III.4.b Tilt monitoring and control

When aligning the interferometer, it's necessary to adjust the tilt of the experiment (changing the projection of **g**) to verify the verticality of the launch or to test the effects associated with this parameter. Additionally, it's crucial to monitor the tilt value and its temporal fluctuations to quantify the phase attributed to DC acceleration, as we'll discuss in the following sections.

Monitoring: We use a 2 axes precision inclinometer (A701-2) mounted on the experiment to monitor the X and Y tilt of the experiment. This sensor covers a range of $\pm 0.046°$ with a sensitivity of 0.1μrad/mV.

Control: Two voice-coil actuators are placed on the ground and act on the floating platform in a locking loop to maintain a predefined setpoint that ensured vertical launching along the plumb line. However, these coils do not allow large modifications for the tilt of the experiment and coils may heat when a high current is applied. Therefore, these coils are used to maintain the lock around the setpoint by performing minor adjustments. Bigger tilt adjustments are done by manually moving heavy masses around the experiment.

During my thesis, we came up with a better system that consists of motorized sliders which are a 3D printed rail system that uses a NEMA 17 stepper motor controlled with an Arduino to translate a 2 Kg mass along one axis using a belt-pulley mechanism. This system allows it to cover 10 times the range allowed by coils. We used TMC2208 driver which introduces less vibrations on the system as well as vibration dampeners on the motors. To integrate this into the acquisition software of the experiment, the Arduino is programmed to respond to a pre-defined set of commands via serial communication that enables it to move to an absolute or a relative position, calibrate the system, get the position of sliders, or set the acceleration and the speed of the sliders.

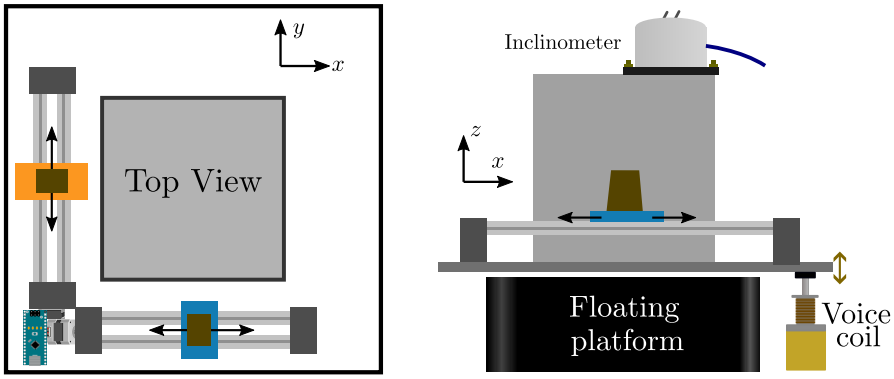

Figure III.23: Illustration of tilt monitoring and control system. (**left**) Automatisation sliders are controlled via an Arduino servo. (**right**) Position of one of the voice coils (X) which stabilizes the tilt value, by acting on the floating platform, based on the inclinometer readings.

III.4.c Orientation and position sensors

As previously mentioned, the entirety of the experiment, including the floating platform, is situated on a rotation platform (model: ALAR-250LP from AeroTech). This configuration enables us to rotate the experiment through a full turn, allowing us to

measure the Sagnac Phase at different projections of Earth's rotation (refer to Chapter IV). While it is possible to automate this platform and control it via a computer, the team has found this approach to be potentially risky. Consequently, we manually turn the experiment and secure it with heavy masses when performing measurements. The platform's internal sensor, via its associated software, provides the relative orientation angle with an accuracy of 10 μrad.

However, given that the experiment is floating and is surrounded by dozens of BNC cables and optical fibers, the upper part of the floating platform (i.e., the sensor head) may experience slight stress and therefore become misaligned with respect to the bottom part. Even without external stress, as this would be evident on the seismometers, the platform's strings may undergo relaxation movements that could cause such effects.

The amplitude of the Sagnac effect (a sine function) is expected to be around 220 rad, which means that at the point of maximum sensitivity, a change in the angle of 1 mrad will be translated to a phase error of $\sim$ 200 mrad, affecting the quality of our measurements. Consequently, we use position sensors to correct the orientation angle value.

The concept here is to measure the displacement of the floating platform at two points relative to a fixed target outside of it. For this, we use two position sensors (DW-AS-509-M12-390 from Contrinex) which operate based on a magnetic induction effect. When the sensor is close to the metallic target surface, the current changes, and thus the induced voltage can be calibrated to a distance measurement by using a travel translation stage. The system and its calibration are displayed in Figure III.24.

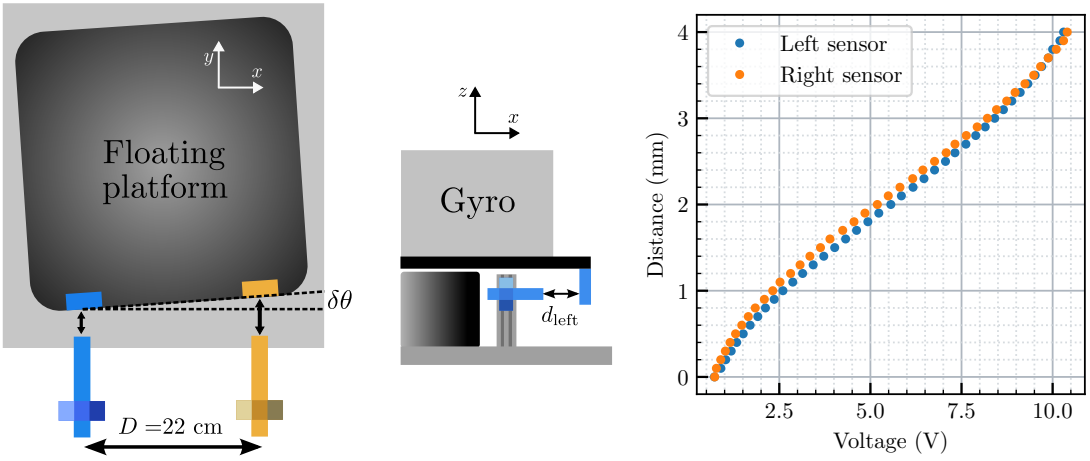

FIGURE III.24: Position sensors (**left**) Illustration of mis-alignment.(**middle**) Location of the actual setup (**right**) Calibration of the system.

The voltage reading is thus continuously monitored during the measurements inside the acquisition software. To calculate the angle correction, we use the simple relationship:

$$\delta\theta = \arctan\left(\frac{d_{\text{right}} - d_{\text{left}}}{D}\right), \tag{III.6}$$

here, D is the distance between the two points and positive angles indicate clockwise rotations.

III.5 Real-time vibrations compensation and mid-fringe lock

Due to the long interrogation duration, the phase that we measure is highly susceptible to external noise factors, particularly vibrations. Generally, vibration noise is the most important source of sensitivity degradation in cold-atom inertial sensors of large areas. From the perspective of the atoms, these vibrations manifest as AC accelerations, resulting in random phase shift, denoted as Φ_{vib}, accumulated during the interferometric measurement. This phase noise can span several radians, effectively obscuring the interference fringes (Figure III.25).

To deal with the vibrations, the experiment sits on a floating platform (Minus K - BM1) which dampens ground vibrations beyond its resonance frequency of 0.5 Hz. The well functioning of this platform is ensured by heavy-mass distribution on the platform. However, this is not sufficient due to the large area of our interferometer.

We use a method called "Batman" [42] (referring to the Batman or twin-horned distribution) to estimate the parameters of interferometer fringes, i.e. contrast C and offset P, independently from phase noise present in the signal. It also allows us to evaluate the standard deviation of the transition probability noise, σ_P. With that, we can calculate the signal-to-noise ratio, SNR $\equiv C/2\sigma_P$ and the sensitivity of the atomic interferometer, $\sigma_{AI} \equiv 1/\text{SNR}$.

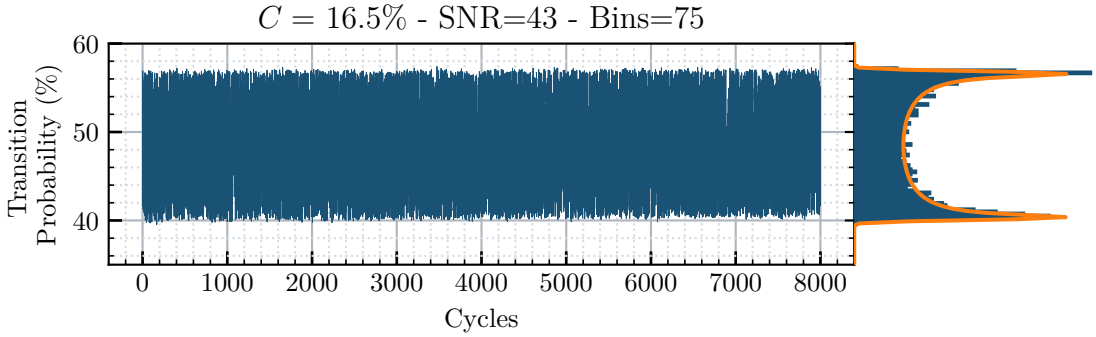

FIGURE III.25: Raw signal of the interferometer for 8000 cycles. (**left**) we plot the measured transition probability of the interferometer while the phase is randomized due to vibrations. (**right**) The histogram of the data (batman).

Our goal here is to estimate at best the true phase due to vibrations, Φ_{vib}. This calculated phase is then used to recover the interference fringes by plotting the measured transition probability as a function of the phase, $\Phi_{\text{vib}}^{\text{calc}}$, for a large enough cycles of measurement (few 1000). When disregarding other sources of phase noise and bias, the relationship between the two is expressed as:

$$P = P_0 + \frac{C}{2}\cos\left(\Phi_{\text{rot}} + \Phi_{\text{vib}}^{\text{calc}} + \delta\Phi_{\text{vib}}\right), \tag{III.7}$$

where $\delta\Phi_{\text{vib}}$ is a small phase error with respect to the real vibration phase. I will discuss the various methods we can use to convert the raw data produced by the seismometers into a phase contribution:

1) Weighted mean method: This method consists of taking the acquired signals of each seismometer, $v_i^{\text{top}}(t)$ and v_i^{bot} $(i = x, y, z)$ during the measurement cycle, multiply by the sensitivity function, $g_v(t)$ of the total interferometer, and integrate to get a phase

contribution. This can be expressed as follows:

$$\Phi_i^{\text{top}} = \int_0^{2T} v_i^{\text{top}}(t) g_v(t) \mathrm{d}t \quad \text{and} \quad \Phi_i^{\text{bot}} = \int_0^{2T} v_i^{\text{bot}}(t) g_v(t) \mathrm{d}t \tag{III.8}$$

Subsequently, we use a linear weighted combination of the calculated top and bottom phases to determine the effective vibrational phase:

$$\Phi_{\text{vib}}^{\text{calc}} = \sum_i \left(\alpha_i \Phi_i^{\text{top}} + \beta_i \Phi_i^{\text{bot}} \right). \tag{III.9}$$

When the seismometers are properly aligned, for the Raman X interferometer for example, the predominant coefficients are α_x and β_x, that is, along the wave vector. These coefficients approach 0.5, implying that this phase originates from a common acceleration on both mirrors. Furthermore, the use of the sensitivity function for velocity $g_v(t)$, which behaves like a second-order highpass filter, eliminates any offset between the two seismometers.

2) Displacement of each mirror: The phase shift due to vibration can be expressed (Eq. II.48) as a displacement of the mirrors the top and bottom mirror which can be calculated simply by integrating the velocity signals as follows:

$$\begin{aligned} \Phi_{\text{vib}}^{\text{calc}} &= \varphi_{14} - 2\varphi_{23} \\ &= \mathbf{k}_{\text{eff}} \cdot \int_0^{2T} \mathbf{v}_{\text{mirror}}^{\text{bot}}(t)\, \mathrm{d}t - 2 \int_{\frac{T}{2}}^{\frac{3T}{2}} \mathbf{v}_{\text{mirror}}^{\text{top}}(t)\, \mathrm{d}t, \end{aligned} \tag{III.10}$$

where $\varphi_{14} = \varphi_1 - \varphi_4$ and $\varphi_{23} = \varphi_2 - \varphi_3$.

In practice, we use a combination of coefficients for each velocity signal since they do not measure directly the velocity of the mirrors. Furthermore, the two seismometers might have different DC offsets, which are indistinguishable from a real inertial signal. This will result in a bias during integration. Hence, a second-order high-pass filter with a cutoff frequency f_c is numerically implemented[1] resulting in $\tilde{\mathbf{v}}^{\text{top}}(t)$ and $\tilde{\mathbf{v}}^{\text{bot}}(t)$:

$$\mathbf{v}_{\text{mirror}}^{\text{bot}} = \alpha \tilde{\mathbf{v}}^{\text{top}}(t) + \beta \tilde{\mathbf{v}}^{\text{bot}}(t) \quad \text{and} \quad \mathbf{v}_{\text{mirror}}^{\text{top}} = \gamma \tilde{\mathbf{v}}^{\text{top}}(t) + \delta \tilde{\mathbf{v}}^{\text{bot}}(t). \tag{III.11}$$

This leaves us with a total of five parameters (α, β, γ, δ, and f_c) that need to be optimized.

3) Acceleration and rotation: This method uses a combination of common velocity (half-sum) weighted by the sensitivity function $g_v(t)$, along with rotations (half-difference) which is weighted by the sensitivity function for rotation $g_{\text{rot}}(t, L)$ (refer to Appendix B). The latter is impacted by the seismometer's self-noise at low frequencies and the fact that $G_{\text{rot}}(\omega)$ does not truncate at these frequencies. For that, we apply the same high-pass filtering process that we used for the previous method. The resulting calculated phase is then given by:

$$\Phi_{\text{vib}}^{\text{calc}} = \frac{1}{2} \int_0^{2T} \mathrm{d}t \left[\alpha \left(\mathbf{v}^{\text{bot}}(t) + \mathbf{v}^{\text{top}}(t) \right) + \beta \left(\tilde{\mathbf{v}}^{\text{bot}}(t) - \tilde{\mathbf{v}}^{\text{top}}(t) \right) \right], \tag{III.12}$$

which leaves us with a set of four coefficients to adjust (α, β, f_c and L).

[1] by applying twice the discrete-time algorithm: $y_i = \alpha(y_{i-1} + x_i - x_{i-1})$, with $\alpha = \frac{1}{1+2\pi f_c\, \mathrm{d}t}$.

Optimization process: The coefficients for each method are optimized to maximize the correlation between the ideal sinusoidal signal and the experimental data, where $\Phi_{\text{vib}}^{\text{calc}}$, approximates Φ_{vib}. This is done by fitting the measured transition probability which is plotted as a function of $\Phi_{\text{vib}}^{\text{calc}}$ with a sine function $y(x) = A\sin(x + x_0)$. Then, we use the χ^2 parameter[1] of the resulting fit as a cost to minimize by the optimization algorithm. In Figure III.26, we show the results of correlation for each method after the coefficients optimization process. For that, we use the acceleration/rotation method as it provides the best correlation.

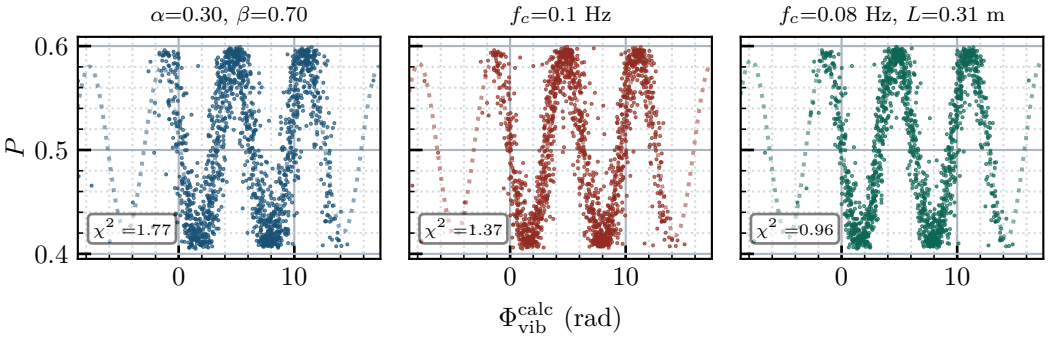

FIGURE III.26: Comparison between the correlation methods. The used coefficients result from the optimization process.

Extracting inertial phase: Once the vibration phase noise is correlated, the inertial phase, which represents the shift of the fringes relative to zero, is extracted by averaging the phase offset of the fitted curves corresponding to n-packets of 100 measurement cycles each, for example.

The main disadvantage of this method is that, statistically, the majority of data points fall outside the linear region where the interferometer is most sensitive to phase variations. Additionally, this results in a lower sampling rate, as it requires many cycles to estimate the phase shift of the interferometer. To circumvent this problem we will employ a real-time control method to operate the interferometer at mid-fringe.

III.5.a Real-time compensation (RTC)

Here, we will show that we can perform real-time vibrational phase measurements and also compensate for that phase using by changing the relative phase of the lasers during the last $\frac{\pi}{2}$-pulse (refered to as: a phase jump). In short, we acquire in real-time the signals of the seismometers, pass them through a transfer function (methods described above), and then feed-feedforward the calculated phase on the lasers by the end of the interferometer cycle.

The software behind real-time compensation (RTC) consists of using *ring-buffers* to store the acquired data for each seismometer channel. These are fixed-size tables that correspond to the duration of one interferometer cycle, $N = 2Tf_s$, where $f_s = 40\,\text{kHz}$ is the sampling frequency.

In a triggered fashion (Figure III.27), the buffers are reset when a new measurement

[1]The χ^2 is a number that tells how much difference exists between the data fit model. It is calculated as the sum of fit residuals, each divided by the variance of the data.

cycle is initiated. As raw signals are acquired, we continuously populate these buffers with chunks of the acquired signals (2.5 ms intervals). Once a buffer is updated, the data is multiplied by the corresponding part of the sensitivity function, integrated and stored inside phase accumulators. Towards the end of the measurement cycle ($2T - T_{\mathrm{RTC}}$), a hardware trigger arrives to stop the integrators and estimate the remaining phase based on the last acquired data. The final phase value, $\Phi_{\mathrm{vib}}^{\mathrm{RTC}}$ is evaluated using the pre-optimized coefficients of the selected correlation method. Finally, this phase contribution is used to provide feedback on the relative lasers phase ϕ_L, to cancel out the phase caused by vibrations.

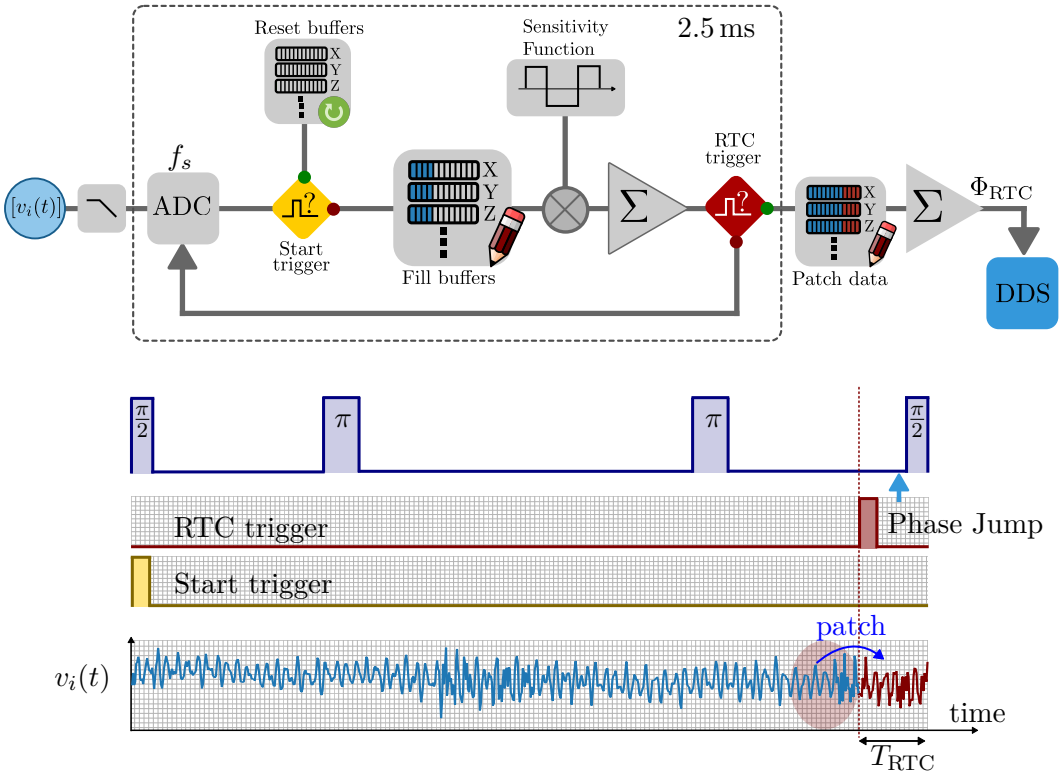

FIGURE III.27: Real-time compensation for vibrations. (**top**) the logic behind the software implementation to acquire and convert the seismometers' signals (total of 6 signals) to an accumulated phase. (**bottom**) the position of the triggers and an example of a vibration signal. The missing data chunk is patched from the last acquired data and the estimated phase, Φ_{RTC}, is written on the DDS and applied prior to the last pulse (before 1 ms) as a phase jump.

By using the RTC method, the interferometer's phase is no longer subject to random phase scanning due to vibrations. Furthermore, we can introduce, an additional phase, Φ_{add}, on top of the RTC phase, for example, to scan the fringes of the interferometer in a controlled manner. With that, we measure:

$$P = P_0 + \frac{C}{2}\cos\left(\Phi_{\mathrm{rot}} + \cancel{\Phi_{\mathrm{vib}}} - \cancel{\Phi_{\mathrm{vib}}^{\mathrm{RTC}}} + \Phi_{\mathrm{add}} + \delta\Phi\right), \tag{III.13}$$

here, $\delta\Phi = \Phi_{\mathrm{vib}}^{\mathrm{calc}} - \Phi_{\mathrm{vib}}^{\mathrm{RTC}}$ is the difference between the calculated and the estimated phase contribution. The standard deviation of this residue is at the order of 60 mrad with a mean value $\bar{\delta\Phi} = 0$ mrad (Figure III.28).

The RTC delay, denoted as T_{RTC}, is limited by the communication delay with the DDS ($\sim$ 5 ms using an ethernet TCP protocol). However, due to the 50 Hz component

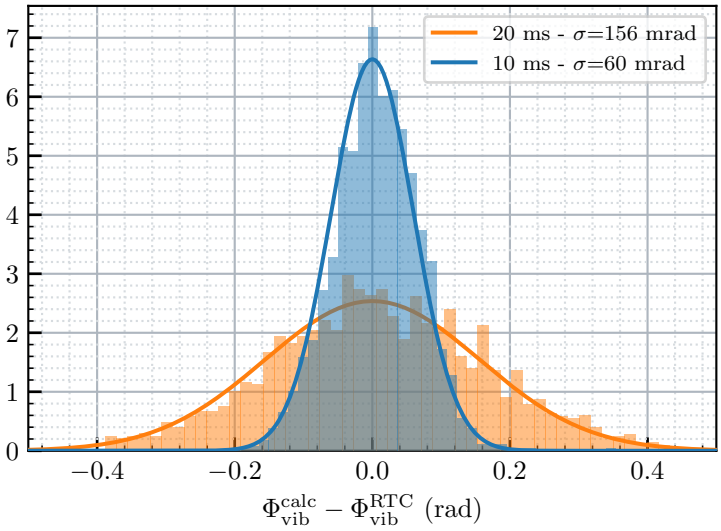

Figure III.28: The residue due to the difference between the calculated phase using the total signals and the RTC phase for two RTC delays, T_{RTC}.

in the signals we choose a delay of 10 ms (and multiples of that) to average out this frequency.

III.5.b Mid-fringe lock (MFL)

To ensure maximum sensitivity to phase variations, we can drive the interferometer phase towards its linear region, specifically the mid-fringe position. This is verified when the added phase, Φ_{add}, cancels the cosine term in equation III.13, i.e,

$$\Phi_{\text{add}} = \frac{\pi}{2} - (\Phi_{\text{rot}} + \Phi_{\text{bias}}), \tag{III.14}$$

where Φ_{bias} represents other phase bias terms if present. We can see that using this technique, the inertial phase can be directly read on the added phase and that the contrast value becomes irrelevant.

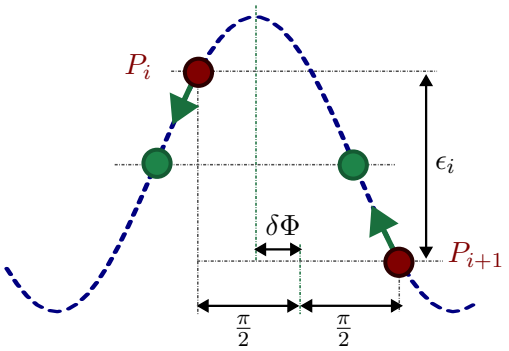

Figure III.29: Mid-Fringe lock technique: the applied phase drives the interferometer to its linear region. The lock uses the difference of transition probability of two successive measurements done at $\pm\frac{\pi}{2}$ as an error signal.

This technique is called mid-fringe lock (MFL) and its implementation in the experiment consists of altering measurements on the right ($-90°$) and left ($+90°$) sides of the

fringe to find the point where $P_i = P_{i+1}$. The error signal is therefore the probability difference between the two sides (Figure III.29). The lock is then done by using an error integrator where:

$$\phi^{i+1}_{\mathrm{MFL}} = \phi^{i}_{\mathrm{MFL}} + (-1)^i G(P_i - P_{i-1}) + (-1)^i \frac{\pi}{2}, \tag{III.15}$$

where G is the gain of the integrator which depends only on the contrast of the interferometer. We initiate the locking phase ϕ^0_{MFL} with an estimation based on the initial probability, $P_{i=0}$ and the knowledge of the offset and contrast values (P_0 and C), for faster convergence.

Once the mid-fringe lock converges (upon a few tens of cycles), we can quantify the residual vibrational phase noise $\delta\Phi_{\mathrm{vib}} = \Phi_{\mathrm{vib}} - \Phi^{\mathrm{calc}}_{\mathrm{vib}}$, which is the non-correlated noise by our methods. This is done by converting the probability noise around P_0 to a phase noise using $\Phi = \arcsin\left[2(P - P_0)/C\right]$, which results in a standard deviation of 358 mrad (III.30).

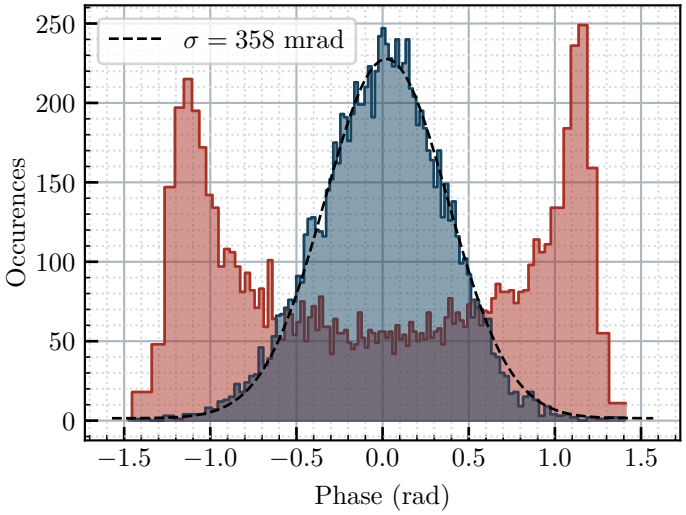

FIGURE III.30: Histogram of the probability phase noise. In red, without RTC method and in blue with RTC and MFL techniques. The dashed line is a Gaussian fit. This was done for an interferometer with 800 ms with 16% of contrast.

III.6 Interferometer configurations

Now that we have explained how we experimentally create an atomic cloud, generate the Raman beams to interrogate it and detail the mechanism of detecting the population of each state, we will show how we can perform sequential interferometric measurements. Here, we will present the different operating modes of the cold-atom gyroscope. We will demonstrate that it is possible to perform measurements without dead times and how this can be extended to interleave the measurements for higher sampling rates. Additionally, we will illustrate how we alternate measurements using the $\pm k_{\text{eff}}$ and also $\pm \mathrm{d}T_a$ in order to reject some systematic effects associated with these parameters.

The most rudimentary sequence of measurement is depicted in Figure III.31. The sequence begins with the trapping and cooling stage, after which the atomic cloud is launched and passes through the interferometer pulse sequence $\frac{\pi}{2} - \pi - \pi - \frac{\pi}{2}$ separated by $\frac{T}{2} - T - \frac{T}{2}$ time periods. The sequence ends when the atoms are detected and the transition probability is measured. The total cycle time in this mode is set to $T_c = 1.3\,\text{s}$ in order to accommodate all the steps of the cycle.

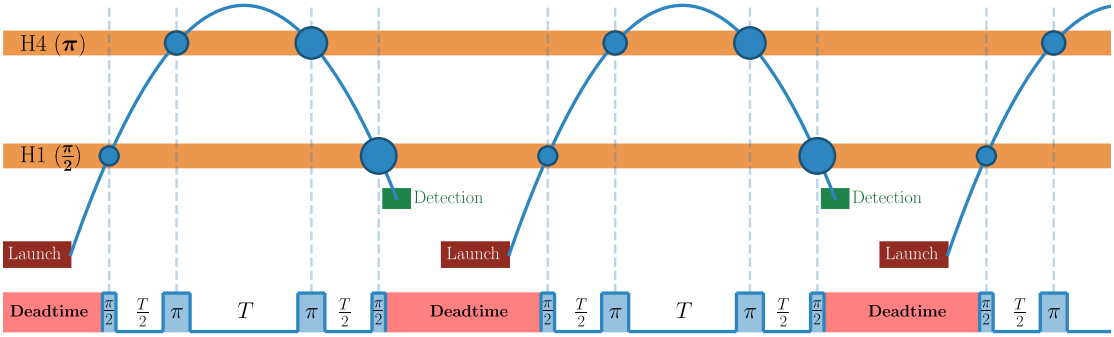

FIGURE III.31: (**top**) Trajectories of the successively launched atom clouds in time. (**bottom**) Sequence of pulses for the 4-pulse interferometer.

Here, we can observe that between two successive measurements, there are deadtimes during which the atoms are not engaged in the interferometric sequence (38% of the cycle time). Dead-times in atom interferometers correspond to the time needed to prepare and detect the atoms before and after the interferometric sequence. These periods result in a loss of inertial information, preventing fast averaging of the vibration noise. Noise aliasing arising from the sequential operation also degrades the AI sensitivity in the presence of dead times, similar to the Dick effect observed in cold atomic clocks [52].

III.6.a Simple-Joint Mode

The demonstration of continuous measurements, i.e., no dead times where atoms are performing an interferometric measurement all the time, was conducted in 2016, and the results of this work have been published in [53]. This was achieved by joining two consecutive sequences, where the preparation of the atomic cloud for an interferometer (n) takes place while the atoms are inside interferometer $(n-1)$ and are detected slightly after the start of interferometer $(n+1)$. As a result, the cycle time is reduced to $T_c = 800\,\text{ms}$ and the last and first $\frac{\pi}{2}$-pulses of consecutive interferometers are shared (Figure III.32).

This is made possible by implementing a k_{eff}-reversal technique, i.e., alternating

measurements using $\pm k_{\text{eff}}$. The reason for this is that the frequency of the last pulse of a $+k_{\text{eff}}$ interferometer corresponds to the frequency of the first pulse of the $-k_{\text{eff}}$ interferometer. Using the k_{eff}-reversal technique provides also the possibility to reject parasitic non-inertial phase shifts which are independent of the direction of the wave-vector $\mathbf{k}_{\text{eff}}$ (differential lightshift as an example).

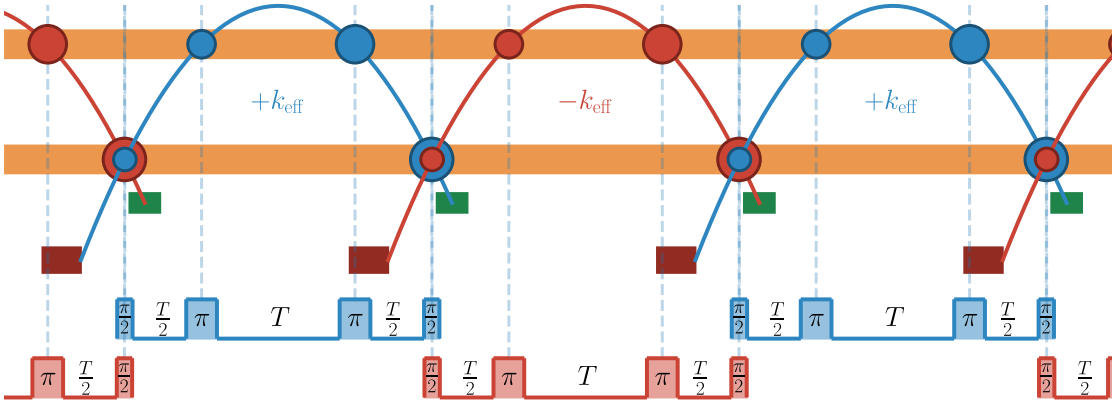

FIGURE III.32: Sequence of the simple joint mode which uses alternating measurements of $\pm k_{\text{eff}}$. The last and the first $\frac{\pi}{2}$-pulses of two successive interferometers are shared.

This operational mode will be the one used throughout this thesis. We note that this scheme can be expanded to accommodate higher sampling rates, achieving a cycle time of $T_c = 2T/3 = 267\,\text{ms}$ (3.75 Hz). This was demonstrated in [49] and involves the interweaving of measurements by extending the joint sequence to a triple-joint sequence where three atomic clouds are interrogated simultaneously using atom juggling technique.

The main issue with interleaved measurements is the loss of contrast due to the scattered resonance light coming from the MOT region which deteriorates the coherence of the atoms participating in the interferomeric sequence. This was partially avoided by reducing the loading time in the preparation stage (less number of atoms).

Noise correlations: To understand how this can ameliorate the correlation of vibration noise. Let us consider the phase shift induced by a displacement of mirrors due to vibrations. Using equation II.48, we can express the phase shift as:

$$\delta\Phi = k_{\text{eff}}\left(x_1^{\text{bot}} - 2x_2^{\text{top}} + 2x_3^{\text{top}} - x_4^{\text{bot}}\right) = \delta\Phi^{\text{acc}} + \delta\Phi^{\text{rot}}, \tag{III.16}$$

where we can decompose this phase shift as:

- $\delta\Phi^{\text{acc}} = k_{\text{eff}}\left(x_1 - 2x_2 + 2x_3 - x_4\right)$ is due to the common acceleration between the two mirrors.
- $\delta\Phi^{\text{rot}} = k_{\text{eff}}\left(\Delta x_1 - \Delta x_4\right)$, with $\Delta x_i = x_i^{\text{bot}} - x_i^{\text{top}}$, is due to a rotation of the bottom mirror about the position of the top one. Using The distance between the two mirrors, L, and $\delta\theta = \theta(0) - \theta(2T)$ as the angular change between the first and the last pulses, this phase can be written as: $\delta\Phi^{\text{rot}} = k_{\text{eff}} L \delta\theta$.

Statistically, when considering N measurements, taken from a noise distribution[1] with a standard deviation σ_{vib}. In the case where these measurements are independent which

[1] we note that ground seismic noise is often modeled as a stochastic process, meaning it is random and unpredictable. It does follow a simple statistical distribution like a Gaussian or uniform distribution due to the wide variety of different phenomena that contribute to it.

is the case of the non-joint mode, this phase shift behaves as a non-correlated noise associated with a standard error of $\sigma_{\overline{\delta\Phi}} = \sigma_{\text{vib}}/\sqrt{N}$.

This is not the case in the joint-mode where we introduce a correlation in our measurement when sharing the $\frac{\pi}{2}$-pulses. The mean value of this phase noise writes as:

$$\overline{\delta\Phi} = \frac{1}{N}\sum_{i=0}^{N-1}\delta\Phi_i^{\text{acc}} + \frac{1}{N}k_{\text{eff}}L\,[\theta(0) - \theta(2TN)] \tag{III.17}$$

as a consequence, the variance of the mean writes as[1]:

$$\sigma^2_{\overline{\delta\Phi}} = \frac{\sigma^2_{\text{acc}}}{N} + 2\frac{\sigma^2_{\text{rot}}}{N^2}, \tag{III.18}$$

which mean than the rotation noise averages out as N^{-1}, faster than the non-correlated noise of acceleration which scales as $\sqrt{N}$. In metrology, particularly in the analysis of our time series data, we often use the Allan Variance as a tool for characterizing system stability with the averaging time τ taking the role of N.

However, the uncorrected acceleration noise is significantly larger than the correlated rotation noise, which could mask the gyroscope's expected sensitivity scaling of τ^{-1}. Furthermore, the instrument's cycle time constrains us in the frequency bands ($< 0.1\,\text{Hz}$) where rotation noise prevails. Therefore, through the use of interleaving to oversample these fluctuations, correlations between consecutive measurements and the τ^{-1} sensitivity become more pronounced.

III.6.b Double-Joint Mode

So far, we have only discussed sharing the $\frac{\pi}{2}$-pulses. A natural question that arises is: why not share the π-pulses as well? Figure III.33 presents a sequence for such a configuration. This can be interpreted as two simple-joint sequences interleaved together, with the second sequence shifted by T. This results in a cycle time $T_c = T$. In this mode, all pulses are shared.

In this double-joint mode, we can see that all the phase contributions due to vibration noise (which include both acceleration and rotation) mutually cancel out (see Figure III.33). This leaves us with noise only from the very first and very last measurements which lead to a standard error given by:

$$\sigma_{\overline{\delta\Phi}} = \sqrt{2}\sigma_{\text{vib}}N^{-1}. \tag{III.19}$$

However, this mode is not allowed with the current experimental setup because the lasers cannot verify the resonance condition for both clouds at the same time (due to the Doppler effect) for certain π-pulses.

An approach called the quasi double-joint has been tested by my predecessor R. Gautier (preliminary results in [45]), which consists of shifting the two joint sequences by a few milliseconds. This will not scale the sensitivity as N^{-1} as the perfect double-joint, but slightly improves it.

The "perfect" double-joint mode could be accomplished either by using a third laser, similar to reference [54], which would require extensive modifications to the experiment

[1] we use Bienaymé formula: $\sigma^2_{\overline{\delta\Phi}} = \text{Var}(\bar{x}) = \frac{1}{N^2}\sum_{i=0}^{N-1} x_i$

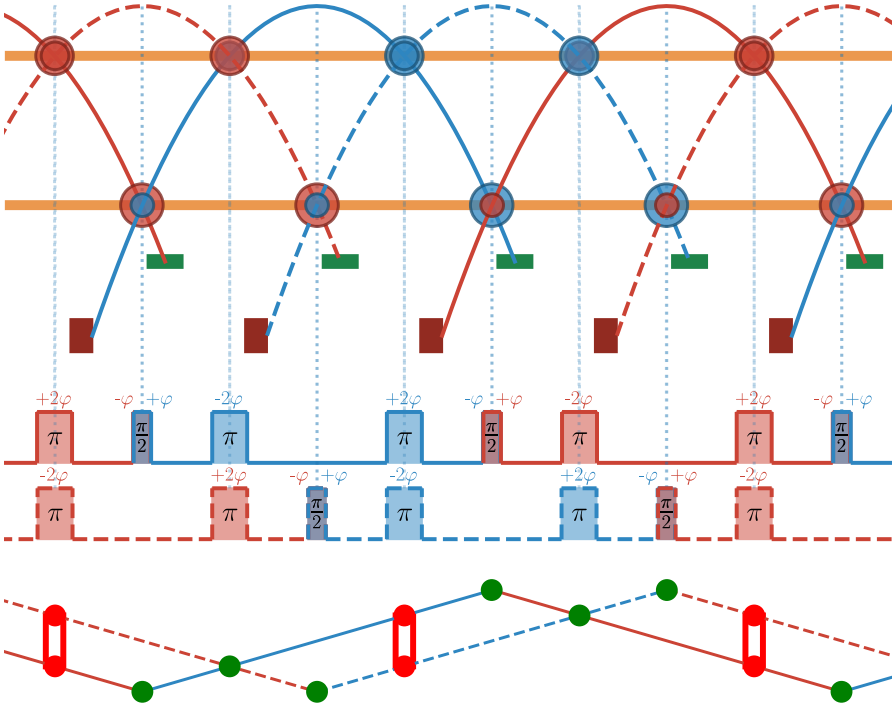

FIGURE III.33: Double Joint Mode Sequence: Both the $\frac{\pi}{2}$ and π pulses are shared in this sequence. In each cycle, two clouds are interrogated simultaneously. The sequence can be viewed as two interwoven simple-joint sequences (dashed and solid lines) separated by a time shift, T. The frequency ramps compensating for the Doppler effect are plotted at the bottom. We highlight in red the π-pulses where the implementation of the ramp is not experimentally possible.

and an additional laser setup. Alternatively, we could operate within the Raman double-diffraction regime, which has already been implemented and tested on an earlier atom gyroscope version [55]. In this regime, we would be free from the Doppler effect due to the absence of an angle for the collimators, thereby solving our problem. Also, it will double the area of the interferometer hence the gyroscope's sensitivity. However, applying this technique is not straightforward, and we aim to address some of the challenges associated with it in this work. More discussions can be found in Chapter V.

III.6.c Parasitic interferometers and time assymetry

The efficiency of our Raman pulses is not perfect due to several reasons: velocity distribution, intensity inhomogeneities, spontaneous emission, etc. Therefore, there will be some atoms that do not participate in the interferometer sequence. These atoms will leak and eventually form parasitic interferometers that recombine at the same time as the main interferometer (Figure III.34). These interferometers, being larger in area than the main interferometer and lacking symmetry with respect to the apogee, are highly sensitive to both DC acceleration and rotation, which will add probability noise to the system and reduce the SNR of the interferometer.

One of the two methods at our disposal to eliminate these parasitic interferometers involves using a time asymmetry of the middle π-pulses, where we shift these pulses by an amount $\mathrm{d}T_a$ in the same direction (thus asymmetrically with respect to the apogee). This has the effect of altering the closure moment of the parasitic interferometers while

keeping the one of the main interferometer unchanged (Figure III.34).

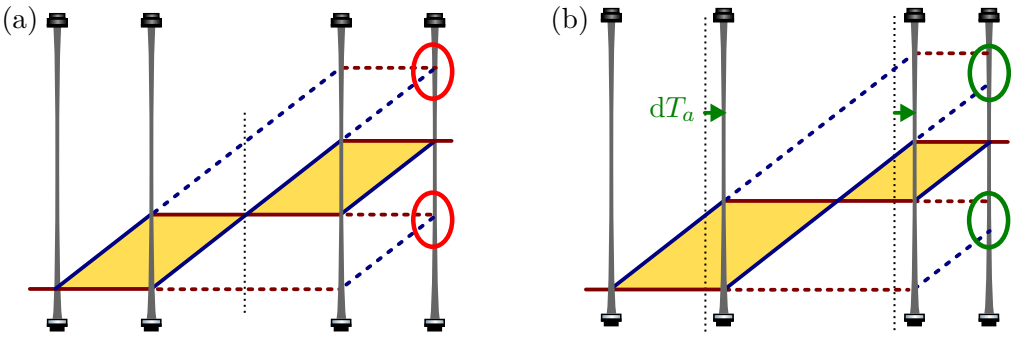

FIGURE III.34: Space-time diagrams of the interferomter w/o the time assymetry. (a) Without time asymmetry where parasitic interferometers are shown with red circles. (b) The effect of the time asymmetry where only the main interferometer is closed.

Comparing the separation of the two wavepackets at the last pulse, $dx = 4v_{\text{rec}}dT_a$ with the coherence length[1] L_{coh} which has been measured to be $\sim 40\,\text{nm}$ [38], we must verify this condition:

$$dT_a > \frac{L_{\text{coh}}}{2v_{\text{rec}}} \approx 6\,\mu\text{s}. \tag{III.20}$$

This has been characterized in ref [38] where SNR of the interferometer (and other observables) has been quantified as a function of the parameter dT_a (Figure III.35). We choose a value $dT_a = 40\,\mu\text{s}$, that ensures the best SNR value.

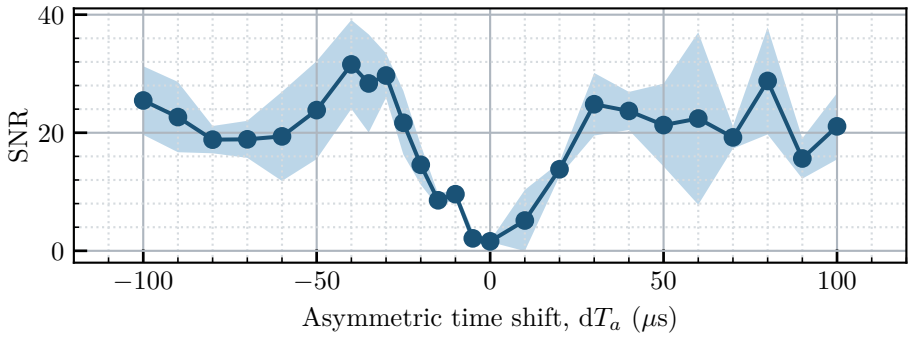

FIGURE III.35: SNR of the interferometer as a function of the time asymmetry δT_a.

However, this comes at a cost where we break the symmetry of the interferometer with respect to the apogee arising a sensitivity to DC accelerations. The induced phase shift is given by:

$$\Delta\Phi_{dT_a} = 2T\,dT_a\,\mathbf{k}_{\text{eff}} \cdot \mathbf{g}, \tag{III.21}$$

which can amount to $\sim 400\,\text{rad}$. Nevertheless, when we take into account the ramp that compensates for the Doppler effect, with a rate α (in Hz.s^{-1}), this acceleration phase is canceled to a large extent when the ramp is well adjusted. The residual acceleration phase writes as:

$$\Delta\Phi_{\text{acc}} = 2T\,dT_a(k_{\text{eff}}g\sin\theta_0 - 2\pi\alpha). \tag{III.22}$$

[1]The coherence length is directly related to the velocity distribution σ_v of the atoms, according to the relationship [56]: $L_{\text{coh}} = \hbar/m\sigma_v$.

Even in the case where this bias is zeroed. The fluctuations of the projection of $\mathbf{g}$ due to tilt variations for example will not be compensated. For that, to reject this bias even more, we alternate measurements in $\pm \mathrm{d}T_a$ to remove any residual sensitivity to DC acceleration (similar to the k_{eff}-reversal technique).

III.6.d Gyroscope measurements and data analysis

In the previous sections, we mentioned alternating measurements in $\pm k_{\mathrm{eff}}$, $\pm \mathrm{d}T_a$, to mitigate unwanted phase contribution and also the $\pm\frac{\pi}{2}$ for the mid-fringe lock technique. Here, we will explain how these sequences are implemented and how the various phase contributions can be separated from the measurements we obtain.

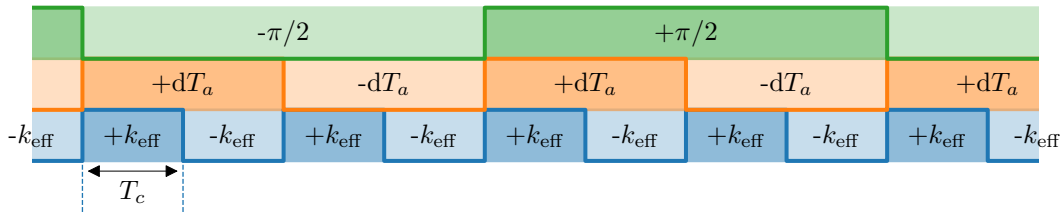

FIGURE III.36: Measurements sequence when alternating parameters $\pm k_{\mathrm{eff}}$, T_a, and $\pm\frac{\pi}{2}$ measurements.

In Figure III.36, we show how the measurements are chronologically being taken. From a technical perspective, to orchestrate all of this we use the TTL that triggers the Doppler ramp[1] (blue). This TTL is then divided by 2 using a frequency divider which results in the signal for $\mathrm{d}T_a$ (orange). This signal is then used to switch the signal of the pre-generated Raman pulses with either $+\mathrm{d}T_a$ or $-\mathrm{d}T_a$ time asymmetry. These two signals are acquired by the control software to decide on which fringe side $\pm\frac{\pi}{2}$ we are working with, choose the sign of the applied phase for RTC, and save the configuration parameters on the results file for each cycle.

Once the measurements are performed for a sufficient number of cycles. The results are analyzed as follows: First, we divide the data into 4 sets of measurements ($\pm k_{\mathrm{eff}}$, $\pm \mathrm{d}T_a$). Then for each set, we center the applied laser phase, i.e. Φ_{MFL} by removing the added $\pm\pi/2$ phase contributions. Finally, we perform the different possible phase combinations. For simplification, I will use the following notation:

$$\oplus_k{}^{\pm} = \frac{1}{2}(\Phi^{\pm \mathrm{d}T_a}_{+k_{\mathrm{eff}}} + \Phi^{\pm \mathrm{d}T_a}_{-k_{\mathrm{eff}}}) \quad \text{and} \quad \ominus_k{}^{\pm} = \frac{1}{2}(\Phi^{\pm \mathrm{d}T_a}_{+k_{\mathrm{eff}}} - \Phi^{\pm \mathrm{d}T_a}_{-k_{\mathrm{eff}}}), \tag{III.23}$$

which are simply, the half-sum and half-difference of k_{eff} for a given $\pm \mathrm{d}T_a$ sign. With that, we have:

- $\Phi_{\mathrm{rot}} = (\ominus_k{}^{+} + \ominus_k{}^{-})/2$ removes the residual acceleration and non-inertial terms which do not depend on the wave vector $\mathbf{k}_{\mathrm{eff}}$.
- $\Phi_{\mathrm{acc}} = (\ominus_k{}^{+} - \ominus_k{}^{-})/2$ gives only the residual DC accelerations.
- $\Phi_{\mathrm{free}} = (\oplus_k{}^{+} + \oplus_k{}^{-})/2$ gives all the phase shifts due to non-inertial effects: light-shift for example.
- $\Phi_{\mathrm{zero}} = (\oplus_k{}^{+} - \oplus_k{}^{-})/2 = 0$ cancels all the measured phase shifts.

[1] We note that the ramp is programmed to cover two sequences $+k_{\mathrm{eff}}$ and $-k_{\mathrm{eff}}$ at once.

III.7 Stern-Gerlach coil replacement

In December 2022, we experienced a loss in contrast in the interferometer, which disrupted our planned Sagnac effect measurement (Chapter IV). After conducting diagnostics, we traced the problem to the Stern-Gerlach (SG) coil, which appeared to have suffered significant damage, likely due to a sequence failure. This was first noticed when we performed a Raman spectroscopy, where we observed a loss of efficiency in rejecting the m_F states.

The Stern-Gerlach coil in our setup is designed to operate on short pulses lasting 25 milliseconds with a current of 17 Amps. However, due to an unexpected sequence failure, the coil was left powered on for an extended period of time. This prolonged operation led to overheating, causing damage to the coil (Figure III.37). This unexpected problem required us to replace the coil, a process that involves opening the magnetic shields around the experiment which is a delicate process.

With the necessity of opening the magnetic shield, we saw an opportunity to carry out other planned modifications and upgrades to the experimental setup simultaneously: adding B-field compensation coils along the Y direction and also installing the new mirror support used in Chapter V.

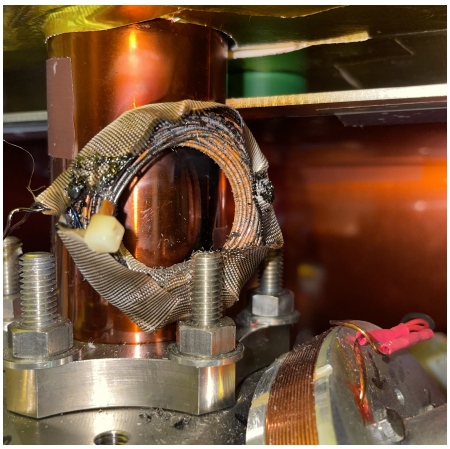

Figure III.37: The state of the Stern-Gerlach when the magnetic-shield are opened.

The characterization of the previous coil was not extensively documented in earlier theses, so I will outline the optimization process for the new coil. First of all, there are geometric constraints owing to the placement of the SG coil, which was not part of the gyroscope's original design. We are restricted to a height of 3.5 cm and a thickness of 0.5 cm, to be as close as possible to the center of the tube, where the atoms pass.

In Figure III.38, we display the characterization of two coils that are dimensionally suitable with different windings: one with roughly 100 turns, and the other resembling the original one. The measured resistances of these two coils are 0.5 Ohm and 0.35 Ohm, respectively. Concerning heat generation, the coils reach temperatures of 92°C and 76°C, respectively, when subjected to an 18 A, 25 ms pulse.

To characterize the two coils, we performed Raman spectroscopy using co-propagating Raman beams, and we measured the transition probability when different currents were applied to the coils, using a pulse width of 25 ms. The first coil requires less current to reach optimal performance, hence we decided to proceed with this one.

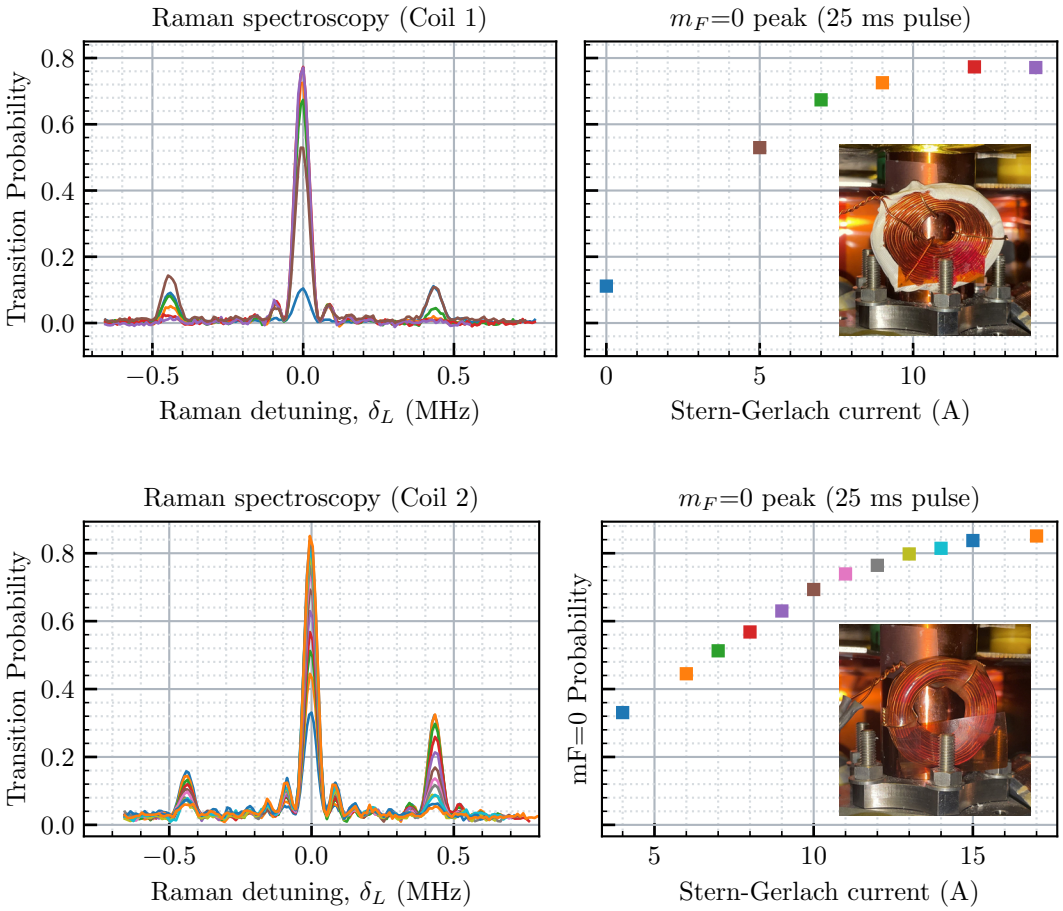

FIGURE III.38: Characterization of two test coils. (**left**) Raman spectroscopy done in a co-propagating configuration for different current values. (**right**) The transition probability of the peak at the center as a function of the SG current. The absolute maximum efficiency value is not strictly relevant here. This is because it depends on the alignment of the quarter-wave plate, which is used to achieve the co-propagating Raman configuration.

In Figure III.39, we also demonstrate the optimization of the pulse's optimal parameters: timing, duration, and current value. Initially, we identified the optimal timing (the time after launching the atomic cloud) using a pulse duration of 2 ms at 18A. Here, we find a central timing value $T_c = 20$ms. Subsequently, we varied the pulse duration at this optimal timing and found it to be 10 ms. Finally, we also varied the current to observe its effect.

The SG coils generate vibrations within the experiment due to the magnetostriction effect when rapidly switched from on to off and vice-versa. These vibrations last approximately 150 ms (as shown in Figure III.40). We should note that this signal, which is at a frequency of 150 Hz, is underestimated in amplitude by a factor of -10dB due to the transfer function of the seismometer (refer to Figure III.21).

Given the joint mode configuration of the experiment, these vibrations occur within the interval where we calculate the RTC phase, which can result in a phase offset on the applied phase. In Figure III.41, we show the evolution the phase offset, $\delta\Phi$ as we vary the timing of the SG pulse.

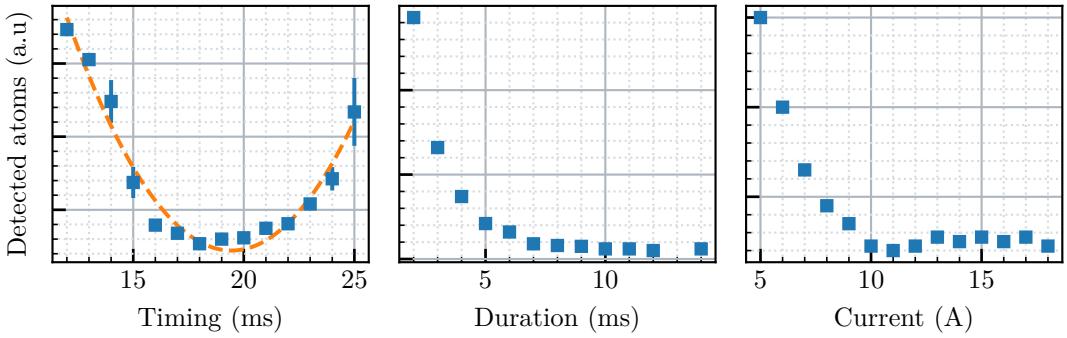

Figure III.39: Characterization of the SG pulse parameters.

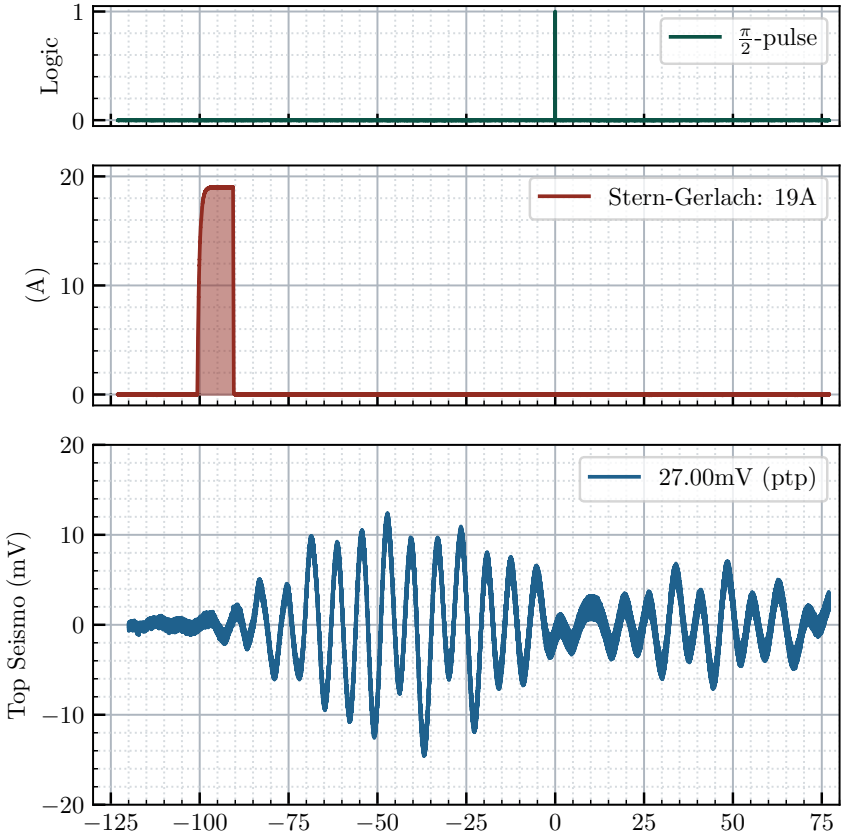

Figure III.40: Vibrations due to Stern-Gerlach before optimization measured by the top seismometer.

The vibrations produced are synchronous with the measurement cycle, and as a result, the phase bias remains constant. However, we have implemented several measures to mitigate the impact of these vibrations. First, we sealed the coil with an epoxy resin capable of withstanding temperatures up to 200°C. Also, we placed chunks of Sorbothane between the coil and the tube to absorb these vibrations.

Moreover, we considered modifying the pulse shape by introducing a Gaussian pulse, which allows a smoother transition from low to high current while maintaining the same pulse area. This was achieved by using an analog pulse with a Gaussian profile, instead of

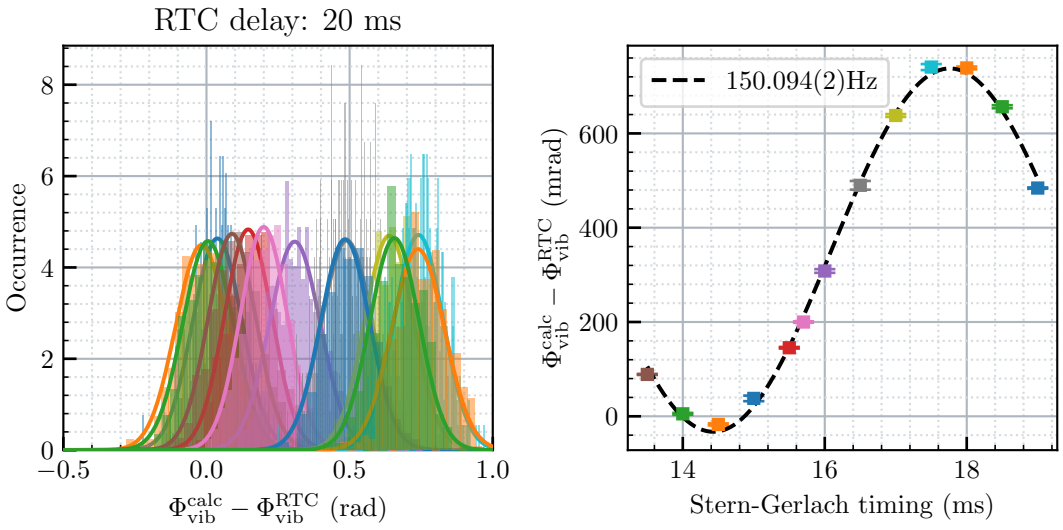

FIGURE III.41: Aliasing of the vibration burst due to the SG coil on the RTC phase residue, when the duration between the last $\frac{\pi}{2}$-pulse and the timing of the SG pulse is varied.

a square TTL pulse, to drive the input of the MOSFET. This Analog Output (AO) pulse (with a Gaussian waveform) is generated by one of our NI cards, which uses a triggered task to synchronize the pulse with the experimental sequence. Taking all these factors into account, we present the final response of the seismometers to the Stern-Gerlach pulses (Square and Gaussian) in Figure III.42.

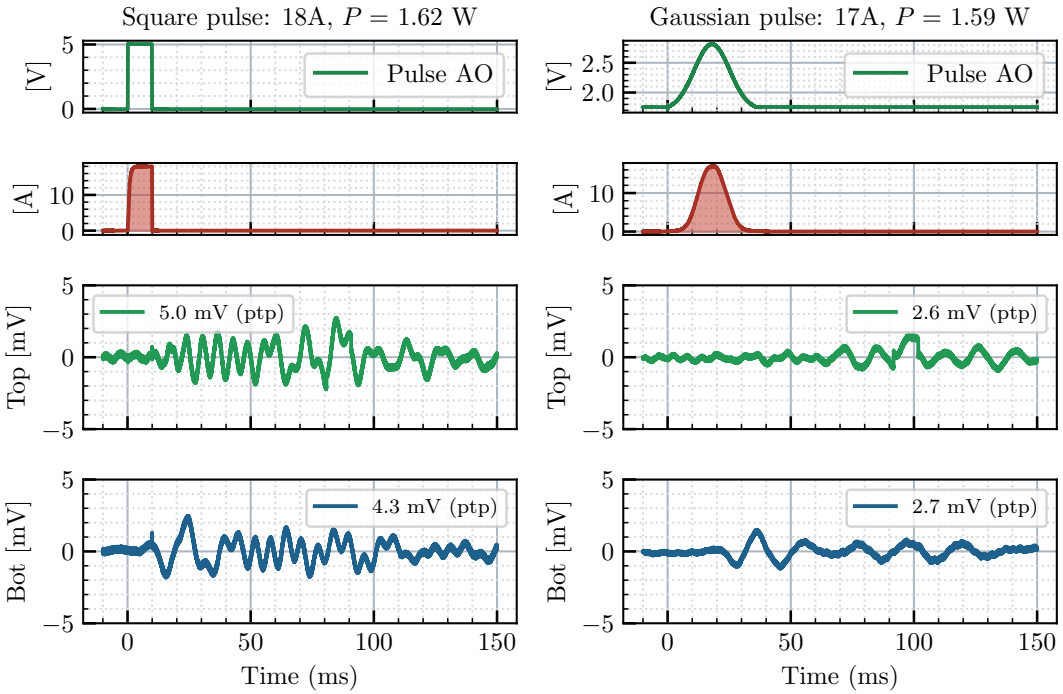

FIGURE III.42: The impact of the SG pulse on the experiment measured by the seismometers after the modifications.

To prevent a recurrence of the same problem, namely coil overheating due to a sequence failure, we incorporated a time-protection circuit (a non-retriggerable monostable) in addition to the existing one. This circuit emits fixed-duration pulses, the duration of which can be adjusted using a trimmer. However, a pulse is generated only once and only upon receiving a rising edge on its input. Being non-retriggerable implies that if the input signal remains high, due to a malfunction in the control sequence, no additional pulse is generated. This pulse, fixed at a 20 ms duration, is used to operate a switch that determines whether or not the analog waveform (shaped pulse) is passed to the MOSFET (as illustrated in Figure III.43).

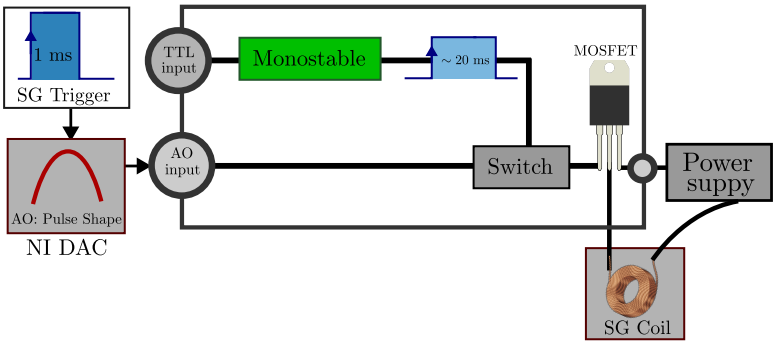

Figure III.43: Illustration of the new circuit behind the Stern-Gerlach pulse generation.

III.8 Software

In this section, I will outline the various software tools that are employed to manage the experiment and collect the associated data. The existing code has been continually maintained and enhanced with new features for the past eight years. I will highlight my own contributions, which include refactoring the code for improved organization and clarity. I will also describe the new laser lock/relock system that has been implemented to ensure extended periods of stable measurements in the future.

III.8.a Sequencer software

During my thesis, I made the switch from LabWindows/CVI to a Python GUI application with `nidaqmx` official library, `PyQt5/pyqtgraph` for the GUI and `numpy` for faster buffers manipulation (Figure III.44). This new software offers enhanced flexibility, allowing for easy addition of sequence steps without requiring code modifications. It also provides advanced options for TTL generation, improved buffer visualization capabilities, on-the-fly sequence updating, and integration of machine learning techniques, among other features.

To generate the control sequence, we make use of National Instruments PCI cards for analog and digital input/output (I/O) functions. These cards are synchronized and clocked using a 20 MHz signal derived from the SYRTE's maser reference. The specific hardware used includes:

- a PCI-6733 (16-Bit, 8Ch, 1MS/s): where 3 analog output channels are utilized for the cooling stage as depicted in Figure III.3.
- a PCI-6733 (Digital board, 32Ch): where 16 channels are used for the cooling stage and 16 channels for Raman/Interrogation stage.

The analog sequence is constructed with individual steps defined by a timing parameter T, which indicates when a voltage change is required. Each step also has a ramp duration $\mathrm{d}t$ and a corresponding voltage value V. To ensure the synchronization of voltage updates, the analog output buffer is designed to update the voltage value whenever a rising edge is detected on the board clock. As a result, a pseudo-clock is generated using the digital board to dictate the timing for updating the next voltage value. This approach enables us to simplify the analog sequence, focusing only on the moments when the voltage actually changes. Here, the voltage ramps are discretized into steps of 2 μs.

The digital signals are managed within a fixed-size buffer that aligns with the duration of the sequence. The pulses are structured in a table format, and adding a pulse is as simple as selecting the desired channel and specifying the start time, duration, and state of the TTL (0 or 1). The software also offers advanced options, such as selecting a reference timing (e.g., variables from the analog sequence such as the launch moment), incorporating time delays, or using centered pulses around the specified start time.

The software sets up three tasks on the mentioned PCI boards:

- **Analog Task**: This task is responsible for generating the analog output buffers, which control the voltage levels for different channels in time.

- **Digital Task**: Generate the TTLs used to control shutters, triggering signals for detection acquisition, launch, Stern-Gerlach,..etc. This is the reference task since it generates the pseudo-clock for the AO task and a TTL to start the Raman task which is defined as the moment we launch the atoms.
- **Raman Task** (digital): Generates Raman pulses and triggers for vibration acquisition and compensation, ..., etc. The timings of this task are relative to the launch timing.

I added on the software a layer of machine learning using the library `M-LOOP` which allows to graphically select any experimental parameters to be tuned. The algorithm uses machine learning to minimize a cost function. I established a link between the acquisition software and the sequencer in order to have an observable that defines the cost function: the number of atoms and the cloud's temperature, transition probability, or a multi-parameter function. This tool has been tested on the gyro with 3 parameters however it has not been fully explored due to other priorities on the experiment.

III.8.b Software acquisition

The acquisition software is written in Python and features a GUI interface. Throughout my thesis, I migrated the software from Python 2.7 to 3.10, which involved significant refactoring, code optimizations and some added features: real-time Allan deviation plotting, fitting the TOF, etc.

The software operates as a multi-process program within a server-client architecture. The server component remains active, continuously awaiting messages (commands) from the clients. Upon receiving a message, the server executes the necessary commands on other clients and facilitates the exchange of results and parameters among clients. The different processes (clients) involved are as follows:

- **GUI Process**: Handles user inputs for parameters, actions, and real-time plotting of experimental results.
- **Result Saver**: Logs results and control values for each cycle in a text file for later analysis.
- **Gyro Acquisition**: Utilizes triggered NI tasks to acquire analog signals from various sources, including detection (TOF) signals, experiment tilt, position sensors and other photodiodes such as MOT, detection power, and Raman photodiodes.
- **Gyro Controllers**: Responsible for managing different locks such as tilt (X, Y) and power locks, launch velocity, Raman axis switching, and tilt sliders control.
- **Digital Acquisition**: Continuously acquires digital triggers ($\pm k_{\text{eff}}$, $\pm dT_a$) and communicates the current configuration with other clients.
- **Vibrations Manager**: Functions as a continuous task that acquires signals from seismometers, performs real-time compensation using phase integrators, and applies mid-fringe lock techniques.
- **Real-Time Control**: This high-priority process was added to support the work done on Chapter V. It features the driver for the nanopositioner and handles the communication with the DDS and NI-cards for the frequency jumps.

III.8.c Lasers auto-relock

To ensure long-term measurement stability, an initiative was undertaken to enhance the lasers' lock system. I developed a software program to monitor the lasers and control the lock/relock process. The method involved replacing the manual switches for the analog integrators with relays. The hardware configuration includes a NI-6003 card, which provides 8 analog input channels (AIs), 2 analog output channels (AOs), and 13 digital input/output channels (DIO). With this card, we can manage two lasers simultaneously. One of the AO channels is used to provide piezo modulation (and offset), while the error signal and modulation signal are monitored using 2 AI channels. The laser lock is enabled by activating relays through a digital output channel.

The Python software is designed with two NI tasks that continuously acquire analog signals and generate modulation signals. The software includes a GUI with a multi-dashboard layout (Figure III.45), where each dashboard corresponds to a specific laser. Each dashboard features an oscilloscope component that plots the signals (the error signal and modulation). Additionally, control buttons for various functionalities are included within each dashboard, allowing easy access and management of the laser settings and operations.

- **Modulation**: The modulation can be configured as either sinusoidal or triangular, allowing adjustment of parameters such as amplitude, frequency, and offset. When modulation is activated, the triggering can be set to occur on either a falling or rising edge.
- **Lock**: The lock method varies depending on the type of error signal. For instance, in the case of L2, the lock can be as simple as finding the zero-crossing point. Alternatively, a correlation method can be employed to track a specific spectroscopy peak. Once the lock point is determined, the modulation amplitude is gradually reduced, and eventually, the relays are engaged.
- **Lock monitoring and relock**: Once the lasers are locked, the software continuously monitors the error signal. If the error signal exceeds a predetermined threshold, an auto-relock operation is triggered. In our case where lasers are locked in series, the auto-relock process verifies that the reference laser is locked before attempting to lock the subsequent laser. This ensures the stability and proper functioning of the laser locking sequence.
- **Remote control**: The software incorporates a Telegram bot feature to send real-time notifications whenever a laser becomes unlocked, providing instantaneous updates. Additionally, if the auto-relock functionality is enabled, a report on the auto-relock process is sent via the Telegram bot as well. Furthermore, the software allows the user (administrator) to send predefined commands through messages to the bot. This enables the user to request screenshots or remotely lock a specific laser, providing convenient control and monitoring capabilities at a distance.
- **Logging**: The lock status for the lasers is logged permanently on a file. This allows the other software (GyroSequencer and GyroAcquition) to check the lock state.

Currently, the software includes only lasers L1 and L2. However, the design allows for easy extension to lasers L3 and L4 by incorporating a second NI-6003 card. This ex-

pansion enables full automation of laser locking for the experiment. The auto-relock operation takes 1.3 seconds per laser to complete. This duration could potentially span multiple measurement cycles. However, the logging feature can be utilized to facilitate appropriate actions when performing interferometric measurements, particularly in maintaining the mid-fringe lock until all lasers are successfully locked. The limiting problem comes from the drift of the region of stability of our lasers which necessitates readjusting the temperature setpoint. This drift introduces mode hops on the transition peak of interest. This may be solved by implementing analog control on the temperature locking module.

III.9 Conclusion

In this chapter, we have described the atomic gyroscope experiment. We outlined the experimental setup behind our interferometric measurements. This includes the various steps involved in preparing an atomic source within the 3D MOT chamber and launching it toward the interferometry region. We detailed how we implement the Raman interrogation scheme and the various technical subtleties that arise during the process, as well as our strategies to overcome these challenges. We also elaborated on the detection scheme that enables us to measure the output of the interferometer. We discussed the generation of a variety of laser frequencies required for the experiment. Additionally, we addressed the main source of noise in this instrument - vibration noise - and the techniques we use to mitigate its effects. I summerized the replacement of the Stern-Gerlach system that I did, the characterization of the new coil and also the protection circuit that we installed. Then, I explained how we manage to eliminate dead times in our measurements and provided insights into the chronological sequencing of measurements. Finally, we described the new software that controls the experiment and acquires the data as well as the automation of laser locking systems.

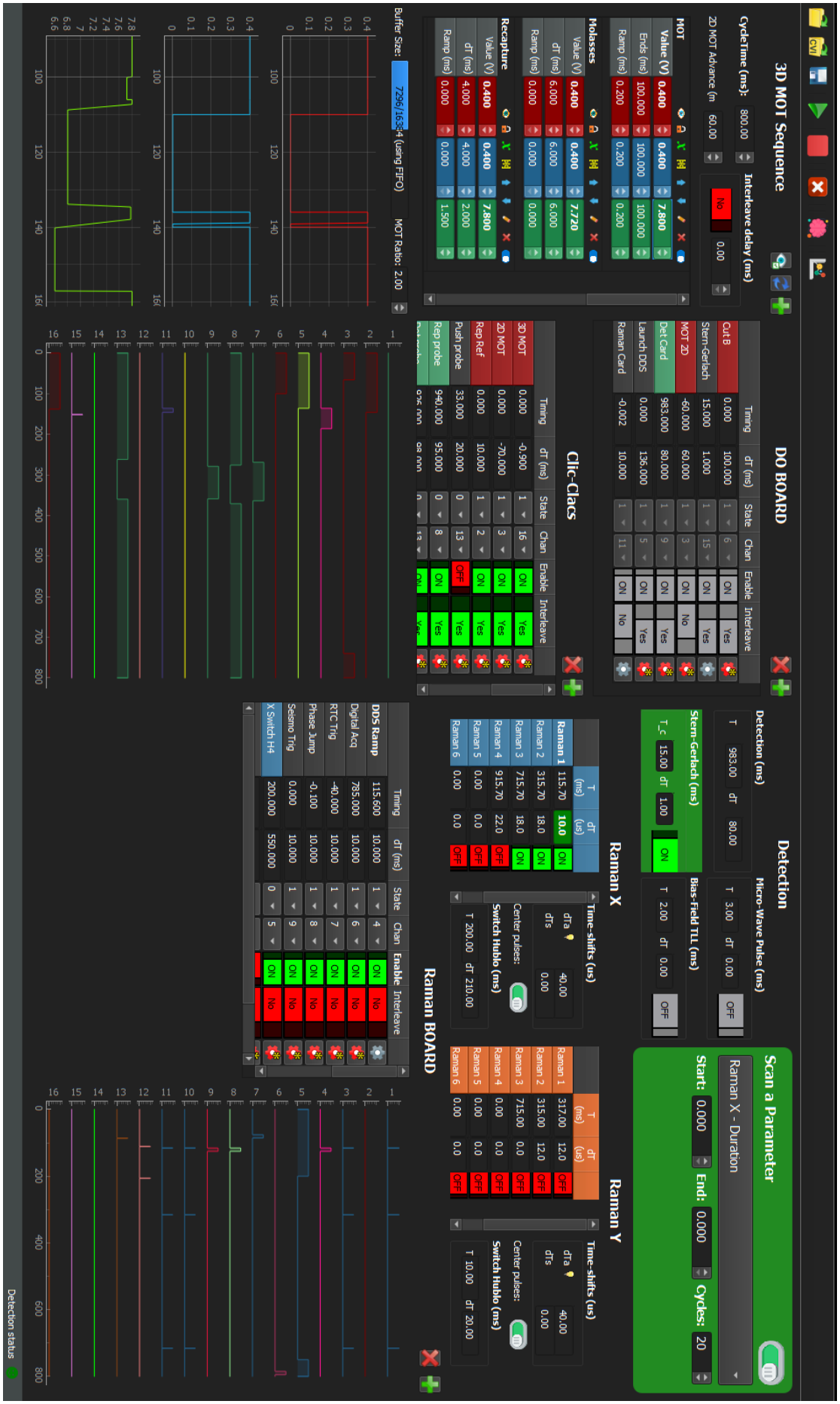

FIGURE III.44: The GUI of the Gyro Sequencer software.

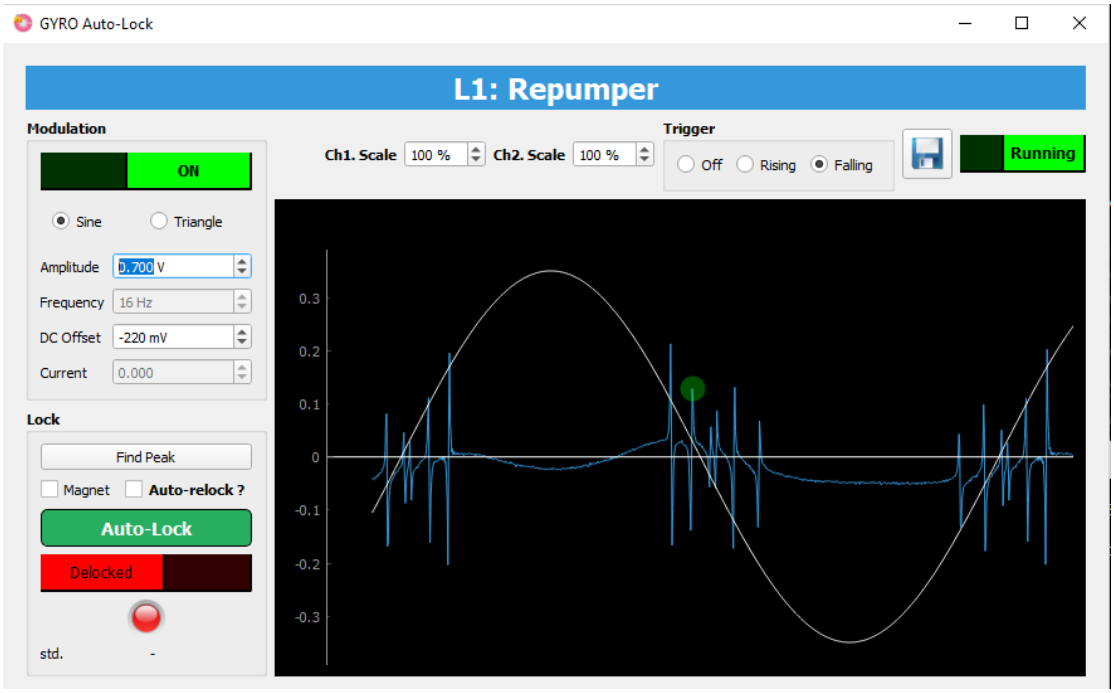

FIGURE III.45: Screenshot of a typical dashboard (GUI) of one of the lasers, L1. On the graph is plotted the error signal in blue and the modulation signal in white. The green dot indicates the detected peak on which the laser will be locked.

Chapter IV

Sagnac Effect Measurements over a year

The Sagnac effect states that any interferometer with a physical area is subject to a phase shift in its output due to rotations. In 1913, Georges Sagnac made the first observation of this effect by measuring the phase shift in the fringes of a rotating interferometer with a constant rotation rate [57]. At the time, he posited the existence of a stationary mechanical aether to explain the phenomenon. This experiment was later explained in the framework of relativity by Paul Langevin in 1921 [58]. The experiment of Sagnac was repeated by Michelson and Gale in 1925 [59], but this time using Earth's rotation rate and a large interferometer of $0.2\,\mathrm{km}^2$ area, and measured the effect with 3% accuracy.

The advent of laser technology paved the way for the development of gyroscopes based on the Sagnac effect: ring laser gyroscopes (RLG) [60] and fiber optical gyroscopes (FOG) [61, 62], which are a key component of contemporary navigation systems.

The quest to understand the fundamental nature of the Sagnac effect, to enhance our understanding of modern physics, motivated the realization of rotating interferometers of increasing precision, involving other-than-optical waves. Proof-of-principle observations have since been made on various systems to illustrate the universality of this effect: Superconducting electrons [63], neutral particles (neutrons [64] and thermal atoms [2]), electron jet [65], Superfluid quantum liquids [66, 67] and Bose-Einstein condensate [68].

Precision measurements were conducted, first in 1991 for a thermal matter-wave interferometer with a reported accuracy of 1%. This was carried out with an increasing precision level up to 0.05% with the development of cold-atom experiments [29, 69] before this work.

In this chapter, we will present a series of measurements of the Sagnac Effect induced by Earth rotation using our dual-axis cold-atom gyroscope over a one-year long period. We will show that we obtained an unprecedented accuracy of 23 parts-per-million which demonstrates a factor of 20 compared to previous realizations.

IV.1 The Sagnac Effect

As seen in Chapter II , the phase shift of the 4-pulse interferometer due to earth rotation writes as follows:

$$\Phi_\Omega = \frac{T^3}{2}\,(\mathbf{k}_{\text{eff}} \times \mathbf{g}) \cdot \mathbf{\Omega}_E. \tag{IV.1}$$

From this general formula, we shall express the phase shift in terms of the experimentally accessible parameters. In our case, for a given orientation of the experiment Θ with respect to geographical north and taking into account the tilt of Raman beams θ_0 with respect to the horizontal plane, the projection of the rotation vector on the area of the interferometer is given by:

$$\Phi_\Omega(\Theta) = \frac{T^3}{2} k_{\text{eff}} g \cos\theta_0 \times \Omega_E \cos\psi \times \cos\left(\Theta - \Theta_N\right), \tag{IV.2}$$

where ψ is the astronomical latitude of the experiment, Ω_E is earth's rotation rate, and Θ_N is the angle that corresponds to the geographic north.

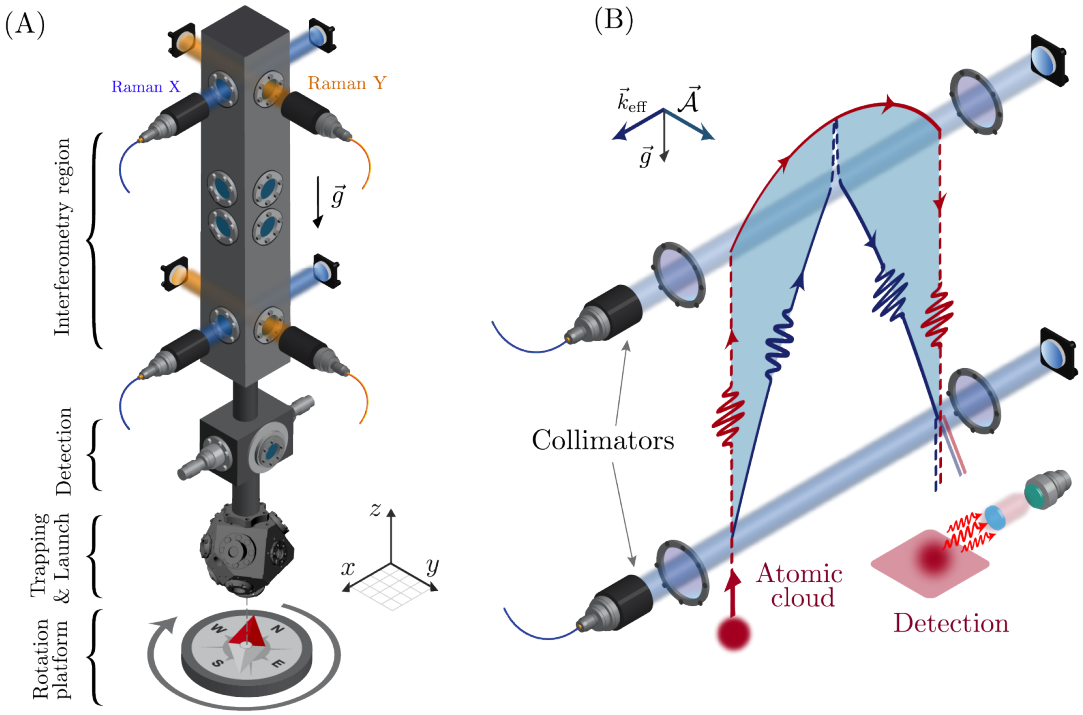

FIGURE IV.1: (**A**) Sketch of the sensor head showing the dual-axis configuration. Atoms being trapped and cooled inside the 3D MOT are launched toward the interferometry region where retro-reflected Raman beams interrogate the atoms along two possible axis X (blue) or Y (orange). At the decent atoms pass through the detection region to measure the transition probability via fluorescence means. (**B**) Space diagram of the trajectories of the atoms inside the interferometer (not to scale). The physical area of 11 cm^2 opened by the interferometer is highlighted in cyan. The compass represents the orientation of the interferometer toward the geographical north.

Correction for the scale factor

Since we use two Raman collimators, the magnitude for $\mathbf{k}_{\text{eff}}$ vectors for the top and bottom Raman beams may differ and therefore a non-equal momentum transfer will occur for the $\pi/2$-pulses and the π-pulses. This will modify the area of the interferometer and also change the closure moment for the interferometer (Figure IV.2).

Defining $k_{\text{eff}}^{(B)} \equiv k_{\text{eff}}$, we introduce the parameter ϵ such as: $k_{\text{eff}}^{(T)} = (1-\epsilon)k_{\text{eff}}$ (reduction of the momentum transfer at the π-pulses). To ensure the closing of the main interferometer, we compensate for the reduction of momentum transfer by introducing a symmetrical time shift ΔT_s with respect to the apogee timing T (middle of the interferometer). This effect has been fully explored in [70] and we can demonstrate that the closing condition is met when

$$\Delta T_s = \frac{T}{2}\frac{\epsilon}{1+\epsilon}. \tag{IV.3}$$

Finally, considering the modification of the area of the interferometer, the scale factor of the Sagnac Phase is modified and we write:

$$\boxed{\Phi_\Omega^{\text{theo}} = \left(1 - \frac{2\epsilon}{3}\right)\Phi_\Omega.} \tag{IV.4}$$

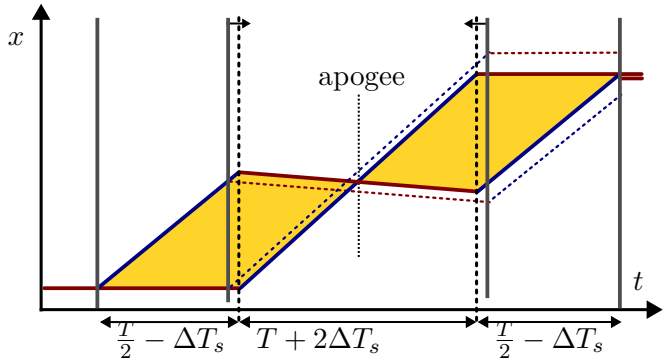

FIGURE IV.2: Space time diagram for non-equal momentum transfer. In dashed lines, the interferometer with a non-equal momentum transfer. In solid lines, the same interferometer where the closure is ensured by the time shift ΔT_s of the π-pulses with respect to the apogee time T. The blue and red colors represent the state $|F=3\rangle$ and $|F=4\rangle$, respectively.

Other corrections have been investigated such as the finite pulse duration and have been neglected to their negligible relative contribution (Appendix A).

IV.2 Scale factor estimation

In order to compare the experimental data from the two-axis gyroscope with the theoretical expectation from Eq.IV.2 and Eq.IV.4, we shall first measure and determine the parameters involved in the above equation. This will allow us to establish an error budget table for this measurement and compare experimental data with the expected value for the scale factor.

IV.2.a Measurement of the interrogation time, $2T$

The timings for the sequence are generated using NI PCI cards, which are supplied with an external clock of 20 MHz derived from the SYRTE MASER (100 MHz reference frequency). The duration of the interferometer is measured using a Tektronix 4 Series MSO oscilloscope, and it is found to be $2T = 800.0000(1)\,\text{ms}$, limited by the resolution of the oscilloscope. Prior to referencing the NI cards on the maser , the measured value using the same oscilloscope was $2T = 800.0040(2)\,\text{ms}$. At present, the relative uncertainty due to T is negligible, below 10^{-10}.

IV.2.b The effective wave-number, k_{eff}

The effective wave-number k_{eff} is deducted from the frequency of the two lasers L3 and L4 (Figure IV.3) and writes as,

$$k_{\text{eff}} = |\mathbf{k}_3 - \mathbf{k}_4| \approx \frac{2\pi}{c}(f_3 + f_4)\left(1 - \frac{\delta\theta^2}{8}\right), \tag{IV.5}$$

where $\delta\theta$ is the relative misalignment between the two vectors. Since L3 is locked on L1 with a frequency offset $\Delta = 350\,\text{MHz}$ and the two beams pass through an AOM (order -1) at 80 MHz, we write

$$f_3 = \Delta f_{\text{L1}} - \Delta - f_{\text{AOM}}, \tag{IV.6}$$

where Δf_{L1} is locking frequency of L1 which is locked on the transition $|F = 3\rangle$ toward the crossover of $|F' = 2, 3\rangle$. On the other hand, L4 is locked on L3 and we have,

$$f_4 = f_3 - f_{\text{HFS}} \tag{IV.7}$$

The retro-reflection is ensured either by re-injecting the light into the fiber or by using an IR camera to align small laser spots. In both cases, the angle $\delta\theta$ is zeroed within 0.1 mrad range. Finally, the effective wave-number value is

$$\boxed{k_{\text{eff}} = 14743247.08(4)\,\text{m}^{-1}}. \tag{IV.8}$$

Here, the main uncertainty comes from the frequency of L1 since the locking scheme is based on a saturated absorption spectroscopy, the frequency is known up to 2 MHz.

IV.2.c Local gravity, g

The value of g has been already measured inside the lab using a compact relative gravimeter based on an absolute gravimeter (FG-5) measurement that where conducted

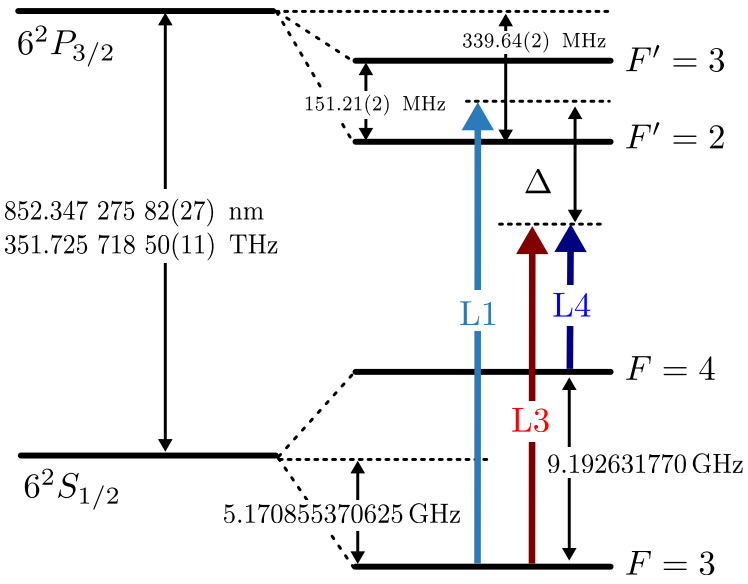

FIGURE IV.3: Raman lasers frequencies arrangement. The two beams for L3 and L4 pass through an AOM (order -1) with an RF frequency $f_{\text{AOM}} = 80\,\text{MHz}$

at two locations not far from the lab. The measured value at a height of 28 cm from the ground is $9.80927947\,\text{m.s}^{-2}$. The uncertainty on this value is taken as the vertical gravity gradient of $305\,\mu\text{Gal/m}$ [1] accounting for an experiment of 1 m heigh. The value of g is

$$\boxed{g = 9.809279(3)\,\text{m.s}^{-2},} \tag{IV.9}$$

We note that the gravity fluctuates in time mainly due to tidal variations with no more than $\pm 1\,\mu\text{m.s}^{-2}$ which is already taken into account in the given uncertainty.

IV.2.d Raman collimators angle, θ_0

The tilting angle of the Raman collimators was measured using interferometric measurements. This was done for different asymmetric timeshifts ΔT_a for the 4-pulse interferometer mirror pulses. As we have seen in Chapter 3, this asymmetry introduces a sensitivity for DC acceleration which can be canceled by finding the optimal frequency ramp rate α. The phase shift expression is given by

$$\Delta\Phi_{\text{acc}} = 2T\Delta T_a(k_{\text{eff}} g \sin\theta_0 - \alpha) \tag{IV.10}$$

Therefore, by analyzing this dependency, one can extract the value of θ_0 when the optimal ramp rate is found. Figure IV.4 shows a typical analysis conducted on the X-axis. From this analysis, we extract the optimal frequency rate, $\alpha_{\text{opt}} = k_{\text{eff}} g \sin\theta_0$ and therefore the value of θ_0. By propagating the errors and using the uncertainty of the fit algorithm, we can determine the value of this angle up to 5 μrad accuracy level.

[1] The Gal unit, called after Galileo Galilei is a unit of acceleration typically used in gravimetry where $1\,\text{Gal} = 0.01\,\text{m.s}^{-2}$

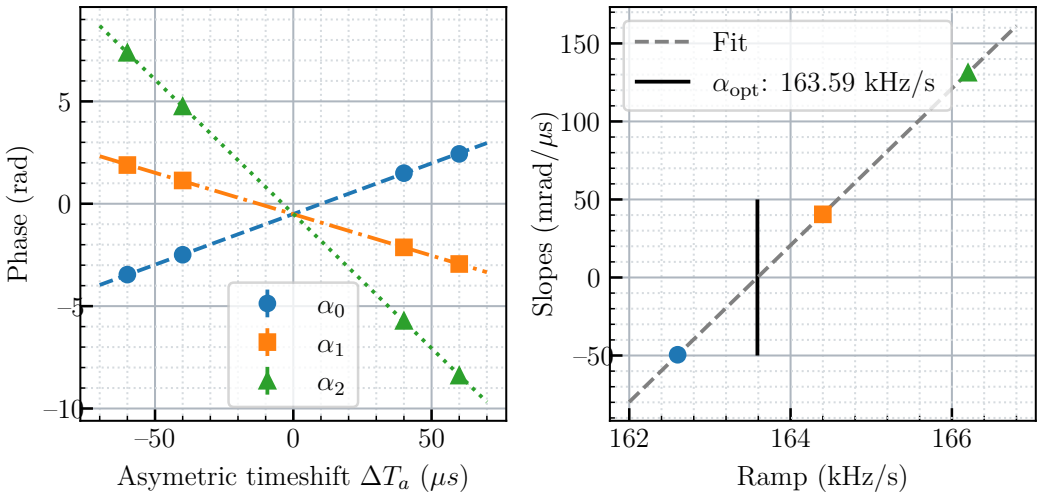

FIGURE IV.4: Measurement of the angle of the Raman collimators. (left) The phase shift of the interferometer $\Delta\Phi$ as a function of the time asymmetry ΔT_a for three ramp rate values. (right) The slope of each curve $\frac{d\Delta\Phi}{d\Delta T_a}$ as a function of the frequency ramp rate α.

IV.2.e Earth Rotation rate and latitude, Ω_E and ψ

The value of Earth's rotation rate is obtained from the International Earth Rotation Service (IERS) database, and it is given by:

$$\boxed{\Omega_E = 7.29221150(1) \times 10^{-5}\,\text{rad.s}^{-1}} \tag{IV.11}$$

This angular velocity is derived from the duration of a solar day. However, there exists a difference between the astronomically determined day duration and $t = 86400$ SI seconds (24h), known as the length of day (LOD), expressed in milliseconds. The relationship between the two is:

$$\Omega_E = \Omega_E^N(1 - \text{LOD}/t),$$

where $\Omega_E^N = 7.2921151467064 \times 10^{-5}\,\text{rad.s}^{-1}$ is the nominal rotation rate corresponding to the mean rotation rate of the epoch 1820.

The LOD fluctuates slowly over time (smaller than 2.5 ms in absolute value) due to various factors such as tides, atmosphere, and others. Nevertheless, these fluctuations are relatively small (10^{-8} relative contribution with respect to Ω_E) and do not significantly impact the error budget.

Regarding latitude, we use the astronomical latitude ψ, which is defined as the angle between the equatorial plane and the local plumb line (Figure IV.5). In contrast to the geodetic latitude[1], denoted as B, which can be determined using GNSS data, the astronomical latitude requires field studies for its determination. In fact, due to local masses anomalies such as nearby mountains, the gravity direction at a given point of interest is rotated with respect to the normal to the ellipsoid. The difference between these two vectors is called vertical deviation, which has two components (ξ: North deviation, η: East deviation). The North deviation is the difference between

[1]The geodetic latitude is defined as the angle between the equatorial plane and the normal to the reference ellipsoid at a specific point on the Earth's surface.

the two latitudes, denoted as $\xi = \psi - B$. In mountain regions, this correction can reach tens of arcseconds, however, where we are in Paris, the correction is relatively small. To obtain the accurate value for our laboratory location $(48°50'08''N, 2°20'05''E)$, we established a private communication with the National Institute of Geographic and Forest Information (IGN) service. The communicated value we obtain is $\xi = +0.95(4)$ arcsec. Consequently, the corrected latitude value for our location amounts to

$$\boxed{\psi = 48.83586(3)\,^\circ} \tag{IV.12}$$

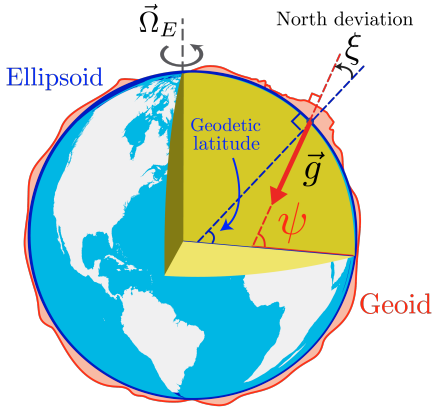

FIGURE IV.5: Astronomical latitude

IV.2.f Wave-vectors difference, ϵ

The presence of a non-equal momentum transfer induces a phase shift (Eq IV.4) which can be compensated for by introducing a symmetrical time shift ΔT_s for the middle π-pulses with respect to the apogee. By studying the evolution of the contrast of the interferometer as a function of ΔT_s (Figure IV.6), we can extract the optimal temporal shift $\Delta T_s^{(\mathrm{opt})}$ that ensures closing the interferometer paths during the last pulse. The relationship between this duration and ϵ is given by [70]:

$$\Delta T_s = \frac{T}{2}\frac{\epsilon}{1+\epsilon} \tag{IV.13}$$

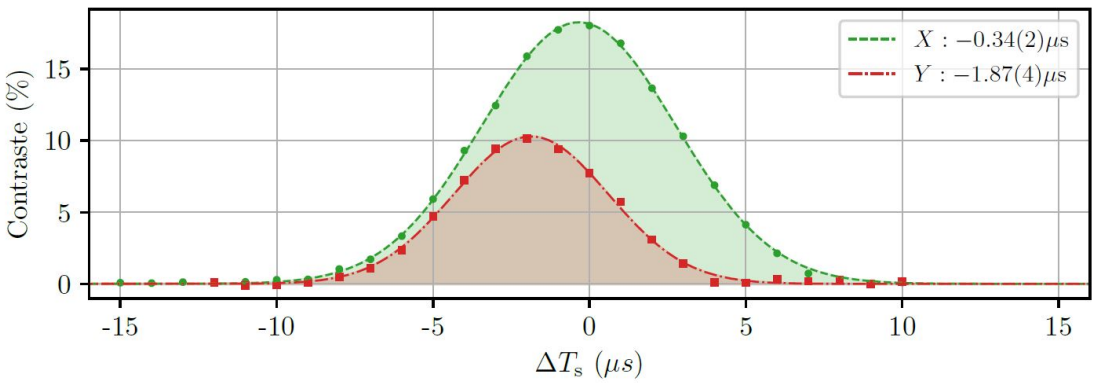

FIGURE IV.6: Evolution of contrast as a function of the symmetric time shift ΔT_s

We recapitulate by giving the error budget for all of these parameters and the expected value for the Sagnac phase-shift (Table IV.1)

Parameter	X	Y	Relative uncertainty (ppm)
k_{eff}	14743247.08(4) m^{-1}		0.003
T	400.0020(1) ms		0.75
g	9.809279(3) m.s^{-2}		0.3
θ_0	4.0750(5)°	4.1251(3)°	0.6 | 0.4
ϵ	$-1.7(1) \times 10^{-6}$	$-9.3(2) \times 10^{-6}$	0.07 | 0.13
ψ	48.83587(3)°		0.6
Ω_E	$7.2921150(1) \times 10^{-5}$ rad.s^{-1}		0.01
Theoretical Sagnac Phase	221.5702(3) rad	221.5574(2) rad	1.2 | 1.1

TABLE IV.1: **Error budget for the determination of theoretical Sagnac phase shift.** The table lists the parameters shown in the scale factor of the cold-atom gyroscope. The right column is the uncertainty on the scale factor resulting from error propagation on each parameter.

IV.3 Scale factor measurement

In this section, we will detail the Sagnac Effect measurement procedure from the preparation phase which takes two days, to the rotation phase measurements. The whole dataset takes around one week to be completed.

IV.3.a Preparation phase: Trajectories alignement

In this phase, all the parameters of the experiment are optimized: number of atoms, temperature, and Raman beams power by checking the fiber injections and tuning cooling and launch parameters.

Also, a very important procedure is to ensure the alignment of the trajectories. We will see in what follows that mirrors alignment can slowly degrade due to external factors such as temperature and therefore this bias can fluctuate when long measurements are performed.

In a previous work [71], we showed that a phase bias appears when the trajectories are not well aligned. In fact, this phase shift arises from the coupling of the angular misalignment between the top and bottom Raman retro-reflecting mirrors, $\delta\theta$ and the trajectory of the atom inside the interferometer which is defined by the initial velocity vector $\mathbf{v}_0$ (see: Figure IV.7). The expression for this phase bias writes as :

$$\Delta\Phi^{\text{traj}} = 2Tk_{\text{eff}}\delta\theta\mathbf{e}_\theta \cdot (\mathbf{v}_0 + T\mathbf{g}) \tag{IV.14}$$

where $\mathbf{g}$ is the gravity vector and $2T$ is the interferometer duration. Hence, there exist an optimal launch velocity $\mathbf{v}_{\text{opt}} = -T\mathbf{g}$ for which this phase bias is canceled. Here, we denote $\delta\mathbf{v} = \mathbf{v}_{\text{opt}} - \mathbf{v}_0$, the velocity offset from the optimal one.

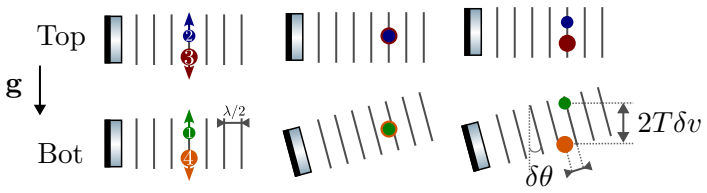

FIGURE IV.7: Illustration of the systematic phase shift induced by the coupling of launch velocity to mirrors misalignment. No phase shift when: (left) mirrors are parallel even if the launch velocity is not optimal, or (middle) the launch velocity is the optimal one even if the mirrors are misaligned. (right) The atom falls into different laser equiphase surfaces (during pulses 1 and 4) when the mirrors are misaligned and the initial velocity is not the optimal one, resulting in a phase shift $\Delta\Phi^{\text{traj}} = 2Tk_{\text{eff}}\delta\theta\delta v$

.

The alignment procedure consists of tuning the launch velocity components along the z direction, and the orthogonal component: y direction for Raman X axis and the x direction for Raman Y axis. Practically, changing the z-axis velocity component v_z is equivalent to varying the starting time of the interferometer and it is coupled to the relative vertical misalignment $\delta\theta_{y,x}$ between the two Raman beams. On the other hand, the y (x)-axis component $v_{y,x}$ is changed by changing the tilt of the experiment using the distributed masses around the experiment and it is coupled to the relative misallignement in the horizontal plane $\delta\theta_z$. As we showed in chapter III, the bottom

mirrors are motorized which enables to change the orientation of the mirror in the vertical and the horizontal planes with a resolution (step) of $n = 0.38\,\mu$rad per step.

The idea is to measure the slope of this phase bias as the angular misalignment of the mirrors get deliberately changed: $\mathrm{d}\Phi/\mathrm{d}n$. We then repeat this slope measurement for slightly different velocity values in order to find the one for which the slope is zeroed, i.e., the phase bias is uncoupled from mirrors' misalignment. For what concerns the parallelism of the two mirrors, the optimal mirror position, for which $\delta\theta = 0$, corresponds to the crosssection point of the three curves. In Figure IV.8, we show a typical analysis for this procedure where each point is measured by integrating interferometric phase measurement over 1500 cycles using the mid-fringe lock technique.

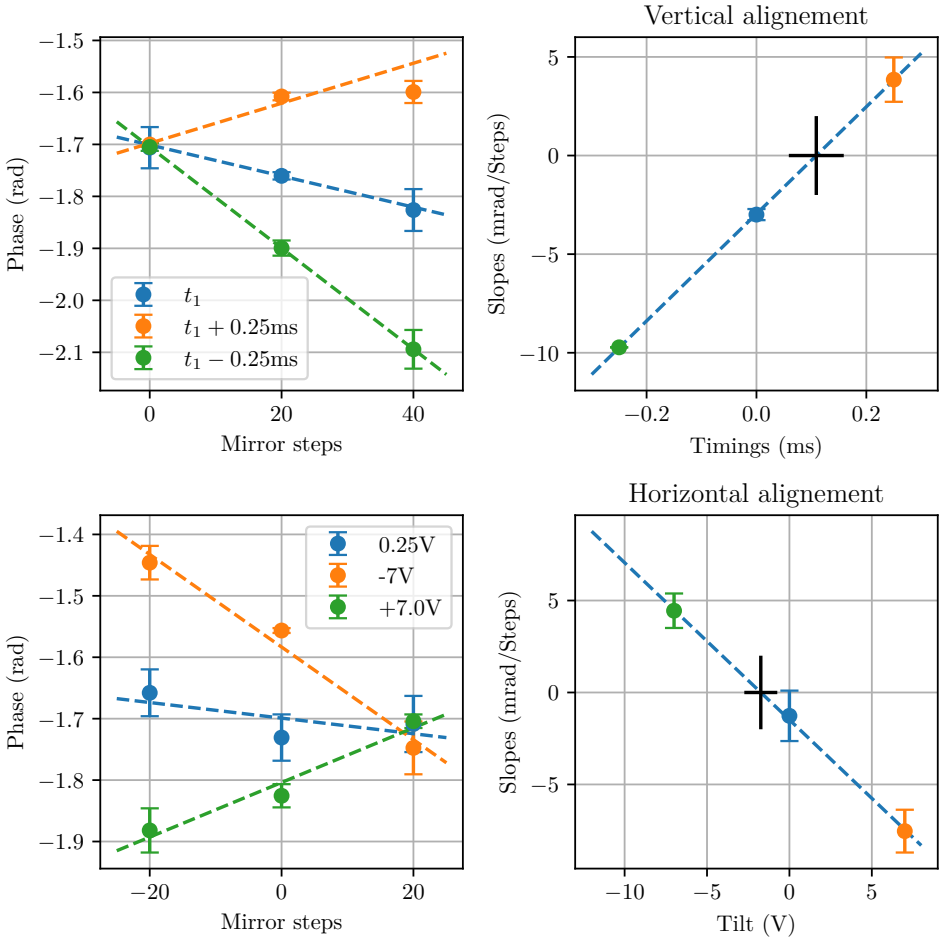

FIGURE IV.8: Trajectories alignement. (top) Vertical alignment done for 3 z-velocities (timings). For each timing, we plot the phase of the interferometer as a function of the vertical angle of the bottom mirror. (bottom) idem horizontal alignment for three x-velocity values (tilt of the experiment). From this analysis, we extract the optimal velocity that minimizes the phase bias variation when mirrors alignment degrades.

This procedure allows us to find the optimal launch velocity within $0.2\,\mathrm{mm.s^{-1}}$ accuracy level for both directions; together with an optimal mirror position with an accuracy of $0.2\,\mu$rad which limits the phase bias error to 0.5 mrad.

IV.3.b Rotating the experiment

Once the preparation phase is done, we start to perform interferometric measurements. The experiment is rotated by hand to the desired position[1]. The experiment is then blocked from rotating using heavy metallic rods. The orientation of the experiment Θ_{platform} is logged from the rotation platform (with 10 μrad accuracy). Additionally, we monitor the signals of the position sensors in order to correct the angle given by the rotation platform (Figure IV.9). The amplitude of the corrections, $\delta\Theta$ shows the importance of position sensors for the Sagnac measurement.

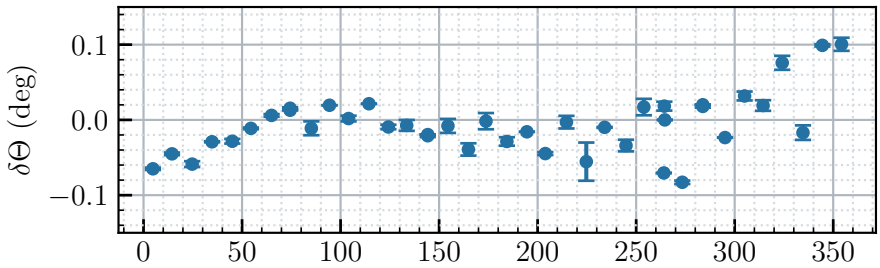

FIGURE IV.9: Measured angle corrections using position sensors as a function of the angle given by the rotation platform Θ_{platform}.

For each orientation, we use the configuration where we alternate $\pm k_{\text{eff}}$ and $\pm dT_a$. This will allow us to track the evolution of different phase contributions: rotation, acceleration, non-inertial phase and zero, (Figure IV.12). We integrate the interferometric signal for approximately a half hour per axis ($\sim$ 2000 cycles) . This integration time allows to reach a typical rotation rate resolution of 20 nrad.s^{-1}.

A typical data set for the Scale factor measurement is presented in Figure IV.11. The results for two axes, X and Y, are shown. For each axis, the mean of the measured rotational phase is plotted. The data correspond to one full turn of the experiment and the points are separated by rotation step of 10° ($\sim$ 40 points). It is important to note that the output of the interferometer is wrapped within a 2π range compared to $\sim$ 200 rads for the expected Sagnac Effect amplitude.

In Figure IV.10, we show an example of a few "raw" rotation phase measurements plotted on the wrapped sine envelope (modulo 2π). Here, we notice that inside the interval around Θ_N (the maximum of the sine function), the phase variations are small. In fact, this particularity allowed us to point precisely to the geographic north by performing several measurements in that range for the very first realization.

To address the wrapping issue, the data has been unfolded by adding the appropriate $n\pi$ phase contribution (shifting n-times the sides of the fringe) . This unwrapping process is done using an iterative algorithm that takes the estimated scale factor value and an approximation for the orientation to the north θ_N, as inputs. Subsequently, a fitting procedure is employed to align the measurement points with a sine function of the form

$$\Phi_{\Omega}^{x,y}(\Theta) = \Phi_0^{x,y} \sin(\Theta - \Theta_N^{x,y}) + B^{x,y}, \tag{IV.15}$$

where $\Phi_0^{x,y}$, $\Theta_N^{x,y}$ and $B^{x,y}$ are the parameters to be optimized ($\Phi_0^{x,y}$ is what we refer to as the scale factor). At first, these parameters are kept fixed in the first run in order

[1]For most of the curves, since we want to perform a full turn with 10 $^{\circ}$ step, we chose to go perform 20° step in one direction, then go back after a 10° step to cover all the steps.

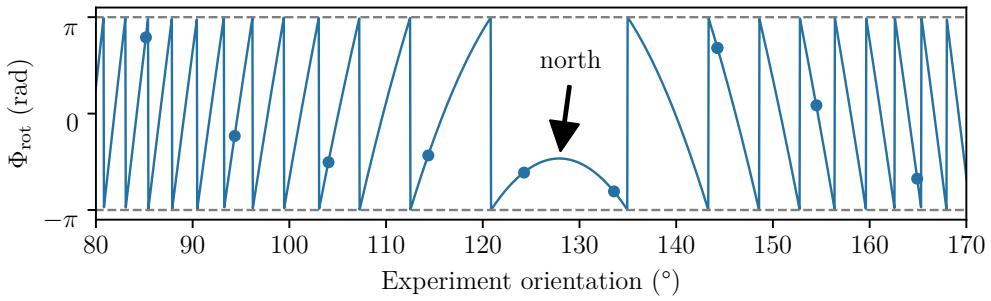

FIGURE IV.10: Measured "raw" rotation phase (dots) as a function of the orientation angle $\Theta_{platform}$. We plot also in solid line the wrapped sine function.

to unwrap the phase by minimizing the fit residual errors. Then, a second run where we free all the parameters for the fit procedure to get the optimal parameters: Sagnac effect amplitude, geographical north, the bias of the measurement and consequently, the orthogonality between the X and Y axis.

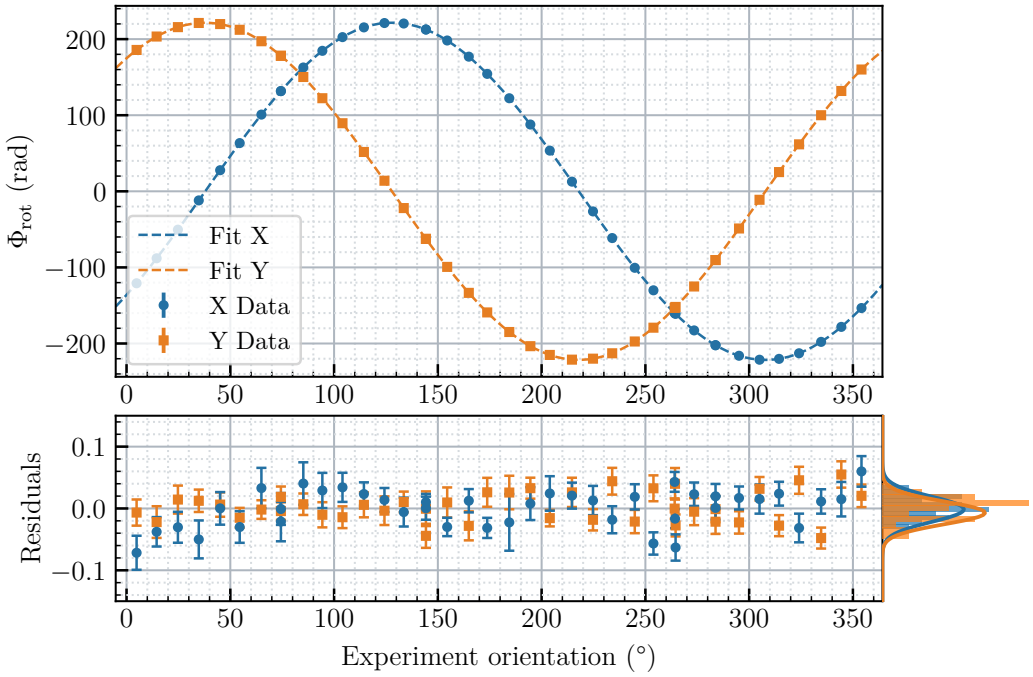

FIGURE IV.11: Typical Sagnac Effect measurement dataset. (**top**) the mean of the integrated rotation phase for both Raman axes, X (blue) and Y (orange) as a function of the rotation angle Θ (Error bars are smaller than the data markers). In dashed lines, the fitted curves with a sine function. (**bottom**) The fit residuals for both axes and their respective histogram projected on the right side with an SD of 40 mrad.

.

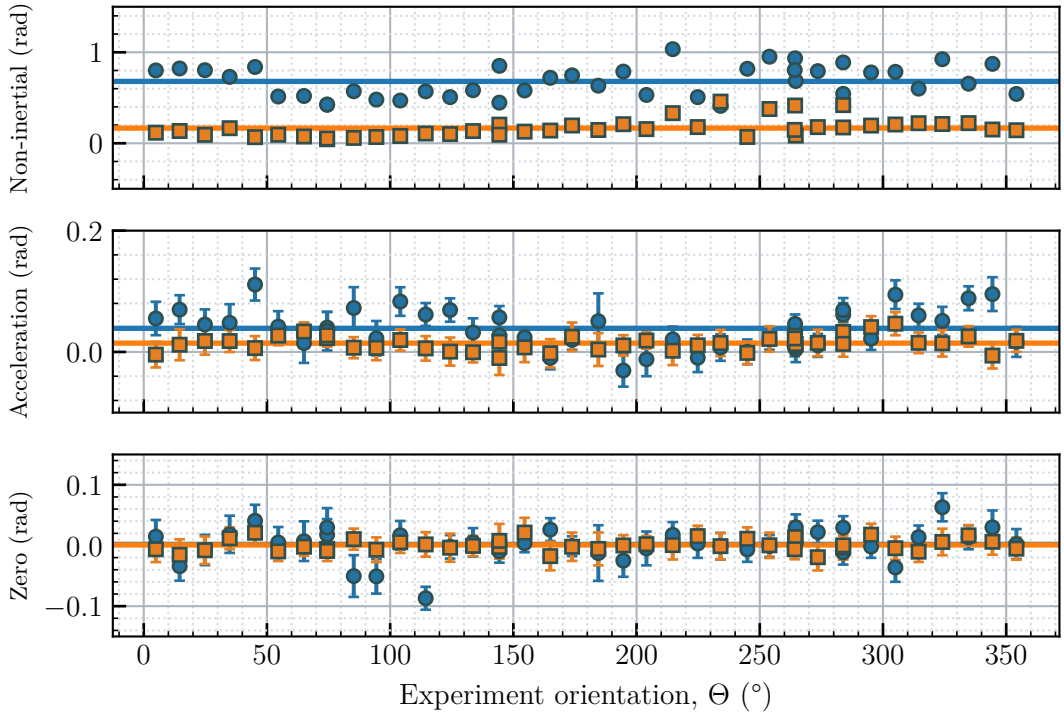

FIGURE IV.12: Other phase contributions using combinations of $\pm k_{\text{eff}}$ and $\pm \mathrm{d}T_a$ (canceled in rotation phase) as a function of the orientation angle.

IV.4 Results

In order to gain confidence in our measurements and furthermore, provide a population for statistical analysis, we repeated these measurements for both axis X and Y, in 9 realizations spanning the period from 13 April 2021 to September 2022. My predecessor Ph.D. R. Gautier and I, conducted the initial measurements, which were published in the journal Science Advances [72]. During that period, our main focus and effort was to perform several measurements per month for the article. After the article was published, the priorities changed, however, I continued to conduct these measurements by scheduling a Sagnac effect measurement every three months. The goal was to gather more statistical data and monitor the measured values throughout the year. Then, the measurements have been stopped in December 2022 due to a failure in the Stern-Gerlach mechanism which lead to a significant loss in contrast to the interferometer.

We applied identical data treatment and fitting procedures (as described above) to all datasets and extracted corresponding fit parameters. In Table IV.2, we show the fit results for all the realizations. For each measurement, we give the parameters that have been varied: $2T$ and $\mathrm{d}T_a$, the number of measured angles N per set, the optimal fit parameters (Φ_0, Θ_N and B) and the reduced chi-squared χ^2_{red}, as an indicator of the quality of the fit.

To visualize the results, we chose to present the difference between the expected and experimental scale factor values $\delta\Phi^{x,y} = \Phi_0^{x,y} - \Phi_{\text{theo}}^{x,y}$ (Figure IV.13). The overall statistic results in a mean value for the 18 measurements of 3.1 mrad which translates to 23 ppm accuracy compared to the mean expected value for the scale factor.

#	$2T$	$\mathrm{d}T_a$	N	Φ_0 (rad)	Θ_N (rad)	B (rad)	χ^2_{red}	$\Theta_\perp$ (mrad)
0	800	60	41	221.564(7)	+0.909951(41)	0.787(6)	2.6	0.87(4)
1	800	60	41	221.540(7)	-0.659978(39)	0.628(6)	2.7	
2	800	60	24	221.573(15)	0.909489(73)	1.004(12)	4.5	0.78(11)
3	800	60	24	221.544(21)	-0.660527(95)	0.678(15)	12.4	
4	801	60	24	222.405(11)	0.909585(57)	0.979(8)	3.0	0.65(9)
5	801	60	24	222.382(19)	-0.660557(83)	0.665(14)	11.7	
6	800	40	42	221.567(15)	0.910079(72)	0.731(11)	10.5	0.43(10)
7	800	40	41	221.585(15)	-0.660291(74)	0.690(11)	13.2	
8	800	60	46	221.527(9)	0.909408(43)	0.833(7)	2.3	0.77(5)
9	800	60	43	221.561(8)	-0.660618(51)	0.545(8)	4.1	
10	800	60	41	221.591(6)	0.909112(40)	0.972(6)	2.0	0.80(4)
11	800	60	41	221.548(5)	-0.660879(31)	1.238(5)	1.7	
12	800	40	17	221.558(13)	0.909072(40)	0.972(6)	3.9	1.00(10)
13	800	40	20	221.558(21)	-0.660894(31)	1.238(5)	12.6	
14	800	40	25	221.536(17)	0.909072(40)	0.972(6)	6.8	0.89(10)
15	800	40	25	221.592(15)	-0.660894(31)	1.238(5)	12.0	
16	800	40	24	221.576(25)	0.909072(40)	0.972(6)	37.1	0.71(10)
17	800	40	24	221.582(32)	-0.660894(31)	1.238(5)	94.7	

TABLE IV.2: **Details of the 9 realizations taken for the two axes with the fitted parameters and their extracted uncertainties.** Are presented the parameters for each measurement including the total interrogation time $2T$, the time asymmetry (in μs) used to prevent the parasitic interferometers from recombining ΔT_a, the number of points per datasets N, the fitted values of the control parameters Φ_0, Θ_N, and B and the corresponding reduced chi-squared for the least-square fit. Datasets 10 and 11 correspond to the data in Figure IV.11.

We used a bootstrapping approach on this dataset which resulted in a standard error of 5.2 mrad showing a good agreement with what we expected given that the mean is compatible with zero.

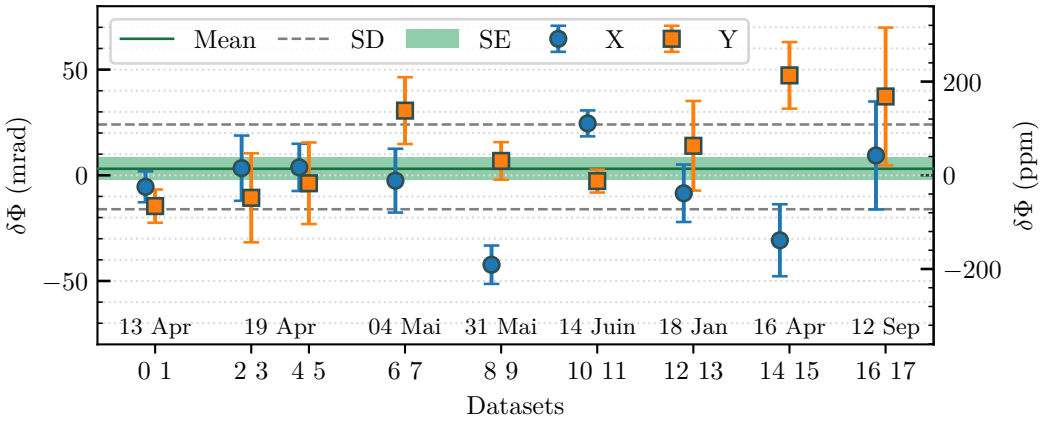

FIGURE IV.13: All Sagnac effect measurement realizations from 13 April 2021 to 12 September 2022. We plot the difference between the expected and experimental scale factor values for both axes. The green solid line is the mean value for all measurements. The shaded region corresponds to the standard error of the mean (±SE). The dashed gray line indicates the standard deviation (SD) on the set of measurements.

.

The discrepancy between the measurements is not fully accounted for by the fit uncertainties for specific values of $\Phi_0^{x,y}$. This can be attributed to a systematic error arising from a phase bias that drifts over time. Hypothetically, this can be associated with the phase bias resulting from trajectory misalignment, as discussed in section IV.3.a. This is given by:

$$\Delta\Phi^{\text{traj}} = 2Tk_{\text{eff}}\,\delta\theta\,\delta v \tag{IV.16}$$

The root cause of this misalignment could be temperature fluctuations experienced when opening the thermal isolation box to adjust the experiment's orientation. This can be noticed via the contrast variations observed during the measurement which translates into mirror angular variations, yielding values of $\delta\theta$ between 3 and 9 μrad.

To simulate this effect, we consider velocity fluctuations δv selected from a normal distribution with a standard deviation of 1 mm.s^{-1}, which corresponds to typical fluctuations that we have. The misalignment is modeled by a linear drift that ramps from 0 to a value $\delta\theta$. For each angle, the simulated phase is the phase given by:

$$\Phi_{\text{sim}}(\Theta) = \Phi_\Omega(\Theta) + \Delta\tilde{\Phi}^{\text{traj}} + \delta\tilde{\Phi}_{\text{MFL}}, \tag{IV.17}$$

with $\delta\tilde{\Phi}_{\text{MFL}}$ is the residual vibration phase noise generated randomly from a Gaussian distribution with a $\sigma = 350$ mrad. The resultant sine data, which resembles the one presented in Figure IV.11, is then fitted and we compare the amplitude to the pre-set scale factor which gives $\delta\Phi$. In Figure IV.14, we present the results of this simulation both with and without mirror misalignments where we can see how we can reproduce the discrepancy in our experimental measurements.

Currently, adjusting the mirrors during measurements is not feasible due to the unpredictable nature of the misalignments (in both directions) and the absence of a

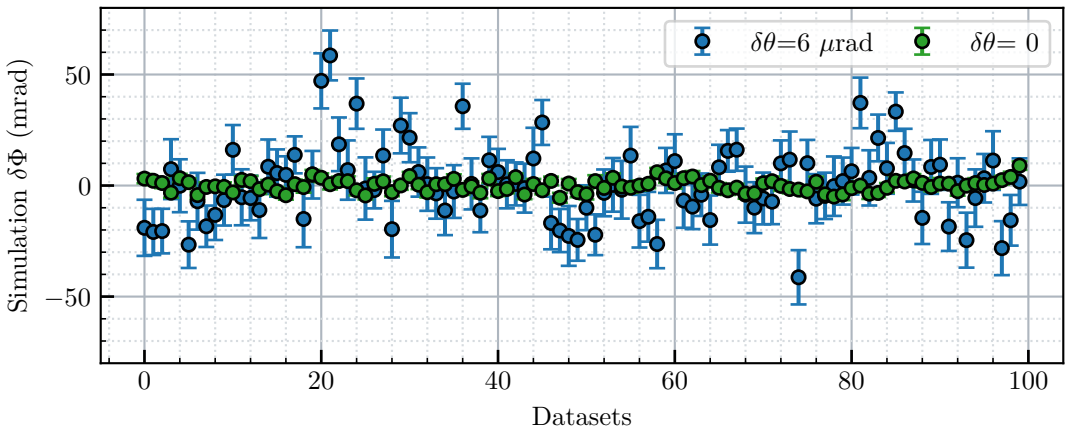

FIGURE IV.14: Simulation of 100 datasets in the presence of trajectory phase bias drift. Each value of $\delta\Phi$ is the result of 41 orientation values.

monitoring signal. Nevertheless, once the north/south angles are precisely determined, several strategies can be considered to mitigate this effect such as: Executing a full rotation within a single day to encompass both the north and south angles (representing the maximum and minimum of the sine function). Then, average the measured scale factor value over several days. Another approach might be to alternate between north and south measurements successively.

Orthogonality: Through these measurements, we can extract the orthogonality between the two axes of the gyroscope X and Y, given by the angle:

$$\Theta_{\perp} = \pi/2 - (\Theta_N^x - \Theta_N^y) \tag{IV.18}$$

We plot the results in Figure IV.15, the statistics of this observable lead to a mean value of 0.77(15) mrad. This shows good stability for this angle which is defined mechanically by the position of the collimators, therefore, it can be brought close to zero with minor adjustments in the yaw direction of the collimators. We note that in precision gyroscope technologies, this is one of the critical aspects to provide independent axes measurements and reduce cross-coupling errors.

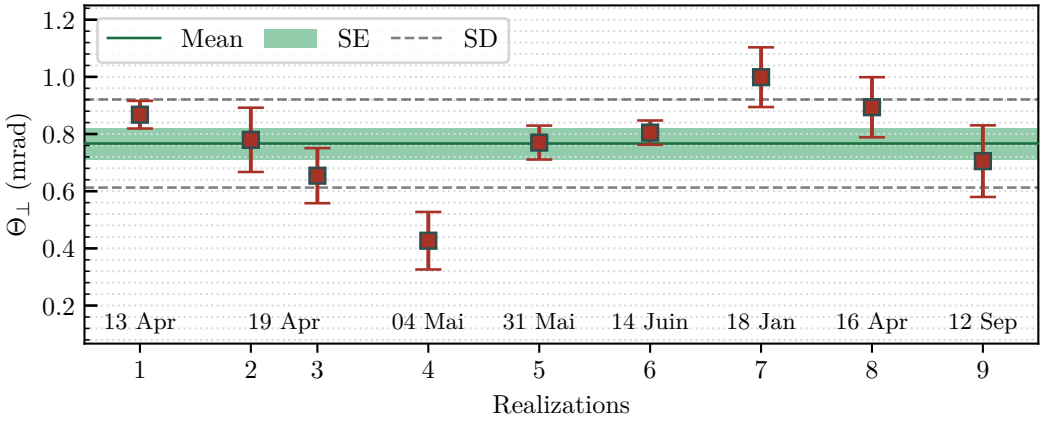

Figure IV.15: The measured angle between the two Raman axis.

.

IV.5 Conclusion

In this chapter, we provided a comprehensive characterization of the scale factor value of the cold-atom gyroscope as determined by the Sagnac effect. We meticulously measured each parameter contributing to its value using frequency measurements, except for the astronomical latitude. Subsequently, we illustrated the methodology employed to conduct measurements by rotating the experiment to extract the value of the Earth-rotation-induced phase shift. The results from our measurement campaign were presented, demonstrating a confirmation of the Sagnac effect with an accuracy of 23 ppm. To our knowledge, this is the most accurate determination of the Sagnac effect for matter waves, with an increase of accuracy of more than 20 compared to previous results.

Throughout the year, we observed no unusual deviations apart from systematic error deviations. These were attributed to the thermal fluctuations impacting the mirrors. Our findings illuminate the precision with which the scale factor can be determined for a cold-atom gyroscope. Furthermore, using two axes for this measurement revealed that the orthogonality of such an instrument is maintained consistently over an extended period of more than a year to a level better than 1 mrad.

The fundamental interest of our cold-atom gyroscope lies in its capacity to measure multiple components of local angular velocity, exploring rotational signals across various directions, unlike large ring laser gyroscope infrastructures which have fixed gyroscope axes. This adaptability offers the potential to probe subtler signals beyond just Earth's rotation and it may be possible, up to the provided upper limit, to test alternative theories such as the search for a Lorentz violation in the theoretical framework of the Standard Model Extension (SME), as shown in [73].

Another practical application, due to the precise knowledge of the scale factor, together with Earth rotation rate can allow precise measurements of the vertical deflection at the level of a few arcseconds. This provides a measurement of the local gravity direction which depends on local mass anomalies in regions where an astronomical determination is impossible (underground facilities for example).

Finally, our work paves the way toward applications in rotation seismology [74], a field that studies rotation motions induced by earthquakes which can theoretically improve their sources [75] and their localization [76] which is important for seismic alert systems. This requires a transportable gyroscope with a scale factor that is stable for weeks to sample low frequencies and known with high accuracy (better than 100 ppm). While FOG technology has been particularly deployed for rotational seismology sensing [20, 77], reaching such stability and accuracy levels is challenging. Our cold-atom gyroscope, with proper engineering, may lead to a transportable laboratory instrument [9] or even a commercial product as achieved for cold-atom gravimeters [22]. Here, a specific effort should address the trajectories bias drift which appeared as a limiting factor in the present work.

Chapter V

Real-time control of the atom interferometer phase for the double diffraction regime

Double diffraction consists of using stimulated Raman transitions to diffract atoms in the same internal state with a momentum separation of $2k_{\text{eff}}$. The advantages of this technique are multiple:

Rejection of systematic effects: On the one hand, interferometers made using this method imply atoms traveling in the same internal state analogously to Bragg regime interferometers [78]. They are therefore inherently insensitive to systematic effects induced by light shifts and temporal fluctuations of the Zeeman effect. Generally speaking, since the atoms are in the same internal state, all clock effects are absent.

State labeling: On the other hand, although the atoms travel in the same internal state within the interferometer, the final phase shift remains, however, readable on the population ratio of the internal states at the output of the interferometer thanks to the use of stimulated Raman transitions. It is then possible to measure the phase shift at the output of the interferometer, even if the initial width of the velocity distribution of the atomic source is not smaller than the momentum separation of the output paths.

Sensitivity improvement: Moreover, due to the spatial separation imposed by the beamsplitter ($\frac{\pi}{2}$-pulse), the area of the interferometer, hence its sensitivity to inertial effects, is increased by a factor of 2 compared to an interferometer in simple diffraction regime for the same interferometer duration $2T$.

Double-joint mode: Working in double diffraction will enable to join the π-pulses of two consecutive interferometers which is not perfectly feasible in the simple diffraction mode, as we have seen in section III.6.

This method has been fully detailed and experimentally tested in previous work as part of the old version of the atomic gyroscope [79] during the thesis of T. Lévèque [34, 33].

We will show in what follows that the primary problem with this method is the absence of a control parameter for the phase shift of the interferometer, given that the relative phase of the Raman lasers is inaccessible. This implies that neither real-time vibration compensation nor the mid-fringe lock techniques can be employed.

Here, we will present two alternative methods to control in real-time the phase of the atom interferometer when working in a double diffraction regime. First, we will demonstrate how variation in the Raman detuning during the interferometer can induce phase variation, and how we can exploit this degree of freedom by performing frequency jumps. Following that, we will introduce another technique that involves using a translation piezo stage on which the Raman mirror is mounted to control the imprinted phase on the atoms. For both methods, we will present the hardware and the experimental implementation and characterize the scale factor (conversion factor) using interferometric measurements and compare the performances of each method.

V.1 Frequency jumps

In Figure V.1, we show the laser configuration of the retro-reflected Raman beams and the possible laser pairs.

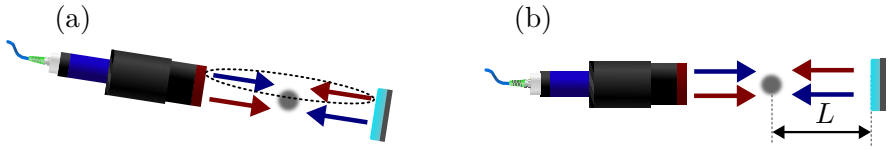

FIGURE V.1: Retro-reflected Raman lasers configuration. (**a**) Simple diffraction where only one pair (dashed circle) verifies the resonance condition (Doppler effect). (**b**) Double diffraction configuration where both pairs are resonant.

In the simple diffraction regime, the Raman collimators are tilted and ω_L is chosen to be resonant *only with one of the two pairs*, due to the Doppler effect. The imprinted phase during a Raman pulse for the first pair is given by:

$$\begin{aligned}\varphi^{(+)}(t) &= \phi_3(t) - \phi_4(t-\tau) \\ &= \left(\mathbf{k}_3 \cdot \mathbf{r} - \omega_3 t + \phi_3^0\right) - \left(\mathbf{k}_4 \cdot \mathbf{r} - \omega_4(t-\tau) + \phi_4^0\right) \\ &= \mathbf{k}_{\text{eff}} \cdot \mathbf{r}(t) - \omega_L t - \omega_4 \tau + \phi^0 \end{aligned} \tag{V.1}$$

where $\omega_L = \omega_3 - \omega_4$ and $\tau = 2L/c$, is the time delay due to a round trip of the laser traveling a distance L from the atom to the mirror and $\phi_0 = \phi_3 - \phi_4$ is the relative phase of the two laser. For the second pair, we have

$$\begin{aligned}\varphi^{(-)}(t) &= \phi_3(t-\tau) - \phi_4(t) \\ &= -\mathbf{k}_{\text{eff}} \cdot \mathbf{r}(t) - \omega_L t + \omega_3 \tau + \phi^0 \end{aligned} \tag{V.2}$$

Now considering the case where the Raman lasers detuning, Δ, get jumped by an amount $\mathrm{d}\omega$, i.e. $\omega_3 \to \omega_3 + \mathrm{d}\omega$ and $\omega_4 \to \omega_4 + \mathrm{d}\omega$, we have:

$$\boxed{\varphi^{(\pm)}(t) \to \varphi^{(\pm)}(t) \mp \mathrm{d}\omega\, \tau.} \tag{V.3}$$

We demonstrated here the sensitivity of the interferometer to the absolute frequency of the Raman lasers. The influence of lasers propagation delay on atom interferometers has been explored for other applications such as the study of the phase noise due to fluctuations of lasers frequency in [80], for gravitational-wave detectors in [15] and the effect of frequency-chirping for zero-velocity atom interferometers [81].

For the double diffraction regime, both pairs are resonant and the phase difference between the two arms is

$$\varphi_{\text{double}}(t) = \varphi^{(+)} - \varphi^{(-)} = 2\mathbf{k}_{\text{eff}} \cdot \mathbf{r}(t) - (\omega_3 + \omega_4)\tau. \tag{V.4}$$

Here, we can see that the relative phase of the lasers, ϕ^0 is canceled as well as the clock term[1] $\omega_L t$ and when considering the frequency jump, the associated phase contribution is doubled and we get

$$\boxed{\varphi_{\text{double}}(t) \to \varphi_{\text{double}}(t) - 2\,\mathrm{d}\omega\,\tau.} \tag{V.5}$$

For our experiment, the distance $L \approx 10\,\text{cm}$, which means that in order to achieve a $\pm\pi$ (one fringe span) in a double diffraction regime, we need to perform frequency jumps of approximately $\pm 400\,\text{MHz}$ which is experimentally feasible.

V.1.a Lightshift variation

The validation of the concept will be first demonstrated in the simple diffraction regime. Therefore, we need to take into account the sensitivity to frequency due to differential lightshift variations, $\delta^{\text{AC}}(\Delta)$.

As discussed in Section II.2.b, the differential lightshift is compensated for by selecting the optimal power ratio of the two Raman lasers, $R(\Delta)$. When performing frequency jumps (altering Δ) with a fixed power ratio, a phase contribution due to variations in lightshift will emerge. It is important to note that, in the double diffraction regime, the interferometer becomes insensitive to these variations.

Without a compensation strategy, our objective is to identify a central detuning frequency, Δ_0, that minimizes the lightshift variations within the range of frequency-jumps of interest ($\mathrm{d}\omega = \pm 400\,\text{MHz}$). For that, we employ the same equations in Section II.2.b and express the differential lightshift as follows:

$$\delta^{\text{AC}}(\Delta) = \Gamma^2 \frac{I_3}{I_{\text{sat}}}\Big[g(\Delta) - e(\Delta - \omega_{\text{HFS}}) + R_0\big[g(\Delta + \omega_{\text{HFS}}) - e(\Delta)\big]\Big], \tag{V.6}$$

where $R_0 = R(\Delta_0)$ and the g, e function have been already defined.

The calculations are done by fixing the power-ratio at R_0 (see Eq. II.43), i.e canceling the lightshift at $\Delta = \Delta_0$. Then, varying the detuning as $\Delta = \Delta_0 + \mathrm{d}\omega$. Finally, we consider to take the peak-to-peak variations as a quantity to minimize.

We present in Figure V.2 numerical evaluations of this effect where we extracted the peak-to-peak lightshift variations, for different central detuning values. Considering these results, we can limit these variations to a few kHz when using a central detuning around 1150 MHz. In addition, we tried to quantify the lightshifts variations experimentally using the same concept. For each measurement, we performed a Raman Spectroscopy to quantify the shift in frequency of a counter-propagating peak which is supposed to be δ^{AC}.

Note: In theoretical calculations, Δ is defined with respect to level $|F' = 3\rangle$. To correlate this with the beatnote frequency f_{beat} between L1 and L3, we must consider the

[1] This term was not considered in the simple diffraction regime since it cancels out as well as any term in t^2 due to the odd symmetry of the sensitivity function of the 4-pulse interferometer.

frequency difference between $|F' = 3\rangle$ and the crossover $|F' = 2, 3\rangle$, which is 75.6 MHz, plus an additional 80 MHz due to the AOM. Therefore, $\Delta = f_{\text{beat}} + 155.6\,\text{MHz}$ (Figure III.20).

To conclude, we decided to work at a central detuning that corresponds to 1 GHz on the beatnote frequency i.e. $\Delta = 1155\,\text{MHz}$ which is close to the optimal value.

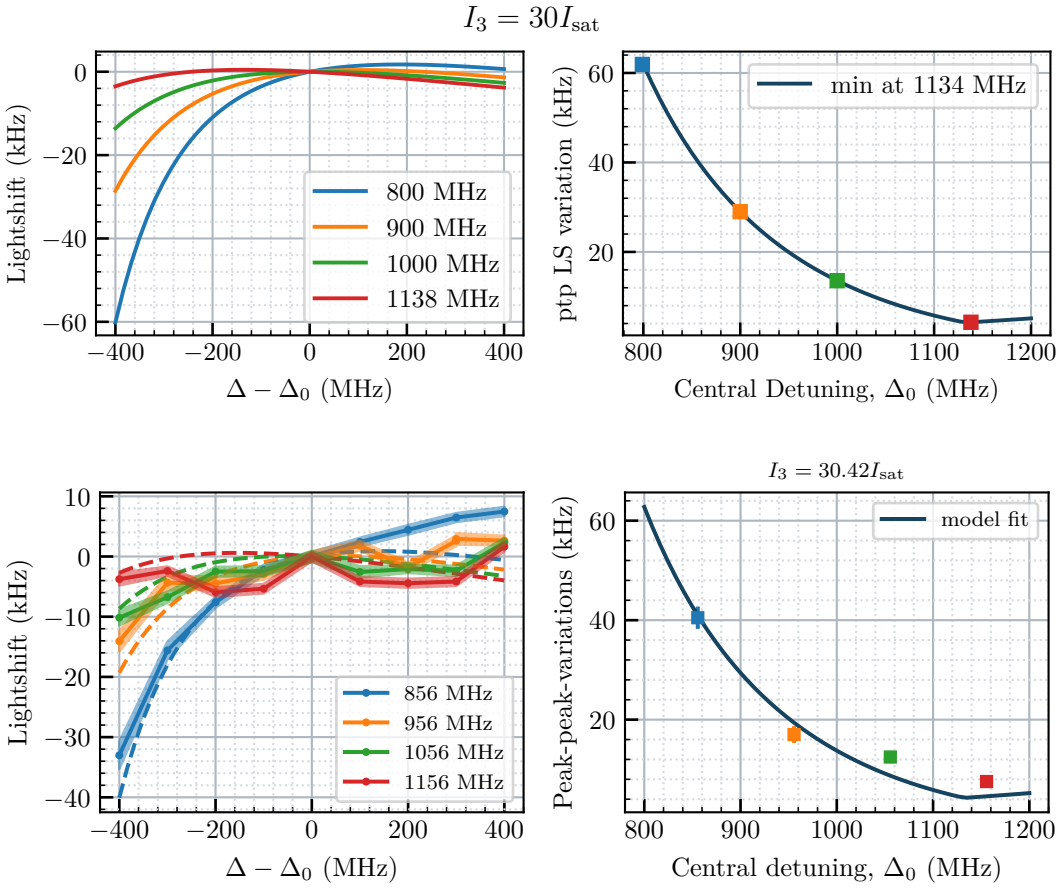

FIGURE V.2: Variations in differential lightshift. (**Left**) The graph depicts lightshift variations as a function of detuning frequency jumps, $\Delta - \Delta_0$, for various values of Δ_0. For each curve, the power ratio is kept constant at $R(\Delta_0)$. (**Right**) Peak-to-peak lightshift variations within a range of ± 400 MHz as a function of the central detuning frequency Δ_0. The minimum value, a few kHz, is found to occur around 1150 MHz relative to the level $|F' = 3\rangle$. The orange dots represent several experimental measurements, obtained by performing Raman spectroscopy on the atoms.

V.1.b Effective Rabi frequency Ω_{eff} compensation

The effective Rabi frequency, denoted as Ω_{eff} (see: Equation II.37), also depends on the detuning frequency, proportional to P_{tot}/Δ. Variations in the latter can lead to a change in population transfer efficiency, which consequently results in contrast fluctuations. We chose to compensate for Ω_{eff} by changing the total optical power P_{tot}.

Given that we are utilizing the maximum power of our lasers, performing positive jumps with respect to Δ_0 requires an increase in power, which is not practically feasi-

ble. Hence, we can afford to sacrify some optical power to enable compensation. The proposed solution involves setting the duration of the Raman pulses at the maximum detuning allowed by the jumps, i.e., $\Delta_0 + 400\,\text{MHz}$, while using the full optical power. Subsequently, we aim to characterize the optimal power that ensures the condition $\Omega_{\text{eff}}\tau = \pi$ when the detuning is altered.

Power adjustments can be readily achieved by utilizing an analog input on our AOM driver, which modulates the power of the RF signal (characterization in Figure V.3).

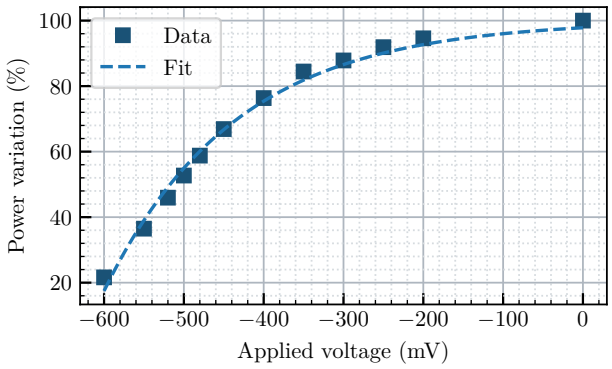

FIGURE V.3: Response of the optical power vs modulation voltage.

To determine the percentage of power needed for compensation per MHz, we scanned the optical power of the Raman beams at various detuning values. This process is equivalent to conducting Rabi oscillation measurements. In Figure V.4, we present the analysis that was done, which yielded a correction rate of 4.5% per 100 MHz.

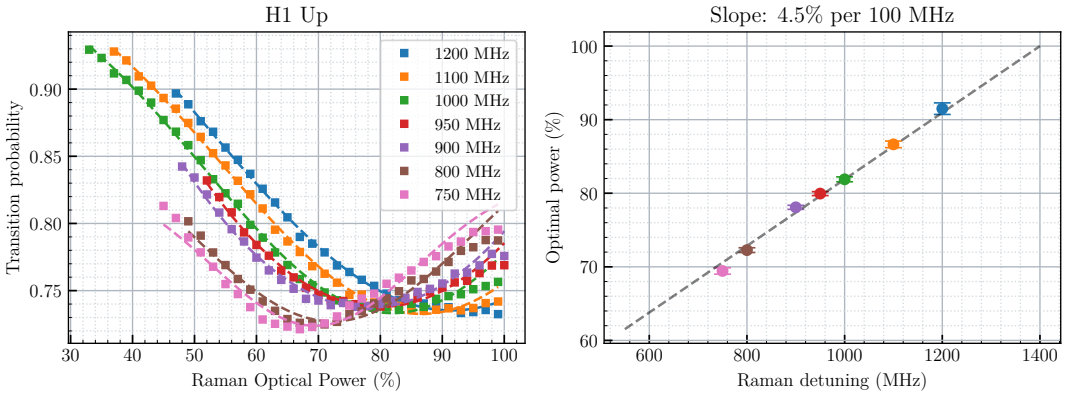

FIGURE V.4: Characterization of the effective Rabi frequency compensation with optical power. The duration of the pulse is fixed at τ_π at a detuning of 1400 MHz. (left) Rabi oscillations using the optical power for different values of the Raman detuning. (right) The optimal optical power (where we have max transfer) as a function of the Raman detuning. The slope of the fitted curve is used for the compensation of the effective Rabi frequency.

With this characterization complete, we plan to dynamically adjust the optical power during each shot in the measurement cycles to align with the frequency jumps we intend to execute. Experimentally, this analog signal will be generated from the NI cards, with a triggering mechanism in place to ensure synchronization with the pulse timings. For the majority of the time, the interferometer is operated at a nominal power corresponding

to Δ_0 (82%), which corresponds to a voltage V_0. Then, during the pulse of interest, the voltage shifts to a predetermined value, V_{jump}, depending on the magnitude of the executed frequency jump.

V.1.c Upgrading the lasers system

The Raman detuning, Δ, is predominantly determined by the frequency of L3 which is locked based on a beatnote with L1. Prior to this study, we used an offset lock technique which uses a frequency-to-voltage converter that takes the beatnote signal which was at 350 MHz as an input, divides the frequency by 2 (RF range), and outputs a voltage. This voltage is then compared to a voltage offset to generate the error signal which is fed back to lock the laser.

For the sake of robustness, we switched to a PLL system to provide more accuracy when altering the lock frequency of the laser. The new locking scheme is depicted in Figure V.5. We used an identical PLL system that is used on the L4 laser. The generated error signal is integrated and then fed back on both the current (Fast) and the piezo (Slow) of the laser. The beatnote of L1/L3 is presented in Figure V.7 when the laser is locked.

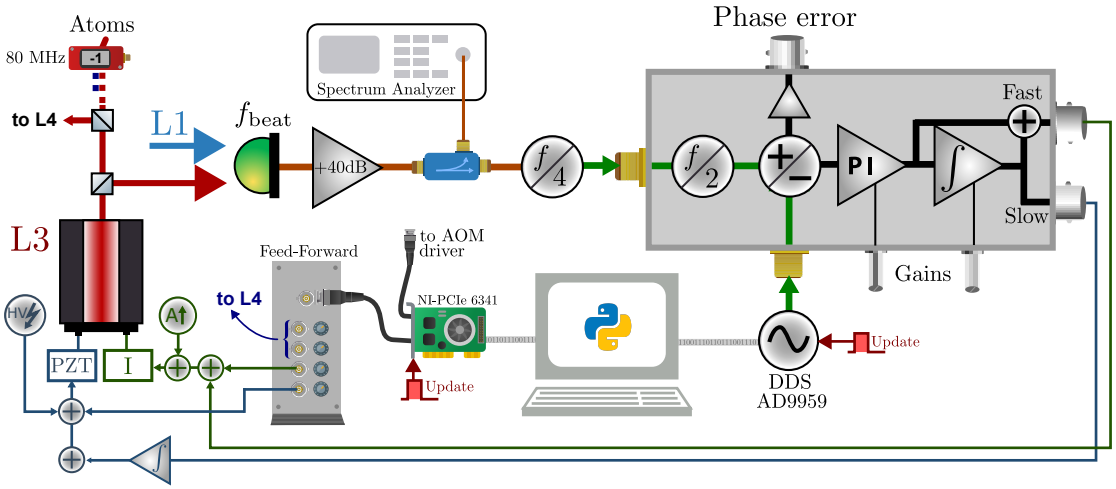

FIGURE V.5: Diagram of the new locking scheme. We also included the feedforward connections and the logic behind frequency jumps.

To finalize the system we need to address some issues:

Tunability: Since we want to span a range of frequencies of ±400 MHz around a beatnote frequency of 1 GHz. This is beyond the reach of the Local Oscillator's (LO) frequency, which is a DDS AD9959 clocked at 500 MHz. To address this subtlety, we use two frequency dividers, the first to divide the beatnote frequency by 4, and then by 2 within the PLL circuit (resulting in a total division of 8). This means that the reference signal for the PLL will be $f_{\text{LO}} = 125 \pm 50$ MHz which is feasible using the DDS. The circuit for the frequency divider $f/4$ (which uses a MC12093 Prescaler[1]) outputs a signal with a constant amplitude to ensure the same lock gains for the PLL . However, the input signal must exceed a certain power level (-13 dBm). Since usually amplifiers don't provide a flat gain curve, we used a special high-frequency amplifier (Wenteq Microwave

[1]The MC12093 is a prescaler for low power frequency division that allows a divide ratio of 2, 4 or 8. The output is a square signal which means besides the carrier frequency it outputs odd harmonics also.

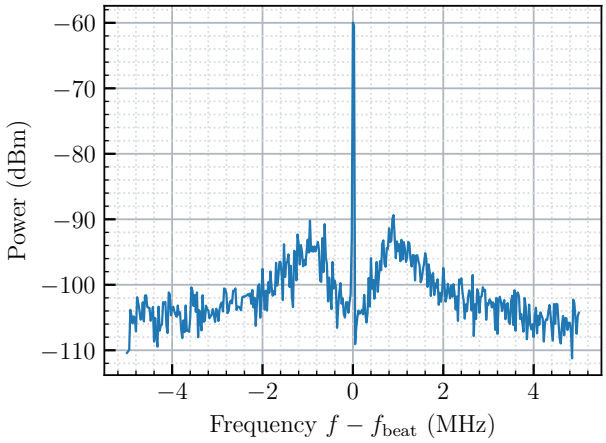

Figure V.6: The beatnote L1/L3 when L3 is locked.

ABL0200-05-4013B) to ensure constant beatnote amplification (+40 dB) across a wide range of frequencies.

Feedforwarding: To execute fast frequency jumps, feed-forwarding is crucial to assist the lasers during the transition from one frequency to another. This is achieved by applying a voltage to the laser's piezo driver in proportion to the frequency jump. Additionally, the lasers L3 and L4 possess limited mode-hop-free regions. Therefore, when large frequency jumps are applied, the lasers' setpoints must be adjusted by modifying the laser current. Experimentally, this is accomplished by using one analog output of the NI cards to generate a signal ranging from ±1 V, proportional to the frequency jump. This signal is sent to an electronic circuit that generates four analog outputs (two for each laser), each with adjustable gains. We optimized the system's response by executing constant frequency jumps on the lasers, ensuring that the lasers remain locked even for large jumps, and that response times are minimized (Figure V.7).

Synchronization: We use a digital trigger signal in the sequencer to synchronize the frequency jump with both the software feedforwarding and the compensation of the effective Rabi frequency. If we aim to perform a frequency jump at time t_{jump} (TTL timing), we program the DDS registers with the new frequency, and adjust the voltages corresponding to the feedforward and new optical power at time $t_{\text{jump}} - \Delta t$, where[1] $\Delta t \geq 7\,\text{ms}$. This programming process does not immediately update these values. In fact, the DDS supports hardware triggering to update the frequency, and the task on the NI card is configured to wait for a digital trigger to output the new values. The timing, t_{jump}, is set to 5 ms prior to the pulse, which exceeds the PLLs' recovery time after the frequency jump. After the pulse, we use the same procedure again with another digital trigger in order to reset the voltages and the frequency to their default values.

V.1.d Measuring the scale factor, L

In equation V.3, the phase due to the frequency jump depends on the duration τ, which in turn depends on the distance L. To precisely control the phase, this parameter needs to be measured.

[1] The delay of 7 ms is mainly limited by the communication time with the NI cards.

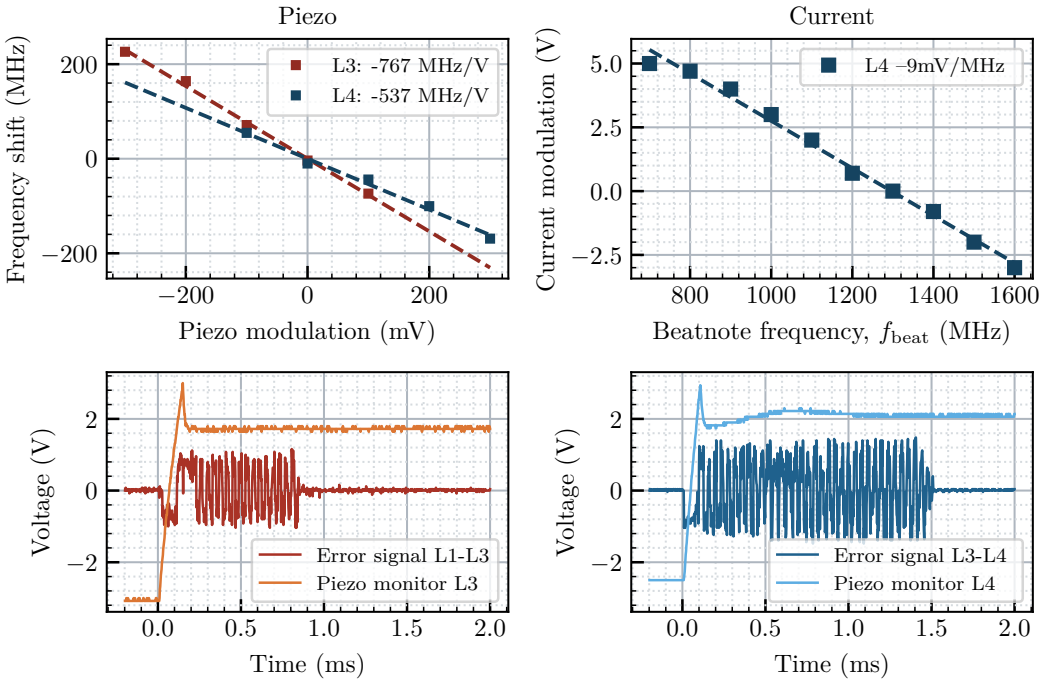

FIGURE V.7: (**top**): Characterization of the response of the laser: to a piezo modulation, on the righ-side, and the DC voltage on the current driver to minimize the PLL's noise, on the left-side. (**bottom**) Response of the laser systems L3 and L4 to a frequency jump of 400 MHz using a feedforward. For each laser, we plot the PLL's error signal and the response of the piezo driver.

We consider performing constant frequency jumps during one of the four pulses and measure the phase-shift of the interferometer. As we have seen in section **??**, one can correlate the vibrational phase noise to the measured probability and extract the offset of the fringes using fitting by packets. However, a better approach is to perform measurements using the mid-fringe lock technique. We note that is only feasible in the simple diffraction regime, as we can utilize the phase of the lasers to compensate for vibrations and drive the mid-fringe locking.

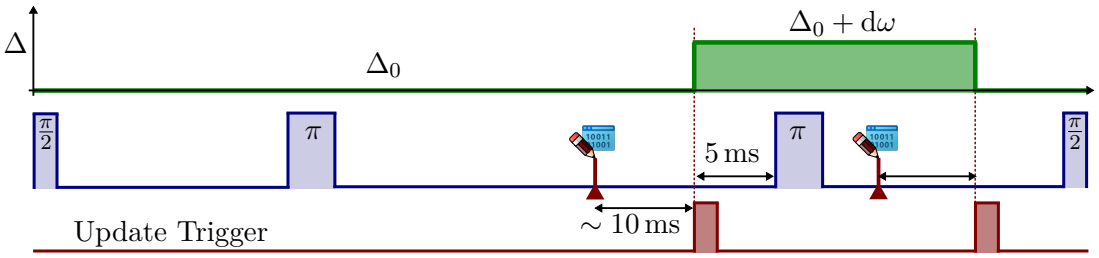

FIGURE V.8: Sequence for frequency jump.

For different frequency jumps $d\omega$ with respect to Δ_0 , we integrate the phase of the interferometer over approximately 2000 cycles. These measurements were repeated for different central detuning values (Figure V.9). All of these measurements were conducted on the π-pulses (using the mirror on H4 when atoms are moving upwards or downwards) in a simple-joint sequence (where the $\frac{\pi}{2}$-pulse is shared between two interferometers). The choice of these pulses was due to their straightforward implementation and their

ability to imprint twice the contribution of the phase (see Eq.II.48), with opposite signs for up and down pulses. From each curve, we can fit the experimental data with a linear model and using Eq.V.3 and we extract the parameter L. The weighted mean of all the realizations results in a value of 101.22(92) mm which represents relative uncertainty better than 1%. Moreover, as expected this value does not depend on the value of central detuning, Δ_0.

The measured distance can be compared with the expected one by extracting its value from the gyro 3D schematics, with a distance from the center of the vacuum tube to the surface of the mirror, $D = 91.13\,\text{mm}$. Additionally, we must consider the index of refraction, $n = 1.5098$, of the window's glass, which has a thickness $d = 1\,\text{cm}$. Consequently, we calculate the geometrical distance as: $L_{\text{geometric}} = D + d(n-1)$, which adds up to 96.23 mm. This value is off by 5 mm from the measured distance probably because the atoms may not pass exactly at the center of the vacuum tube .

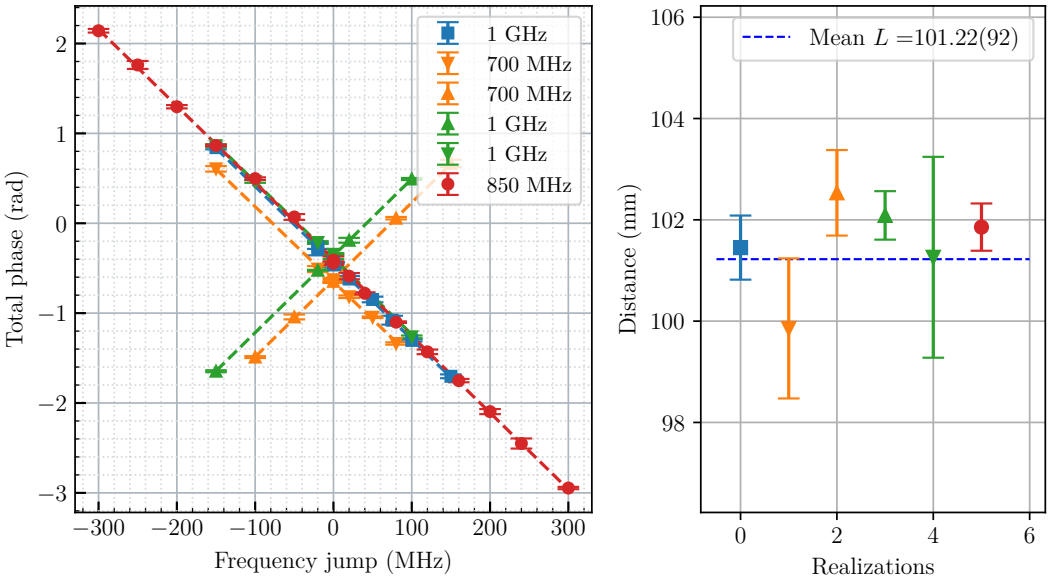

Figure V.9: Measurements of the distance L using mid-fringe lock. (**left**) Interferometer phase evolution as a function of the frequency jumps for different central Raman detunings. (**right**) The measured distance extracted from the slope of the fitted curves.

Once we characterized the system and confirmed the concept, we conducted similar measurements on H1 ($\frac{\pi}{2}$-pulses) which resulted in a distance $L = 91.9(3)\,\text{mm}$, which differs from H4 due to the distinct mirror support design. We note that even with a new design for mirror support, we cannot extend this distance due to spatial constraints. The support housing barely fits inside the magnetic shields, and the presence of piezo actuators on the mirror adds additional width.

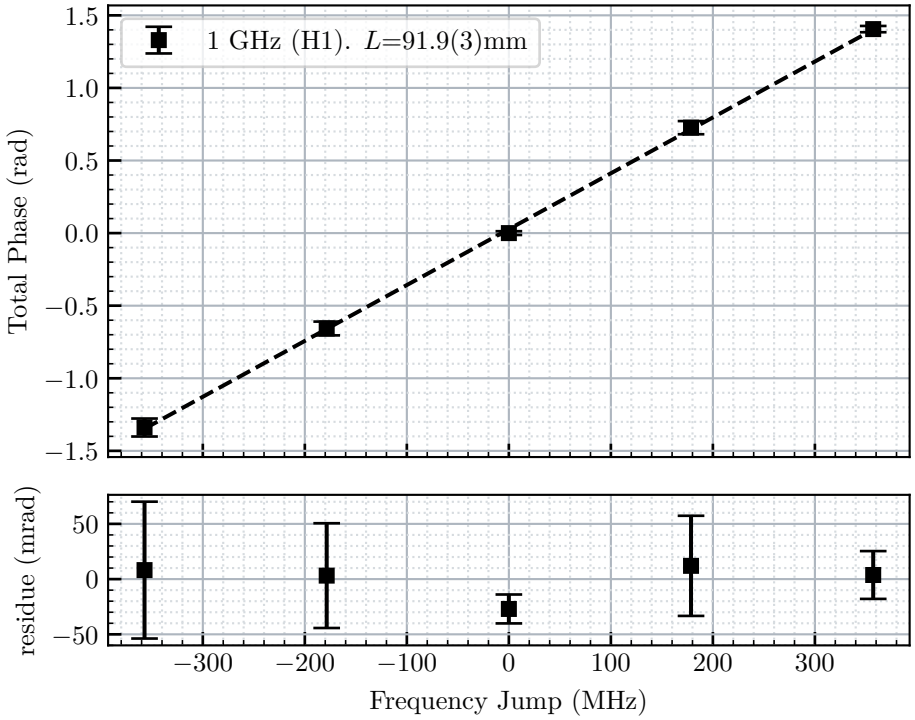

FIGURE V.10: Measurement of the distance L on H1.

V.2 Mirror position jumps

Our second approach to control the phase of the interferometer consists of changing the parameter L. This can be achieved by mounting the retro-reflecting mirror on a translation stage controlled by a piezo motor.

In principle, we use the same derived expressions in Eqs. V.1 and V.2 and we consider a mirror displacement along the Raman propagation axis, that we denote $\mathrm{d}l$, we have for the simple diffraction regime:

$$\boxed{\varphi^{(\pm)}(t) \to \varphi^{(\pm)}(t) \mp k_{\mathrm{eff}}\,\mathrm{d}l\,,} \tag{V.7}$$

where we did the approximation: $k_{\mathrm{eff}} \approx \frac{2\omega_3}{c} \approx \frac{2\omega_4}{c}$. And for the double diffraction regime, we will have (without approximation):

$$\boxed{\varphi_{\mathrm{double}}(t) \to \varphi_{\mathrm{double}}(t) - 2\,k_{\mathrm{eff}}\,\mathrm{d}l,} \tag{V.8}$$

Hence, spanning one period of the fringes can be done by spanning a distance $\mathrm{d}l = \lambda/2$ on the mirror i.e. $\sim 426\,\mathrm{nm}$ (half of that in double diffraction regime).

V.2.a System design and implementation

This method necessitated a modification to the experimental setup, which included revising the design of the mirror support at window H1 (which requires removing the magnetic shield). This support, which is attached to the vacuum chamber using M6 screws, accommodates not only the seismometer used for vibration correlation but also the Raman retro-reflecting motorized mirror, an adjustable quarter-wave plate, and a sliding cache enabling co-propagating Raman configuration when needed. The new support (Figure V.11) is designed to accommodate a translation stage (a piezo nanopositioner, model: Mad City Labs Nano-OP30M), upon which the mounted mirror is placed.

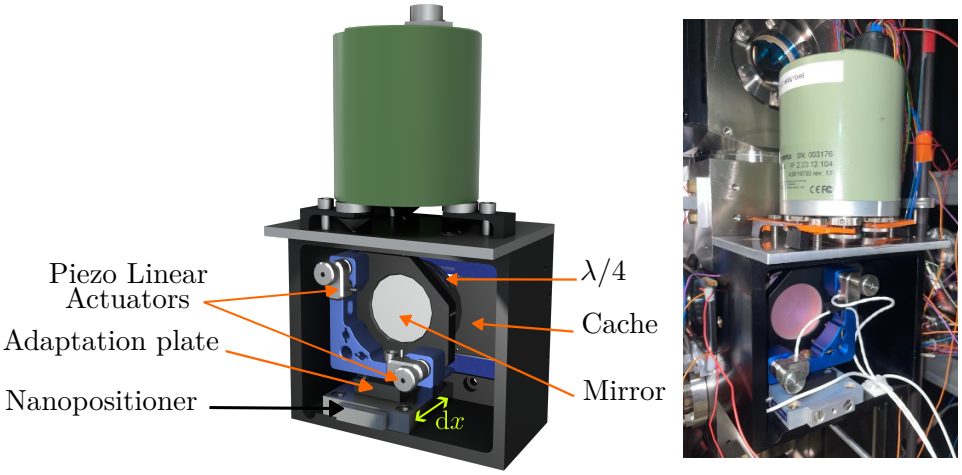

FIGURE V.11: Design of the new mirror support.

Specifications and performance: The piezo nanopositioner features a motion range of $30\,\mu\mathrm{m}$ with a resolution of $0.06\,\mathrm{nm}$ and can support a maximum mass of $1\,\mathrm{kg}$ (compared to $\sim 350\,\mathrm{g}$ for the mounted mirror). This nanopositioner uses internal sensors

to deliver absolute and repeatable position measurements under a closed-loop control scheme.

Control and monitoring: The nanopositioner system comes with a module: the Nano-Drive, which powers the stage and hosts the closed-loop servo/drivers. The Nano-Drive offers two standard analog control inputs (0-10V) through front panel BNCs. The first input produces a real-time position sensor signal, and the second serves as an input command signal. Additionally, a USB 2.0 port allows for software control or position monitoring using Python[1]. However, this communication interface is relatively slow and does not support triggering options, making it unsuitable for our intended application.

Step response: The step response of the nanopositioner is shown in Figure V.12, this was obtained by modulating the position with a 4 Hz square signal with different amplitudes. Generally, the step response is set so that the system is critically damped. This means that the step response is as fast as it can be while maintaining stability and having no overshoot or ringing in the system[2]. We can see that the settling time (time to hit the setpoint) does not depend on the size of the step. We measure a settling time of 30 ms. This is one of the downsides of this system when compared to the frequency jumps method ($\sim$ 4 ms recovery time).

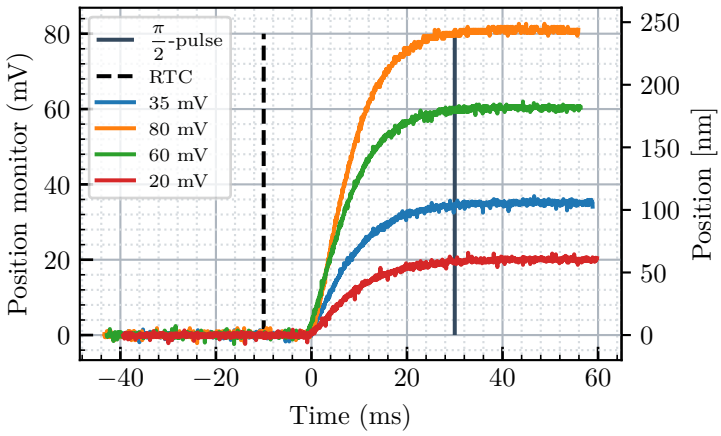

FIGURE V.12: Step response of the nanopositioner. Here we plot the analog position monitor of the Nano-Drive for different step values. We also show the relative timing of both the last pulse and RTC.

[1]The manufacturer provides a C driver via a `.dll` file. However, I developed a Python wrapper library in case we want to integrate this functionality into the acquisition software.

[2]The responsiveness of the system can be adjusted via two internal trimmers within the Nano-Drive unit. The "Int" trimmer adjusts the closed-loop bandwidth, directly influencing the speed of the system's response. The "LP Filter" trimmer, on the other hand, regulates the filter frequency, offering additional damping to the nanopositioner's resonance. This initially slows the system but also allows the "Int" trimmer to be adjusted for greater speed while maintaining stability

V.2.b Measurement of the scale factor for the piezo mirror.

To determine the exact scale factor of the nanopositioner (in μm.V^{-1}), we implemented the control sequence illustrated in Figure V.13. This sequence demonstrates how to imprint a constant phase on the final $\frac{\pi}{2}$-pulse. The implementation requires the use of one analog output, configured within an NI task triggered by a digital signal synchronized with the experiment sequence. This analog signal controls the position of the mirror. From the range of the nanopositioner, we can estimate the necessary voltage to span one full fringe (approximately 30 μm within a span of 10 V). Therefore, a voltage change of ± 75 mV is sufficient to cover a $\pm\pi$ phase-shift range.

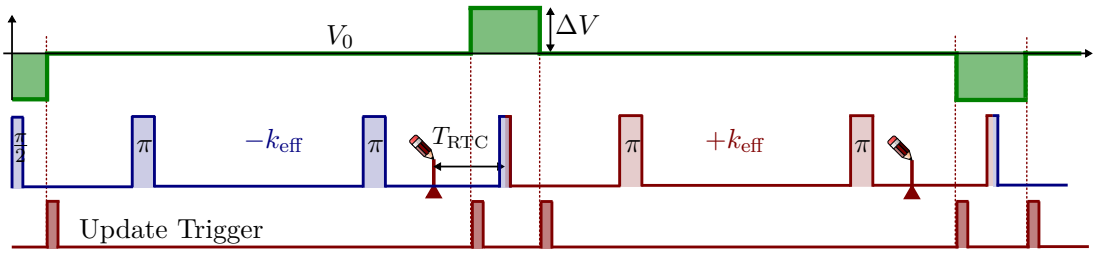

FIGURE V.13: Sequence of control for mirror position jumps. We show two consecutive interferometers (with $\pm k_{\text{eff}}$) in a simple-joint configuration. In green, we plot the command voltage for the nanopositioner and also the triggers configuration (not-to-scale).

Since we operate the gyro measurements in a simple joint mode, the first and the last $\frac{\pi}{2}$-pulses are shared. Moreover, we use a configuration where we alternate between $\pm k_{\text{eff}}$ by switching the frequency ramp slope rates. In this configuration, the imprinted phase on the last pulse will be also imprinted on the first pulse of the next interferometer with an opposite sign.

Analogous to the methodology used for the frequency jump technique, we measured the phase of the interferometer using the mid-fringe lock technique; when constant mirror position jumps are applied, ΔV (in Volts) with respect to an offset position V_0. To keep up with the $\pm k_{\text{eff}}$ sequence, we switched between $\pm\Delta V$ between two interferometers. With that, we expect an additional phase contribution to the total phase of $2\varphi(\Delta V)$.

For timing considerations, we incorporated the programming of position jumps (writing voltage values) into the RTC callback function and we reset the position at the start of the interferometer[1]. To account for the nanopositioner's settling time and the delay in communication with the NI card, we set the RTC delay to $T_{\text{RTC}} = 40$ ms.

The results of the analysis are presented in Figure V.15. We fit the data with a linear model,

$$\Delta\varphi = k_{\text{eff}}\,\alpha\,\Delta V, \tag{V.9}$$

in order to extract the value of the scale factor, α which was found to be 2.9207(100) μm.V^{-1}. For comparison, we used the driver of the nanopositioner to retrieve a numerical value of the position when we applied constant voltages to the input port. These readings are based on a factory calibration, which differs from our measurements since the combined mass of the mirror (including the mount, optic, and piezo motors) is greater than the mass we communicated to the manufacturer. As depicted in Figure V.14, the measured

[1]Inside the acquisition program, triggers are used to synchronize the software with the experiment. Therefore, we can get the information about the current time inside the interferometer.

value is 3.013(3) μm.V^{-1}. Furthermore, both measurements exhibit a linear response to the applied voltage.

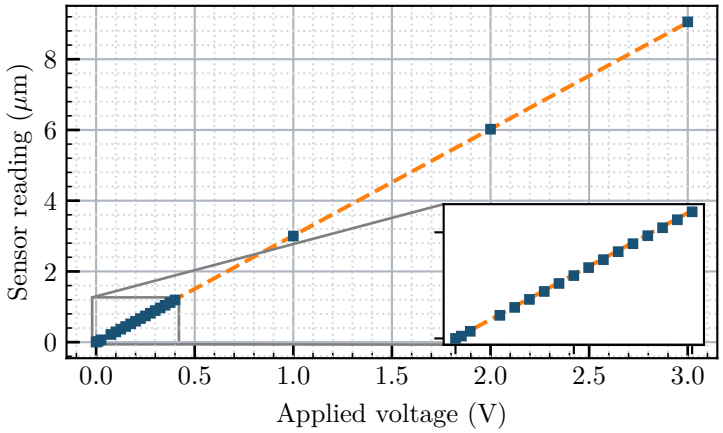

FIGURE V.14: Scale factor measurement based on the factory calibration of the piezo nanopositioner.

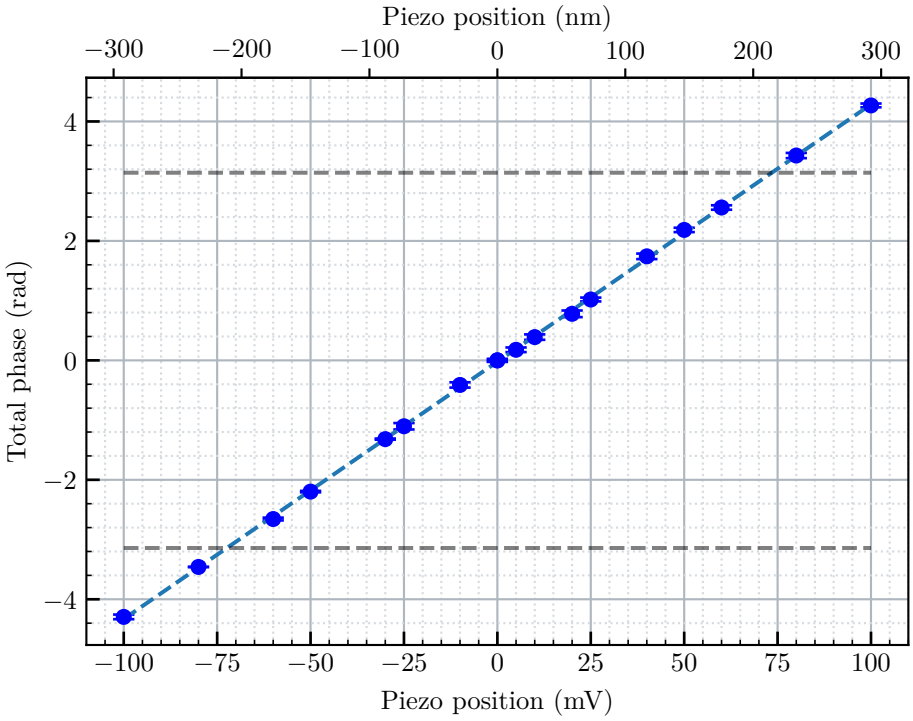

FIGURE V.15: The mean value of the phase-shift of the interferometer measured with the mid-fringe lock, $2\Delta\varphi$ (in rads) as a function of the mirror position jump, ΔV (in mV). The dashed blue line is a linear fit of the experimental data.

V.3 Implementing RTC for vibrations

In the previous sections, we showed the two alternative methods to control the phase of the interferometer by imprinting constant phase contribution. We used the advantage of being in the simple diffraction regime where the lasers' relative phase is accessible to control the phase shift of the interferometer: compensate for the vibrational phase and lock the interferometer on its mid-fringe.

Here, we will consider using the alternative methods to replace the lasers' phase by the alternative methods in order to show the performances of each method. In addition, we will work in the join-mode sequence which means that we need to handle the common jump due to the shared $\frac{\pi}{2}$-pulse where the phase is imprinted on two interferometers with opposite sign (reversal k_{eff}).

Mirror position jumps:

The nanopositioner can fully replace the lasers' phase since it allows to scan a full fringe ($\pm\pi$ phase) as we have demonstrated in Figure V.15. Moreover, since the phase shift of the interferometer is relative to the phase of the first pulse of the interferometer, the position offset given by V_0 can change from cycle to cycle. The control sequence can be simplified by removing the second jump that resets the position. However, to prevent the mirror from displacing too far, we limit the range of the position jumps first by working with modulo 2π phases offset by π, and then mapping $\pm\pi$ range to $V_0 \pm V_{\text{max}}$.

Frequency jumps: Unlike mirror position jumps, in the simple diffraction regime, the phase contribution is restricted to $\pm\frac{\pi}{2}$ for the $\frac{\pi}{2}$-pulses with jumps of $\pm 400\,\text{MHz}$. Moreover, it's necessary to reset the detuning to Δ_0 after the frequency jump to prevent variations in the lightshift for the π-pulses. Given the issue of the limited range, we chose to implement a hybrid phase control using the following approach:

1. At the end of the interferometer cycle, $2T - T_{\text{RTC}}$, we aim to apply a phase $\Phi_{\text{tot}} = \Phi_{\text{RTC}} + \Phi_{\text{MFL}}$, where Φ_{RTC} compensates for vibrations and Φ_{MFL} provides an additional phase to operate the interferometer at its mid-fringe.

2. The total phase Φ_{tot} is written in modulo 2π, subtracting a global offset of π to end-up with a phase range of $\pm\pi$.

3. This phase is divided into two equal contributions. The first contribution is applied using the phase of the lasers and the second one is applied using frequency jumps (or mirror position jumps for comparison).

For comparison, we use the Allan deviation tool as a performance indicator. In Figure V.16, we plot the Allan deviation of the measured inertial phase while mid-fringe locking the interferometer, using all the mentioned methods. We show that the new methods do not affect the performance of the gyroscope when compared to the laser phase jumps. The short-term stability is not relevant to the used method since it depends on the amount of vibration noise present when performing the measurement.

Also, we plot the Allan deviation of the non-inertial phase (Figure V.17), extracted from the half-sum of $\pm k$ configurations, and we can see the drift caused by lightshift variations in the Phase/Frequency jumps hybrid method.

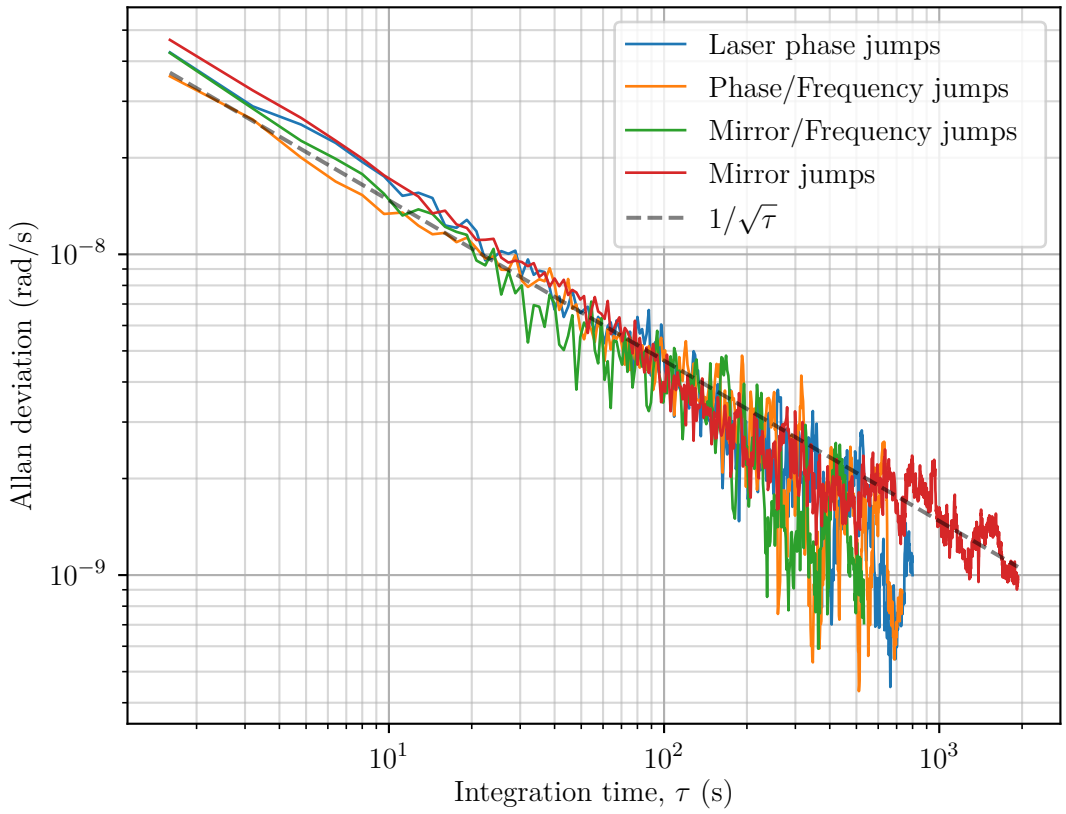

FIGURE V.16: Performance for each method: We plot the Allan deviation of the measured rotation rate σ_Ω (in rad.s^{-1}) as a function of the integration time, τ (in seconds).

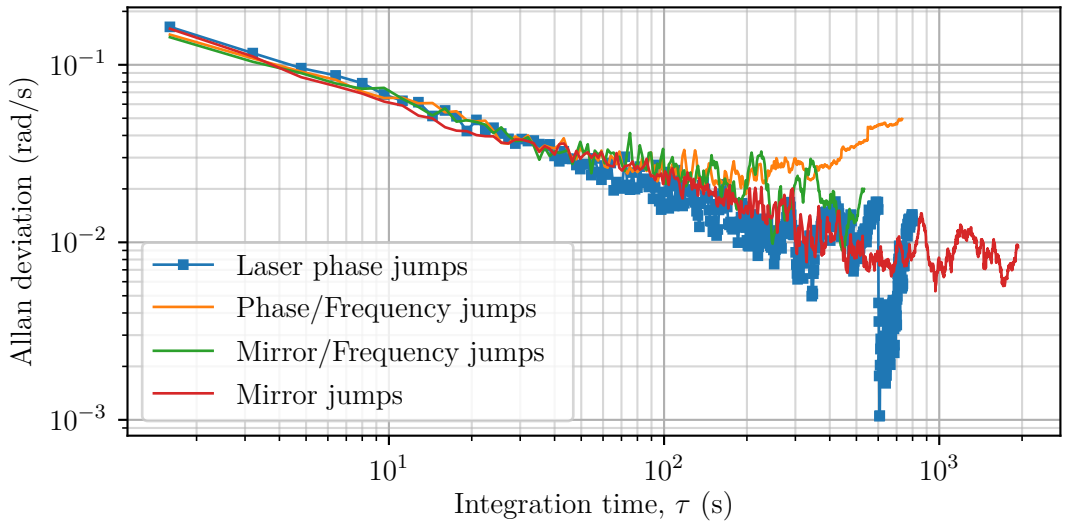

FIGURE V.17: Allan deviation for the non-inertial phase: mainly lightshift (in rad) as a function of the integration time

Conclusion

In this chapter, we have introduced two alternative methods for controlling the phase of the interferometer in the double diffraction regime. Each method's working principle has been detailed, and their experimental implementation has been outlined. Moreover, we have characterized the scale factor for each method using interferometric measurements in the simple diffraction regime where the laser's phase is accessible. However, if this was not accessible, we could have used an alternative method that consists of observing the fringes of the interferometer as we linearly scan the phase for different scale factor values to optimize its value.

For what concern frequency jumps technique, we have carefully considered the relevant effects, particularly the differential lightshift variations (which should pose less of an issue in the double diffraction regime) and the compensation of the effective Rabi frequency. The main drawback of this method is the loss of contrast when operating at high Raman detuning frequency (1 GHz). This method was also more challenging to accomplish, necessitating stable lasers and a complete harmony of frequency jumps and feedforwarding to maintain the lasers lock. Laser delocks may occur due to software failures in configuring the NI cards. A potential solution for this issue in the future could be the use of a dedicated real-time system or an FPGA or using a more robust laser system for the Raman beams.

On the other hand, the mirror position jumps method was easier to implement from a technical standpoint, primarily due to the use of a plug-and-play nanopositioning system. The key limitation of this approach is the nanopositioner's settling time, which sets a minimum RTC delay of 40 ms.

Finally, we showed the performance of each method to compensate for vibrations and lock the interferometer on its mid-fringe. The absence of any noticeable degradation, apart from variations attributable to light shifts, serves as a testament to the viability of the methods discussed. As mentioned before, these lightshift variations, won't present significant challenges when transitioning to the double diffraction regime.

In light of the results of this work, the immediate next steps involve transitioning to the double diffraction regime, and ultimately, with a double-joint sequence to significantly enhance both the sensitivity and performance of the cold-atom gyroscope.

Chapter VI

Conclusion and perspectives

In this manuscript, I have explained the principles of atom interferometry using Stimulated Raman transitions, detailing their application in a 4-pulse interferometer designed for the pure rotation rate measurement through the Sagnac effect. I have introduced the concept of the sensitivity function, calculated in both time and frequency domains, as an indispensable tool for quantifying the impact of various noise sources on the interferometer's phase.

In Chapter III, I have outlined the physical implementation and experimental setup, encompassing atomic source preparation, Raman pulse generation, and the detection scheme. I have shown the impact of vibrations on the interferometer, how we correlate them with our measurements using classical sensors and discussed our approach for real-time compensation by acting on the lasers' relative phase. I showed that phase contributions dominate short-term noise and that this noise averages out as $1/\sqrt{\tau}$ for uncorrelated measurements. I also demonstrated that using a simple-joint sequence effectively rejects the rotation-induced component of this noise and scales vibration noise as $1/\tau$ in the short-term and that the effect is not apparent at long-term stability since acceleration noise dominates at these integration times. I introduced the so-called double joint sequence which has the potential to efficiently average all vibration noise, but which cannot be implemented in the simple diffraction regime.

In Chapter IV, I presented the results of an extensive campaign spanning over a year, focused on precision measurement of the gyroscope scale factor. I detailed how this factor is expressed as a function of various parameters, each of which can be accurately determined using frequency measurements. I explained the dedicated experimental protocol used for measuring and extracting the rotation phase. The experimental data, collected from two separate axes of measurement, align closely with the theoretical predictions based on the Sagnac effect formula; the observed discrepancy is zeroed within a 23 ppm accuracy level, representing a 20-fold improvement over previous realizations. Furthermore, I discussed the excessive dispersion in the experimental data, attributing it to a slow bias drift caused by a systematic effect linked to the mirrors misalignment. In addition to providing more confidence in what we measured, the two axes of the gyroscope demonstrated robust stability in terms of orthogonality across the nine realizations. Given the reported level of accuracy in the knowledge of the scale factor, our cold-atom gyroscope holds promise for applications requiring precise measurements of vertical deflection (arcsecond level), especially in regions where astronomical determina-

tion is not feasible. This level of precision also provides new avenues for testing theories related to the Sagnac effect up to the established upper limit, subject to collaboration with theoretical researchers.

In the near future, our focus will be on applications in rotational seismology. Monitoring ground rotation signals is a challenging task in conventional seismology and is not routinely done, typically requiring array-derived measurements from seismometers at multiple locations. Gyroscopes offer a way to directly measure such signals, as demonstrated in [77]. Initially, we plan to validate our instrument by comparing its performance to that of a commercial fiber-optic gyroscope with similar performances (maybe the BleuSeis-3A). Subsequently, we aim to probe seismic signals at the mHz level, that are out of reach for current FOG technology (bias instability), by conducting extended measurement campaigns. For instance, the implementation of more robust laser control methods presented in this thesis will facilitate long (week) data campaigns that are required for such rotational seismology applications.

In the final chapter, we introduced novel real-time techniques for controlling the interferometer's output phase as an initiative to transition to the Raman double-diffraction regime. In addition to other advantages, this regime allows us to double the interferometer's area, thereby doubling its sensitivity to rotations. It also enables the implementation of the double-joint mode, which has the potential to improve long-term stability by scaling the vibration noise as $1/\tau$. I highlighted the primary challenge—losing the lasers' relative phase as a control parameter for the interferometer's phase shift, which is currently used for vibration compensation. I discussed two proposed solutions to overcome this issue: Raman detuning frequency jumps and mirror position jumps. Both methods exploit the lasers' propagation delay in a retro-reflecting configuration. I detailed the experimental modifications, the physical implementations, and the characterization of each method's scale factor using interferometric measurements. I presented proof-of-principle tests in the simple-diffraction regime to validate each method using constant phase jumps on one of the interferometer pulses. Finally, I implemented real-time compensation for vibrations using these techniques and compared their performance to the conventional method. For the frequency jumps, additional considerations are required: lightshift variations—which will not pose an issue in the double-diffraction regime— and variations in the effective Rabi frequency, which have been compensated for. For the mirror jumps method, implementation required modifying the mirror support within the magnetic shields and installing a commercial nanopositioner system. The only drawback of this system is the response time, limiting the real-time compensation delay to 40 ms. Nevertheless, when comparing the methods, the gyroscope's performance remained unaffected. Both methods have been permanently integrated into the control software, allowing for an easy switch between them.

Beyond improving the sensitivity and stability of our cold-atom gyroscope, these methods apply to other interferometer geometries that use double-diffraction. In microgravity applications for example: [82, 83], the atoms remain at rest, therefore, the Doppler effect is null consequently the double diffraction regime is inevitable when using stimulated Raman transitions. For such space applications, the frequency jumps method is more suitable since it does not require the use of moving parts. This absence of moving parts is a critical advantage in spaceborne settings, where mechanical reliability and system simplicity are paramount.

Appendix A

Sagnac Effect

A.1 Calculation of the area

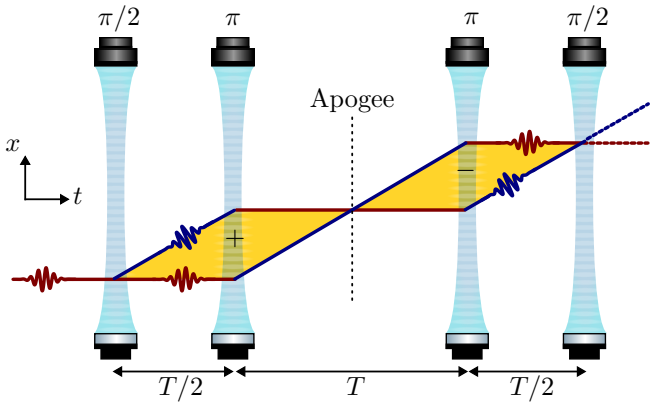

FIGURE A.1: The space-time geometry of a 4-pulse interferometer. Shaded in yellow, is the physical area enclosed by the interferometer.

The Sagnac phase is given by:

$$\Phi_{\text{Sagnac}} = \frac{4\pi E}{hc^2}\boldsymbol{\Omega}\cdot\mathcal{A} \tag{A.1}$$

Considering the geometry of our interferometer, $\boldsymbol{\Omega} = \Omega\mathbf{e}_y$ and the area is calculated using the classical trajectories of the atom and evaluated as:

$$\mathcal{A} = 2\times\left(\left|\int_0^{\frac{T}{2}} z(t)\frac{\mathrm{d}x}{\mathrm{d}t}\mathrm{d}t\right| + \left|\int_{\frac{T}{2}}^{T}[z(t)-z(T/2)]\frac{\mathrm{d}x}{\mathrm{d}t}\mathrm{d}t\right|\right) \tag{A.2}$$

where we employ the classical trajectory of the two wave packets,

$$x(t) = \frac{\hbar k_{\text{eff}}}{m}(t-T) \quad \text{and} \quad z(t) = -\frac{3g}{8}T^2 + g\left(Tt - \frac{t^2}{2}\right) \tag{A.3}$$

yielding to,

$$\boxed{\mathcal{A} = \frac{1}{4}\frac{\hbar k_{\text{eff}}}{m}gT^3 \quad \text{and} \quad \Phi_\Omega = \frac{1}{2}k_{\text{eff}}gT^3\Omega} \tag{A.4}$$

A.2 Analytic analysis of the Sagnac Effect

Numerical Values

$g = 9.80928$, $\Omega = 7.292115 \times 10^{-5}$, $\lambda = 48.835735°$, $\mathbf{k}_{\text{eff}} = \frac{4\pi}{852\text{nm}}$, $T = 400\text{ms}$, $\mathrm{d}T = 60\mu\text{s}$, $\theta_0 = 4.123°$, and, $t_0 = 114\text{ms}$ ($\dot{z}_0 = 5.04197\text{m.s}^{-1}$).

A.2.a Trajectories

Equation of motion The equation of motion for an object close to the surface of Earth under Coriolis effect[1]

$$\boxed{\ddot{\mathbf{r}} = \mathbf{g} - 2\boldsymbol{\Omega} \times \dot{\mathbf{r}}} \tag{A.5}$$

Frame of reference The acceleration due to gravity $\mathbf{g}$ is the effective one and is along the plumb line. We choose a z-axis directed vertically outward (along $\mathbf{g}$) from the surface of the Earth. The y-axis points to the east (perpendicular to $\boldsymbol{\Omega}$) and therefore (right-hand rule) the x-axis is pointing to the southerly direction. The correspondant basis $\{\hat{\mathbf{e}}_x, \hat{\mathbf{e}}_y, \hat{\mathbf{e}}_z\}$ is represented in Figure A.2.

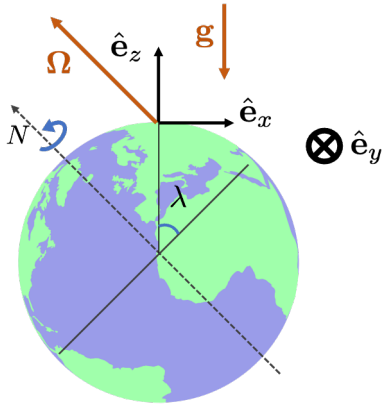

FIGURE A.2: Frame of reference used in this analysis

Coupled differential system We can project to our basis vectors,

$$\mathbf{r} = \begin{pmatrix} x \\ y \\ z \end{pmatrix}, \qquad \boldsymbol{\Omega} = \begin{pmatrix} \Omega_x \\ 0 \\ \Omega_z \end{pmatrix} = \begin{pmatrix} -\Omega\cos\lambda \\ 0 \\ \Omega\sin\lambda \end{pmatrix}, \qquad \text{and} \qquad \mathbf{g} = \begin{pmatrix} 0 \\ 0 \\ -g \end{pmatrix}, \tag{A.6}$$

where, λ is the latitude andΩ, the earth's rotation rate. Therefore, Eq. A.5 writes as a set of coupled differential equations (2nd order ODE),

$$\begin{cases} \ddot{x} = 2\Omega_z \dot{y} \\ \ddot{y} = 2\Omega_x \dot{z} - 2\Omega_z \dot{x} \\ \ddot{z} = -g - 2\Omega_x \dot{y} \end{cases} \tag{A.7}$$

[1] Marion, J. B. Classical Dynamics of Particles and Systems: Chapter 12.

ICs We use a general form of initial conditions:

$$\begin{cases} \dot{\mathbf{r}}_0 = (\dot{x}_0, \dot{y}_0, \dot{z}_0) \\ \mathbf{r}_0 = (x_0, y_0, z_0) \end{cases} \tag{A.8}$$

Solving the ODE system: One can use Laplace transform to solve exactly (Eq A.2.a). We can make the passage to the s-domain using this transformation:

$$\begin{aligned} \mathcal{L}\{y'\} &= sY(s) - y(0) \\ \mathcal{L}\{y''\} &= s^2 Y(s) - sy(0) - y'(0) \end{aligned}$$

This transforms Eqs A.2.a to,

$$\begin{pmatrix} s^2 & -2\Omega_z s & 0 \\ -2\Omega_z s & s^2 & -2\Omega_z s \\ 0 & -\Omega_x s & s^2 \end{pmatrix} \begin{pmatrix} X(s) \\ Y(s) \\ Z(s) \end{pmatrix} = \begin{pmatrix} \dot{x}_0 + sx_0 - 2\Omega_z y_0 \\ \dot{y}_0 + sy_0 + 2\Omega_z x_0 - 2\Omega_x z_0 \\ \dot{z}_0 + sz_0 + 2\Omega_x y_0 - \frac{g}{s} \end{pmatrix} \tag{A.9}$$

For the calculations which will follow, I used `SymPy` library in Python to solve this system and then calculated the inverse Laplace transform[1]. These are the resulting temporal coordinates:

$$\begin{cases} x(t) = x_0 + g\frac{\sin(2\lambda)}{4}\left(t^2 - \frac{\sin^2(\Omega t)}{\Omega^2}\right) + \dot{x}_0 \sin^2(\lambda)\frac{\sin(2\Omega t)}{2\Omega} + \dot{y}_0 \sin(\lambda)\frac{\sin^2(\Omega t)}{\Omega} + \dot{z}_0\frac{\sin(2\lambda)}{2}\frac{\sin(2\Omega t)}{2\Omega} \\ y(t) = y_0 + \frac{g\cos(\lambda)}{2\Omega}\left(1 - \frac{\sin(2\Omega t)}{2\Omega}\right) - \dot{x}_0 \sin(\lambda)\frac{\sin^2(\Omega t)}{\Omega} + \dot{y}_0\frac{\sin(2\Omega t)}{2\Omega} - \dot{z}_0 \cos(\lambda)\frac{\sin^2(\Omega t)}{\Omega} \\ z(t) = z_0 - \sin^2(\lambda)\left(\frac{gt^2}{2} - z_0 t\right) - g\cos^2(\lambda)\frac{\sin^2(\Omega t)}{2\Omega^2} + \dot{x}_0\frac{\sin(2\lambda)}{2}\left(\frac{\sin(2\Omega t)}{2\Omega} - t\right) \\ \qquad\qquad + \dot{y}_0 \cos(\lambda)\frac{\sin^2(\Omega t)}{\Omega} + \dot{z}_0 \cos^2(\lambda)\frac{\sin(2\Omega t)}{2\Omega} \end{cases} \tag{A.10}$$

The apogee: The apogee point is reached when $\dot{z}(t) = 0$, this corresponds in our case to time $t = T + t_1$,

$$\dot{z}_0 = \left.\frac{\mathrm{d}z}{\mathrm{d}t}\right|_{T+t_1} = (T + t_1)\, g - 2\Omega \cos(\lambda)\,(T + t_1) + \mathcal{O}\left(\Omega^2\right) \tag{A.11}$$

A.2.b Raman beams

We define the Raman beam vector along the x-axis. Since the Raman beams are tilted with an angle θ_0 (to remove the degeneracy of the $\pm k_{\text{eff}}$), we multiply this vector by rotation matrix around the y-axis of our basis,

$$\mathbf{k}_{\text{eff}} = R_y(\theta_0) \begin{pmatrix} k_{\text{eff}} \\ 0 \\ 0 \end{pmatrix} = \begin{pmatrix} k_{\text{eff}} \cos(\theta_0) \\ 0 \\ k_{\text{eff}} \sin(\theta_0) \end{pmatrix}. \tag{A.12}$$

[1] The code files can be found in my directory in Gyro drive: Data Analysis/Users/Mohamed/Calculs formels Trajectoires.

A.2.c Rotating the experiment

In my approach here, I keep working in the same frame of reference. Therefore, rotating the experiment is equivalent to turning the $\mathbf{k}_{\text{eff}}$ = vector and the initial conditions $(\mathbf{r}_0, \dot{\mathbf{r}}_0)$ with an angle θ_N around the z-axis i.e around local $\mathbf{g}$. Since this angle describes the orientation of the interferometer's area to the north, we do a rotation of $(\frac{\pi}{2} - \theta_N)$ instead, the corresponding rotation matrix is,

$$R_z(\frac{\pi}{2} - \theta_N) = \begin{bmatrix} \sin(\theta_N) & \cos(\theta_N) & 0 \\ -\cos(\theta_N) & \sin(\theta_N) & 0 \\ 0 & 0 & 1 \end{bmatrix} \tag{A.13}$$

A.2.d Phase shift due to the interferometer (pur gyroscope)

During the interaction of the Raman beam with the atoms, the phase of the laser is imprinted on the atomic state. This phase shift is given by[1], $\phi(t) = \mathbf{k}_{\text{eff}}.\mathbf{r}(t)$. For the gyroscope configuration, we use a 4-pulse sequence $\pi/2 - \pi - \pi - \pi/2$ separated by durations of $T/2 - T - T/2$. The inertial phase shift due to such an interferometer is given by,

$$\boxed{\Phi_{\text{Sagnac}} = \phi(t_1) - 2\phi(t_1 + \frac{T}{2}) + 2\phi(t_1 + \frac{3T}{2}) - \phi(t_1 + 2T)} \tag{A.14}$$

Using what we have calculated and by doing a series expansion of the 2^{nd} order of Ω, we the phase due to the Sagnac effect,

$$\boxed{\Phi_{\text{Sagnac}} = \frac{1}{2} k_{\text{eff}} g T^3 \Omega \cos(\lambda) \cos(\theta_0) \cos(\theta_N).} \tag{A.15}$$

A numerical application gives,

$$\Phi_{\text{Sagnac}} = \mathbf{221.554077} \cos(\theta_N) \tag{A.16}$$

A.2.e Higher order terms

a) Experimental measurement simulation:

In the experiment, we introduce a time asymmetry $\mathrm{d}T$ to avoid spurious interferometers, also we change the sign of k_{eff} between measurements (in order to eliminate some phase bias terms: mainly lightshift). Finally, we use a combination of the measured phases to extract the phase due to rotation. This combination is given by:

$$\Phi_{\text{rot}} = \frac{1}{2}\left(\frac{\Phi_{+k}^{+\mathrm{d}T} - \Phi_{-k}^{+\mathrm{d}T}}{2} + \frac{\Phi_{+k}^{-\mathrm{d}T} - \Phi_{-k}^{-\mathrm{d}T}}{2}\right) \tag{A.17}$$

By doing this combination at the 2^{nd} order of Ω, in addition to the Φ_{Sagnac}, an additional term (varies with θ_N) appears,

$$\boxed{\delta\Phi_{\mathrm{d}T} = -2\Omega T \mathrm{d}T^2 g k_{\text{eff}} \cos(\lambda) \cos(\theta_0) \cos(\theta_N)} \tag{A.18}$$

Numerically, the relative contribution

$$\frac{\delta\Phi_{\mathrm{dT}}}{\Phi_{\text{Sagnac}}} = -4\frac{\mathrm{d}T^2}{T^2} = -9 \times 10^{-8} \tag{A.19}$$

[1] Here, $\mathbf{k}_{\text{eff}}$ and $\mathbf{r}(t)$ are the rotated vectors.

b) Introducing non-equal k (NEK)

As studied in the article about NEK[1], The top Raman collimator can be further inclined by a small adjustable angle $\delta\theta$, leading to a different modulus of the effective Raman wave-vector of the top beam, $k_{\text{eff}}^{(T)}$, with respect to the bottom one, $k_{\text{eff}}^{(T)} = k_{\text{eff}}$ without changing its direction:

$$k_{\text{eff}}^{(B)} - k_{\text{eff}}^{(T)} = \pm\epsilon k_{\text{eff}} \tag{A.20}$$

Equation A.14 of the total phase becomes:

$$\Phi_{\text{Sagnac}}^{\text{NEK}} = \phi_1^{(B)} - 2\phi_2^{(T)} + 2\phi_3^{(T)} - \phi_4^{(B)} \tag{A.21}$$

If we do exactly what we have done before: first, we expand to the 2nd order of Ω. I substitute here analytically $\dot{z}_0$ with its expression calculated in equation (A.11) of the apogee. Also I used as an initial condition $\dot{\mathbf{r}}_0 = (\delta\dot{x}_0, \delta\dot{y}_0, \dot{z}_0 + \delta\dot{z}_0)$ to into account the launching velocity errors (The tilt of the experiment, moving molasses, Raman beams timings..., etc). The total phase writes,

$$\boxed{\Phi_{\text{Sagnac}}^{\text{NEK}} = \Phi_{\text{Sagnac}} + \delta\Phi_{\text{d}T} \pm \epsilon\left(\delta\Phi_0 + \delta\Phi_{\dot{z}_0} + \delta\Phi_{\dot{z}_0} + \delta\Phi_{\dot{x}_0}\right)} \tag{A.22}$$

where,

$$\begin{cases} \delta\Phi_0 & = -2k_{\text{eff}}T\cos(\theta_0)\cos\lambda\cos\theta_N g\left[(T+t_1)^2 - \frac{T^2}{12} - \text{d}T^2\right] \\ \delta\Phi_{\delta\dot{z}_0} & = -2k_{\text{eff}}T\cos(\theta_0)\delta\dot{z}_0\left[2\Omega(T+t_1)\cos\lambda\cos\theta_N + \tan\theta_0\right] \\ \delta\Phi_{\delta\dot{y}_0} & = +2k_{\text{eff}}T\cos(\theta_0)\delta\dot{y}_0\left[(\sin\theta_N - 1)\cos\theta_N\sin\theta_N - 2\Omega\,(T+t_1)\sin\lambda\left(\left(\cos^2\theta_N + \sin\theta_N + \frac{\tan\theta_0}{\tan\lambda}\right.\right.\right. \\ \delta\Phi_{\delta\dot{x}_0} & = +2k_{\text{eff}}T\cos(\theta_0)\delta\dot{x}_0\left[2\Omega\,(T+t_1)\sin\lambda\cos\theta_N\left(\cos^2\theta_N + \frac{\tan\theta_0}{\tan\lambda}\right) - \left(\sin^3\theta_N - \sin\theta_N + 1\right)\right] \end{cases} \tag{A.23}$$

Now, if we do a numerical application, we have (I give here the order of magnitude of the coefficients.),

$$\begin{cases} \delta\Phi_0 & = -10^3\cos\theta_N \\ \delta\Phi_{\dot{z}_0} & = \delta\dot{z}_0\left(-6\times10^2\cos\theta_N - 10^6\right) \\ \delta\Phi_{\dot{y}_0} & = \delta\dot{y}_0\left(+7\times10^2\sin^3\theta_N - 6\times10^2\sin\theta_N + 10^7\cos\theta_N\sin\theta_N - 7\times10^2\sin\theta_N + 10^7\cos^3\theta_N - 10\right. \\ \delta\Phi_{\dot{x}_0} & = \delta\dot{x}_0\left(-10^7\sin^3\theta_N + 10^7\sin\theta_N + 7\times10^2\cos^3\theta_N + 50\cos\theta_N - 10^7\right) \end{cases} \tag{A.24}$$

If we are in the presence of an $\epsilon \sim 10^{-5}$, Figure (A.3), shows how the phase shift due to NEK propagates with θ_N for let's say [2] a $\delta v = 0.2$mm/s.

c) Correcting NEK with a symmetric $\text{d}T_s$

In the NEK article, to minimize the phase shift, we introduce a symmetric delay $\text{d}T_s$ for the middle π-pulses,

$$\text{d}T_s = \frac{\epsilon T}{2(1-\epsilon)} \tag{A.25}$$

[1] Sidorenkov, L. A., et al. "Tailoring Multiloop Atom Interferometers with Adjustable Momentum Transfer." PRL 125.21 (2020)

[2] Altorio, M., et al. "Accurate trajectory alignment in cold-atom interferometers with separated laser beams." PRA 101.3 (2020).

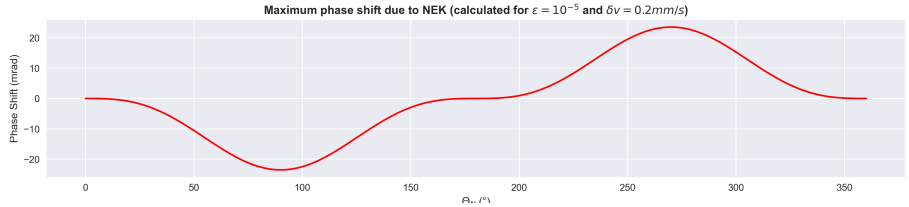

FIGURE A.3: NEK phase shift contribution when rotating the interferometer for an $\epsilon = 10^{-5}$ (positive) and velocity tuning accuaracy of 0.2mm/s.

Therefore, using the coordinates that we have calculated, to verify this result, we do the following,

$$\Phi_{\text{Sagnac}}^{\text{NEK}} = \phi_1^{(B)} - 2\phi_2^{(T)}(-\mathrm{d}T_s) + 2\phi_3^{(T)}(+\mathrm{d}T_s) - \phi_4^{(B)} \tag{A.26}$$

we get,

$$\begin{aligned}\Phi_{\text{Sagnac}}^{\text{NEK}} &= \frac{1}{2}k_{\text{eff}}\Omega g T^3 \cos\theta_0 \cos\lambda \cos\theta_N \left(1 - \frac{2\epsilon}{3}\right) \\ &= \Phi_{\text{Sagnac}} + \delta\Phi_{\mathrm{d}T_s}\end{aligned} \tag{A.27}$$

NEK and Time asymmetry (what we do right now) Now, in the experiment, we do the same configuration as discussed in a) and in addition, we add the time symmetry. Therefore, the measured phase for an $\epsilon \sim 10^{-6}$ is

$$\boxed{\Phi_{\text{Sagnac}}^{\text{NEK/dT}} = \Phi_{\text{Sagnac}} + \delta\Phi_{\mathrm{d}T_s} + \delta\Phi_{\mathrm{d}T_s} = \mathbf{221.553910}\cos\theta_N} \tag{A.28}$$

The relative contribution of the last two terms is

$$\frac{\delta\Phi_{\mathrm{d}T} + \delta\Phi_{\mathrm{d}T_s}}{\Phi_{\text{Sagnac}}} = -4\frac{\mathrm{d}T}{T^2} - \frac{2\epsilon}{3}. \tag{A.29}$$

Appendix B

Sensitivity function for rotations

B.1 Time domain

Let's consider a rotation in the interferometer's area plane with a small angle $\delta\theta$ about a center of rotation $\mathcal{O}$. We define L as the distance from the center of the two Raman collimators, which are separated with a distance $2d = \frac{3}{8}gT^2$ (Eq.III.2.c), to the z-component of $\mathcal{O}$ as depicted in Figure B.1.a.

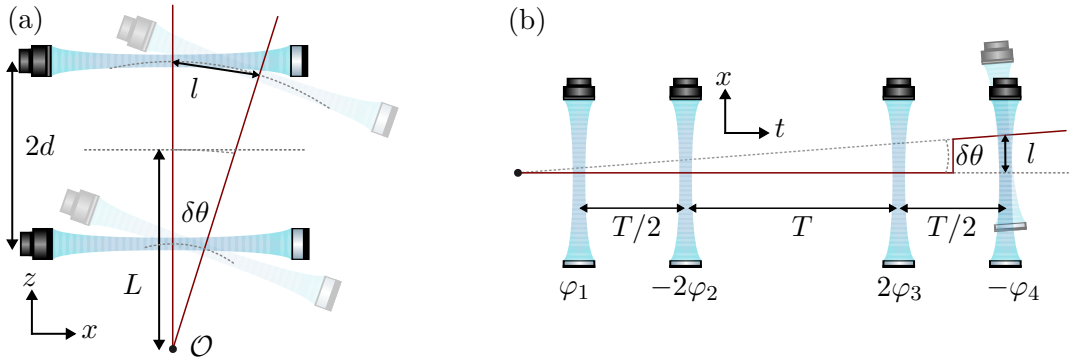

FIGURE B.1: (**a**) Raman collimators under rotation about $\mathcal{O}$. (**b**) The effect of a rotation that occurs at a time t between the last two pulses.

This will change the position of the equiphases of a Raman beam by a quantity l given by:

$$l = 2(L \pm d)\sin\frac{\delta\theta}{2} \approx (L \pm d)\delta\theta \tag{B.1}$$

where we have $+d$ for the top collimator and $-d$ for the bottom one. Given the total phase of the interferometer (Eq. II.48),

$$\Delta\Phi = \varphi(-T) - 2\varphi(-\frac{T}{2}) + 2\varphi(\frac{T}{2}) - \varphi(T) \tag{B.2}$$

$$= k_{\text{eff}}\left(x_1^B - 2x_2^T + 2x_3^T - x_4^B\right), \tag{B.3}$$

the sensitivity function $g_\theta(t)$ is given by

$$g_\theta(t) = \lim_{\delta\theta\to 0}\frac{\delta\Delta\Phi(\delta\theta)}{\delta\theta}. \tag{B.4}$$

For example, if the angle changes between the third and the last pulse (Figure B.1.b), only the last phase is affected and we get,

$$\Delta\Phi \to \Delta\Phi - k_{\text{eff}}(L-d)\delta\theta. \tag{B.5}$$

Therefore, the sensitivity function is calculated to be:

$$g_\theta(t) = k_{\text{eff}}(d-L)\begin{cases} 1 & \text{if } t \in [-T,-T/2] \\ 1+2\frac{d+L}{d-L} & \text{if } t \in [-T/2,T/2] \\ 1 & \text{if } t \in [T/2,T] \\ 0 & \text{otherwise} \end{cases} \tag{B.6}$$

B.2 Frequency Domain

We can write the angle $\delta\theta$ as a sinusoidal perturbation,

$$\delta\theta(t,\omega) = \sqrt{2}\frac{\Omega_\omega}{\omega}\cos(\omega t + \psi). \tag{B.7}$$

The resultant phase perturbation is written as:

$$\delta\Delta\Phi(\omega) = k_{\text{eff}}\Big[l_B(-T) - 2l_T(-T/2) + 2l_T(T/2) - l_B(T)\Big] \tag{B.8}$$

$$= 8k_{\text{eff}}\sqrt{2}\sin(\psi)\frac{\Omega_\omega}{\omega}\left[d\cos^2\left(\frac{\omega T}{4}\right) + L\sin^2\left(\frac{\omega T}{4}\right)\right]\sin\left(\frac{\omega T}{2}\right) \tag{B.9}$$

The transfer function is obtained by taking the RMS over the random fluctuations of ψ and dividing it by the amplitude Ω_ω:

$$\boxed{|H_\theta(L,\omega)|^2 = 64\frac{k_{\text{eff}}^2}{\omega^2}\left[d\cos^2\left(\frac{\omega T}{4}\right) + L\sin^2\left(\frac{\omega T}{4}\right)\right]^2\sin^2\left(\frac{\omega T}{2}\right).} \tag{B.10}$$

B.3 Sagnac phase derivation

Another approch to calculate the Sagnac phase is by using the sensitivity function in Eq.B.10 by considering slow rotation rates i.e. $\omega T \ll 1$, we have:

$$|H_\theta(L,\omega)| \simeq \frac{3}{4}k_{\text{eff}}gT^3 \tag{B.11}$$

For Earth's rotation-rate for example, we get

$$\Delta\Phi_\Omega \simeq \frac{3}{4}k_{\text{eff}}gT^3\Omega_E, \tag{B.12}$$

which differs from what we calculated using the area of the interferometer in Eq. A.4. This is due to the fact that in addition to rotation, we need to take account for the rotation-induced acceleration seen by atoms in the Raman direction which brings another phase contribution. This phase can be evaluated using Eq. B.2 with $\ddot{\varphi}(t) = k_{\text{eff}}g\sin\delta\theta(t) \simeq k_{\text{eff}}g\delta\theta(t)$. After integration we find:

$$\Delta\Phi_{\text{acc}} \simeq -\frac{1}{4}k_{\text{eff}}gT^3\Omega_E \tag{B.13}$$

With that, we find the expression for the Sagnac phase,

$$\Delta\Phi_{\mathrm{rot}} = \Delta\Phi_{\Omega} + \Delta\Phi_{\mathrm{acc}} = \frac{1}{2} k_{\mathrm{eff}} g T^3 \Omega_E. \tag{B.14}$$

Appendix C

Publications

C.1 Papers

Accurate measurement of the Sagnac effect for matter waves
R. Gautier, M. Guessoum, L. A. Sidorenkov, Q. Bouton, A. Landragin, R. Geiger.
Science Advances. 10.1126/sciadv.abn8009

> During my first year, I assisted the Sagnac measurement campaign detailed in Chapter IV. I contributed to preparing the experimental setup, automating tilt adjustments, data acquisition, analysis of the data, investigating systematic effects, designing visualization figures and participating in the editing process.

Real-time control of the phase of an atom interferometer for the double diffraction regime
M. Guessoum, N. Marlière, C. Charfan, A. Landragin, R. Geiger.
In preparation...

C.2 Conferences

Test of the Sagnac Effect by Accurate Measurements with a Dual-Axis Cold-Atom Gyroscope (Oral presentation)
R. Gautier, M. Guessoum, L. A. Sidorenkov, Q. Bouton, A. Landragin, R. Geiger.
EFTF & the IEEE IFCS joint conference (Paris 2022) - Paper Id: 5244
Paris, France (Apr 24-28, 2022)

Dual-Axis Cold-Atom Gyroscope (Poster)
R. Gautier, M. Guessoum, L. A. Sidorenkov, Q. Bouton, A. Landragin, R. Geiger.
IEEE International Symposium on Inertial Sensors & Systems (Avignon 2022)
Avignon, France (May 8-11, 2022)

SCIENCE ADVANCES | RESEARCH ARTICLE

PHYSICS

Accurate measurement of the Sagnac effect for matter waves

Romain Gautier, Mohamed Guessoum, Leonid A. Sidorenkov, Quentin Bouton, Arnaud Landragin, Remi Geiger*

A rotating interferometer with paths that enclose a physical area exhibits a phase shift proportional to this area and to the rotation rate of the frame. Understanding the origin of this so-called Sagnac effect has played a key role in the establishment of the theory of relativity and has pushed for the development of precision optical interferometers. The fundamental importance of the Sagnac effect motivated the realization of experiments to test its validity for waves beyond optical, but precision measurements remained a challenge. Here, we report the accurate test of the Sagnac effect for matter waves, by using a Cesium atom interferometer featuring a geometrical area of 11 cm^2 and two sensitive axes of measurements. We measure the phase shift induced by Earth's rotation and find agreement with the theoretical prediction at an accuracy level of 25 parts per million. Beyond the importance for fundamental physics, our work opens practical applications in seismology and geodesy.

INTRODUCTION

The study of the effect of rotations on interferometers dates back to the late 19th century and is intimately tied to the development of the theory of relativity. In 1913, Georges Sagnac was the first to report an experimental observation of the shift of the fringes in an interferometer subject to a constant rotation rate and its interpretation in the framework of an eather theory (*1*–*3*). Observing the small phase shift induced by Earth's rotation motivated Michelson, Gale, and Pearson (*4*) to build an interferometer of 0.2-km^2 area; in 1925, they reported a measurement of the predicted effect with 3% accuracy. The advent of the laser boosted the development of gyroscopes based on the Sagnac effect with the realization of ring laser gyroscopes (*5*) and later of fiber optical gyroscopes (*6*, *7*), which are a key component of modern navigation systems.

The importance of understanding the fundamental nature of the Sagnac effect for the development of modern physics has motivated the realization of rotating interferometers of increasing precision involving other-than-optical waves. Observations were subsequently made with various systems, starting with superconducting electrons (*8*) as one of the first demonstration of a macroscopic matter wave coherence in superconductors. It was followed by measurements with neutral particles: first with neutrons (*9*) and then with thermal atoms (*10*), where the Sagnac effect was found to be in good agreement with theory. A measurement with electron jet (*11*) has extended its validity toward matter waves of free charged particles. Study of the Sagnac effect in superfluid quantum liquids [helium 4 (*12*) and helium 3 (*13*)] and gases [Bose-Enstein Condensate (BEC) (*14*)] has illustrated its universality. These proof-of-principle experiments served to underline the relativistic nature of the Sagnac effect. The first precision measurement was done in 1997, with a reported accuracy of 1% for a thermal matter wave interferometer (*15*). Development of cold atom experiments allowed for measurements of increasing precision (*16*, *17*) up to 0.05% preceding this work.

According to the Sagnac effect, the phase shift in an interferometer of oriented area $\vec{\mathcal{A}}$ and subject to a constant rotation rate $\vec{\Omega}$ can be expressed as

$$\Phi_\Omega = \frac{4\pi E}{hc^2}\vec{\mathcal{A}}\cdot\vec{\Omega} \tag{1}$$

where E is the total energy of the interfering particle, and h is the Planck's constant ($E = h\nu$ for photons, $E \simeq mc^2$ for slow massive particles). Precisely testing the validity of this equation requires an accurate knowledge of the interferometer geometry (i.e., of the area vector $\vec{\mathcal{A}}$) and of the rotation rate ($\vec{\Omega}$). Exploiting Earth's rotation, which is known with high accuracy, meets the latter requirement. However, precisely controlling the geometry of a matter wave interferometer of large area (i.e., of high sensitivity) remains a challenge; for example, the accuracy of superfluid helium interferometers has been barely assessed (*18*), while neutron interferometers could test Eq. 1 at best with 0.4% accuracy (*9*).

Cold-atom interferometers feature a high degree of accuracy owing to the good knowledge of the light-matter interaction process exploited to realize the interferometer building blocks, which offers the possibility to quantify the interferometer scale factor using frequency measurements (*19*, *20*). Here, we use a two-axis cold-cesium atom interferometer with a macroscopic area $\mathcal{A} \simeq 11$ cm^2 (in each direction) rotated by Earth. Our measurements confirm the prediction of Eq. 1 with an accuracy of 25 parts per million (ppm), which represents an improvement of more than 20 compared with previous experiments (*16*, *17*) and allows us to place a constraint on Gödel's model of a rotating universe (*21*). Moreover, the ability to accurately determine the scale factor of our gyroscope combined with its relative compactness and control of its area orientation [compared with giant ring laser gyroscopes (*22*)] opens practical applications in seismology and geodesy. The configuration of our instrument has advantages over other geometries of cold atom gyroscopes. Its single source folded interferometer rejects accelerations while preventing systematic errors because of trajectory mismatch in twin atom source sensors (*16*, *23*–*25*). Our sensor offers substantial sensitivity gain compared with that of compact atomic gyroscopes (*26*–*28*), allowing us to test the Sagnac effect due to Earth's rotation with the accuracy level reported in this work.

LNE-SYRTE, Observatoire de Paris-Université PSL, CNRS, Sorbonne Université 61 avenue de l'Observatoire, 75014 Paris, France.
*Corresponding author. Email: remi.geiger@obspm.fr

RESULTS

The core of our experiment and its principle are illustrated in Fig. 1 and have been described in previous works (*29*, *30*) and summarized in Materials and Methods. The interferometric sequence comprises four Raman pulses of Rabi area $\pi/2$, π, π, $\pi/2$ occurring at times $t \simeq (0, T/2, 3T/2, 2T)$, with $T \simeq 400$ ms.

The two-photon Raman transition transfers a momentum $\hbar\vec{k}_{\mathrm{eff}}$ to the deflected atom, which, together with the action of gravity acceleration $\vec{g}$ along the path, results in an interferometer area (for perfectly parallel Raman beams)

$$\vec{\mathcal{A}} = \frac{T^3}{4}\frac{\hbar}{m}\vec{k}_{\mathrm{eff}} \times \vec{g} \tag{2}$$

With the total energy of the interfering atom given by $E \simeq mc^2$ (valid for atoms moving much slower than light), the Sagnac phase shift becomes

$$\Phi_\Omega = \frac{T^3}{2}(\vec{k}_{\mathrm{eff}} \times \vec{g}) \cdot \vec{\Omega} \tag{3}$$

The Raman beams are set to an angle θ_0 with respect to the horizontal plane (perpendicular to $\vec{g}$) to lift the degeneracy associated with the two possible directions of momentum transfer and thereby choose the direction of atom diffraction $[\pm\vec{k}_{\mathrm{eff}}]$. The vector product is then expressed as $\vec{k}_{\mathrm{eff}} \times \vec{g} = k_{\mathrm{eff}} g \cos(\theta_0)\vec{n}$, where $\vec{n}$ is a unit vector in the direction of interferometric area $(\vec{\mathcal{A}}/|\vec{\mathcal{A}}|)$ lying in the horizontal plane.

The experiment is placed on a rotation stage, which allows us to change the angle between $\vec{n}$ and the angular velocity of the Earth $\vec{\Omega}$ pointing from south to north. The rotation angle Θ can be varied within 2π with μrad accuracy, thus permitting a precision measurement that is not limited by uncertainty in positioning of the north.

The Sagnac phase shift can therefore be explicitly written in terms of the control parameters as

$$\Phi_\Omega(\Theta) = \frac{T^3}{2} k_{\mathrm{eff}} g \cos(\theta_0) \times \cos(\psi)\,\Omega_E \times \cos(\Theta - \Theta_N) \tag{4}$$

where Ω_E is the modulus of the Earth rotation vector, ψ is the astronomic latitude at the position where the experiment is performed on the site of Paris Observatory, and Θ_N is the angle of the rotation stage corresponding to geographical north.

We realize two independent measurements with Raman beams oriented in the X and Y directions, i.e., with interferometer areas perpendicular to each other (Fig. 1). The two interferometers operate on the same physical principle (Eq. 3) but with different scale factor and bias term, thus increasing our confidence in the final result.

The phase shift measured at the output of the atom interferometer, Φ, is dominated by the rotation-induced Sagnac term of interest (of the order of 200 rad) and contains other bias terms on the order of a few tens of mrad detailed in Materials and Methods.

Figure 2 shows a typical measurement of the phase shift of the atom interferometer for both directions, acquired during 1 week in April 2021. Despite the interferometer measuring a phase shift modulo 2π in a given orientation, the complete 360° variation of the

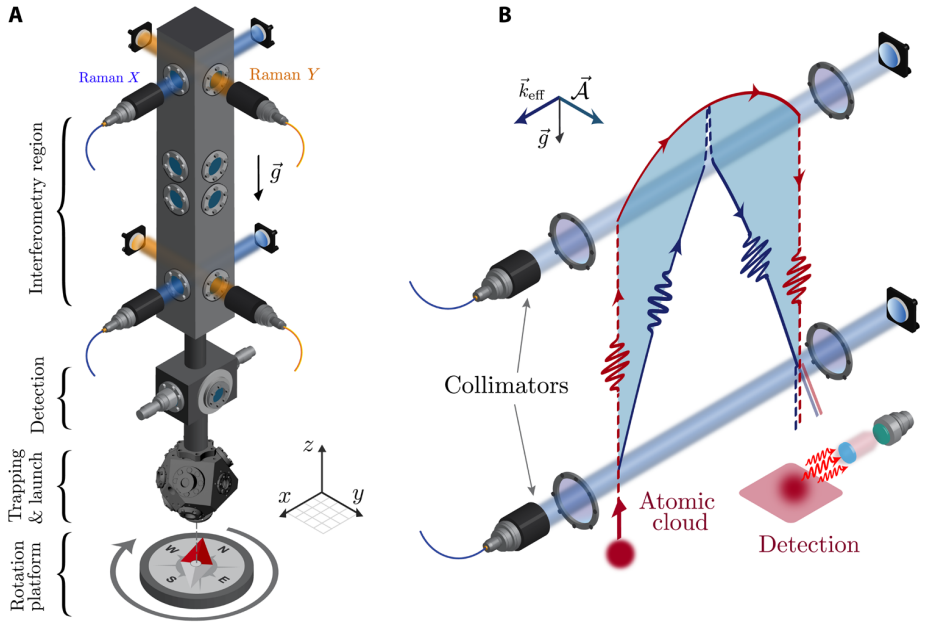

Fig. 1. Principle of the experiment. (**A**) Schematic of the sensor head. In the lower part of the vacuum chamber, the cesium atoms are laser cooled and trapped in a magneto-optical trap (MOT), and then launched vertically in the hyperfine state $F = 4$. Subsequently, the atoms enter the interferometer where a sequence of four Raman transitions is driven by retro-reflected laser beams at the top and the bottom of the upper part of the vacuum chamber. The interferometer can be operated either in the X (blue beams) or Y (orange beams) direction. At the output of the interferometer, the probability for an atom to occupy one of the two internal states $F = 3$ and $F = 4$ is measured by fluorescence detection. The experiment is placed on a rotation stage that allows us to vary the projection of the oriented interferometer area on the Earth rotation vector. (**B**) Schematic of the wave packet propagation in the interferometer (here in the X direction, not to scale). The red and blue lines show the two distinct paths of the splitted matter waves enclosing a physical area, underlined by the cyan color. Dashed and plain lines encode the two internal states of the atom.

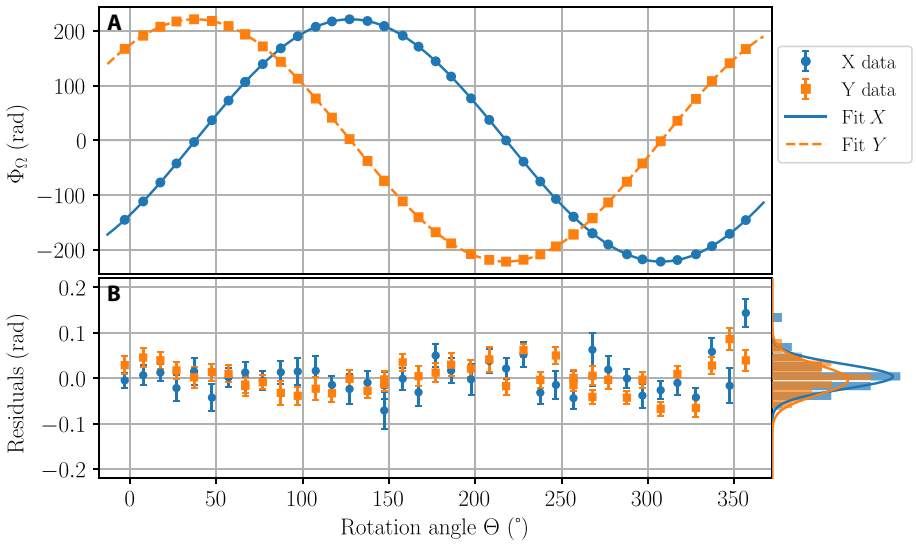

Fig. 2. Measurement of the Sagnac phase shift with the two-axis atom interferometer. (**A**) Phase shift acquired for the *X* (blue dots) and *Y* (orange squares) directions as a function of the rotation angle Θ. Each point is a mean of typically 1500 realizations, with statistical error smaller than the symbol size. Lines are the least-squares fits with Eq. (5). (**B**) Difference between the data and the fits for *X* (blue dots) and *Y* (orange squares). Statistical error of each point is on the order of 30 mrad, and the histogram of the residuals (projected on the right side) has an SD of 40 mrad.

rotation angle allows us to unambiguously "unfold" the full ~200 rad dephasing (see the Supplementary Materials). The data are fitted with

$$\Phi_\Omega^{x,y}(\Theta) = \Phi_0^{x,y}\cos\left(\Theta - \Theta_N^{x,y}\right) + B^{x,y} \quad (5)$$

where $\Phi_0^{x,y}$, $\Theta_N^{x,y}$, and $B^{x,y}$ are free parameters (three for each direction). We extract $\Phi_0^x = 221.572(9)$ rad and $\Phi_0^y = 221.545(9)$ rad with fit residuals characterized by histograms with Gaussian width of about 40 mrad, comparable with the error bar of the individual points. Additional deviation in fit residuals can be explained by slow drifts of the bias during the measurement (see the Supplementary Materials). The extracted relative angular mismatch of the *X* and *Y* directions from being perfectly orthogonal is found to be 0.7(1) mrad, compatible with mechanical tolerance on the orthogonality of the sides of the vacuum chamber.

We now estimate the gyroscope scale factor for both directions (*X* and *Y*), i.e., evaluate the parameters entering Eq. 4. As we will show, all the parameters can be determined solely by frequency (or time) measurements, i.e., with high accuracy.

We measured the angle $\theta_0^{x,y}$ with the four-pulse interferometer by exploiting its residual sensitivity to continuous accelerations (see the Supplementary Materials) and obtained $\theta_0^x = 4.0750(5)°$ and $\theta_0^y = 4.1251(3)°$. The interrogation time is derived from the clock of the experimental control system that is referenced to a highly stable and reproducible frequency standard. To check for small possible systematic deviations, we measure the time interval between the Raman pulses with a high-speed oscilloscope and find a value $T = 400.0020(1)$ ms, with error bar limited by available temporal resolution. The local gravity acceleration value *g* has been previously measured in the laboratory using a transportable cold atom gravimeter. Since the value of *g* was affected by tides during the present measurement campaign, we take the maximal annual tide-induced variation of 3×10^{-6} m s^{-2} as an upper bound for the uncertainty on the value of *g*.

Table 1. Error budget for the determination of theoretical Sagnac phase shift. The table lists the parameters entering the scale factor of the cold atom gyroscope. The right column is the uncertainty on the scale factor resulting from error propagation on each parameters.

Parameter	*X*	*Y*	Relative uncertainty (ppm)
k_{eff}	14743247.08(4) m^{-1}		0.003
T	400.0020(1) ms		0.75
g	9.809279(3) m s^{-2}		0.3
θ_0	4.0750(5)°	4.1251(3)°	0.6 | 0.4
ϵ	$-1.7(1) \times 10^{-6}$	$-9.3(2) \times 10^{-6}$	0.07 | 0.13
ψ	48.83587(3)°		0.6
Ω_E	$7.2921150(1) \times 10^{-5}$ rad s^{-1}		0.01
Theoretical Sagnac phase	221.5702(3) rad	221.5574(2) rad	1.2 | 1.1

At the level of accuracy of typically 50 ppm (as demonstrated by the presented single dataset), we must account for the fact that the modulus of the wave vectors for the bottom $[k_{eff}^{(B)}]$ and top $[k_{eff}^{(T)}]$ Raman beams might differ by $\Delta k_{eff} \equiv k_{eff}^{(B)} - k_{eff}^{(T)}$, which introduces a correction to Eq. 4 at first order in $\epsilon = \Delta k_{eff}/k_{eff}$ (*31*).

We measure the values of $\epsilon^{x,y}$ via an interferometric measurement as explained in the Supplementary Materials, leading to $\epsilon^x = 0.7(9) \times 10^{-6}$ and $\epsilon^y = 6.0(9) \times 10^{-6}$.

We evaluate the astronomical latitude ψ—the angle between the local vertical (i.e., the vector perpendicular to the geoid) and the

equatorial plane. It differs from the geographic latitude by the vertical north deflection, which can reach several arc seconds in regions where the geoid deviates noticeably from the ellipsoid of reference (e.g., close to mountains). Our experiment is positioned in a room of the Paris Observatory, at the geographic latitude of 48.83561(2)°. The vertical deflection was estimated to +0.95(4)″, yielding ψ = 48.83587(3)°.

Second order ($\propto\Omega^2$), recoil [$\propto \hbar^2 k_{\mathrm{eff}}^2/(2m)$], and other residual terms appear in the expression of the Sagnac phase shift when the full calculation is developed (see the Supplementary Materials). These contributions would correspond to a relative correction of a few 10^{-7} to the estimation of the scale factor, which is two orders of magnitude below the accuracy of our measurement and have thus been neglected in this study.

Table 1 summarizes the measurements of the parameters for both directions. On the basis of these measurements, we estimate the theoretical values for the Sagnac phase shift as Φ^x_{theo} = 221.5702(3) rad and Φ^y_{theo} = 221.5574(2) rad.

To reinforce the overall confidence in our measurements, we acquired six full-turn data from April to June 2021 and with different experimental parameters (e.g., variation of interrogation time T). We applied identical data treatment and fitting procedures (as described above) to all datasets and extracted corresponding fit parameters $\Phi_0^{x,y}$ (see the Supplementary Materials for the raw data and full fit results). In Fig. 3, we present the differences between the measured values and the corresponding theoretical expectations, $\delta\Phi^{x,y} = \Phi_0^{x,y} - \Phi_{\mathrm{theo}}^{x,y}$.

The results have an overall good agreement, with a mean value close to zero (horizontal dashed line) and a standard error on the mean covering a substantial part of the data (gray-shaded region). The dispersion between the measurements is not fully captured by the uncertainties in fitted values of $\Phi_0^{x,y}$ of the corresponding datasets. We show in the Supplementary Materials with additional simulations that the deviations are consistent with a residual shift of the bias during the week-long measurements necessary to rotate the experiment. In conclusion, the data are consistent with the Sagnac phase shift prediction within an uncertainty of 25 ppm, dominated by the statistical uncertainty.

DISCUSSION

The fundamental interest in our cold atom interferometer relies on its ability to measure several components of the local angular velocity and to explore rotational signals along different directions, in contrast to large ring laser gyroscope infrastructures where the gyroscope axes are fixed. This allows search for smaller signals beyond Earth's rotation: In addition to local angular velocities induced by geological origins, one can constrain astrophysical rotations (orbit in the solar system, rotation in the Galaxy) or even rotations related to the fundamental structure of the universe. As shown in (*21*), Gödel's model of the universe predicts a global rotation rate inducing a Sagnac phase shift. The mass density of the universe inferred from the 2018 Planck mission data (*32*) corresponds to a rotation rate of the order 10^{-19} rad s^{-1}, far beyond the accuracy of current gyroscopes. However, the accuracy of our experiment gives an upper limit on the Gödel's rotation obtained for matter waves (instead of photons in the case of the Planck mission) in a local measurement. From another point of view, the ability to detect signals at different frequencies in the experiment is a powerful tool to explore violation of Lorentz invariance. Following (*33*), our experiment might put constraints on parameters of alternative theories such as the standard model extension.

In addition, the precise knowledge of the scale factor of our gyroscope together with that of Earth's rotation rate allows us to perform measurements of the vertical deflection at the level of few arc seconds. This provides a measure of the local gravity direction that depends on local mass anomalies. Accurate knowledge of the vertical deflection (which can amount to angles of a few arc seconds in flat areas and up to 50″ in mountainous terrain) is widely used in geodesy and for geophysical purposes. A high-accuracy gyroscope such as ours allows to measure at least the north-south component of the vertical deflection in the zones where astronomical determination is impossible, e.g., for geodesy and geographical positioning in underground facilities.

Our work paves the way toward applications in rotational seismology, a field that studies rotational motions induced by earthquakes, explosions, and ambient vibrations (*34*), of interest for the understanding of the underground structure (*35*) or seismic hazard assessment in civil engineering (*36*). Theoretical studies have shown the benefit of using precision rotational sensing to improve the characterization of earthquake sources (*37*) and their localization (*38*)—the information of prime importance for seismic alert systems.

Accurate assessment of ground rotational signals is also of prime importance in the development of ground-based gravitational wave detectors, which is expected to be limited at low frequencies

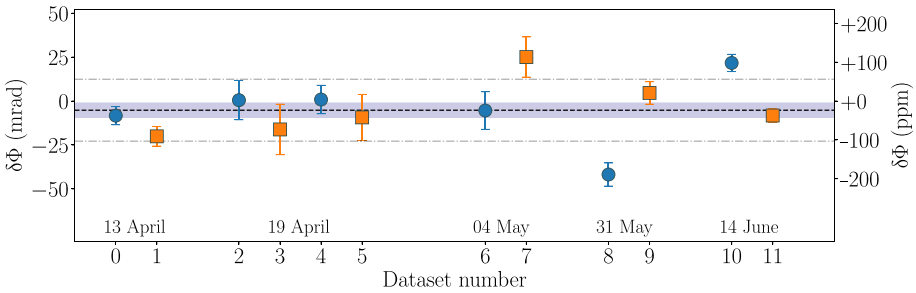

Fig. 3. Comparison between experiment and theory. The data points represent the difference between the measured gyroscope phase shift and the theoretical Sagnac phase shift. Blue points (orange squares) are the data for the *X* (*Y*) axis. The dashed line represents the mean value of all the data (*X* and *Y*), and the shaded region is the standard error on the mean. Point-dashed lines indicates the SD on the set of measurement. The week of dataset acquisition (during year 2021) is indicated at the bottom along with the dataset number.

(below 1 Hz) by Newtonian noise (*39*, *40*) and rotational ground motion (*41*). Measuring and compensating these effects requires highly sensitive and accurate rotational sensors on the level of performances of our instrument (*42*).

These measurements at geophysical sites of interest require transportable gyroscopes with scale factors that are stable over weeks and are known with high accuracy (better than 100 ppm). While fiber optic gyroscopes (*43*) have been particularly developed and deployed for rotational seismology applications, reaching such stability and accuracy levels is challenging. Our cold atom sensor could lead to a transportable laboratory instrument (*44*) or even to an industrial product with increased robustness against environmental instabilities (temperature, vibrations, etc.), as achieved for cold atom gravimeters (*45*). A specific effort should address the control of the bias drift of our gyroscope because of the fluctuations of atomic trajectory coupled to relative mirror misalignment (*46*), which appeared as a limiting factor in the present work (see the Supplementary Materials). Provided with such proper engineering, the level of accuracy reported by our work opens a field of applications, with major scientific and societal impacts.

MATERIALS AND METHODS

Preparation of the atoms

Cesium atoms laser cooled to a temperature of 1.8 μK are launched vertically in a fountain configuration at a velocity of 5 m s^{-1}. After a quantum state selection in the least sensitive magnetic sublevel $|m_F = 0\rangle$, the atoms enter the light-pulse interferometer, where a sequence of stimulated two-photon Raman transitions split, deflect, and recombine the atomic de Broglie waves.

At the output of the interferometer, the phase difference between the two paths is inferred by measuring the internal state (entangled with the external state) populations of the atoms via fluorescence detection. We operate the interferometer in joint mode (*29*) such that the time of a full cycle equals the total interrogation time $2T \simeq 800$ ms.

Alignment of the interferometer

We use a dedicated alignment protocol (*46*) that allows setting the atomic launch velocity parallel to vertical (local $\vec{g}$) with an accuracy of typically 200 μrad. Once set, this alignment is preserved upon variation of the rotation angle during the full-turn acquisition by actively stabilizing the sensor's tilt at the nrad level during the acquisition (see the Supplementary Materials).

Phase shift of the interferometer

We write the total phase shift at the output of the interferometer as $\Phi = \Phi_\Omega + \Phi_1 + \Phi_2$, where Φ_1 and Φ_2, respectively, encode $\vec{k}_{\text{eff}}$-independent and $\vec{k}_{\text{eff}}$-dependent bias phase shifts. The contribution of Φ_1 is mostly due to the one-photon lightshift and is maintained below 10 mrad by alternating measurements every cycle between $+k_{\text{eff}}$ and $-k_{\text{eff}}$ and computing the half-difference between the data (see the Supplementary Materials).

The most important terms contributing to Φ_2 are (i) a continuous accelerations–induced phase shift (*17*, *31*) and (ii) a phase shift associated with the imperfect alignment of the bottom and top mirrors retro-reflecting the Raman beams (see Fig. 1) coupled to imperfect launching of the atoms along gravity (*46*). We recall in the Supplementary Materials the origin of these phase shifts and explain the methods used to mitigate their contribution all along the measurements, for both the X and Y directions.

SUPPLEMENTARY MATERIALS

Supplementary material for this article is available at https://science.org/doi/10.1126/sciadv.abn8009

REFERENCES AND NOTES

1. G. Sagnac, L'éther lumineux démontré par l'effet du vent relatif d'éther dans un interféromètre en rotation uniforme. *C. R. Acad. Sci. (Paris)* **157**, 708–710 (1913).
2. E. J. Post, Sagnac effect. *Rev. Mod. Phys.* **39**, 475–493 (1967).
3. R. Anderson, H. R. Bilger, G. E. Stedman, "Sagnac" effect: A century of Earth-rotated interferometers. *Am. J. Phys.* **62**, 975–985 (1994).
4. A. A. Michelson, H. G. Gale, The effect of the Earth's rotation on the velocity of light, II. *ApJ* **61**, 140 (1925).
5. W. M. Macek, D. T. M. Davis Jr., Rotation rate sensing with traveling-wave ring lasers. *Appl. Phys. Lett.* **2**, 67–68 (1963).
6. V. Vali, R. W. Shorthill, Fiber ring interferometer. *Appl. Optics* **15**, 1099–1100 (1976).
7. H. C. Lefèvre, The fiber-optic gyroscope, a century after Sagnac's experiment: The ultimate rotation-sensing technology? *C. R. Phys.* **15**, 851–858 (2014).
8. J. E. Zimmerman, J. E. Mercereau, Compton wavelength of superconducting electrons. *Phys. Rev. Lett.* **14**, 887–888 (1965).
9. S. A. Werner, J.-L. Staudenmann, R. Colella, Effect of Earth's rotation on the quantum mechanical phase of the neutron. *Phys. Rev. Lett.* **42**, 1103–1106 (1979).
10. F. Riehle, T. Kisters, A. Witte, J. Helmcke, C. J. Bordé, Optical ramsey spectroscopy in a rotating frame: Sagnac effect in a matter-wave interferometer. *Phys. Rev. Lett.* **67**, 177–180 (1991).
11. F. Hasselbach, M. Nicklaus, Sagnac experiment with electrons: Observation of the rotational phase shift of electron waves in vacuum. *Phys. Rev. A* **48**, 143–151 (1993).
12. K. Schwab, N. Bruckner, R. E. Packard, Detection of the Earth's rotation using superfluid phase coherence. *Nature* **386**, 585–587 (1997).
13. R. W. Simmonds, A. Marchenkov, E. Hoskinson, J. C. Davis, R. E. Packard, Quantum interference of superfluid 3he. *Nature* **412**, 55–58 (2001).
14. K. C. Wright, R. B. Blakestad, C. J. Lobb, W. D. Phillips, G. K. Campbell, Driving phase slips in a superfluid atom circuit with a rotating weak link. *Phys. Rev. Lett.* **110**, 025302 (2013).
15. A. Lenef, T. Hammond, E. Smith, M. Chapman, R. Rubenstein, D. E. Pritchard, Rotation sensing with an atom interferometer. *Phys. Rev. Lett.* **78**, 760–763 (1997).
16. A. Gauguet, B. Canuel, T. Lévèque, W. Chaibi, A. Landragin, Characterization and limits of a cold-atom Sagnac interferometer. *Phys. Rev. A* **80**, 063604 (2009).
17. J. K. Stockton, K. Takase, M. A. Kasevich, Absolute geodetic rotation measurement using atom interferometry. *Phys. Rev. Lett.* **107**, 133001 (2011).
18. Y. Sato, Sagnac-based rotation sensing with superfluid helium quantum interference devices. *C. R. Phys.* **15**, 898–906 (2014).
19. B. Barrett, R. Geiger, I. Dutta, M. Meunier, B. Canuel, A. Gauguet, P. Bouyer, A. Landragin, The Sagnac effect: 20 years of development in matter-wave interferometry. *C. R. Phys.* **15**, 875–883 (2014).
20. R. Geiger, A. Landragin, S. Merlet, F. Pereira dos Santos, High-accuracy inertial measurements with cold-atom sensors. *AVS Quantum Sci.* **2**, 024702 (2020).
21. A. Delgado, W. P. Schleich, G. Süssmann, Quantum gyroscopes and Gödel's universe: Entanglement opens a new testing ground for cosmology. *New J. Phys.* **4**, 37–37 (2002).
22. A. Gebauer, M. Tercjak, K. U. Schreiber, H. Igel, J. Kodet, U. Hugentobler, J. Wassermann, F. Bernauer, C.-J. Lin, S. Donner, S. Egdorf, A. Simonelli, J.-P. R. Wells, Reconstruction of the instantaneous earth rotation vector with sub-arcsecond resolution using a large scale ring laser array. *Phys. Rev. Lett.* **125**, 033605 (2020).
23. P. Berg, S. Abend, G. Tackmann, C. Schubert, E. Giese, W. P. Schleich, F. A. Narducci, W. Ertmer, E. M. Rasel, Composite-light-pulse technique for high-precision atom interferometry. *Phys. Rev. Lett.* **114**, 063002 (2015).
24. A. V. Rakholia, H. J. McGuinness, G. W. Biedermann, Dual-axis high-data-rate atom interferometer via cold ensemble exchange. *Phys. Rev. Appl.* **2**, 054012 (2014).
25. Z.-W. Yao, H.-H. Chen, S.-B. Lu, R.-B. Li, Z.-X. Lu, X.-L. Chen, G.-H. Yu, M. Jiang, C. Sun, W.-T. Ni, J. Wang, M.-S. Zhan, Self-alignment of a large-area dual-atom-interferometer gyroscope using parameter-decoupled phase-seeking calibrations. *Phys. Rev. A* **103**, 023319 (2021).
26. Y.-J. Chen, A. Hansen, G. W. Hoth, E. Ivanov, B. Pelle, J. Kitching, E. A. Donley, Single-source multiaxis cold-atom interferometer in a centimeter-scale cell. *Phys. Rev. Appl.* **12**, 014019 (2019).
27. C. L. G. Alzar, Compact chip-scale guided cold atom gyrometers for inertial navigation: Enabling technologies and design study. *AVS Quantum Sci.* **1**, 014702 (2019).
28. X. Wu, F. Zi, J. Dudley, R. J. Bilotta, P. Canoza, H. Müller, Multiaxis atom interferometry with a single-diode laser and a pyramidal magneto-optical trap. *Optica* **4**, 1545 (2017).

29. I. Dutta, D. Savoie, B. Fang, B. Venon, C. L. Garrido Alzar, R. Geiger, A. Landragin, Continuous cold-atom inertial sensor with 1 nrad/sec rotation stability. *Phys. Rev. Lett.* **116**, 183003 (2016).
30. D. Savoie, M. Altorio, B. Fang, L. A. Sidorenkov, R. Geiger, A. Landragin, Interleaved atom interferometry for high-sensitivity inertial measurements. *Sci. Adv.* **4**, eaau7948 (2018).
31. L. A. Sidorenkov, R. Gautier, M. Altorio, R. Geiger, A. Landragin, Tailoring multiloop atom interferometers with adjustable momentum transfer. *Phys. Rev. Lett.* **125**, 213201 (2020).
32. P. Collaboration, Planck 2018 results. *A&A* **641**, A4 (2020).
33. S. Moseley, N. Scaramuzza, J. D. Tasson, M. L. Trostel, Lorentz violation and Sagnac gyroscopes. *Phys. Rev. D* **100**, 064031 (2019).
34. W. H. K. Lee, Rotational seismology, in *Encyclopedia of Natural Hazards*, P. T. Bobrowsky, Ed. (Springer Netherlands, 2013), pp. 877–879.
35. M. Bernauer, A. Fichtner, H. Igel, Inferring Earth structure from combined measurements of rotational and translational ground motions. *Geophysics* **74**, WCD41–WCD47 (2009).
36. D. Basu, A. S. Whittaker, M. C. Constantinou, Characterizing rotational components of earthquake ground motion using a surface distribution method and response of sample structures. *Eng. Struct.* **99**, 685–707 (2015).
37. S. Donner, M. Bernauer, H. Igel, Inversion for seismic moment tensors combining translational and rotational ground motions. *Geophys. J. Int.* **207**, 562–570 (2016).
38. Z. Li, M. van der Baan, Elastic passive source localization using rotational motion. *Geophys. J. Int.* **211**, 1206–1222 (2017).
39. J. Harms, E. L. Bonilla, M. W. Coughlin, J. Driggers, S. E. Dwyer, D. J. McManus, M. P. Ross, B. J. J. Slagmolen, K. Venkateswara, Observation of a potential future sensitivity limitation from ground motion at LIGO Hanford. *Phys. Rev. D* **101**, 102002 (2020).
40. B. Canuel, S. Abend, P. Amaro-Seoane, F. Badaracco, Q. Beaufils, A. Bertoldi, K. Bongs, P. Bouyer, C. Braxmaier, W. Chaibi, N. Christensen, F. Fitzek, G. Flouris, N. Gaaloul, S. Gaffet, C. L. G. Alzar, R. Geiger, S. Guellati-Khelifa, K. Hammerer, J. Harms, J. Hinderer, M. Holynski, J. Junca, S. Katsanevas, C. Klempt, C. Kozanitis, M. Krutzik, A. Landragin, I. L. Roche, B. Leykauf, Y.-H. Lien, S. Loriani, S. Merlet, M. Merzougui, M. Nofrarias, P. Papadakos, F. P. dos Santos, A. Peters, D. Plexousakis, M. Prevedelli, E. M. Rasel, Y. Rogister, S. Rosat, A. Roura, D. O. Sabulsky, V. Schkolnik, D. Schlippert, C. Schubert, L. Sidorenkov, J.-N. Siemß, C. F. Sopuerta, F. Sorrentino, C. Struckmann, G. M. Tino, G. Tsagkatakis, A. Viceré, W. von Klitzing, L. Woerner, X. Zou, ELGAR—A European laboratory for gravitation and atom-interferometric research. *Class. Quantum Gravity* **37**, 225017 (2020).
41. M. P. Ross, K. Venkateswara, C. Mow-Lowry, S. Cooper, J. Warner, B. Lantz, J. Kissel, H. Radkins, T. Shaffer, R. Mittleman, A. Pele, J. Gundlach, Towards windproofing LIGO: Reducing the effect of wind-driven floor tilt by using rotation sensors in active seismic isolation. *arXiv*, 2003.06447 (2020).
42. B. Lantz, R. Schofield, B. O'Reilly, D. E. Clark, D. DeBra, Review: Requirements for a ground rotation sensor to improve advanced LIGO. *Bull. Seismol. Soc. Am.* **99**, 980–989 (2009).
43. F. Bernauer, J. Wassermann, F. Guattari, A. Frenois, A. Bigueur, A. Gaillot, E. de Toldi, D. Ponceau, U. Schreiber, H. Igel, Blueseis3a: Full characterization of a 3c broadband rotational seismometer. *Seismol. Res. Lett.* **89**, 620–629 (2018).
44. T. Farah, C. Guerlin, A. Landragin, P. Bouyer, S. Gaffet, F. P. dos Santos, S. Merlet, Underground operation at best sensitivity of the mobile LNE-SYRTE cold atom gravimeter. *Gyroscopy Navig.* **5**, 266–274 (2014).
45. V. Ménoret, P. Vermeulen, N. Le Moigne, S. Bonvalot, P. Bouyer, A. Landragin, B. Desruelle, Gravity measurements below 10^{-9} g with a transportable absolute quantum gravimeter. *Sci. Rep.* **8**, 12300 (2018).
46. M. Altorio, L. A. Sidorenkov, R. Gautier, D. Savoie, A. Landragin, R. Geiger, Accurate trajectory alignment in cold-atom interferometers with separated laser beams. *Phys. Rev. A* **101**, 033606 (2020).
47. P. Cheinet, B. Canuel, F. P. dos Santos, A. Gauguet, F. Yver-Leduc, A. Landragin, Measurement of the sensitivity function in a time-domain atomic interferometer. *IEEE Trans. Instrum. Meas.* **57**, 1141–1148 (2008).
48. K. U. Schreiber, T. Klügel, J.-P. R. Wells, R. B. Hurst, A. Gebauer, How to detect the Chandler and the annual wobble of the Earth with a large ring laser gyroscope. *Phys. Rev. Lett.* **107**, 173904 (2011).

Acknowledgments: We thank M. Altorio for contribution at the early stage of this work, M.-C. Angonin and C. Le Poncin-Lafitte for stimulating discussions, and F. Pereira Dos Santos for the careful reading of the manuscript. We thank as well J. Gazeaux of the Service de Géodésie et de Métrologie department of the IGN for giving us the precise value of the North deviation at the location of the Paris Observatory. **Funding:** We acknowledge the financial support from Agence Nationale pour la Recherche (project PIMAI, ANR-18-CE47-0002-01) and Centre National d'Etudes Spatiales (CNES). L.A.S. was funded by Conseil Scientifique de l'Observatoire de Paris (PSL fellowship in astrophysics at Paris Observatory), R.Ga. by the EDPIF doctoral school, and M.G. by SIRTEQ. **Author contributions:** R.Ga., M.G., and L.A.S. performed the experiments. R.Ga., M.G., L.A.S., and Q.B analyzed the data and did the calculations. R.Ge. and A.L. conceived the experiment and supervised the research. R.Ga. and R.Ge. wrote the manuscript, with inputs from all the authors. All authors discussed the manuscript. **Competing interests:** The authors declare that they have no competing interests. **Data and materials availability:** All data needed to evaluate the conclusions in the paper are present in the paper and/or the Supplementary Materials. Data and code are available at https://doi.org/10.5281/zenodo.6372385.

Submitted 20 December 2021
Accepted 27 April 2022
Published 10 June 2022
10.1126/sciadv.abn8009

Test of the Sagnac effect by accurate measurements with a dual-axis cold-atom gyroscope

M. Guessoum, R. Gautier, Q. Bouton, L.A. Sidorenkow, A. Landragin, R. Geiger
Atom Interferometry and Inertial Sensors division
LNE SYRTE, Observatoire de Paris, Université PSL, CNRS, Sorbonne Université
Paris, France
mohamed.guessoum@obspm.fr

Abstract— **The Sagnac effect appears when an interferometer with a physical area is rotated. This results in a measurable phase at the output of the interferometer, which is proportional to both the angular velocity and the area enclosed by the interferometer. As a fundamental principle, it played a crucial role in our understanding of modern physics as we know today. Beside its fundamental aspect, it dragged technological innovations being at the essence of the most sophisticated rotation sensors. Testing precisely the Sagnac effect with matter-waves is now possible thanks to the development of cold-atom interferometers. We report a measurement of the Sagnac phase, induced by the Earth rotation, using a large-area (11cm²) cold-atom dual-axis interferometer. This work demonstrates a level of agreement with theoretical expectation of 25 parts-per-million.**

Keywords—Inertial sensor; Sagnac Effect; cold-atoms; atom-interferometer.

I. Introduction

In 1913, Georges Sagnac performed an experiment where for the first time, a phase-shift in an interferometer induced by rotation was reported [1]. This phase is expressed as,

$$\Phi_\Omega = \frac{4\pi E}{hc^2}\vec{\mathcal{A}}.\vec{\Omega}_E \quad , \tag{1}$$

where, E is the energy of the particles ($h\nu$ for photons and mc^2 for massive particles), $\vec{\mathcal{A}}$ the area vector of the interferometer, and $\vec{\Omega}_E$ is the Earth's angular velocity. Despite the interpretations of Sagnac himself on his work relating it to an eather theory, the study of this effect paved the way to technological breakthroughs in positioning systems and inertial sensors such as ring-laser gyroscopes and fiber-optic gyroscopes. Many experiments succeeded over the years [2] with an increasing level of precision. The interest of measuring this effect using matter-waves rise from the remarkable performance of atom interferometry and the mastery of controlling the light-matter interaction processes. Indeed, cold-atom interferometer represents the state-of-art wave-matter sensor [3].

II. Methods/Results

A. Experimental setup

The experimental apparatus used in this work is described in more details in our recent paper [4]. Figure 1.a sketches the essential of the experimental dispositive. Here, cesium atoms are trapped inside a 3D MOT, cooled down to a temperature of about 1.8µK, then launched at 5 m.s^{-1} toward the interrogation region.

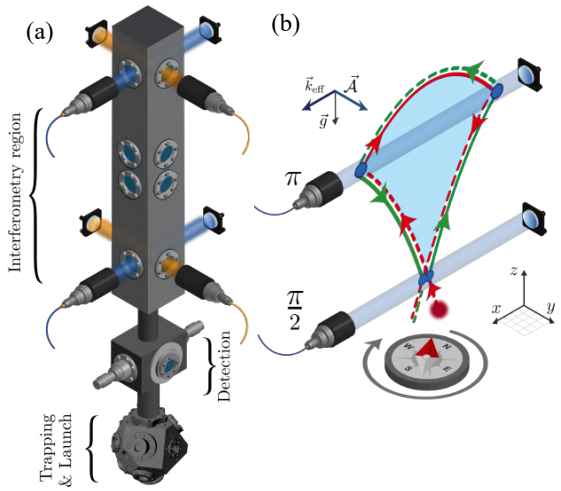

Figure 1: (a) Sketch of vacuum chamber showing the axis. Atom being trapped and cooled inside the 3D MOT (bottom), launched toward the interferometry region where retro-reflected Raman beams interrogate the atoms along two possible axis x (blue) or y (orange). At the decent atoms pass through the detection region to measure the transition probability via fluorescence means. (b) Space diagram of the trajectories of the atoms inside the interferometer (not to scale). The ^{133}Cs atoms are launched in the state $|F=4\rangle$. As soon as they enter the interrogation region, a first $\pi/2$ pulse (blue dots), opens the arms of the interferometer (green and red) by creating a coherent superposition of states $|F=3\rangle$ (solid) and $|F=4\rangle$ (dashed), acting as a beam-splitter. The second and the third pulses π (mirror pulses), redirect the atoms, and finally, at the output, the fourth pulse recombine the arms. The physical area of 11cm^2 opened by the interferometer is highlighted in cyan. The compass represents the orientation of the interferometer toward the geographical north.

The atoms further go through a sequence of four laser pulses with rabi areas π/2-π-π-π/2. These perform two-photon Raman transitions which provide internal and external control over the matter-waves. The four-pulse sequence shapes the geometry of the interferometer by redirecting the atoms along the two arms forming two opposite loops (Figure 1.b). The difference of the accumulated phase along the two paths for this sequence reads:

$$\Phi_\Omega = \frac{T^3}{2}\left(\vec{k}_{\text{eff}} \times \vec{g}\right).\vec{\Omega}_E \cos(\psi) \, , \tag{2}$$

where, $2T \approx 800$ms is the total interrogation time and $\vec{k}_{\text{eff}}$ is the effective wave-vector of the Raman beams. Also, the two pairs

of Raman beam point in two orthogonal directions (x and y) allowing to measure the two components of the projection of the rotation rate on the horizontal plane for a given orientation of the experiment. On their way down, after the interferometer sequence, the atoms pass through a fluorescence-based detection system that allows to measure the output of the interferometer (i.e., the transition probability). The latter is directly linked to the phase difference Φ_Ω.

B. Sagnac effect scale factor measurement

We further can expand the phase Φ_Ω in (2) as follows:

$$\Phi_\Omega = \frac{T^3}{2} k_{\text{eff}}\, g \cos(\theta_0) \times \Omega_E \cos(\psi) \times \cos(\theta - \theta_N), \qquad (3)$$

where θ_0 is the tilt angle of the collimators[1], ψ is the astronomic latitude of the experiment, and θ is the relative angle of the experiment towards the true North. We shall note that the quantities that appears in the first term can be determined using frequency measurements, which imply an accurate knowledge of the interferometer's area.

Prior to the measurements, we ensure that the atomic trajectory is aligned by setting the parallelism of the Raman mirrors and that the launch velocity is along local $\vec{g}$ at the 200 nrad level of accuracy using a dedicated procedure [5].

The whole experiment rests on a rotation stage that allows to change the orientation of the interferometer's area toward the geographic North. By varying this angle, one can measure the full amplitude of the Sagnac effect and precisely determine the scale factor of the interferometer.

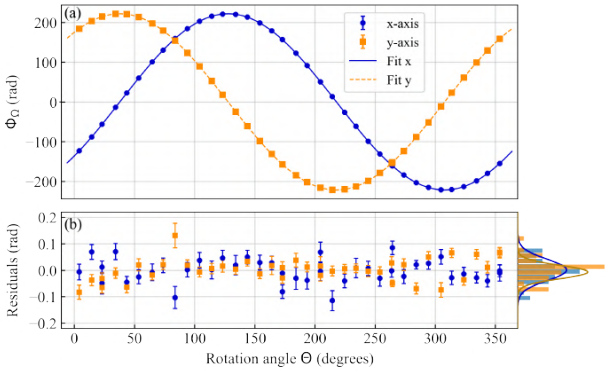

Figure 2: Typical dataset of Sagnac phase measurement on two axes of the interferometer. (A) Measured phase along x-axis (blue dots) and y-axis (orange squares) as a function of the relative orientation angle of the experiment. Each point is the result of averaging ~2000 interferometer cycles. The lines are the resultant fit with a cosine function. (B) The residual of the fitting for both axes. The error distribution shows a standard deviation of 40 mrad (25 mrad) for the x-axis (y-axis), represented with the histogram at the right side.

For a better statistical analysis, we repeated this measurement over three months and a campaign of measurements was conducted resulting six datasets for each axis of the interferometer. Each set of data correspond to a week of measurement, where the interferometer is rotated one full turn with steps of 10 degrees (Figure 2). The two axes help to gain confidence and test the agreement between x and y interferometers. In addition, we varied parameters in the scale factor (such as the interrogation time T), demonstrating the fine control and reproducibility of interferometer's scale factor.

III. DISCUSSION/INTERPRETATION

A complete analysis of the different contributions to the measured phase, considering systematic effects and higher order terms, gave an expected value of 221.5677(3) rad and 221.5523(2) rad for the x-axis and y-axis, respectively, associated with a relative uncertainty of 1.2 ppm. The error budget is dominated by the knowledge of the exact latitude of the experiment taking into account the correction due to deflection to the North when using the geoid model of the Earth. The results extracted from a typical dataset (Figure 2), reveals values of 221.527(9) rads for the x-axis and 221.561(8) rads for y-axis, showing a good agreement with the predicted values. Moreover, the overall statistics of the six taken datasets, gave a mean value close to zero for the difference between the measurements and the theoretical expectation, leading to an uncertainty of 25 ppm. The main limitation of the cold-atom gyroscope for this test comes from the drift of the mirrors alignment due to environmental factors accumulated during long periods of measurement (one week).

IV. CONCLUSIONS

This work demonstrates an improvement of a factor twenty on the measurement of the Sagnac effect with matter-waves compared to previous realizations [6]. Probing rotations with such precision, the cold-atom gyroscope opens new horizons to test other fundamental theories such as the Standard Model Extension or Gödel model of rotating universe. On the other hand, it stands as a powerful tool for technological applications, especially for rotational seismology and inertial navigation systems.

References

[1] G. Sagnac, "L'éther lumineux démontré par l'effet du vent relatif à l'éther dans un interféromètre en rotation uniforme, " C. R. Acad. Sci. (Paris), vol. 157, p. 708, 1913

[2] A. Gebauer, M. Tercjak, K. U. Schreiber, H. Igel, J. Kodet, U. Hugentobler, J. Wassermann, F. Bernauer, C.-J. Lin, S. Donner, S. Egdorf, A. Simonelli, and J.-P. R. Wells, "Reconstruction of the instantaneous earth rotation vector with sub-arcsecond resolution using a large scale ring laser array," Phys. Rev. Lett., vol. 125, p. 033605, 2020.

[3] R. Geiger, A. Landragin, S. Merlet, and F. Pereira Dos Santos, "High-accuracy inertial measurements with cold-atom sensors." AVS Quantum Science, 2(2), p. 024702, 2020.

[4] D. Savoie, M. Altorio, B. Fang, L. A. Sidorenkov, R. Geiger, and A. Landragin, "Interleaved atom interferometry for high-sensitivity inertial measurements," Sci Adv, vol. 4, no. 12, p. eaau7948, 2018.

[5] M. Altorio, L. A.Sidorenkov, R. Gautier, D. Savoie, A. Landragin, and R. Geiger, "Accurate trajectory alignment in cold-atom interferometers with separated laser beams ". Phys. Rev. A, vol. 116, p. 033606, 2020.

[6] J. K., Stockton, K. Takase, and M. A. Kasevich. "Absolute geodetic rotation measurement using atom interferometry." Phys. Rev. Lett., 107.13, 2011.

[1] The Raman collimators are tilted with an angle $\theta_0 \approx 4°$ in order to remove the degeneracy of two the state $\pm k_{\text{eff}}$ [4].

Dual axis cold-atom gyroscope

M. Guessoum, R. Gautier, Q. Bouton, L. A. Sidorenkov, R. Geiger and A. Landragin

LNE-SYRTE, Observatoire de Paris, Université PSL, CNRS, Sorbonne Université
61 avenue de l'Observatoire, 75014 Paris

Applications

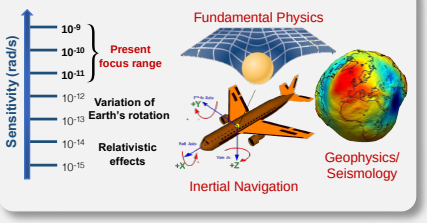

Manipulating matter waves

Raman pulses

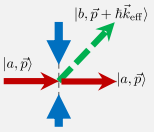

Couple **Internal** states and **External** momentum of the atom.

Momentum transfer $|\vec{k}_{\text{eff}}| \approx 7\ \text{mm.s}^{-1}$

Mirror / Beamsplitter

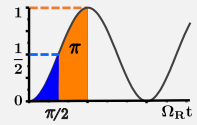

Controling **pulse duration** to implement coherent superposition (**beamsplitter**) or tansfer from one state to another (**mirror**).

Imprinted phase

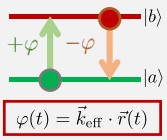

$$\varphi(t) = \vec{k}_{\text{eff}} \cdot \vec{r}(t)$$

Position dependent laser phase *imprinted* on the diffracted matter-wave.

Sagnac Effect

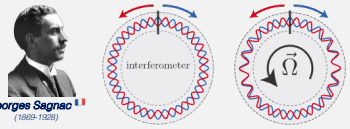

The **phase-shift** induced by a **rotating** interferometer

$$\Delta\Phi_\Omega = \frac{4\pi E}{hc^2}\vec{\mathcal{A}}\cdot\vec{\Omega}$$

$\vec{\mathcal{A}}$: Physical area. E : Particle's energy. $\frac{E_{\text{atom}}}{E_{\text{photon}}} \sim 10^{11}$

4-pulse interferometer

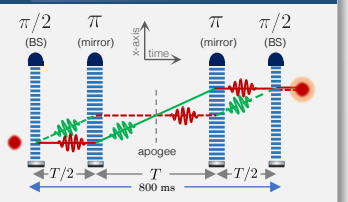

Due to symmetry, **zero sensitivity to DC accelerations.**

Interleaved measurements

3 interferometers per interrogation time 2T=801 ms.
3.75 Hz samplerate (**no deadtimes**)

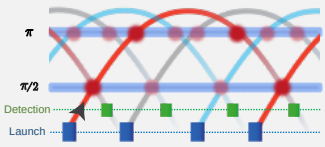

The π/2 pulses are shared between the clouds entering and exiting each interferometer.

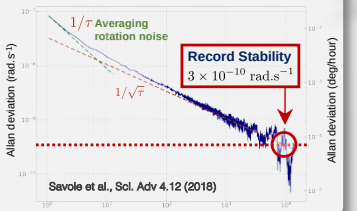

Savoie et al., Sci. Adv 4.12 (2018)

Dual-axis gyroscope

Orthogonal Raman beams enables measurement of two projections Ω_x and Ω_y for the same orientation.

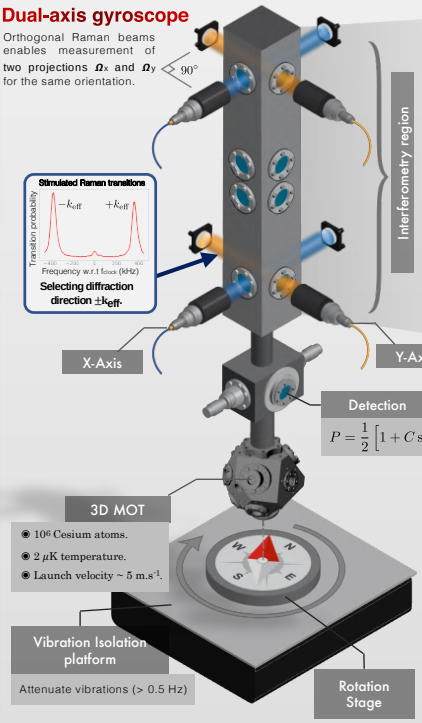

Trajectories

(not-to-scale)

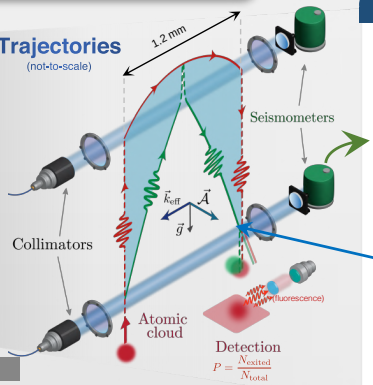

Detection

$$P = \frac{1}{2}\left[1 + C\sin(\Phi_\Omega + \delta\tilde{\Phi})\right]$$

$$\Phi_\Omega = \frac{T^3}{2}\left(\vec{k}_{\text{eff}} \times \vec{g}\right)\cdot\vec{\Omega}$$

Large area $\mathcal{A} \sim 11\ \text{cm}^2$

Vibration correlation

Extremely sensitive to **vibrations**.
Classical sensors are used to estimate their contribution ($\sigma = 6$ rads) in order to identify **fringes**.

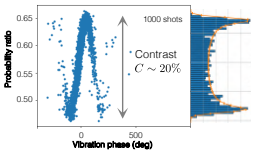

Real-Time compensation

Compensating vibrations using the **laser phase**

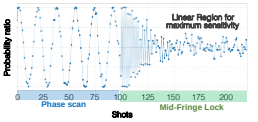

$$P = \frac{1}{2}\left[1 + C\sin(\Phi_\Omega + \Phi_{\text{vib}} + \Phi_{\text{RTC}} + \Phi_{\text{laser}})\right]$$

Lautier et al, Applied Phys. Lett. 105 144102 (2014)

Trajectories allignement

Misalignement of retro-reflecting mirrors (**parallelism**) and trajectories of the atoms (**launch velocity**) are coupled, arising a phase shift bias.

$$\Delta\Phi = 2k_{\text{eff}}\delta\vec{v}\cdot\delta\vec{\theta} \qquad \delta\vec{v} = \vec{v} - \vec{v}_{\text{opt}}$$

Sensitivity: 12 mrad / mm.s⁻¹ / μrad

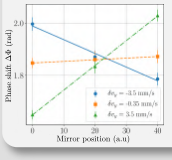

Find the **optimal launch velocity** → zero slope.

Accuracy levels:
- Parallelism: zeroed within 0.2 μrad
- Launch velocity: set within 0.2 mm.s⁻¹

Fine tuned phase bias to 0.5 mrad.

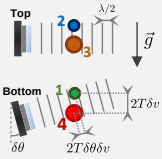

Altorio, M., et al. * Physical Review A 101.3 (2020)

Tailoring multi-loop atom interferometers

Non perfect atomic mirrors leads to leaked matter-waves that result **spurious interferometer**.

▶ Asymmetric time-shift for the π-pulses

Flaws: Breaks symmetry which induce sensitivity to DC acceleration.

Solution: Alternating $\pm\Delta T_a$ measurements.

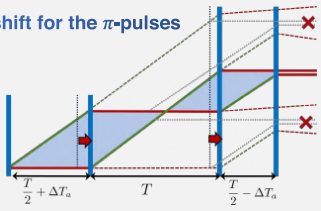

▶ Adjustable momentum transfer (AMT)

Introducing a difference in modulus of k_{eff} between the top and bottom beams compensated with a **symmetrical time shift**.

$$\Delta T_s = \frac{T\epsilon}{2(1-\epsilon)}$$

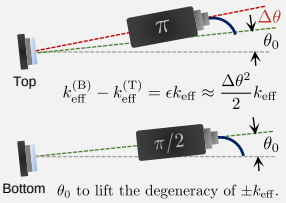

Modifies sensitivity to rotation

$$\Phi_{\text{rot}} = (1 - \frac{2\epsilon}{3})\Phi_\Omega$$

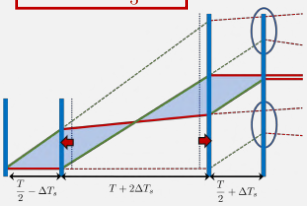

Immune against DC acceleration

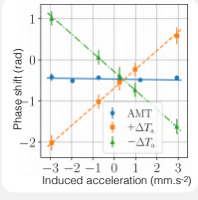

L. A. Sidorenkov, et al., Phys. Rev. Lett. 125, 213201 (2020)

Sagnac Effect Measurement with 25 ppm accuracy

$$\Phi_\Omega(\Theta) = \underbrace{\frac{T^3}{2}k_{\text{eff}}g\cos\theta_0}_{\text{Scale factor}} \times \underbrace{\cos(\psi)\Omega_E}_{\text{Earth rotation rate}} \times \underbrace{\cos(\Theta - \Theta_N)}_{\text{Orientation toward north}}$$

Scale factor (Determined using time-frequency measurements) — Latitude

Main term:
The phase shift of the projection of the **earth's angular velocity** on the **interferometer's area.**

Recorded on the two axes of the gyroscope for 360° rotation.

Typical dataset of the Sagnac Phase Measurement

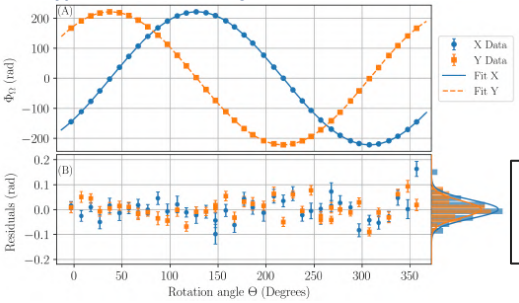

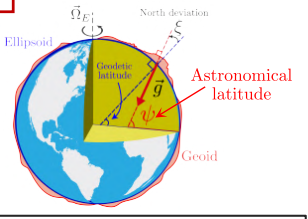

- ▶ Each phase point is the result of ~20 minutes of integration time.
- ▶ One full datasets takes one week to complete.
- ▶ **Current limitation:** drift of trajectories allignement due to environmental factors.

Statistics for total of 6 datasets, ranging 3 months

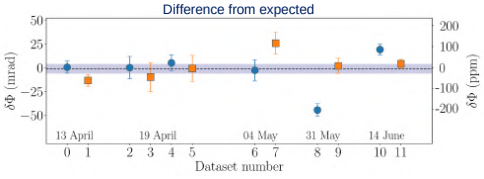

Gautier, R., et al. Submitted for publication (2022)

Perspectives

Fundamental physics

- ▶ Testing Sagnac Effect by measuring over one year
- ▶ Search for smaller signals beyond Earth rotation: solar system, galaxy or universe (Gödel model).

Geophysics/Seismology

- ▶ Local gravity direction (north deviation) measurements at the level of few arcseconds.
- ▶ Toward applications with precise sensing for rotational seismology.

IACI Team
syrte.obspm.fr

Bibliography

[1] M. Kasevich and S. Chu. "Atomic Interferometry Using Stimulated Raman Transitions". In: *Physical Review Letters* 67.2 (July 1991), pp. 181–184 (cited on pages 7, 13).

[2] F. Riehle, T. Kisters, A. Witte, J. Helmcke, and C. J. Bordé. "Optical Ramsey Spectroscopy in a Rotating Frame: Sagnac Effect in a Matter-Wave Interferometer". In: *Physical Review Letters* 67.2 (July 1991), pp. 177–180 (cited on pages 7, 79).

[3] N. F. Ramsey. "History of Atomic Clocks". In: *Journal of Research of the National Bureau of Standards (1977)* 88.5 (1983), pp. 301–320 (cited on page 7).

[4] S. Bize et al. "Cold Atom Clocks and Applications". In: *Journal of Physics B: Atomic, Molecular and Optical Physics* 38.9 (Apr. 2005), S449 (cited on page 7).

[5] M. Kasevich and S. Chu. "Measurement of the Gravitational Acceleration of an Atom with a Light-Pulse Atom Interferometer". In: *Applied Physics B* 54.5 (May 1992), pp. 321–332 (cited on page 7).

[6] J. M. McGuirk, G. T. Foster, J. B. Fixler, M. J. Snadden, and M. A. Kasevich. "Sensitive Absolute-Gravity Gradiometry Using Atom Interferometry". In: *Physical Review A* 65.3 (Feb. 2002), p. 033608 (cited on page 7).

[7] T. L. Gustavson, A. Landragin, and M. A. Kasevich. "Rotation Sensing with a Dual Atom-Interferometer Sagnac Gyroscope". In: *Classical and Quantum Gravity* 17.12 (June 2000), p. 2385 (cited on pages 7, 10).

[8] M. Hauth, C. Freier, V. Schkolnik, A. Senger, M. Schmidt, and A. Peters. "First Gravity Measurements Using the Mobile Atom Interferometer GAIN". In: *Applied Physics B* 113.1 (Oct. 2013), pp. 49–55 (cited on page 7).

[9] T. Farah et al. "Underground Operation at Best Sensitivity of the Mobile LNE-SYRTE Cold Atom Gravimeter". In: *Gyroscopy and Navigation* 5.4 (Oct. 2014), pp. 266–274 (cited on pages 7, 96).

[10] P. Gillot, O. Francis, A. Landragin, F. P. D. Santos, and S. Merlet. "Stability Comparison of Two Absolute Gravimeters: Optical versus Atomic Interferometers". In: *Metrologia* 51.5 (June 2014), p. L15 (cited on page 7).

[11] C. Janvier, V. Ménoret, B. Desruelle, S. Merlet, A. Landragin, and F. Pereira dos Santos. "Compact Differential Gravimeter at the Quantum Projection-Noise Limit". In: *Physical Review A* 105.2 (Feb. 2022), p. 022801 (cited on page 7).

[12] B. Altschul et al. "Quantum Tests of the Einstein Equivalence Principle with the STE–QUEST Space Mission". In: *Advances in Space Research* 55.1 (Jan. 2015), pp. 501–524 (cited on page 7).

[13] L. Morel, Z. Yao, P. Cladé, and S. Guellati-Khélifa. "Determination of the Fine-Structure Constant with an Accuracy of 81 Parts per Trillion". In: *Nature* 588.7836 (Dec. 2020), pp. 61–65 (cited on page 7).

[14] G. Rosi, F. Sorrentino, L. Cacciapuoti, M. Prevedelli, and G. M. Tino. "Precision Measurement of the Newtonian Gravitational Constant Using Cold Atoms". In: *Nature* 510.7506 (June 2014), pp. 518–521 (cited on page 7).

[15] B. Canuel et al. "Exploring Gravity with the MIGA Large Scale Atom Interferometer". In: *Scientific Reports* 8.1 (Sept. 2018), p. 14064 (cited on pages 7, 98).

[16] A. D. King and M. E. Systems. "Inertial Navigation - Forty Years of Evolution". In: *GEC REVIEW* 13.3 (1998) (cited on page 8).

[17] C. W. F. Everitt et al. "Gravity Probe B: Final Results of a Space Experiment to Test General Relativity". In: *Physical Review Letters* 106.22 (May 2011), p. 221101. arXiv: 1105.3456 [gr-qc] (cited on pages 8, 10).

[18] P. G. Savage. "Blazing Gyros: The Evolution of Strapdown Inertial Navigation Technology for Aircraft". In: *Journal of Guidance, Control, and Dynamics* 36.3 (2013), pp. 637–655 (cited on page 8).

[19] *RAFALE : Les équipementiers* (cited on page 8).

[20] F. Bernauer et al. "BlueSeis3A: Full Characterization of a 3C Broadband Rotational Seismometer". In: *Seismological Research Letters* 89.2A (Jan. 2018), pp. 620–629 (cited on pages 8, 10, 96).

[21] F. Delhaye. "HRG by SAFRAN: The Game-Changing Technology". In: *2018 IEEE International Symposium on Inertial Sensors and Systems (INERTIAL)*. Mar. 2018, pp. 1–4 (cited on pages 8, 10).

[22] V. Ménoret et al. "Gravity Measurements below 10-9 g with a Transportable Absolute Quantum Gravimeter". In: *Scientific Reports* 8.1 (Aug. 2018), p. 12300 (cited on pages 8, 96).

[23] *GG1320AN Digital Ring Laser Gyroscope*. https://aerospace.honeywell.com/us/en/products-and-services/product/hardware-and-systems/sensors/gg1320an-digital-ring-laser-gyroscope (cited on page 10).

[24] K. U. Schreiber, T. Klügel, J.-P. R. Wells, R. B. Hurst, and A. Gebauer. "How to Detect the Chandler and the Annual Wobble of the Earth with a Large Ring Laser Gyroscope". In: *Physical Review Letters* 107.17 (Oct. 2011), p. 173904 (cited on page 10).

[25] A. D. V. Di Virgilio et al. "Underground Sagnac Gyroscope with Sub-Prad/s Rotation Rate Sensitivity: Toward General Relativity Tests on Earth". In: *Physical Review Research* 2.3 (Sept. 2020), p. 032069 (cited on page 10).

[26] W.-J. Xu et al. "Effects of Wave-Front Tilt and Air Density Fluctuations in a Sensitive Atom Interferometry Gyroscope". In: *Optics Express* 28.8 (Apr. 2020), pp. 12189–12200 (cited on page 10).

[27] Z.-W. Yao et al. "Self-Alignment of a Large-Area Dual-Atom-Interferometer Gyroscope Using Parameter-Decoupled Phase-Seeking Calibrations". In: *Physical Review A* 103.2 (Feb. 2021), p. 023319 (cited on page 10).

[28] P. Berg et al. “Composite-Light-Pulse Technique for High-Precision Atom Interferometry”. In: *Physical Review Letters* 114.6 (Feb. 2015), p. 063002 (cited on page 10).

[29] A. Gauguet, B. Canuel, T. Lévèque, W. Chaibi, and A. Landragin. “Characterization and Limits of a Cold-Atom Sagnac Interferometer”. In: *Physical Review A* 80.6 (Dec. 2009), p. 063604 (cited on pages 10, 79).

[30] T. W. Kornack, R. K. Ghosh, and M. V. Romalis. “Nuclear Spin Gyroscope Based on an Atomic Comagnetometer”. In: *Physical Review Letters* 95.23 (Nov. 2005), p. 230801 (cited on page 10).

[31] O. Avenel, Y. Mukharsky, and E. Varoquaux. “Superfluid Gyrometers”. In: *Journal of Low Temperature Physics* 135.5 (June 2004), pp. 745–772 (cited on page 10).

[32] M. P. Ledbetter, K. Jensen, R. Fischer, A. Jarmola, and D. Budker. “Gyroscopes Based on Nitrogen-Vacancy Centers in Diamond”. In: *Physical Review A* 86.5 (Nov. 2012), p. 052116 (cited on page 10).

[33] A. Gauguet. “Gyromètre à Atomes Froids : Étude de La Stabilité Limite et Des Effets Systématiques Liés Aux Séparatrices Lasers”. These de Doctorat. Paris 6, Jan. 2008 (cited on pages 11, 31, 40, 97).

[34] T. Lévèque. “Développement d’un Gyromètre à Atomes Froids de Haute Sensibilité Fondé Sur Une Géométrie Repliée”. These de Doctorat. Paris 6, Jan. 2010 (cited on pages 11, 31, 97).

[35] M. Meunier. “Etude d’un Gyromètre à Ondes de Matière de Très Grande Aire”. These de Doctorat. Paris 6, Jan. 2013 (cited on pages 11, 31, 40).

[36] I. Dutta. “Stability Improvement of a Sagnac Cold Atom Interferometer : Towards Continuous Operation”. These de Doctorat. Paris 6, Nov. 2015 (cited on pages 11, 31, 40).

[37] D. Savoie. “Fonctionnements Continu et Entrelacé d’un Gyromètre à Atomes Froids et Amélioration de Sa Stabilité”. These de Doctorat. Paris 6, Nov. 2017 (cited on pages 11, 31, 40).

[38] M. Altorio. “Novel Atom Interferometry Techniques for a Cold-Atom Gyroscope of Large Sagnac Area”. These de Doctorat. Sorbonne université, Dec. 2019 (cited on pages 11, 31, 65).

[39] C. J. Bordé. “Atomic Interferometry with Internal State Labelling”. In: *Physics Letters A* 140.1 (Sept. 1989), pp. 10–12 (cited on page 13).

[40] H. J. Lee, C. S. Adams, M. Kasevich, and S. Chu. “Raman Cooling of Atoms in an Optical Dipole Trap”. In: *Physical Review Letters* 76.15 (Apr. 1996), pp. 2658–2661 (cited on page 19).

[41] D. A. Steck. “Cesium D Line Data”. In: (2003) (cited on page 20).

[42] R. Geiger. “Senseur Inertiel à Ondes de Matière Aéroporté”. These de Doctorat. Paris 11, Oct. 2011 (cited on pages 25, 55).

[43] P. Storey and C. Cohen-Tannoudji. “The Feynman Path Integral Approach to Atomic Interferometry. A Tutorial”. In: *Journal de Physique II* 4.11 (Nov. 1994), pp. 1999–2027 (cited on page 25).

[44] P. Cheinet, B. Canuel, F. Pereira Dos Santos, A. Gauguet, F. Yver-Leduc, and A. Landragin. "Measurement of the Sensitivity Function in a Time-Domain Atomic Interferometer". In: *IEEE Transactions on Instrumentation and Measurement* 57.6 (June 2008), pp. 1141–1148 (cited on page 27).

[45] R. Gautier. "Mesures de Précision Avec Un Gyromètre-Accéléromètre à Atomes Froids Double Axes". These de Doctorat. Sorbonne université, June 2022 (cited on pages 31, 47, 48, 63).

[46] A. Clairon, C. Salomon, S. Guellati, and W. D. Phillips. "Ramsey Resonance in a Zacharias Fountain". In: *Europhysics Letters* 16.2 (Sept. 1991), p. 165 (cited on page 34).

[47] N. Mielec et al. "Atom Interferometry with Top-Hat Laser Beams". In: *Applied Physics Letters* 113.16 (Oct. 2018), p. 161108 (cited on page 39).

[48] N. Mielec. "Études Pour Un Résonateur Optique à Profil d'intensité Plat et Son Application à l'interférométrie Atomique". These de Doctorat. Paris Sciences et Lettres (ComUE), Sept. 2018 (cited on page 39).

[49] D. Savoie, M. Altorio, B. Fang, L. A. Sidorenkov, R. Geiger, and A. Landragin. "Interleaved Atom Interferometry for High-Sensitivity Inertial Measurements". In: *Science Advances* 4.12 (Dec. 2018), eaau7948 (cited on pages 40, 62).

[50] R. Karcher, F. P. Dos Santos, and S. Merlet. "Impact of Direct-Digital-Synthesizer Finite Resolution on Atom Gravimeters". In: *Physical Review A* 101.4 (Apr. 2020), p. 043622 (cited on page 48).

[51] T. Lévèque, A. Gauguet, W. Chaibi, and A. Landragin. "Low Noise Amplification of an Optically Carried Microwave Signal: Application to Atom Interferometry". In: *Applied Physics B* 101.4 (Dec. 2010), pp. 723–729 (cited on page 48).

[52] G. Santarelli, C. Audoin, A. Makdissi, P. Laurent, G. Dick, and A. Clairon. "Frequency Stability Degradation of an Oscillator Slaved to a Periodically Interrogated Atomic Resonator". In: *IEEE Transactions on Ultrasonics, Ferroelectrics, and Frequency Control* 45.4 (July 1998), pp. 887–894 (cited on page 61).

[53] I. Dutta et al. "Continuous Cold-Atom Inertial Sensor with $1\mathrm{nrad}/\mathrm{sec}$ Rotation Stability". In: *Physical Review Letters* 116.18 (May 2016), p. 183003 (cited on page 61).

[54] L. Zhou et al. "Test of Equivalence Principle at $1{0}{\ensuremath{-}8}$ Level by a Dual-Species Double-Diffraction Raman Atom Interferometer". In: *Physical Review Letters* 115.1 (July 2015), p. 013004 (cited on page 63).

[55] T. Lévèque, A. Gauguet, F. Michaud, F. Pereira Dos Santos, and A. Landragin. "Enhancing the Area of a Raman Atom Interferometer Using a Versatile Double-Diffraction Technique". In: *Physical Review Letters* 103.8 (Aug. 2009), p. 080405 (cited on page 64).

[56] J. R. Kellogg, N. Yu, J. M. Kohel, R. J. Thompson, D. C. Aveline, and L. Maleki. "Longitudinal Coherence in Cold Atom Interferometry". In: *Journal of Modern Optics* 54.16-17 (Nov. 2007), pp. 2533–2540 (cited on page 65).

[57] G. Sagnac. "L'éther Lumineux Démontré Par l'effet Du Vent Relatif d'éther Dans Un Interféromètre En Rotation Uniforme". In: *CR Acad. Sci.* 157 (1913), pp. 708–710 (cited on page 79).

[58] P. Langevin. “Sur La Théorie de Relativité et l’expérience de M. Sagnac”. In: *CR Acad. Sci* 173 (1921), pp. 831–834 (cited on page 79).

[59] A. A. Michelson and H. G. Gale. “The Effect of the Earth’s Rotation on the Velocity of Light”. In: *Nature* 115.2894 (Apr. 1925), pp. 566–566 (cited on page 79).

[60] W. M. Macek and D. T. M. Davis Jr. “Rotation Rate Sensing with Traveling-wave Ring Lasers”. In: *Applied Physics Letters* 2.3 (Nov. 2004), pp. 67–68 (cited on page 79).

[61] V. Vali and R. W. Shorthill. “Fiber Ring Interferometer”. In: *Applied Optics* 15.5 (May 1976), pp. 1099–1100 (cited on page 79).

[62] H. C. Lefèvre. “The Fiber-Optic Gyroscope, a Century after Sagnac’s Experiment: The Ultimate Rotation-Sensing Technology?” In: *Comptes Rendus Physique*. The Sagnac Effect: 100 Years Later / L’effet Sagnac : 100 Ans Après 15.10 (Dec. 2014), pp. 851–858 (cited on page 79).

[63] J. E. Zimmerman and J. E. Mercereau. “Compton Wavelength of Superconducting Electrons”. In: *Physical Review Letters* 14.22 (May 1965), pp. 887–888 (cited on page 79).

[64] S. A. Werner, J. .-. Staudenmann, and R. Colella. “Effect of Earth’s Rotation on the Quantum Mechanical Phase of the Neutron”. In: *Physical Review Letters* 42.17 (Apr. 1979), pp. 1103–1106 (cited on page 79).

[65] F. Hasselbach and M. Nicklaus. “Sagnac Experiment with Electrons: Observation of the Rotational Phase Shift of Electron Waves in Vacuum”. In: *Physical Review A* 48.1 (July 1993), pp. 143–151 (cited on page 79).

[66] K. Schwab, N. Bruckner, and R. E. Packard. “Detection of the Earth’s Rotation Using Superfluid Phase Coherence”. In: *Nature* 386.6625 (Apr. 1997), pp. 585–587 (cited on page 79).

[67] R. W. Simmonds, A. Marchenkov, E. Hoskinson, J. C. Davis, and R. E. Packard. “Quantum Interference of Superfluid 3He”. In: *Nature* 412.6842 (July 2001), pp. 55–58 (cited on page 79).

[68] K. C. Wright, R. B. Blakestad, C. J. Lobb, W. D. Phillips, and G. K. Campbell. “Driving Phase Slips in a Superfluid Atom Circuit with a Rotating Weak Link”. In: *Physical Review Letters* 110.2 (Jan. 2013), p. 025302 (cited on page 79).

[69] A. Lenef, T. D. Hammond, E. T. Smith, M. S. Chapman, R. A. Rubenstein, and D. E. Pritchard. “Rotation Sensing with an Atom Interferometer”. In: *Physical Review Letters* 78.5 (Feb. 1997), pp. 760–763 (cited on page 79).

[70] L. A. Sidorenkov, R. Gautier, M. Altorio, R. Geiger, and A. Landragin. “Tailoring Multiloop Atom Interferometers with Adjustable Momentum Transfer”. In: *Physical Review Letters* 125.21 (Nov. 2020), p. 213201 (cited on pages 81, 85).

[71] M. Altorio, L. A. Sidorenkov, R. Gautier, D. Savoie, A. Landragin, and R. Geiger. “Accurate Trajectory Alignment in Cold-Atom Interferometers with Separated Laser Beams”. In: *Physical Review A* 101.3 (Mar. 2020), p. 033606 (cited on page 87).

[72] R. Gautier, M. Guessoum, L. A. Sidorenkov, Q. Bouton, A. Landragin, and R. Geiger. “Accurate Measurement of the Sagnac Effect for Matter Waves”. In: *Science Advances* 8.23 (June 2022), eabn8009 (cited on page 91).

[73] S. Moseley, N. Scaramuzza, J. D. Tasson, and M. L. Trostel. "Lorentz Violation and Sagnac Gyroscopes". In: *Physical Review D* 100.6 (Sept. 2019), p. 064031 (cited on page 96).

[74] W. H. K. Lee. "Rotational Seismology". In: *Encyclopedia of Natural Hazards*. Ed. by P. T. Bobrowsky. Encyclopedia of Earth Sciences Series. Dordrecht: Springer Netherlands, 2013, pp. 877–879 (cited on page 96).

[75] S. Donner, M. Bernauer, and H. Igel. "Inversion for Seismic Moment Tensors Combining Translational and Rotational Ground Motions". In: *Geophysical Journal International* 207.1 (Oct. 2016), pp. 562–570 (cited on page 96).

[76] Z. Li and M. van der Baan. "Elastic Passive Source Localization Using Rotational Motion". In: *Geophysical Journal International* 211.2 (Nov. 2017), pp. 1206–1222 (cited on page 96).

[77] S. Yuan et al. "Six Degree-of-Freedom Broadband Ground-Motion Observations with Portable Sensors: Validation, Local Earthquakes, and Signal Processing". In: *Bulletin of the Seismological Society of America* 110.3 (May 2020), pp. 953–969 (cited on pages 96, 116).

[78] E. M. Rasel, M. K. Oberthaler, H. Batelaan, J. Schmiedmayer, and A. Zeilinger. "Atom Wave Interferometry with Diffraction Gratings of Light". In: *Physical Review Letters* 75.14 (Oct. 1995), pp. 2633–2637 (cited on page 97).

[79] B. Canuel et al. "Six-Axis Inertial Sensor Using Cold-Atom Interferometry". In: *Physical Review Letters* 97.1 (July 2006), p. 010402 (cited on page 97).

[80] J. Le Gouët et al. "Influence of Lasers Propagation Delay on the Sensitivity of Atom Interferometers". In: *The European Physical Journal D* 44.3 (Sept. 2007), pp. 419–425 (cited on page 98).

[81] I. Perrin et al. "Zero-Velocity Atom Interferometry Using a Retroreflected Frequency-Chirped Laser". In: *Physical Review A* 100.5 (Nov. 2019), p. 053618 (cited on page 98).

[82] D. N. Aguilera et al. "STE-QUEST—Test of the Universality of Free Fall Using Cold Atom Interferometry". In: *Classical and Quantum Gravity* 31.11 (May 2014), p. 115010 (cited on page 116).

[83] S. Abend et al. "Technology Roadmap for Cold-Atoms Based Quantum Inertial Sensor in Space". In: *AVS Quantum Science* 5.1 (Mar. 2023), p. 019201 (cited on page 116).